CZECH TECHNICAL UNIVERSITY IN PRAGUE
FACULTY OF NUCLEAR SCIENCES AND PHYSICAL ENGINEERING

DOCTORAL THESIS

Numerical Modeling of Nonlocal Energy Transport in Laser-Heated Plasmas

Praha 2016   Milan HOLEC

Bibliografický záznam

Bibliographic Entry

Abstrakt

Modelování nelokálního transportu energie v laserem generovaném plazmatu není snadnou úlohou. Za účelem začlenit nelokální transport v simulacích plazmatu předkládáme nelokální hydrodynamický model, který zahrnuje jak kinetický, tak klasický popis plazmatu jako tekutiny. Náš model je založen na přímém řešení elektronové a radiační transportní rovnice, kde srážkový BGK operátor zajišťuje přímé provázání transportu energie a modelu plazmové tekutiny. Naše formulace nespojité Galerkinovi metody vysokého řádu je použita k řešení systému BGK transportních rovnic a rovnic energie plazmatu. Kvalita řešení jakéhokoli režimu transportu mezi limitními případy, t.j. difúze a případ volně se pohybujících částic, jsou demonstrovány na numerických příkladech. Jako aplikaci nelokálního hydrodynamického modelu předkládáme výsledky simulací interakce předpulsu ultra-intenzivního laseru s pevnými terči z různých materiálů, a výsledky simulací experimentu laserem generované rázové vlny v plastové pěně, kde se pěna nachází ve stavu ohřáté husté hmoty. Simulace jsou počítány pomocí námi vyvinutého kódu PETE (Plasma Euler and Transport Equations).

Abstract

Modeling of the nonlocal energy transport in laser-heated plasmas is a challenging task. In order to include such a transport into simulations of plasmas, we propose the nonlocal transport hydrodynamic model, which provides a kinetic model and the classical fluid description at the same time. It resides in direct solution of electron and photon transport equations based on the BGK collision operator which gives an inherent coupling of energy transport to the plasma fluid. Our high-order discontinuous Galerkin scheme of the BGK transport equations and the fluid energy equations gives solutions obeying any regime of transport, i.e. between the local diffusion asymptotic and the collisionless transport asymptotic of free-streaming particles, which is demonstrated in the case of exact steady transport and approximate multi-group diffusion numerical tests. As an application of the nonlocal transport hydrodynamic model, we present simulation results of the ultra-intense laser prepulse interaction with solid targets of different atomic numbers, and results of the laser-driven shock in a plastic foam which is related to study of warm-dense-matter state of carbon. The simulations are calculated using our new Plasma Euler and Transport Equations nonlocal transport hydrodynamic code PETE.

Acknowledgements

Contents

Chapter 1

Introduction

Since the discovery that thermonuclear fusion is the source of energy that powers our sun and all the stars, there has been the dream to tame fusion fuel ignition. There have been two desires; to study matter under the extreme conditions needed for fusion burn, and to explore the potential of harnessing the energy released as an attractive energy source for mankind.

Inertial Confinement Fusion (ICF) is one of the major branches of fusion research. Almost all ICF devices to date are using lasers to compress and heat the fuel, which under the conditions known as Lawson criterion would achieve the self ignition. Laser produced plasma is formed when a high power pulsed laser is focused onto a dense medium surface and plays, naturally, an important role in the ICF experiments development. Understanding of the plasma creation process and the plasma behavior then becomes attractive.

The problem of the energy transport is one of the key problems to be solved for successful implementation of inertial confinement fusion. Since most of the absorbed energy of the incident laser radiation deposition takes place near the critical density, the impact on the more deeper placed ignition region is performed by the hydrodynamic motion, i.e. production of shock-wave, and by the nonlocal energy transport, i.e. the energy is carried deep into the plasma by electrons and photons. This energy transport is usually referred as heat flux and determines the heating rate, temperature, and compression ratio of the ICF target [1].

The Knudsen number $K_n = \lambda/L$, where λ is the transported particle mean free path and L the plasma inhomogeneity scale length, is the fundamental quantity characterizing the type of transport regime [2]. When speaking about the nonlocal energy transport in laser-heated plasmas, electrons and photons are those particles responsible for this phenomenon [3]. In the entire text, the Knudsen number related to electrons will be $K_n^e = \lambda_e/L$, where λ_e is the electron mean free path and the Knudsen number of photons will be $K_n^p = \lambda_p/L$, where λ_p is the photon mean free path.

The typical laser-heated plasmas can be divided into three spatial regions being distinguished by the Knudsen number as follows:

- $K_n^{e,p} \in (10^2, \infty)$ - The high Knudsen number corresponds to the region outside the critical density surface of highly ablated plasma. This is a region of high-temperatures, low-density expanding plasma, which creates the corona. Its characteristic is that for photons and electrons it is almost a free streaming medium.

- $K_n^{e,p} \in (10^{-2}, 10^2)$ - The intermediate Knudsen number region, characterized by large temperature and density gradients, is typically created around the critical density, where most of the laser energy is absorbed. It also extends deeper into the target due to the energy transported by electrons and photons. This region

can be characterized by a significant collisionality or opacity with respect to electrons or photons, where, however, neither the collisionality nor opacity is strong enough to cause local thermodynamic equilibrium (LTE).

- $K_n^{e,p} \in (0, 10^{-2})$ - The small Knudsen number correspond to a region of a relatively cold and highly compressed material. This region is highly collisional for electrons and opaque for the most of photons and the resulting transport regime may be considered to be diffusive. This region is also said to be in LTE.

A nice introduction to the quantitative radiation transport can be found in [4]. The process of emission, absorption, and scattering of radiation is due to the strong coupling between radiation and plasma [2, 5, 6]. The effective importance of these processes changes with temperature and density of the medium. Thus, optical properties in the three regions are very different, and they also change with time. Furthermore, the determination of the optical properties from the plasma parameters is not an easy task, which is approximated by atomic codes [7].

When an intense laser radiation irradiates a target of medium or low Z materials, the energy deposited by the laser light first absorbed by the population of free electrons. Subsequently, it is than transported either locally through the hydrodynamic motion and is converted into the kinetic energy of plasma bulk fluid, or nonlocally by thermal electrons and radiation. In the case of greater laser intensity the absorbed energy can be also directly transported by supra-thermal electrons.

In the case of intermediate Knudsen number of photons the radiation transport leads to several effects in the target. First, it can nonlocally couple the time evolution of different parts of the target, and second, the strong emission can produce a net loss of escaping energy. This can reduce the ablative pressure. Eventually, these effects can change the overall plasma hydrodynamics of the target. It is quite clear that the radiation transport plays an important role in hydrodynamic simulations and has to be treated in a detailed way. A special care should be taken to different energy groups of photons, since the photon mean free path varies significantly with respect to the photon frequency. Consequently, the development of simulation tools to be used to predict the plasma dynamics in ICF experiments is a challenging task, either from theoretical or computational point of view.

An extensive, modern, and complete review of the nonlocal transport of electrons was presented in [8, 9], which will serve as a basis for the electron nonlocal transport introduction presented in this work. In the 1950s the so called Spitzer-Harm (SH) heat conduction based on the local Fourier law was derived [10, 11], where the Coulomb collisions of electrons and ions led to the heat conductivity being self consistently dependent on temperature T as $T^{5/2}$ and the temperature gradient.Soon after the first experimental work including high power lasers it was discovered that the SH approach fails to model heat conduction due to the high Knudsen number of electrons K_n^e. It was pointed out that the SH flux overestimated the heat conduction observed in the experiments in order of tens of percents. Consequently, an intensive effort to describe the reasons for real flux inhibition was studied. For example Duderstadt and Moses [12] addressed the inconvenience of the Fourier law under the ICF conditions. Apart from the possible inhibition mechanisms as turbulent transport or magnetic fields, the natural nonlocality of the energy transport was concluded to play an important role in the theoretical study of the failure of the classical heat conduction. Kruer [13] emphasized the importance of the kinetic approach to correctly describe the electron heat transport instead of using the artificial flux inhibition by using the so-called heat flux limiter, which prevailed to be used in the ICF community for many years.

The matter is that different groups of electrons, depending on their velocity (energy), have different mean free paths λ_e, and more importantly K_n^e, and naturally contribute to the heat flux by different means of nonlocality. Consequently, they carry the information on the plasma parameters from the point of their origin into a finite surrounding region of diameter $\approx \lambda_e$. The main consequence of this effect is that the simplest classical SH description [10, 11, 14] is inaccurate in the intermediate Knudsen number region $K_n^e \in (10^{-2}, 10^2)$ and totally fails in the high Knudsen number region $K_n^e \in (10^2, \infty)$. This is due to its theoretical background, where the SH approach is born from the expansion in a small parameter represented by the electron mean free path λ_e. On the contrary, the SH approach works interestingly well in the low Knudsen number region, where $K_n^e < 10^{-2}$.

For example, for a neodymium laser irradiating a solid target, the $\lambda_e \approx 10^{-3}$cm, while the characteristic scale length L at which the electron temperature decays deep in the target is almost always $L < 0.1$cm, i.e. $K_n^e \approx 0.1$ and the electron transport is clearly nonlocal. The same situation is also typical for the interaction of short ($\approx$ 1ps) intense laser pulses with matter. Although the produced plasma does not have time to expand during the laser pulse and its density remains close to that of solids (the plasma electron density is $n_e \approx 10^{23} - 10^{24}$cm^{-3}), which corresponds to a short mean free path ($\lambda_e \approx 10^{-4} - 10^{-5}$cm), a strong skinning of the laser field leads to the appearance of a steep temperature gradient responsible for the characteristic plasma inhomogeneity scale length $L \approx 10^{-5}$cm, and again, the classical SH theory is invalid since $K_n^e > 0.1$.

According to [15] the applicability of SH approach is even more limited in the case of moderate or high-Z plasma, where the electron-ion collisions dominate. They claimed that the Knudsen number should be approximated as $K_n^e = Z\lambda_e/L$, where Z is the plasma ionization level, and that such a definition includes the electron-ion collisions. This is of great importance in the case of indirect ICF settings, where $Z \gg 1$ on the hohlraum wall [16]. Nowadays, there is a lot of experimental data confirming the idea about the nonlocal character of heat transport in laser produced plasmas [17]. Many attempts have been undertaken to develop theoretical models capable to quantitatively explain the experimental data and predicting the character of the energy transport in: actual nuclear fusion conditions [18]; during the heating of solid targets by high contrast short laser pulses; the interaction of the laser radiation with matter [19]; the ablation compression of targets [20]; wide range of phenomena in astrophysical plasma [21]; as well as in studying weakly ionized low temperature plasmas [22]. It has been also found that the nonlocal transport naturally appears in the field of magnetic confinement fusion [23], where $\lambda_e/L > 10^{-2}$ is almost always satisfied at the edge plasma of tokamaks. It can be concluded that an adequate and sufficiently robust theory of the nonlocal transport is still lacking.

The nonlocal transport in plasmas with respect to collisionality has been well studied in some asymptotic cases, such as collisionless plasma described by the Vlasov kinetic equation, i.e. the case of $K_n^e \to \infty$, and the hydrodynamic limit described by a set of highly collisional hydrodynamic equations [24], where i.e. $K_n^e \to 0$.

The most widespread model intending to describe the conductivity of collisional plasma in the entire parameter range is the simplified qualitative model based on the use of the Bhatnagar–Gross–Krook (BGK) [25, 26] collision integral in the kinetic equation for electrons [27]. However, application of the model plasma conductivity obtained in the BGK approach and the corresponding Drude model for the transverse plasma conductivity [27] to fully ionized plasma leads to significant errors in the ranges of moderate and strong collisions [28]. In particular the accuracy of BGK model breaks down in the highly collisional hydrodynamic limit [24].

The theory of the nonlocal transport has been further extended when using the small perturbation approach [29]. An important step towards improving the standard theory was the weakly collisional regime [30], which applies to a quite wide parameter range in which the conductivity of plasma with Coulomb collisions can be described analytically. The construction of a general algorithm using the small perturbation approach for calculating the plasma conductivity without any restrictions to the plasma parameters [31], i.e. a general K_n^e, is of fundamental and practical importance.

For example, it was shown when applied to filamentation instability [32] that the use of the classical heat conductivity importantly reduces the effect of filamentation and underestimates its consequences for ICF. Therefore, the self consistent description of filamentation instability requires knowledge of the nonlocal heat conductivity of laser produced plasma [33].

From the preceding introduction, it is clear that the nonlocal energy transport plays an important role in the ICF research. Since the theoretical description and the experimental effort performed to study the energy transport effect usually did not, or could not, treat theoretically the nonlocal transport of photons and electrons in its naturally mutual way, i.e. the influence of the radiation transport to the electron heat conduction and vice versa, we take the overall description of this reciprocal energy transport effect in the laser-heated plasmas as the goal of the present thesis. For the sake of completeness, we also aim to treat the nonlocal ion transport. This effect is commonly not considered to be of great importance in hydrodynamic simulations. However, as in the case of SH electron model it took decades than the nonlocal electron transport approach was taken into account, the nonlocal ion transport model may become of interest also [34, 35, 36, 37, 38].

The rest of the thesis is organized as follows: the overall description of our nonlocal transport hydrodynamic model is presented in chapter 2. The commonly used electron and radiation transport methods are discussed and further extended by presenting our nonlocal BGK electron and ion transport. Chapter 3 defines the numerical method used to compute the energy transport problem and its coupling to the plasma energy equation. One can find our DG-BGK&Ts scheme defined in 1D slab geometry, in 1D spherically symmetric geometry, and in 2D axis-symmetric geometry, which is further followed by numerical tests showing properties of the scheme. The last chapter, chapter 4, is dedicated to laser-heated plasma simulations, where we present the results obtained with our plasma Euler and transport equations code PETE. This code was developed as a part of this thesis and is based on theoretical and numerical outcomes of chapter 2 and chapter 3.

Chapter 2

Physics

2.1 Equation of State

2.1.1 Laws of Thermodynamics

A gas may change energy with its surroundings by exchange of heat, positive or negative, and by performing mechanical work. Then for the *internal energy* $\epsilon[erg]$ in a volume V of a gas of the mass M holds

$$\mathrm{d}\epsilon = \mathrm{d}Q - \mathrm{d}W\,, \tag{2.1}$$

which is the first law of thermodynamics. Here $\mathrm{d}Q$ is the amount of heat gained or lost and $\mathrm{d}W$ is the work done by the gas, again positive or negative depending on if the gas expands or is compressed. This means that the force exerted by the gas on a surface element by the means of gas pressure applies in the process of the element's displacement which results in an infinitesimal work $\mathrm{d}W = p\mathrm{d}V$.

The first law of thermodynamics (2.1) can be formulated in terms of the *specific internal energy* $\varepsilon[erg/g]$ as

$$\mathrm{d}\varepsilon = \mathrm{d}q + \frac{p}{\rho^2}\,\mathrm{d}\rho\,, \tag{2.2}$$

where we used the differential of $V = \frac{M}{\rho}$ and $\mathrm{d}q[erg/g]$ is a specific heat change. It is useful to define the rate of change of specific internal energy being dependent on primary variables used in hydrodynamics, i.e. as a function of density and temperature. The appropriate form of the first law of thermodynamics than reads

$$\rho\left(\left(\frac{\partial\varepsilon}{\partial T}\right)_\rho \frac{\mathrm{d}T}{\mathrm{d}t} + \left(\frac{\partial\varepsilon}{\partial\rho}\right)_T \frac{\mathrm{d}\rho}{\mathrm{d}t}\right) = \frac{p}{\rho}\frac{\mathrm{d}\rho}{\mathrm{d}t} - \nabla\cdot\mathbf{q}\,, \tag{2.3}$$

where $\nabla\cdot\mathbf{q}$ represents the time rate of heat change due to spatial divergence of a heat flux $\mathbf{q}$ [3].

From practical experience, it is found that certain physical processes cannot actually be realized despite the fact they conserve energy. In certain processes energy may be channeled into forms in which it becomes effectively *unrecoverable* from the gas as useful work or as heat flow to its surroundings. In a sense the energy has been *degraded*; in fact, the energy has been dissipated at the molecular level processes that result in a more highly disordered system [2]. In order to identify the cause of this lost of useful energy, we define a state function called specific entropy $s[erg/g/eV]$ for which holds

$$\mathrm{d}s \geq \frac{\mathrm{d}q}{T}\,. \tag{2.4}$$

The above inequality is called the second law of thermodynamics and states, that any process in the real world is irreversible and equality applies in the ideal case of zero dissipation at the microscopic scale.

One can combine the first and second thermodynamic laws to obtain

$$\mathrm{d}\varepsilon \leq T\mathrm{d}s + \frac{p}{\rho^2}\,\mathrm{d}\rho\,, \tag{2.5}$$

Specific entropy s is exact differential and can be expressed from (2.5) as

$$\mathrm{d}s = \frac{1}{T}\left(\left(\frac{\partial\varepsilon}{\partial T}\right)_\rho \mathrm{d}T + \left(\frac{\partial\varepsilon}{\partial\rho}\right)_T \mathrm{d}\rho + \frac{p}{\rho^2}\,\mathrm{d}\rho\right)\,, \tag{2.6}$$

where we expanded the ε differential as a function of temperature and density. Based on the definition of the exact differential of specific entropy

$$\mathrm{d}s = \left(\frac{\partial s}{\partial T}\right)_\rho \mathrm{d}T + \left(\frac{\partial s}{\partial\rho}\right)_T \mathrm{d}\rho\,, \tag{2.7}$$

it is straightforward to find equalities relating ratios of entropy and internal energy

$$\left(\frac{\partial s}{\partial T}\right)_\rho = \frac{1}{T}\left(\frac{\partial\varepsilon}{\partial T}\right)_\rho\,, \quad \left(\frac{\partial s}{\partial\rho}\right)_T = \frac{1}{T}\left(\left(\frac{\partial\varepsilon}{\partial\rho}\right)_T + \frac{p}{\rho^2}\right)\,. \tag{2.8}$$

2.1.2 Closure Relations Derived From The Equation of State

The equation of state used in hydrodynamics is a necessary tool to close the system of Euler equations of fluid. It usually takes a form of a function depending on density and temperature of the fluid. Since $\mathrm{d}s$ and $\mathrm{d}\rho$ are exact differentials, the form of the first law of thermodynamics (2.5) in the case of equality states that natural state variables of specific internal energy ε are specific entropy s and density ρ.

Thermodynamic theory defines a set of thermodynamic potential with respect to natural state variables. The most appropriate one to be used in hydrodynamics depends on temperature and density (primary hydrodynamic variables). As the name Helmholtz free energy suggests, it provides a potential of a really useful "internal" energy. Definition of *specific free energy* $f\,[erg/g]$ reads

$$f = \varepsilon - Ts\,, \tag{2.9}$$

and one can easily show its natural state variables are temperature and density by expressing the differential of (2.9) completed with equality equation (2.5), and thus obtaining

$$\mathrm{d}f = -s\mathrm{d}T + \frac{p}{\rho^2}\mathrm{d}\rho\,. \tag{2.10}$$

This is yet another form of the first law of thermodynamics. In order to define all necessary closure relations to hydrodynamics, we compare (2.10) with the differential

$$\mathrm{d}f = \left(\frac{\partial f}{\partial T}\right)_\rho \mathrm{d}T + \left(\frac{\partial f}{\partial\rho}\right)_T \mathrm{d}\rho\,, \tag{2.11}$$

which gives us the following equalities

$$\left(\frac{\partial f}{\partial T}\right)_\rho = -s\,, \quad \left(\frac{\partial f}{\partial \rho}\right)_T = \frac{p}{\rho^2}\,. \tag{2.12}$$

The conclusion of this section brings all necessary hydrodynamic closure relations derived directly from the free energy function $f(T, \rho)$. The minimal closure comprises pressure p, specific heat capacity c_V, and specific internal energy ratio due to change in density, where explicit formulas follow

$$p = \rho^2 \left(\frac{\partial f}{\partial \rho}\right)_T, \tag{2.13}$$

$$\left(\frac{\partial \varepsilon}{\partial T}\right)_\rho = -T \left(\frac{\partial^2 f}{\partial T^2}\right)_\rho, \tag{2.14}$$

$$\left(\frac{\partial \varepsilon}{\partial \rho}\right)_T = \left(\frac{\partial f}{\partial \rho}\right)_T - T \left(\frac{\partial}{\partial T}\left(\frac{\partial f}{\partial \rho}\right)_T\right)_\rho. \tag{2.15}$$

A further extension of the closure contains specific internal energy, specific entropy, and adiabatic sound speed defined as $c_s^2 = \left(\frac{\partial p}{\partial \rho}\right)_s$ (refer to adiabatic compressibility [2]). Appropriate formulas depending only on f read

$$\varepsilon = f - T \left(\frac{\partial f}{\partial T}\right)_\rho, \tag{2.16}$$

$$s = -\left(\frac{\partial f}{\partial T}\right)_\rho, \tag{2.17}$$

$$c_s^2 = \left(\frac{\partial}{\partial \rho}\left(\rho^2 \left(\frac{\partial f}{\partial \rho}\right)_T\right)\right)_s. \tag{2.18}$$

The above closure formulas have been obtained from equations (2.8, 2.9, 2.12).

It is worth discussing the sound speed closure (2.18) in more detail. One should notice that the derivative with respect to density acts on pressure while entropy is constant, which imposes a nontrivial condition. A possible approach is to use polytropic approximation of ideal gas, which defines pressure as

$$p = C\rho^\gamma, \tag{2.19}$$

where C reflects a specific constant value of entropy. A resulting formula of *polytropic sound speed* reads

$$c_s^2 = \frac{\gamma p}{\rho} = \frac{p(p - \rho\varepsilon)}{\rho^2 \varepsilon}\,. \tag{2.20}$$

The last equality of (2.20) arises from the polytropic approximation of γ based on the formula [5]

$$p(\rho, T) = (\gamma + 1)\rho\varepsilon(\rho, T)\,. \tag{2.21}$$

One has to be aware of limits of approach (2.20) because of the isentrop (2.19) and definition of γ (2.21) are based on the ideal gas equation of state.

2.2   Kinetic Theory

2.2.1   The Distribution Function and Boltzmann's Equation

Kinetic theory uses a statistical picture that gives the distribution of gas particles in space and over velocity. To describe the physical state of the gas, we introduce the *distribution function* $f(t, \mathbf{x}, \mathbf{v})$ defined such that the average number of particles contained, at time t, in a volume $\mathrm{d}^3 x$ about $\mathbf{x}$ and a velocity-space element $\mathrm{d}^3 v$ about $\mathbf{v}$ is $f\mathrm{d}^3 x \mathrm{d}^3 v$. A finite energy of particles is required, which is guaranteed by imposing $f(t, \mathbf{x}, |\mathbf{v}| \to \infty) = 0$ at any time t and at any point $\mathbf{x}$. The physical interpretation is that there are no particles of velocities approaching infinity.

The distribution function keeps a detailed information about microscopic structure of the gas. On the other hand the macroscopic properties of the gas have to be also fulfilled by kinetic theory. For example, the particle density is

$$n(t, \mathbf{x}) = \int_{-\infty}^{\infty} f(t, \mathbf{x}, \mathbf{v}) \mathrm{d}v_x \mathrm{d}v_y \mathrm{d}v_z \, . \tag{2.22}$$

Similarly the average velocity of an element of gas is

$$\mathbf{u}(t, \mathbf{x}) = \frac{\int_{-\infty}^{\infty} f(t, \mathbf{x}, \mathbf{v}) \mathbf{v} \mathrm{d}v_x \mathrm{d}v_y \mathrm{d}v_z}{\int_{-\infty}^{\infty} f(t, \mathbf{x}, \mathbf{v}) \mathrm{d}v_x \mathrm{d}v_y \mathrm{d}v_z} \, , \tag{2.23}$$

which is the macroscopic fluid velocity. One can make a picture about how to interpret the distribution function as a cloud of particles, a gas within a certain volume (where $n(t, \mathbf{x}) > 0$), which is moving with the velocity $\mathbf{u}$.

We are especially interested in laser-heated plasma, a cloud of charged particles propagating with high velocities and highly influenced by internal electric and magnetic fields. Obviously, the distribution function evolves in time due to the absorption of the energy of laser. The desired equation governing such time evolution is

$$\frac{\partial f}{\partial t} + \mathbf{v} \cdot \nabla_{\mathbf{x}} f + \mathbf{a} \cdot \nabla_{\mathbf{v}} f = \left(\frac{\mathrm{d}f}{\mathrm{d}t} \right)_{coll} \, , \tag{2.24}$$

where $f(t, \mathbf{x}, \mathbf{v})$ represents number of particles located at position $\mathbf{x}$ and moving with velocity $\mathbf{v}$ at time t. The left hand side of (2.24) represents advection of particles, where the motion can be further supplemented by an acting force producing particles acceleration $\mathbf{a} = \frac{\mathbf{F}}{m}$. The term on the right hand side includes possible collisions with other particles causing a change in velocity direction and magnitude. Equation (2.24) introduces a 7D problem and is known as the *Boltzmann transport equation* [39, 40, 41, 42, 43, 44, 45]. An explicit expression for $\left(\frac{\mathrm{d}f}{\mathrm{d}t} \right)_{coll}$ will be discussed in the next section.

2.2.2   Collision Operators

The Boltzmann Collision Operator

The Boltzmann collision theory resides in using a dilute gas approach. The main assumption of this approach is that the occurrence of two body collisions takes over any other, more complicated, collisions. Such a binary collision characterize pre-collision velocities $\mathbf{v}_\alpha$ and $\mathbf{v}_\beta$ and post-collision velocities $\mathbf{v}'_\alpha$ and $\mathbf{v}'_\beta$ of two interacting particles

indexed α and β. The relative particle velocity $\mathbf{g} = \mathbf{v}_\alpha - \mathbf{v}_\beta$ is of great importance in the case of elastic binary collision, because of the following holds [2]

$$g_{\alpha\beta} = |\mathbf{v}_\alpha - \mathbf{v}_\beta| \quad = \quad |\mathbf{v}'_\alpha - \mathbf{v}'_\beta| = g'_{\alpha\beta}, \tag{2.25}$$

$$\mathbf{k}_{\alpha\beta} = \frac{\mathbf{v}_\alpha - \mathbf{v}_\beta}{|\mathbf{v}_\alpha - \mathbf{v}_\beta|} \quad \neq \quad \frac{\mathbf{v}'_\alpha - \mathbf{v}'_\beta}{|\mathbf{v}'_\alpha - \mathbf{v}'_\beta|} = \mathbf{k}'_{\alpha\beta}, \tag{2.26}$$

which states that only the direction of relative velocity $\mathbf{g}$ changes during the collision. In other words, the magnitude of relative velocity is conserved and the effect of collision reflects the change in direction $\mathbf{k}_{\alpha\beta} \rightarrow \mathbf{k}'_{\alpha\beta}$, which poses only two degrees of freedom since $|\mathbf{k}| = 1$. Relations (2.25, 2.26) make the problem of particle collisions much easier.

The *Boltzmann collision integral* characterizing the change of the distribution function $f_\alpha(t, \mathbf{x}, \mathbf{v}_\alpha)$ of particles of some specie α due to collisions with particles of some specie β described by the distribution function f_β takes the form

$$\left(\frac{\mathrm{d}f_\alpha(\mathbf{v}_\alpha)}{\mathrm{d}t} \Big| f_\beta \right)_{coll} = \int \left(f_\alpha(\mathbf{v}'_\alpha) f_\beta(\mathbf{v}'_\beta) - f_\alpha(\mathbf{v}_\alpha) f_\beta(\mathbf{v}_\beta) \right) g_{\alpha\beta} \, \sigma(\mathbf{k}_{\alpha\beta} \rightarrow \mathbf{k}'_{\alpha\beta}) \mathrm{d}^2 k'_{\alpha\beta} \mathrm{d}^3 v_\beta, \tag{2.27}$$

where σ is collision cross section, i.e. the rate at which the collision of particles with pre-collision velocities $\mathbf{v}_\alpha$ and $\mathbf{v}_\beta$ and post-collision velocities $\mathbf{v}'_\alpha$ and $\mathbf{v}'_\beta$ occurs.

It is wroth mentioning that equation (2.27) does not depend on time or space variables, which is the supposed effect of *molecular chaos* where the α and β particles are independently distributed according to f_α and f_β without any correlation between velocity and position or location of other particles. This correlation effect comes into play rather via the mean-field forces.

Equation (2.27) expresses the change of number of particles having the velocity $\mathbf{v}_\alpha$ (direction and magnitude), while scattered-out of the $\mathbf{v}_\alpha$ state due to the contribution of $-f_\alpha(\mathbf{v}_\alpha) f_\beta(\mathbf{v}_\beta) g_{\alpha\beta} \sigma \mathrm{d}^2 k'_{\alpha\beta} \mathrm{d}^3 v_\beta$ and scattered-in to the $\mathbf{v}_\alpha$ state due to the contribution of $f_\alpha(\mathbf{v}'_\alpha) f_\beta(\mathbf{v}'_\beta) g_{\alpha\beta} \sigma \mathrm{d}^2 k'_{\alpha\beta} \mathrm{d}^3 v_\beta$, i.e. a contribution of particles scattered from any $\mathbf{v}'_\alpha$ state to the $\mathbf{v}_\alpha$ state. This rather intricate description can be formulated as a conservation of particles of specie α as

$$\int \left(\frac{\mathrm{d}f_\alpha(\mathbf{v}_\alpha)}{\mathrm{d}t} \Big| f_\beta \right)_{coll} \mathrm{d}^3 v_\alpha = 0, \tag{2.28}$$

which is independent of the distribution function f_β.

The property above is just a special case of the summational invariant conservation of collisional operator [46]. This states that for any summational invariant ψ of the form

$$\psi_\alpha(\mathbf{v}_\alpha) + \psi_\beta(\mathbf{v}_\beta) = \psi_\alpha(\mathbf{v}'_\alpha) + \psi_\beta(\mathbf{v}'_\beta), \tag{2.29}$$

the following conservation law for two particle species α and β holds

$$\int \psi_\alpha(\mathbf{v}_\alpha) \left(\frac{\mathrm{d}f_\alpha(\mathbf{v}_\alpha)}{\mathrm{d}t} \Big| f_\beta \right)_{coll} \mathrm{d}^3 v_\alpha + \int \psi_\beta(\mathbf{v}_\beta) \left(\frac{\mathrm{d}f_\beta(\mathbf{v}_\beta)}{\mathrm{d}t} \Big| f_\alpha \right)_{coll} \mathrm{d}^3 v_\beta = 0. \tag{2.30}$$

By far the most important summational invariants are

$$m_\alpha + m_\beta = m_\alpha + m_\beta \,, \tag{2.31}$$

$$m_\alpha v_\alpha + m_\beta v_\beta = m_\alpha v_\alpha^{'} + m_\beta v_\beta^{'} \,, \tag{2.32}$$

$$m_\alpha \frac{|\mathbf{v}_\alpha|^2}{2} + m_\beta \frac{|\mathbf{v}_\beta|^2}{2} = m_\alpha \frac{|\mathbf{v}_\alpha^{'}|^2}{2} + m_\beta \frac{|\mathbf{v}_\beta^{'}|^2}{2} \,, \tag{2.33}$$

where (2.32) applies to every component of particle velocity **v**. Summational invariants (2.31, 2.32, 2.33) when applied to (2.30) represent mass, momentum, and energy conservation property of the Boltzmann collisional operator (2.27).

In the case of collision interactions among the particles of one specie α, i.e. $f_\beta = f_\alpha$ in (2.27), the conservation law (2.30) simplifies as

$$\int \psi_\alpha(\mathbf{v}_\alpha) \left(\frac{\mathrm{d}f_\alpha(\mathbf{v}_\alpha)}{\mathrm{d}t} \Big| f_\alpha \right)_{coll} \mathrm{d}^3 v_\alpha = 0 \,, \tag{2.34}$$

where we also used $\psi_\alpha = \psi_\beta$. The reason for that can be seen in mass, momentum, and energy summational invariants (2.31, 2.32, 2.33) when $m_\beta = m_\alpha$, which is obviously true for a unique specie of particles.

We conclude that the effect of collisions between any two species α and β (2.30) conserves mass, momentum, and energy, and that this is also true for the case of collisions among particles of one specie only (2.34).

The Maxwellian Velocity Distribution

Suppose that the gas is in a state of equilibrium: the material is homogeneous, isotropic, and at rest (non-accelerating). Accordingly, the distribution function is supposed to be constant, which may be described as

$$\left(\frac{\mathrm{d}f_\alpha}{\mathrm{d}t} \Big| f_\beta \right)_{coll} = 0 \,, \tag{2.35}$$

where we use only one specie described by $f = f_\alpha = f_\beta$ in order to simplify the problem. The steady state (2.35) will be true if it is possible to pair each collision with its inverse, i.e.

$$f_0(\mathbf{v}_\alpha) f_0(\mathbf{v}_\beta) - f_0(\mathbf{v}_\alpha^{'}) f_0(\mathbf{v}_\beta^{'}) = 0 \,, \tag{2.36}$$

which is called *detailed balance*. The subscript zero denotes the equilibrium distribution function. Logarithm of (2.36) takes the following form

$$\ln f_0(\mathbf{v}_\alpha) + \ln f_0(\mathbf{v}_\beta) = \ln f_0(\mathbf{v}_\alpha^{'}) + \ln f_0(\mathbf{v}_\beta^{'}) \,, \tag{2.37}$$

which is obviously a summational invariant (2.29). According to [46], any summational invariant has to be a linear combination of mass, momentum, and energy conservation invariants (2.31, 2.32, 2.33), i.e.

$$\ln f_0 = \alpha_1 + \alpha_2 \cdot \mathbf{v} + \alpha_3 |\mathbf{v}|^2 = \gamma_1 + \gamma_2 (\mathbf{v} - \mathbf{u})^2 \,, \tag{2.38}$$

where **u** is a constant, in this case the fluid velocity. Nevertheless, the distribution function f_0 can be observed as the famous Boltzmann distribution [39] relating the particle

microscopic energy $e = \frac{m}{2}|\mathbf{w}|^2$ to the *kinetic temperature* T, i.e.

$$f_0(\mathbf{v} - \mathbf{u}) = n \left(\frac{m}{2\pi k_B T} \right)^{\frac{3}{2}} \exp \left(-\frac{m(\mathbf{v} - \mathbf{u})^2}{2k_B T} \right) , \qquad (2.39)$$

where m is mass of particle, n density of particles, and $\mathbf{w} = \mathbf{v} - \mathbf{u}$ random microscopic velocity relative to the fluid velocity $\mathbf{u}$. A consequence of (2.39) is that the distribution of particles in speed (magnitude of $\mathbf{w}$) is

$$f_0(|\mathbf{w}|)\mathrm{d}|\mathbf{w}| = n \left(\frac{m}{2\pi k_B T} \right)^{\frac{3}{2}} \exp \left(-\frac{m|\mathbf{w}|^2}{2k_B T} \right) 4\pi |\mathbf{w}|^2 \mathrm{d}|\mathbf{w}| . \qquad (2.40)$$

Then, the *most probable speed* (the maximum of f_0) is

$$|\mathbf{w}|_m = \left(\frac{2k_B T}{m} \right)^{\frac{1}{2}} , \qquad (2.41)$$

and the *average speed* is

$$|\mathbf{w}|_a = \left(\frac{8k_B T}{m} \right)^{\frac{1}{2}} . \qquad (2.42)$$

In order to complete the set of statistically important speeds we add thermal speed

$$|\mathbf{w}|_T = \left(\frac{k_B T}{m} \right)^{\frac{1}{2}} , \qquad (2.43)$$

which is very often used in plasma physics formulary.

The Fokker-Planck-Landau collision operator

The predominance of small deflections in charged-particle collisions present in plasmas gives rise to the Fokker-Planck collision term

$$\left(\frac{\mathrm{d}f_\alpha(\mathbf{v}_\alpha)}{\mathrm{d}t} \Big| f_\beta \right)_{coll} = \nu_{\alpha\beta} \nabla_\mathbf{v} \cdot \int \mathbf{S}(\mathbf{v}_\alpha - \mathbf{v}') \cdot \left(\nabla_\mathbf{v} f_\alpha(\mathbf{v}_\alpha) f_\beta(\mathbf{v}') - f_\alpha(\mathbf{v}_\alpha) \nabla_\mathbf{v} f_\beta(\mathbf{v}') \right) \mathrm{d}^3 v' , \qquad (2.44)$$

where $\nu_{\alpha\beta}$ is the frequency of collisions between particles α and β species, and $\mathbf{S}$ is the Landau tensor defined as

$$\mathbf{S}(\mathbf{u}) = \frac{1}{|\mathbf{u}|^3} \left(|\mathbf{u}|^2 \mathbf{I} - \mathbf{u} \otimes \mathbf{u} \right) , \qquad (2.45)$$

where $\mathbf{I}$ is the unit tensor.

The collision term (2.44) can be seen as a reduced Boltzmann collision operator (2.27), where the minimum deflection angle corresponds to an impact parameter equal to the Debye length due to shielding and f_α and f_β were approximated by their Taylor's series expanded in velocities $\mathbf{v}_\alpha$ and $\mathbf{v}_\beta$, respectively.

The Bhatnagar-Gross-Krook Collision Operator

In many kinetic problems, for example, the nonlocal energy transport in laser-heated plasmas including electron and ion collisions, it is convenient to avoid the complexities

of the Boltzmann collision operator (2.27), or even simpler Fokker-Planck-Landau collision operator (2.44) by using a mean-free-path treatment. One replaces the collision integral by a relaxation term of the form

$$\left(\frac{\mathrm{d}f_\alpha(\mathbf{v}_\alpha)}{\mathrm{d}t}\Big|f_\alpha\right)_{coll} = \nu_{\alpha\alpha}\left(f_0 - f_\alpha\right),\tag{2.46}$$

which is the famous Bhatnagar-Gross-Krook collision operator [25] of particles of the specie α. In (2.46) $\nu_{\alpha\alpha}$ is an average collision frequency independent of velocity and f_0 is an equilibrium state to which the distribution f_α relaxes. In gas dynamics this equilibrium state is very often represented by the Maxwellian velocity distribution (2.39), where the definition

$$n_\alpha = \int f_\alpha \,\mathrm{d}v_\alpha\,,\tag{2.47}$$

of density of α particles leads to the conservation of number of particles α.

Apart from the mean-free-path, proportional to the inverse of the collisional frequency ν, the fluid velocity $\mathbf{u}_\alpha$ and kinetic temperature T_α of (2.39) has to be determined to have the collisional operator (2.46) complete. The following definitions

$$n_\alpha \mathbf{u}_\alpha = \int \mathbf{v}f_\alpha \,\mathrm{d}\mathbf{v}\,,\tag{2.48}$$

$$n_\alpha 3k_B T_\alpha = m_\alpha \int (\mathbf{v} - \mathbf{u}_\alpha)^2 f_\alpha \,\mathrm{d}\mathbf{v}\,,\tag{2.49}$$

directly lead to the conservation of momentum and energy of the collision operator (2.46) when f_0 takes the form of (2.39).

The set of equations (2.46, 2.39, 2.47, 2.48, 2.49) give the simplest form of the Boltzmann transport equation (2.24), the *BGK kinetic model*

$$\frac{\partial f}{\partial t} + \mathbf{v}\cdot\nabla_\mathbf{x}f + \mathbf{a}\cdot\nabla_\mathbf{v}f = \nu(f_0 - f)\,.\tag{2.50}$$

Gross and Krook introduced a two species kinetic model as an extension of (2.46) in [26]. It takes the following form

$$\frac{\partial f_\alpha}{\partial t} + \mathbf{v}\cdot\nabla_\mathbf{x}f_\alpha + \mathbf{a}\cdot\nabla_\mathbf{v}f_\alpha = \nu_{\alpha\alpha}f_0^\alpha + \nu_{\alpha\beta}f_0^\beta - (\nu_{\alpha\alpha} + \nu_{\alpha\beta})f_\alpha\,,\tag{2.51}$$

where, apart from the collision frequency $\nu_{\alpha\alpha}$ between α particles themselves and the collision frequency $\nu_{\alpha\beta}$ between α and β particles, the parameters T_α, $\mathbf{u}_\alpha$, T_β, and $\mathbf{u}_\beta$ have to be specified in order to complete the sources f_0^α and f_0^β defined by (2.39).

2.2.3 Moments of the Boltzmann Transport Equation

The equations of fluid dynamics comprise conservation laws of mass, momentum, and energy. We saw in 2.2.2, that when calculating moments of the Boltzmann collisional integral (2.30) exactly the same quantities are conserved in collisions of particles of a multi-species gas (2.31, 2.32, 2.33). The approach of calculating moments of one specie Boltzmann equation of the multi-species gas

$$\frac{\partial f_\alpha}{\partial t} + \mathbf{v}_\alpha\cdot\nabla_\mathbf{x}f_\alpha + \frac{q_\alpha}{m_\alpha}\left(\mathbf{E} + \mathbf{v}_\alpha\times\mathbf{B}\right)\cdot\nabla_\mathbf{v}f_\alpha = \sum_\beta\left(\frac{\mathrm{d}f_\alpha}{\mathrm{d}t}\Big|f_\beta\right)_{coll}\,,\tag{2.52}$$

leads to the same equations of fluid dynamics, nevertheless, we gain a better under-standing of the physical meaning of the terms that appear in these equations. In (2.52) particles of the specie α interact with particles of other species indexed by β including $\beta = \alpha$, i.e. the interaction with particles of the α specie itself. We have used the Lorentz electromagnetic force $\mathbf{F} = q_\alpha \left(\mathbf{E} + \mathbf{v}_\alpha \times \mathbf{B} \right)$ acting on particles with charge q_α.

Before we start with the general moment equation, we define the mean value oper-ator $\langle A \rangle$ of any quantity $A(\mathbf{v})$ as

$$\langle A \rangle_\alpha = \frac{\int A(\mathbf{v}_\alpha) f_\alpha \, \mathrm{d}^3 v_\alpha}{\int f_\alpha \, \mathrm{d}^3 v_\alpha} = \frac{1}{n_\alpha} \int A(\mathbf{v}_\alpha) f_\alpha \, \mathrm{d}^3 v_\alpha \,, \tag{2.53}$$

where the particle density n_α normalizes the probability function f_α. The mean velocity of particles α

$$\mathbf{u}_\alpha = \langle \mathbf{v}_\alpha \rangle_\alpha = \frac{\int \mathbf{v}_\alpha f_\alpha \, \mathrm{d}^3 v_\alpha}{\int f_\alpha \, \mathrm{d}^3 v_\alpha} \,, \tag{2.54}$$

serves as an example. Equipped with the mean value operator, we can proceed to mo-ment equations of the Boltzmann transport equation (2.52). When multiplying the Boltz-mann transport equation by a general velocity dependent summational invariant $\psi_\alpha(\mathbf{v})$ related to particles α and integrating it over the velocity space $\mathrm{d}^3 v$, the *conservation the-orem* using the velocity dependent Lorentz force can be written as

$$\frac{\partial}{\partial t} \left(n_\alpha \left\langle \psi_\alpha(\mathbf{v}_\alpha) \right\rangle_\alpha \right) + \nabla_\mathbf{x} \cdot \left(n_\alpha \left\langle \psi_\alpha(\mathbf{v}_\alpha) \mathbf{v}_\alpha \right\rangle_\alpha \right) - \frac{n_\alpha q_\alpha}{m_\alpha} \left\langle (\mathbf{E} + \mathbf{v}_\alpha \times \mathbf{B}) \cdot \nabla_\mathbf{v} \psi_\alpha(\mathbf{v}_\alpha) \right\rangle_\alpha =$$
$$\int \psi_\alpha \sum_{\beta/\alpha} \left(\frac{\mathrm{d} f_\alpha}{\mathrm{d} t} \middle| f_\beta \right)_{coll} \mathrm{d}^3 v_\alpha \,, \tag{2.55}$$

where the self-particle collisions of the specie α was excluded due to (2.34).

In what follows we will show that if we use the following five collisional invariants

$$\psi_{\alpha 1} = m_\alpha \,, \psi_{\alpha 2} = m_\alpha v_{\alpha 1} \,, \psi_{\alpha 3} = m_\alpha v_{\alpha 2} \,, \psi_{\alpha 4} = m_\alpha v_{\alpha 3} \,, \psi_{\alpha 5} = \frac{m_\alpha}{2} |\mathbf{v}_\alpha|^2 \,, \tag{2.56}$$

we obtain the equation of continuity, the three equations of momentum, and the energy equation for the fluid.

The Equation of Continuity

The application of the first invariant of (2.56), i.e. $\psi_\alpha = m_\alpha$, to the conservation theorem (2.55) leads to the equation

$$\frac{\partial}{\partial t} \left(n_\alpha m_\alpha \right) + \nabla_\mathbf{x} \cdot \left[n_\alpha m_\alpha \left\langle \mathbf{v}_\alpha \right\rangle_\alpha \right] = 0 \,. \tag{2.57}$$

But $n_\alpha m_\alpha = \rho_\alpha$, the fluid density, and $\langle \mathbf{v}_\alpha \rangle_\alpha = \mathbf{u}_\alpha$, the macroscopic fluid velocity. One can recognize that (2.57) defines the continuity equation

$$\frac{\partial \rho_\alpha}{\partial t} + \nabla_\mathbf{x} \cdot \left[\rho_\alpha \mathbf{u}_\alpha \right] = 0 \,. \tag{2.58}$$

The vector $\rho_\alpha \mathbf{u}_\alpha$ can be interpreted physically as the *momentum density vector* (*the mass flux vector*).

The Momentum Equations

The conservation law of momentum of a fluid is a vector of three equations. These are obtained by applying $\psi_\alpha = [m_\alpha v_{\alpha 1}, m_\alpha v_{\alpha 2}, m_\alpha v_{\alpha 3}]$ of (2.56) to conservation theorem (2.55). This leads to the vector of equations

$$
\frac{\partial}{\partial t} \left(n_\alpha m_\alpha \langle \mathbf{v}_\alpha \rangle_\alpha \right) + \nabla_{\mathbf{x}} \cdot \left(n_\alpha m_\alpha \langle \mathbf{v}_\alpha \otimes \mathbf{v}_\alpha \rangle_\alpha \right) - n_\alpha q_\alpha \langle (\mathbf{E} + \mathbf{v}_\alpha \times \mathbf{B}) \rangle_\alpha =
$$
$$
\int m_\alpha \mathbf{v}_\alpha \sum_{\beta/\alpha} \left(\frac{\mathrm{d} f_\alpha}{\mathrm{d} t} \Big| f_\beta \right)_{coll} \mathrm{d}^3 v_\alpha . \quad (2.59)
$$

The *momentum flux density tensor* can be written

$$
n_\alpha m_\alpha \langle \mathbf{v}_\alpha \otimes \mathbf{v}_\alpha \rangle_\alpha = \rho_\alpha \left(\mathbf{u}_\alpha \otimes \mathbf{u}_\alpha + \langle (\mathbf{v}_\alpha - \mathbf{u}_\alpha) \otimes (\mathbf{v}_\alpha - \mathbf{u}_\alpha) \rangle_\alpha \right) , \quad (2.60)
$$

where we separated the contribution due to the mean velocity $\mathbf{u}_\alpha$ and the contribution due to the microscopic motion described by the random particle velocity $\mathbf{v}_\alpha - \mathbf{u}_\alpha$. Bearing in mind that $n_\alpha m_\alpha = \rho_\alpha$ and $\langle \mathbf{v}_\alpha \rangle_\alpha = \mathbf{u}_\alpha$, we see that (2.59) can be written as

$$
\frac{\partial}{\partial t} \left[\rho_\alpha \mathbf{u}_\alpha \right] + \nabla_{\mathbf{x}} \cdot \left[\rho_\alpha \mathbf{u}_\alpha \otimes \mathbf{u}_\alpha + \rho_\alpha \langle (\mathbf{v}_\alpha - \mathbf{u}_\alpha) \otimes (\mathbf{v}_\alpha - \mathbf{u}_\alpha) \rangle_\alpha \right] =
$$
$$
n_\alpha q_\alpha \left(\mathbf{E} + \mathbf{u}_\alpha \times \mathbf{B} \right) + \int m_\alpha \mathbf{v}_\alpha \sum_{\beta/\alpha} \left(\frac{\mathrm{d} f_\alpha}{\mathrm{d} t} \Big| f_\beta \right)_{coll} \mathrm{d}^3 v_\alpha , \quad (2.61)
$$

which are the three equations of the momentum density vector $\rho_\alpha \mathbf{u}_\alpha$ of the fluid.

The Energy Equation

In order to obtain the energy equation of the fluid, we make use of the summational invariant from (2.56) of the $\psi_\alpha = \frac{m_\alpha}{2} |\mathbf{v}_\alpha|^2$. When applied to conservation theorem (2.55) it gives

$$
\frac{\partial}{\partial t} \left(n_\alpha \frac{m_\alpha}{2} \langle |\mathbf{v}_\alpha|^2 \rangle_\alpha \right) + \nabla_{\mathbf{x}} \cdot \left(n_\alpha \frac{m_\alpha}{2} \langle |\mathbf{v}_\alpha|^2 \mathbf{v}_\alpha \rangle_\alpha \right) - n_\alpha q_\alpha \langle (\mathbf{E} + \mathbf{v}_\alpha \times \mathbf{B}) \cdot \mathbf{v}_\alpha \rangle_\alpha =
$$
$$
\int \frac{m_\alpha}{2} |\mathbf{v}_\alpha|^2 \sum_{\beta/\alpha} \left(\frac{\mathrm{d} f_\alpha}{\mathrm{d} t} \Big| f_\beta \right)_{coll} \mathrm{d}^3 v_\alpha . \quad (2.62)
$$

We aim to separate the contribution due to the mean velocity $\mathbf{u}_\alpha$ and the contribution due to the microscopic motion described by the random particle velocity $\mathbf{v}_\alpha - \mathbf{u}_\alpha$.

After some work with the mean value operator (2.53) and with use of $n_\alpha m_\alpha = \rho_\alpha$ and $\langle \mathbf{v}_\alpha \rangle_\alpha = \mathbf{u}_\alpha$ we obtain that

$$
n_\alpha \frac{m_\alpha}{2} \langle |\mathbf{v}_\alpha|^2 \rangle_\alpha = \rho_\alpha \left(\frac{|\mathbf{u}_\alpha|^2}{2} + \frac{\langle |\mathbf{v}_\alpha - \mathbf{u}_\alpha|^2 \rangle_\alpha}{2} \right) , \quad (2.63)
$$

and even a bit more tedious work leads to equality

$$
n_\alpha \frac{m_\alpha}{2} \left\langle |\mathbf{v}_\alpha|^2 \mathbf{v}_\alpha \right\rangle_\alpha = \rho_\alpha \mathbf{u}_\alpha \left(\frac{|\mathbf{u}_\alpha|^2}{2} + \frac{\left\langle |\mathbf{v}_\alpha - \mathbf{u}_\alpha|^2 \right\rangle_\alpha}{2} \right) + \rho_\alpha \mathbf{u}_\alpha \cdot \left\langle (\mathbf{v}_\alpha - \mathbf{u}_\alpha) \otimes (\mathbf{v}_\alpha - \mathbf{u}_\alpha) \right\rangle_\alpha
$$
$$
+ \rho_\alpha \frac{1}{2} \left\langle |\mathbf{v}_\alpha - \mathbf{u}_\alpha|^2 (\mathbf{v}_\alpha - \mathbf{u}_\alpha) \right\rangle_\alpha . \quad (2.64)
$$

Now we can write the second moment of the Boltzmann transport equation

$$
\frac{\partial}{\partial t} \left[\rho_\alpha \left(\frac{1}{2} \left\langle |\mathbf{v}_\alpha - \mathbf{u}_\alpha|^2 \right\rangle_\alpha + \frac{1}{2} |\mathbf{u}_\alpha|^2 \right) \right] +
$$
$$
\nabla_\mathbf{x} \cdot \left[\rho_\alpha \left(\frac{1}{2} \left\langle |\mathbf{v}_\alpha - \mathbf{u}_\alpha|^2 \right\rangle_\alpha + \frac{1}{2} |\mathbf{u}_\alpha|^2 \right) \mathbf{u}_\alpha + \rho_\alpha \mathbf{u}_\alpha \cdot \left\langle (\mathbf{v}_\alpha - \mathbf{u}_\alpha) \otimes (\mathbf{v}_\alpha - \mathbf{u}_\alpha) \right\rangle_\alpha \right] =
$$
$$
n_\alpha q_\alpha \mathbf{u}_\alpha \cdot \mathbf{E} - \nabla_\mathbf{x} \cdot \left[\rho_\alpha \frac{1}{2} \left\langle |\mathbf{v}_\alpha - \mathbf{u}_\alpha|^2 (\mathbf{v}_\alpha - \mathbf{u}_\alpha) \right\rangle_\alpha \right] + \int \frac{m_\alpha}{2} |\mathbf{v}_\alpha|^2 \sum_{\beta/\alpha} \left(\frac{\mathrm{d}f_\alpha}{\mathrm{d}t} \Big| f_\beta \right)_{coll} \mathrm{d}^3 v_\alpha ,
$$
$$
(2.65)
$$

which is the energy equation of the specie α of the fluid. In (2.65) we made use of the relation $(\mathbf{v}_\alpha \times \mathbf{B}) \cdot \mathbf{v}_\alpha = 0$ which holds for any two vectors $\mathbf{v}_\alpha$ and $\mathbf{B}$.

2.2.4 One Specie Microscopic Fluid Equations

In previous sections we discussed zero, first, and second moments of the Boltzmann transport equation of one specie in a multi-component fluid. In order to summarize the latter results we write mass, momentum, and energy equations of the α specie component (particles of mass m_α and charge q_α) of a multi specie fluid (other components indexed by β)

$$
\frac{\partial \rho_\alpha}{\partial t} + \nabla_\mathbf{x} \cdot (\rho_\alpha \mathbf{u}_\alpha) = 0 . \quad (2.66)
$$
$$
\frac{\partial (\rho_\alpha \mathbf{u}_\alpha)}{\partial t} + \nabla_\mathbf{x} \cdot (\rho_\alpha \mathbf{u}_\alpha \otimes \mathbf{u}_\alpha) = \nabla_\mathbf{x} \cdot \mathbf{T}_\alpha + \rho_\alpha^q (\mathbf{E} + \mathbf{u}_\alpha \times \mathbf{B}) + \mathbf{g}_{\alpha|\beta} , \quad (2.67)
$$
$$
\frac{\partial (\rho_\alpha \xi_\alpha)}{\partial t} + \nabla_\mathbf{x} \cdot (\rho_\alpha \xi_\alpha \mathbf{u}_\alpha) = \nabla_\mathbf{x} \cdot (\mathbf{u}_\alpha \cdot \mathbf{T}_\alpha - \mathbf{q}_\alpha) + \rho_\alpha^q \mathbf{u}_\alpha \cdot \mathbf{E} + g_{\alpha|\beta} , \quad (2.68)
$$

where primary variables of the α specie component are density $\rho_\alpha [g/cm^3]$, velocity $\mathbf{u}_\alpha [cm/s]$, and total specific energy density $\xi_\alpha [erg/g]$. On the right hand side we identify electric and magnetic field intensities $\mathbf{E}$ and $\mathbf{B}$ acting on the α specie component of the fluid via the charge density $\rho_\alpha^q = \frac{\rho_\alpha}{m_\alpha} q_\alpha$, stress tensor $\mathbf{T}_\alpha$, heat flux $\mathbf{q}_\alpha$, and finally momentum and energy exchange between the α specie particles and all other β species particles $\mathbf{g}_{\alpha|\beta}$ and $g_{\alpha|\beta}$, respectively.

The total specific energy density consists of two parts the specific internal energy density part and the specific kinetic energy density part, i.e. $\xi_\alpha = \varepsilon_\alpha + \epsilon_\alpha^{kin}$. The *specific internal energy density* $\varepsilon [erg/g]$ represents microscopic motion and is defined as

$$
\varepsilon_\alpha = \frac{1}{2} \left\langle |\mathbf{v}_\alpha - \mathbf{u}_\alpha|^2 \right\rangle_\alpha . \quad (2.69)
$$

The *specific kinetic energy density* $\epsilon^{kin}[erg/g]$ represents macroscopic motion of the fluid and is defined as

$$\epsilon_\alpha^{kin} = \frac{1}{2}\mathbf{u}_\alpha \cdot \mathbf{u}_\alpha . \tag{2.70}$$

The fluid stress results from momentum exchange on a microscopic level within the fluid and is described by the *stress tensor* $\mathbf{T}[g/cm/s^2]$ and is defined as

$$\mathbf{T}_\alpha = -\rho_\alpha \left\langle (\mathbf{v}_\alpha - \mathbf{u}_\alpha) \otimes (\mathbf{v}_\alpha - \mathbf{u}_\alpha) \right\rangle_\alpha . \tag{2.71}$$

The average of the normal stresses corresponds to the negative of the pressure. Based on this motivation, it is common to write the stress tensor as a composition of the scalar and the viscous parts, i.e.

$$\mathbf{T}_\alpha = -p_\alpha \mathbf{I} + \sigma_\alpha , \tag{2.72}$$

where the *pressure* $p[erg/cm^3]$ and the *viscous tensor* $\sigma[g/cm/s^2]$ are defined as

$$p_\alpha = \frac{1}{3}\rho_\alpha \left\langle |\mathbf{v}_\alpha - \mathbf{u}_\alpha|^2 \right\rangle_\alpha , \tag{2.73}$$

$$\sigma_\alpha = -\rho_\alpha \left(\left\langle (\mathbf{v}_\alpha - \mathbf{u}_\alpha) \otimes (\mathbf{v}_\alpha - \mathbf{u}_\alpha) \right\rangle_\alpha - \frac{1}{3} \left\langle |\mathbf{v}_\alpha - \mathbf{u}_\alpha|^2 \right\rangle_\alpha \mathbf{I} \right) , \tag{2.74}$$

where $\mathbf{I}$ is a unit tensor. The energy flux in the fluid resulting from microscopic motion is identified as the *heat flux vector* $\mathbf{q}[ergcm/s]$ and is defined as

$$\mathbf{q}_\alpha = \frac{1}{2}\rho_\alpha \left\langle |\mathbf{v}_\alpha - \mathbf{u}_\alpha|^2 (\mathbf{v}_\alpha - \mathbf{u}_\alpha) \right\rangle_\alpha . \tag{2.75}$$

Last yet undefined terms are the *momentum exchange* $\mathbf{g}_{\alpha|\beta}[g/cm^2/s^2]$ and the *energy exchange* $g_{\alpha|\beta}[erg/s]$ defined as

$$\mathbf{g}_{\alpha|\beta} = \int m_\alpha \mathbf{v}_\alpha \sum_{\beta/\alpha} \left(\frac{\mathrm{d}f_\alpha}{\mathrm{d}t} \Big| f_\beta \right)_{coll} \mathrm{d}^3 v_\alpha , \tag{2.76}$$

$$g_{\alpha|\beta} = \int \frac{m_\alpha}{2} |\mathbf{v}_\alpha|^2 \sum_{\beta/\alpha} \left(\frac{\mathrm{d}f_\alpha}{\mathrm{d}t} \Big| f_\beta \right)_{coll} \mathrm{d}^3 v_\alpha , \tag{2.77}$$

where β goes over all other components of the multi-species fluid apart from the proper index α. The nature of the collision transfer of momentum and energy then resides on the definition of the collision operator $\left(\frac{\mathrm{d}f_\alpha}{\mathrm{d}t} \Big| f_\beta \right)_{coll}$, e.g. (2.27).

It is important to realize, that even though the continuum model of fluid equations (2.66-2.68) reduces the Boltzmann transport equation (2.52) problem of solving the evolution of the distribution function f_α to the problem of the evolution of its mean values $(\rho_\alpha, \mathbf{u}_\alpha, \varepsilon_\alpha)$, these still rely on the following terms: pressure p_α (2.73), heat flux $\mathbf{q}_\alpha$ (2.75), viscous tensor σ_α (2.74), and momentum and energy exchange terms $\mathbf{g}_{\alpha|\beta}$ (2.76) and $g_{\alpha|\beta}$ (2.77), which pose a microscopic dependence on f_α (in the case of exchange terms even on f_β).

2.2.5   Equations of Two Temperature Single-Fluid Hydrodynamic Model

The plasma state of matter can be characterized by the existence of free electrons and ions. Under certain conditions (quasi-neutrality, collective behavior of particles) the continuum approach can be used to adequately model plasma as a multi-species fluid.

We restrict our model to treat only one ion and one electron specie. In general different species of either ions or electrons can be used. The condition on quasi-neutrality indicates that the position of electrons is firmly tight to the position of ions and vice versa. Whenever a force acts on ions, electrons will move instantaneously with the ions to keep the condition of quasi-neutrality to be valid. Such a tight bond leads to a simplified description referred as *single fluid*.

The single fluid model states that

$$\mathbf{u}_i = \mathbf{u}_e = \mathbf{u}, \tag{2.78}$$

i.e. the fluid velocity $\mathbf{u}$ is common for both ions $\mathbf{u}_i$ and electrons $\mathbf{u}_e$. The explicit condition on quasi-neutrality reflects that the fluid is free of charge, i.e. the ion and electron charge densities ρ_i^q and ρ_e^q screen each other. This means

$$\sum_{\alpha=i,e} \rho_\alpha^q = \rho_i^q + \rho_e^q = n_i q_i + n_e q_e = 0, \tag{2.79}$$

where index α goes over all species, in our case ions and electrons, $n_e[1/cm^3]$ and q_e are electron density and charge, and $n_i[1/cm^3]$ and q_i are ion density and charge. As a consequence of (2.79) we can write the electron density as

$$n_e = \bar{Z} n_i, \tag{2.80}$$

since the ion charge $q_i = -\bar{Z} q_e$ is given by the *mean ionization* $\bar{Z}$.

Now, following Section (2.2.4) of one specie fluid equations, we write the conservation law of mass of the electron-ion plasma fluid

$$\sum_{\alpha=i,e} \left[\frac{\partial \rho_\alpha}{\partial t} + \nabla_{\mathbf{x}} \cdot (\rho_\alpha \mathbf{u}_\alpha) = 0 \right], \tag{2.81}$$

the conservation law of momentum of the electron-ion plasma fluid

$$\sum_{\alpha=i,e} \left[\frac{\partial (\rho_\alpha \mathbf{u}_\alpha)}{\partial t} + \nabla_{\mathbf{x}} \cdot (\rho_\alpha \mathbf{u}_\alpha \otimes \mathbf{u}_\alpha) = \nabla_{\mathbf{x}} \cdot (\sigma_\alpha - p_\alpha \mathbf{I}) + \rho_\alpha^q (\mathbf{E} + \mathbf{u}_\alpha \times \mathbf{B}) + \mathbf{g}_{\alpha|i,e} \right], \tag{2.82}$$

and the conservation law of energy of the electron-ion plasma fluid

$$\sum_{\alpha=i,e} \left[\frac{\partial \left(\rho_\alpha \left(\varepsilon_\alpha + \frac{|\mathbf{u}_\alpha|^2}{2} \right) \right)}{\partial t} + \nabla_{\mathbf{x}} \cdot \left(\rho_\alpha \left(\varepsilon_\alpha + \frac{|\mathbf{u}_\alpha|^2}{2} \right) \mathbf{u}_\alpha \right) = \right.$$

$$\left. \nabla_{\mathbf{x}} \cdot (\mathbf{u}_\alpha \cdot (\sigma_\alpha - p_\alpha \mathbf{I}) - \mathbf{q}_\alpha) + \rho_\alpha^q \mathbf{u}_\alpha \cdot \mathbf{E} + g_{\alpha|i,e} \right]. \tag{2.83}$$

which are conservation laws of mass, momentum, and energy for the electron-ion plasma fluid by definition of the sum of contributions of both electrons and ions.

This section aims to define the single fluid hydrodynamic model. Since equations (2.81, 2.82, 2.83) introduce a general form of conservation laws of mass, momentum, and energy of the two-specie plasma fluid, it is possible to reduce such a system by using the single fluid (2.78) and quasi-neutrality (2.79) assumptions. The reduction due to the single-fluid model can be seen in equation (2.81) which transforms into

the continuity equation of quantity $\sum_{\alpha=i,e} \rho_\alpha$, due to (2.78), and in equation (2.82), which forms the equations of momentum $\mathbf{u} \sum_{\alpha=i,e} \rho_\alpha$, where the effects of the Lorentz force $\sum_{\alpha=i,e} \rho_\alpha^q (\mathbf{E} + \mathbf{u}_\alpha \times \mathbf{B}) = 0$ and collisions $\sum_{\alpha=i,e} \mathbf{g}_{\alpha|i,e} = 0$ cancel out due to (2.79) and (2.30, 2.76), respectively. In the case of energy conservation the ion and electron contributions of (2.83) have to be treated separately.

The single-fluid hydrodynamic model can be defined either in laboratory coordinates system referred as *Eulerian frame* and in the moving material coordinate system referred as *Lagrangian frame*.

Two Species Single Fluid Hydrodynamic Model in Eulerian Frame

Based on the general conservation law formulations (2.81, 2.82, 2.83) further simplified by the conditions of the single-fluid model (2.78) and quasi-neutrality of plasma (2.79), we can define the two species single-fluid hydrodynamic model in Eulerian frame

$$\frac{\partial (\rho_i + \rho_e)}{\partial t} + \nabla_{\mathbf{x}} \cdot [(\rho_i + \rho_e) \mathbf{u}] = 0 , \tag{2.84}$$

$$\frac{\partial ((\rho_i + \rho_e) \mathbf{u})}{\partial t} + \nabla_{\mathbf{x}} \cdot [(\rho_i + \rho_e) \mathbf{u} \otimes \mathbf{u}] = \nabla_{\mathbf{x}} \cdot [(\sigma_i + \sigma_e) - (p_i + p_e) \mathbf{I}] , \tag{2.85}$$

$$\frac{\partial \rho_i \left(\varepsilon_i + \frac{|\mathbf{u}|^2}{2}\right)}{\partial t} + \nabla_{\mathbf{x}} \cdot \left[\rho_i \left(\varepsilon_i + \frac{|\mathbf{u}|^2}{2}\right) \mathbf{u}\right] = \nabla_{\mathbf{x}} \cdot [\mathbf{u} \cdot (\sigma_i - p_i \mathbf{I}) - \mathbf{q}_i] +$$
$$\rho_i^q \mathbf{u} \cdot \mathbf{E} + g_{i|e} , \tag{2.86}$$

$$\frac{\partial \rho_e \left(\varepsilon_e + \frac{|\mathbf{u}|^2}{2}\right)}{\partial t} + \nabla_{\mathbf{x}} \cdot \left[\rho_e \left(\varepsilon_e + \frac{|\mathbf{u}|^2}{2}\right) \mathbf{u}\right] = \nabla_{\mathbf{x}} \cdot [\mathbf{u} \cdot (\sigma_e - p_e \mathbf{I}) - \mathbf{q}_e] +$$
$$\rho_e^q \mathbf{u} \cdot \mathbf{E} + g_{e|i} , \tag{2.87}$$

where its primary variables are $\rho_i, \rho_e, \mathbf{u}, \varepsilon_i, \varepsilon_e$, i.e. ion density, electron density, single-fluid velocity, specific internal energy density of ions, and specific internal energy density of electrons, respectively.

Two Temperature Single Fluid Hydrodynamic Model in Lagrangian Frame

Several algebraic operations is necessary to transform the two species single-fluid hydrodynamic model from Eulerian to Lagrangian frame. Rather simplified hydrodynamic model then takes the form

$$\frac{\mathrm{d}\rho}{\mathrm{d}t} = -\rho \nabla_{\mathbf{x}} \cdot \mathbf{u} , \tag{2.88}$$

$$\rho \frac{\mathrm{d}\mathbf{u}}{\mathrm{d}t} = -\nabla_{\mathbf{x}} (p_i + p_e) + \nabla_{\mathbf{x}} \cdot (\sigma_i + \sigma_e) , \tag{2.89}$$

$$\rho \frac{\mathrm{d}\tilde{\varepsilon}_i}{\mathrm{d}t} = -p_i \nabla_{\mathbf{x}} \cdot \mathbf{u} + \sigma_i : \nabla_{\mathbf{x}} \mathbf{u} - \nabla_{\mathbf{x}} \cdot \mathbf{q}_i + \tilde{g}_{i|e} , \tag{2.90}$$

$$\rho \frac{\mathrm{d}\tilde{\varepsilon}_e}{\mathrm{d}t} = -p_e \nabla_{\mathbf{x}} \cdot \mathbf{u} + \sigma_e : \nabla_{\mathbf{x}} \mathbf{u} - \nabla_{\mathbf{x}} \cdot \mathbf{q}_e - \tilde{g}_{i|e} , \tag{2.91}$$

where $\frac{\mathrm{d}}{\mathrm{d}t} = \frac{\partial}{\partial t} + \mathbf{u} \cdot \nabla_{\mathbf{x}}$ is the Lagrangian material derivative and primary variables of the single-fluid model are single-fluid density $\rho = \rho_i + \rho_e$, single-fluid velocity $\mathbf{u}$, single-fluid specific internal energy density of ions $\tilde{\varepsilon}_i = \frac{\rho_i}{\rho} \varepsilon_i$, and single-fluid specific internal energy density of electrons $\tilde{\varepsilon}_e = \frac{\rho_e}{\rho} \varepsilon_e$.

One can observe an apparent resemblance of the energy equations (2.90) and (2.91) to the first thermodynamic law (2.1) or its formulation (2.3). Temperature is a fundamental quantity which provides crucial information about plasma. And exactly the first thermodynamic law formulation (2.3) allows us to rewrite the energy equations (2.90, 2.91) as

$$\rho \frac{\partial \tilde{\varepsilon}_i}{\partial T_i} \frac{\mathrm{d}T_i}{\mathrm{d}t} = -\rho \frac{\partial \tilde{\varepsilon}_i}{\partial \rho} \frac{\mathrm{d}\rho}{\mathrm{d}t} - p_i \nabla_{\mathbf{x}} \cdot \mathbf{u} + \sigma_i : \nabla_{\mathbf{x}} \mathbf{u} - \nabla_{\mathbf{x}} \cdot \mathbf{q}_i + \tilde{g}_{i|e}, \tag{2.92}$$

$$\rho \frac{\partial \tilde{\varepsilon}_e}{\partial T_e} \frac{\mathrm{d}T_e}{\mathrm{d}t} = -\rho \frac{\partial \tilde{\varepsilon}_e}{\partial \rho} \frac{\mathrm{d}\rho}{\mathrm{d}t} - p_e \nabla_{\mathbf{x}} \cdot \mathbf{u} + \sigma_e : \nabla_{\mathbf{x}} \mathbf{u} - \nabla_{\mathbf{x}} \cdot \mathbf{q}_e - \tilde{g}_{i|e}. \tag{2.93}$$

Equations (2.88, 2.89, 2.92, 2.93) form the *two temperature single-fluid hydrodynamic model* with primary variables single-fluid density ρ, single-fluid velocity $\mathbf{u}$, ion temperature T_i, and electron temperature T_e. In order to solve the two temperature single-fluid hydrodynamic model the *hydrodynamic closure* set

$$\mathrm{cl}_{Hydro} = \left(\frac{\partial \tilde{\varepsilon}_i}{\partial T_i}, \frac{\partial \tilde{\varepsilon}_e}{\partial T_e}, \frac{\partial \tilde{\varepsilon}_i}{\partial \rho}, \frac{\partial \tilde{\varepsilon}_e}{\partial \rho}, p_i, p_e, \sigma_i, \sigma_e, \mathbf{q}_i, \mathbf{q}_e, \tilde{g}_{i|e} \right), \tag{2.94}$$

have to be provided, i.e. ion and electron single-fluid specific internal energy density derivatives with respect to temperature $\frac{\partial \tilde{\varepsilon}_i}{\partial T_i}$ and $\frac{\partial \tilde{\varepsilon}_e}{\partial T_e}$, ion and electron single-fluid specific internal energy density derivatives with respect to density $\frac{\partial \tilde{\varepsilon}_i}{\partial \rho}$ and $\frac{\partial \tilde{\varepsilon}_e}{\partial \rho}$, ion and electron pressures p_i and p_e, ion and electron viscous tensors σ_i and σ_e, ion and electron heat flux vectors $\mathbf{q}_i$ and $\mathbf{q}_e$, and ion-electron energy exchange term $\tilde{g}_{i|e}$.

It is worth noting that the ion-electron energy exchange term takes a special form

$$\tilde{g}_{i|e} = g_{i|e} - \mathbf{u} \cdot \mathbf{g}_{i|e}, \tag{2.95}$$

when used in Lagrangian frame. The exchange terms used on the right hand side of (2.95) were defined in (2.76, 2.77). Since our single-fluid consists of only two species, the ion-electron and electron-ion exchange terms must be equal with minus sign according to (2.30, 2.76, 2.77), i.e. $\tilde{g}_{i|e} = -\tilde{g}_{e|i}$.

Now, since we treat the ion and electron energy equations (2.92, 2.93) as the first thermodynamic law (2.1), temperatures T_i and T_e present thermodynamic quantities, which span a broader range of validity according to plasma conditions, e.g. due to quantum effects, than the kinetic temperature of dilute gas defined in (2.39). Nevertheless the thermodynamic and the kinetic temperatures coincide in a relatively low density high temperature plasmas. Under the same thermodynamic considerations a definition of ion and electron specific internal energy densities $\varepsilon_i(\rho, T_i), \varepsilon_e(\rho, T_e)$ and pressures $p_i(\rho, T_i), p_e(\rho, T_e)$ as thermodynamic functions dependent on density and temperature makes a good sense. Yet another consequence of the thermodynamic approach is additional information about entropy generation. The specific entropy of plasma will evolve as

$$\rho \frac{\mathrm{d}s}{\mathrm{d}t} \geq -\frac{\nabla_{\mathbf{x}} \cdot \mathbf{q}_i}{T_i} - \frac{\nabla_{\mathbf{x}} \cdot \mathbf{q}_e}{T_e} + \frac{\tilde{g}_{i|e}}{T_i} - \frac{\tilde{g}_{i|e}}{T_e}, \tag{2.96}$$

which is a consequence of the second thermodynamic law (2.4) along with (2.1) compared to energy equations (2.92, 2.93).

2.3   Electron Transport Models

In [47] the following form of the Boltzmann transport equation for electrons in the laser-heated plasma was proposed

$$\frac{\partial f_e}{\partial t} + \mathbf{v} \cdot \nabla_{\mathbf{x}} f_e + \frac{q_e}{m_e} \mathbf{E} \cdot \nabla_{\mathbf{v}} f_e = C_{ee}(f_e, f_e) + C_{ei}(f_e, f_i) + I_{IB}(\mathbf{E}_L, f_e), \qquad (2.97)$$

where f_e and f_i are the distribution functions of electrons and ions, respectively, $\mathbf{E}$ is a plasma generated electric field, and $\mathbf{E}_L$ is an electric field of laser. Apart from the transport operator in the phase space placed on the left-hand side of (2.97), we can on the right hand side identify collision operators, namely collisions among electrons them selves C_{ee} and collisions among electrons and ions C_{ei}, and the last term describes the inverse-bremsstrahlung heating I_{IB} of electrons due to the absorption of the laser energy. A ponderomotive laser field pressure effect could be included, but we do not consider it in this work.

The classical diffusive approximation to the deterministic transport of electrons in the laser-heated plasma is presented at first. The most frequently used approximation, introduced by Spitzer and Harm (SH) [10, 48], is based on the expansion in a small parameter further combined with the P_1 anisotropy approximation. This approximation was further extended by applying a convolution operation leading to a close-nonlocality extension introduced in [15] and subsequently defined in more dimensions using the linear transport model [49].

We consider the nonlocality of the electron transport (2.97) to be a necessary further step to be applied in hydrodynamic codes. Our BGK nonlocal electron transport model based on the direct solution of the BGK transport equation of electron specific intensity [50, 51], naturally captures the nonlocal property of transport and we also focus on its definition in multiple dimensions. As an important property we further show the comparison of the diffusive limit of our model to the standard SH approach. As an extension, we also add the nonlocal ion transport formulation resulting from the BGK transport equation applied to ion specific intensity. As a consequence, the charge continuity equation can be formulated, which paves the way to treat plasma under conditions, when the quasi-neutrality concept should be violated.

2.3.1   The Spitzer-Harm Approximation

An appropriate analysis related to the diffusive approach to transport is based on the combination of the Hilbert expansion in a small parameter λ and the angular Legendre polynomials expansion [52]

$$f_e = \sum_{i=0}^{\infty} f_i \lambda^i \sum_k f_k P_k(cos(\phi)) = f_e^{(0)} + f_e^{(1)} \lambda \cos(\phi) + f_e^{(2)} \lambda + f_e^{(3)} \cos(\phi) + O(\lambda^2, \cos^2(\phi)),$$

$$(2.98)$$

where ϕ is the polar angle (see Fig. 2.1) with respect to z-axis, and the right hand side of (2.98) shows its explicit series to the second order. We will use the notation $\cos(\phi) = \mu$.

Even though it is extremely difficult to solve (2.97) analytically, it is satisfactory to find an approximate axis-symmetric solution having the form

$$\tilde{f}_e = f_e^{(0)} + f_e^{(1)} \lambda \mu, \qquad (2.99)$$

which reflects a small spatial deviation with respect to λ and a small anisotropy effect given by μ from the dominant term $f_e^{(0)}$, which is homogeneous in space and isotropic in angle.

A detailed procedure of the analysis of the approximate solution 2.99 is described in Appendix A.1. In order to conclude, the approximate electron distribution function satisfying the electron transport equation (2.97) takes the form

$$\tilde{f}_e = \frac{n_e}{\left(\pi \, \frac{2 \, k_B \, T_e}{m_e} \right)^{\frac{3}{2}}} \exp \left(-\frac{m_e |\mathbf{v}|^2}{2 \, k_B \, T_e} \right) \left(1 - D \left(\frac{m_e \, |\mathbf{v}|^2}{2 \, k_B \, T_e} \right) \right) , \qquad (2.100)$$

where the transport function reads

$$D(w) = \lambda \ (w - 4) \, \frac{\mathbf{n} \cdot \nabla_{\mathbf{x}} T_e}{T_e} . \qquad (2.101)$$

The form of (2.100) follows the notation used in the original work of Spitzer and Harm (SH) [10] and reflects the results of the Lorentz gas approximation [53, 54, 55]. The commonly used term SH transport refers more precisely to the work [48], where the transport function $D(w)$ was further extended by the electron-electron collision operator, which had to be solved numerically. The latter concludes, that the mean free path of electrons should be adjusted as

$$\lambda_{SH} = \frac{0.024\bar{Z} + 0.058}{1 + 0.24\bar{Z}}\lambda . \qquad (2.102)$$

Last, but not least, is the SH formulation of the electron heat flux, which provides the transport closure to the hydrodynamic system. This formulation can be directly evaluated by integrating the distribution function (2.100) over the velocity space as

$$\mathbf{q}_{SH} = \int_{4\pi} \int_{|\mathbf{v}|} |\mathbf{v}|\mathbf{n}|\mathbf{v}|^2 \, \tilde{f}_e |\mathbf{v}|^2 \, \mathrm{d}|\mathbf{v}|\mathrm{d}\mathbf{n} = \frac{256}{\sqrt{8\pi}} \frac{k_B^{\frac{3}{2}}}{\sqrt{m_e}} \bar{\lambda}_{SH} \sqrt{T_e} \nabla_{\mathbf{x}} T_e , \qquad (2.103)$$

where we used the thermal mean free path

$$\bar{\lambda}_{SH} = \frac{0.24\bar{Z} + 0.058}{1 + 0.24\bar{Z}}\bar{\lambda} = \frac{0.24\bar{Z} + 0.058}{1 + 0.24\bar{Z}} \frac{n_i Z^2 \, e^4}{(4 \, \pi \, \epsilon_0)^2} \frac{m_e^2 \, v_{T_e}^4}{4 \, \pi \, \ln \Lambda} , \qquad (2.104)$$

reflecting the electrons with thermal velocity $v_{T_e} = \sqrt{\frac{k_B T_e}{m_e}}$.

The above heat flux (2.103) presents the diffusion approximation of the transport closure to be used in hydrodynamic model. It is worth mentioning that the effect of inverse-bremsstrahlung heating I_{IB} of (2.97) was omitted in (2.103). An appropriate treatment and the resulting effect of I_{IB} can be found in Appendix A.1.

2.3.2 The Lucciani-Mora-Virmont Nonlocal Electron Transport Model

In order to summarize the motivation and the main principle of the nonlocal method of Lucciani Mora Virmont (LMV) presented in [15], the two important observations should be mentioned. Since Spitzer-Harm (SH) approximation depends only on the local plasma parameters, namely temperature, it fails to incorporate a possible transport of energy carried by electrons from the surrounding region. This is for example the

case of the head of the heat front, the conductivity exceeds the SH conductivity due to the nonlocal part of the hot, nearly collisionless electrons. On the contrary, the localized SH flux very often over estimates the actual electron heat flux, when the gradient of temperature is to steep. This leads to the definition of the free-streaming electron distribution flux $g_{fs} = n_e\, m_e\, |\mathbf{v}_T|^3$, where $|\mathbf{v}_T|, = (k_B T_e/m_e)^{1/2}$. The flux limiting based on the free-streaming flux is very often adopted in the fluid codes simulating laser matter interaction. The SH overestimation is cured by a local law of the type $q = min(q_{SH}, f_{lim}\, q_{fs})$ where f_{lim} is the flux-limit factor.

Lucciani, Mora and Virmont came with the idea of convolution taking into account the nonlocal transport, which should fix the inconsistency of the classical SH flux. The proposed form of the nonlocal heat flux

$$\mathbf{q}(\mathbf{x}) = \int \mathbf{q}_{SH}(\mathbf{x}')\, w(\mathbf{x}, \mathbf{x}')\, \mathrm{d}\mathbf{x}'\,, \tag{2.105}$$

where the convolution kernel reads

$$w(\mathbf{x}, \mathbf{x}') = \frac{1}{2\, a\, (Z+1)^{\frac{1}{2}} \lambda_0(\mathbf{x}')} \exp\left(-\left|\frac{\int_{\mathbf{x}'}^{\mathbf{x}} n_e(\mathbf{x}'')\, \mathrm{d}\mathbf{x}''}{a\, (Z+1)^{\frac{1}{2}} \lambda_0(\mathbf{x}')\, n_e(\mathbf{x}')}\right|\right)\,, \tag{2.106}$$

where $\mathbf{q}_{SH}$ is the heat flux 2.103 defined in [10], n_e the electron density and Z the ionization state of plasma. This model is enclosed by determining the parameter a, which have to be done following simulation results. According to [15] the parameter $a \in (30, 35)$ models the laser-heated plasmas in an appropriate way. The expressions (2.105, 2.106) strongly improve the SH value all along the profile due to the fact that they do not build on the localizaiton of the heat flux, i.e. the unique cause of the breakdown of the SH model.

The LMV model was further extended into more dimensions in the model of Schurtz, Nicolai, and Busquet (SNB) [49]. A study focused on the nonlocal electron transport in high-energy-density plasmas can be found in [56, 57, 58], which continues in the line of the above SNB model and the M1 angular moment method [59, 60] based on the entropy closure [61].

2.3.3   The Nonlocal BGK Electron and Ion Transport Model

In [2, 62] the similarity between the Boltzmann transport equation of electrons and the radiation transport equation was pointed out. As later in the case of radiation in section 2.4.1, we define the *electron specific intensity* $I_e^{|\mathbf{v}|}(\mathbf{x}, t, \mathbf{n}, |\mathbf{v}|)[erg/cm^3/sr]$ of electrons at position $\mathbf{x}$ and time t, traveling in direction $\mathbf{n}$ with non-relativistic energy $\frac{m_e}{2}|\mathbf{v}|^2$, to be such that amount of energy transported by electrons of energies within the interval $(|\mathbf{v}|, |\mathbf{v}| + \mathrm{d}|\mathbf{v}|)$ across an oriented surface element $\mathrm{d}\mathbf{S}$, in a time $\mathrm{d}t$, into a solid angle $\mathrm{d}\omega$ around $\mathbf{n}$, is

$$\mathrm{d}E = I_e^{|\mathbf{v}|}(\mathbf{x}, t, \mathbf{n}, |\mathbf{v}|)\, \mathbf{n} \cdot \mathrm{d}\mathbf{S}\mathrm{d}\omega\mathrm{d}|\mathbf{v}|\mathrm{d}t\,. \tag{2.107}$$

The *electron distribution function* f_e is defined such that $f_e(\mathbf{x}, t, \mathbf{v})\mathrm{d}^3x\mathrm{d}^3v$ is the number of electrons per volume d^3x at $(\mathbf{x}, t)$ with velocity within $(\mathbf{v}, \mathbf{v} + \mathrm{d}\mathbf{v})$, where $\mathbf{v} = |\mathbf{v}|\mathbf{n}$ ($m_e|\mathbf{v}|\mathbf{n}$ is electron momentum). Using the velocity space defined in spherical coordinates where $\mathrm{d}^3v = |\mathbf{v}|^2\mathrm{d}|\mathbf{v}|\mathrm{d}\omega$, we find that the number of electrons can be equally

expressed as

$$\frac{I_e^{|\mathbf{v}|}(\mathbf{x}, t, \mathbf{n}, |\mathbf{v}|)}{|\mathbf{v}|\frac{m_e}{2}|\mathbf{v}|^2}\, \mathrm{d}^3 x \mathrm{d}|\mathbf{v}|\mathrm{d}\omega = f_e(\mathbf{x}, t, \mathbf{n}, |\mathbf{v}|)|\mathbf{v}|^2\, \mathrm{d}^3 x \mathrm{d}|\mathbf{v}|\mathrm{d}\omega\,,$$

which leads to an important relation between the electron specific intensity and the electron distribution function

$$I_e^{|\mathbf{v}|}(\mathbf{x}, t, \mathbf{n}, |\mathbf{v}|) = f_e(\mathbf{x}, t, \mathbf{n}, |\mathbf{v}|)\frac{m_e}{2}|\mathbf{v}|^5\,, \tag{2.108}$$

where we used $\mathrm{d}^3 x = \mathbf{n} \cdot \mathrm{d}\mathbf{S}|\mathbf{v}|\mathrm{d}t$ in (2.108).

In spherical coordinates ϕ and θ describe the direction $\mathbf{n}$ of traveling electrons, where $\phi \in (0, \pi)$ and $\theta \in (0, 2\pi)$ (see Fig. 2.1) are the polar and azimuthal angles, respectively [63], which should not be confused with the notation used in [64]. Thus, we can write the momentum phase space velocity $\mathbf{v}$ in Cartesian coordinates system in terms of spherical coordinates $(|\mathbf{v}|, \phi, \theta)$ as

$$\mathbf{v} = |\mathbf{v}|\mathbf{n} = |\mathbf{v}|\begin{bmatrix} \cos(\theta)\sin(\phi) \\ \sin(\theta)\sin(\phi) \\ \cos(\phi) \end{bmatrix}\,. \tag{2.109}$$

When making use of (2.109), the Lorentz force $\mathbf{F}$ acting on a charged particle can be expressed as

$$\mathbf{F} = q\,(\mathbf{E} + \mathbf{v} \times \mathbf{B}) = q\begin{bmatrix} E_x + |\mathbf{v}|\,(\sin(\theta)\sin(\phi)B_z - \cos(\phi)B_y) \\ E_y + |\mathbf{v}|\,(\cos(\phi)B_x - \cos(\theta)\sin(\phi)B_z) \\ E_z + |\mathbf{v}|\,(\cos(\theta)\sin(\phi)B_y - \sin(\theta)\sin(\phi)B_x) \end{bmatrix}\,, \tag{2.110}$$

where q and $\mathbf{v}$ are charge and velocity of the particle, E_i and B_i are components of electric and magnetic vector fields at $(\mathbf{x}, t)$ in Cartesian coordinates.

In principle, we always treat the velocity phase space by using $(|\mathbf{v}|, \phi, \theta)$ components in the spherical coordinates system. For instance, the corresponding form of the gradient of the distribution function f_e in spherical coordinates reads

$$\nabla_\mathbf{v} f_e = \hat{\mathbf{r}}\frac{\partial f_e}{\partial |\mathbf{v}|} + \frac{1}{|\mathbf{v}|}\hat{\phi}\frac{\partial f_e}{\partial \phi} + \frac{1}{|\mathbf{v}|\sin(\phi)}\hat{\theta}\frac{\partial f_e}{\partial \theta}\,, \tag{2.111}$$

which makes use of the orthonormal curvilinear basis vectors shown in Fig. 2.1 having the following form

$$\hat{\mathbf{r}} = \begin{bmatrix} \cos(\theta)\sin(\phi) \\ \sin(\theta)\sin(\phi) \\ \cos(\phi) \end{bmatrix}\,, \quad \hat{\phi} = \begin{bmatrix} \cos(\theta)\cos(\phi) \\ \sin(\theta)\cos(\phi) \\ -\sin(\phi) \end{bmatrix}\,, \quad \hat{\theta} = \begin{bmatrix} -\sin(\theta) \\ \cos(\theta) \\ 0 \end{bmatrix}\,, \tag{2.112}$$

in Cartesian coordinates. Thus, the corresponding gradient in Cartesian coordinates system expressed in terms of spherical coordinates is formed by inserting (2.112) into (2.111) and reads

$$\nabla_\mathbf{v} f_e = \begin{bmatrix} \cos(\theta)\sin(\phi)\frac{\partial f_e}{\partial |\mathbf{v}|} + \frac{\cos(\theta)\cos(\phi)}{|\mathbf{v}|}\frac{\partial f_e}{\partial \phi} - \frac{\sin(\theta)}{|\mathbf{v}|\sin(\phi)}\frac{\partial f_e}{\partial \theta} \\ \sin(\theta)\sin(\phi)\frac{\partial f_e}{\partial |\mathbf{v}|} + \frac{\sin(\theta)\cos(\phi)}{|\mathbf{v}|}\frac{\partial f_e}{\partial \phi} + \frac{\cos(\theta)}{|\mathbf{v}|\sin(\phi)}\frac{\partial f_e}{\partial \theta} \\ \cos(\phi)\frac{\partial f_e}{\partial |\mathbf{v}|} - \frac{\sin(\phi)}{|\mathbf{v}|}\frac{\partial f_e}{\partial \phi} \end{bmatrix}\,. \tag{2.113}$$

We can finally express the acceleration of electrons expressed as a scalar product of (2.110) and (2.113) as

$$
\frac{q_e}{m_e} \left(\mathbf{E} + \mathbf{v} \times \mathbf{B} \right) \cdot \nabla_{\mathbf{v}} f_e = \frac{q_e}{m_e} \left(\left(E_x \cos(\theta) + E_y \sin(\theta) \right) \sin(\phi) + E_z \cos(\phi) \right) \frac{\partial f_e}{\partial |\mathbf{v}|}
$$
$$
+ \frac{q_e}{m_e |\mathbf{v}|} \left(\left(E_x \cos(\theta) + E_y \sin(\theta) \right) \cos(\phi) - E_z \sin(\phi) + |\mathbf{v}| \left(\sin(\theta) B_x - \cos(\theta) B_y \right) \right) \frac{\partial f_e}{\partial \phi}
$$
$$
+ \frac{q_e}{m_e |\mathbf{v}|} \left(E_y \frac{\cos(\theta)}{\sin(\phi)} - E_x \frac{\sin(\theta)}{\sin(\phi)} + |\mathbf{v}| \left(\frac{\cos(\phi)}{\sin(\phi)} \left(\cos(\theta) B_x + \sin(\theta) B_y \right) - B_z \right) \right) \frac{\partial f_e}{\partial \theta},
$$
$$(2.114)$$

where q_e and m_e are electron charge and mass.

The general formula (2.114) might seem to be difficult to interpret, however, when expressed in particular geometries, which provide some kind of symmetry, it becomes simpler. For example, in the case of slab (using the z axis) or spherically symmetric (defined with respect to the z axis (see Fig. 2.1) geometries only z component of the Lorentz force (2.110) is non-zero for any velocity magnitude $|\mathbf{v}|$. After some algebra this results in a very simple form of (2.114), i.e. the 1D acceleration term

$$
\frac{q_e}{m_e} \left(\mathbf{E} + \mathbf{v} \times \mathbf{B} \right) \cdot \nabla_{\mathbf{v}} f_e = \frac{q_e}{m_e} E_z \cos(\phi) \frac{\partial f_e}{\partial |\mathbf{v}|} .
\tag{2.115}
$$

One can observe, that apparently the effect of magnetic field cancels out in (2.114) in the 1D case (2.115). The second case we are interested in is the axis-symmetric geometry. This symmetry leads to that y component of the Lorentz force (2.110) is equal to zero. In this case the scalar product (2.114) takes the form

$$
\frac{q_e}{m_e} \left(\mathbf{E} + \mathbf{v} \times \mathbf{B} \right) \cdot \nabla_{\mathbf{v}} f_e = \frac{q_e}{m_e} \left(E_x \cos(\theta) \sin(\phi) + E_z \cos(\phi) \right) \frac{\partial f_e}{\partial |\mathbf{v}|}
$$
$$
+ \frac{q_e}{m_e |\mathbf{v}|} \left(E_x \cos(\theta) \cos(\phi) - E_z \sin(\phi) + |\mathbf{v}| \left(\sin(\theta) B_x - \cos(\theta) B_y \right) \right) \frac{\partial f_e}{\partial \phi}
$$
$$
- \frac{q_e}{m_e |\mathbf{v}|} \left(E_x \frac{\sin(\theta)}{\sin(\phi)} - |\mathbf{v}| \left(\frac{\cos(\phi)}{\sin(\phi)} \left(\cos(\theta) B_x + \sin(\theta) B_y \right) - B_z \right) \right) \frac{\partial f_e}{\partial \theta} . \quad (2.116)
$$

Under the assumption of almost isotropic distribution function, we can write a reasonably simple form of the acceleration term (2.114)

$$
\frac{q_e}{m_e} \left(\mathbf{E} + \mathbf{v} \times \mathbf{B} \right) \cdot \nabla_{\mathbf{v}} f_e \approx \frac{q_e}{m_e} \mathbf{n} \cdot \mathbf{E} \frac{\partial f_e}{\partial |\mathbf{v}|} ,
\tag{2.117}
$$

while we neglect the magnetic field $\mathbf{B}$ and we use an approximation that $\frac{\partial f_e}{\partial |\mathbf{v}|} \gg \frac{1}{|\mathbf{v}|} \frac{\partial f_e}{\partial \phi} + \frac{1}{|\mathbf{v}| \sin(\phi)} \frac{\partial f_e}{\partial \theta}$ and we make use of (2.109) in order to express the electron transport direction $\mathbf{n}$.

In order to model the nonlocal electron transport, we propose to use the BGK form of the Boltzmann transport equation (2.51) of section 2.2.1. It takes the following form

$$
\frac{\partial f_e}{\partial t} + \mathbf{v} \cdot \nabla_{\mathbf{x}} f_e = -\frac{q_e}{m_e} \mathbf{n} \cdot \mathbf{E} \frac{\partial f_e}{\partial |\mathbf{v}|} + \frac{n_i}{n_e} \frac{\partial \bar{Z}}{\partial t} S_e + \nu_{ei} \left(S_e - f_e \right) + \nu_{\sigma_e} \left(\bar{f}_e - f_e \right) , \quad (2.118)
$$

where S_e is a general distribution source function of electrons, n_i the ion density, n_e the electron density, $\bar{Z}$ mean ionization, ν_{ei} is the ion-electron collision frequency, and

ν_{σ_e} is the electron scattering frequency.

The angular mean of the distribution function f_e is defined as

$$\bar{f}_e(\mathbf{x}, t, |\mathbf{v}|) = \frac{1}{4\pi} \int_{4\pi} f_e(\mathbf{x}, t, \mathbf{n}, |\mathbf{v}|) \mathrm{d}\omega \,. \tag{2.119}$$

Based on the BGK form of the Boltzmann transport equation (2.51), a similar model can be applied to ions. It takes the form

$$\frac{\partial f_i}{\partial t} + \mathbf{v} \cdot \nabla_{\mathbf{x}} f_i = -\frac{q_i}{m_i} \mathbf{n} \cdot \mathbf{E} \frac{\partial f_i}{\partial |\mathbf{v}|} + \nu_{ii} \left(S_i - f_i \right) \,, \tag{2.120}$$

where f_i is the distribution function of ions, S_i is a general distribution source function of ions, q_i the charge of ion, m_i the ion mass, ν_{ii} is the ion-ion collision frequency, which we expect to dominate the ion-electron collision frequency effect. We use (2.117) in both equations (2.118) and (2.120).

We define the *total electron intensity operator* acting on a quantity g as

$$\langle g \rangle_{|\mathbf{v}|}^e = \int_0^\infty g \, \frac{m_e}{2} |\mathbf{v}|^5 \mathrm{d}|\mathbf{v}| \,, \tag{2.121}$$

which arises from the relation (2.108). The operator (2.121) brings up the definition of the *total electron intensity*

$$I_e(\mathbf{x}, t, \mathbf{n}) = \langle f_e(\mathbf{x}, t, \mathbf{n}, |\mathbf{v}|) \rangle_{|\mathbf{v}|}^e \,. \tag{2.122}$$

The application of operator (2.121) on the BGK transport equation (2.118) gives

$$\frac{\partial \langle f_e \rangle_{|\mathbf{v}|}^e}{\partial t} + \mathbf{n} \cdot \nabla_{\mathbf{x}} \langle |\mathbf{v}| f_e \rangle_{|\mathbf{v}|}^e = \frac{q_e}{m_e} \mathbf{n} \cdot \mathbf{E} \, \langle 5|\mathbf{v}|^{-1} f_e \rangle_{|\mathbf{v}|}^e +$$

$$\frac{n_i}{n_e} \frac{\partial \bar{Z}}{\partial t} \langle S_e \rangle_{|\mathbf{v}|}^e + \left(\langle \nu_{ei} S_e \rangle_{|\mathbf{v}|}^e - \langle \nu_{ei} f_e \rangle_{|\mathbf{v}|}^e \right) + \left(\langle \nu_{\sigma_e} \bar{f}_e \rangle_{|\mathbf{v}|}^e - \langle \nu_{\sigma_e} f_e \rangle_{|\mathbf{v}|}^e \right) \,, \quad (2.123)$$

where we applied $\langle \frac{\partial f_e}{\partial |\mathbf{v}|} \rangle_{|\mathbf{v}|}^e = -\langle 5|\mathbf{v}|^{-1} f_e \rangle_{|\mathbf{v}|}^e$.

The BGK model requires a unique transport velocity, a unique collision frequency, and a unique scattering frequency. These are expressed based on the form of (2.123) as the following

$$|\tilde{\mathbf{v}}|_e \;\; = \;\; \frac{\langle |\mathbf{v}| f_e \rangle_{|\mathbf{v}|}^e}{\langle f_e \rangle_{|\mathbf{v}|}^e} \approx \frac{\langle |\mathbf{v}| S_e \rangle_{|\mathbf{v}|}^e}{\langle S_e \rangle_{|\mathbf{v}|}^e} \,, \tag{2.124}$$

$$\tilde{\nu}_{ei} \;\; = \;\; \frac{\langle \nu_{ei}(|\mathbf{v}|^{-3}) f_e \rangle_{|\mathbf{v}|}^e}{\langle f_e \rangle_{|\mathbf{v}|}^e} \approx \frac{\langle \nu_{ei}(|\mathbf{v}|^{-3}) S_e \rangle_{|\mathbf{v}|}^e}{\langle S_e \rangle_{|\mathbf{v}|}^e} \,, \tag{2.125}$$

$$\tilde{\nu}_{\sigma_e} \;\; = \;\; \frac{\langle \nu_{\sigma_e}(|\mathbf{v}|^{-3}) f_e \rangle_{|\mathbf{v}|}^e}{\langle f_e \rangle_{|\mathbf{v}|}^e} \approx \frac{\langle \nu_{\sigma_e}(|\mathbf{v}|^{-3}) S_e \rangle_{|\mathbf{v}|}^e}{\langle S_e \rangle_{|\mathbf{v}|}^e} \,, \tag{2.126}$$

where the right most terms express the electron source function S_e based approximations, which are, in general, easy to evaluate.

Finally, we can write the *one energy group BGK electron transport equation*

$$\frac{1}{|\tilde{\mathbf{v}}|_e}\frac{\partial I_e}{\partial t} + \mathbf{n}\cdot\nabla_{\mathbf{x}}I_e = \frac{5\,q_e}{m_e}\frac{\langle|\mathbf{v}|^{-1}S_e\rangle^e_{|\mathbf{v}|}}{\langle|\mathbf{v}|S_e\rangle^e_{|\mathbf{v}|}}\mathbf{n}\cdot\mathbf{E}\,I_e + \frac{n_i}{|\tilde{\mathbf{v}}|_e n_e}\frac{\partial\bar{Z}}{\partial t}\langle S_e\rangle^e_{|\mathbf{v}|}$$

$$+\,\tilde{k}_e\left(\langle S_e\rangle^e_{|\mathbf{v}|} - I_e\right) + \tilde{\sigma}_e\left(\bar{I}_e - I_e\right)\,. \quad (2.127)$$

which results from (2.123) when divided by $|\tilde{\mathbf{v}}|_e$ (2.124) and where $\tilde{k}_e = \frac{\tilde{\nu}_{ei}}{|\tilde{\mathbf{v}}|}$ is the extinction coefficient and $\tilde{\sigma}_e = \frac{\tilde{\nu}_{\sigma e}}{|\tilde{\mathbf{v}}|}$ is the scattering coefficient and the term $\frac{\langle|\mathbf{v}|^{-1}f_e\rangle^e_{|\mathbf{v}|}}{\langle|\mathbf{v}|f_e\rangle^e_{|\mathbf{v}|}}$ accompanying the electric field was simplified by using the source function S_e approximation.

The *mean total electron intensity* is defined as

$$\bar{I}_e(\mathbf{x},t) = \langle\bar{f}_e(\mathbf{x},t,|\mathbf{v}|)\rangle^e_{|\mathbf{v}|}\,. \quad (2.128)$$

We define the *total ion intensity operator* acting on a quantity g as

$$\langle g\rangle^i_{|\mathbf{v}|} = \int_0^\infty g\,\frac{m_i}{2}|\mathbf{v}|^5\mathrm{d}|\mathbf{v}|\,, \quad (2.129)$$

which can be obtained from a relation similar to (2.108). The operator (2.129) brings up the definition of the *total ion intensity*

$$I_i(\mathbf{x},t,\mathbf{n}) = \langle f_i(\mathbf{x},t,\mathbf{n},|\mathbf{v}|)\rangle^i_{|\mathbf{v}|}\,. \quad (2.130)$$

The application of operator (2.129) on the BGK transport equation (2.120) gives

$$\frac{\partial\langle f_i\rangle^i_{|\mathbf{v}|}}{\partial t} + \mathbf{n}\cdot\nabla_{\mathbf{x}}\langle|\mathbf{v}|f_i\rangle^i_{|\mathbf{v}|} = \frac{q_i}{m_i}\mathbf{n}\cdot\mathbf{E}\,\langle 5|\mathbf{v}|^{-1}f_i\rangle^i_{|\mathbf{v}|} + \left(\langle\nu_{ii}S_i\rangle^i_{|\mathbf{v}|} - \langle\nu_{ii}f_i\rangle^i_{|\mathbf{v}|}\right)\,, \quad (2.131)$$

where we applied $\langle\frac{\partial f_i}{\partial|\mathbf{v}|}\rangle^i_{|\mathbf{v}|} = -\langle 5|\mathbf{v}|^{-1}f_i\rangle^i_{|\mathbf{v}|}$.

The BGK model requires a unique transport velocity, a unique collision frequency, and a unique scattering frequency. These are expressed based on the form of (2.131) as the following

$$|\tilde{\mathbf{v}}|_i = \frac{\langle|\mathbf{v}|f_i\rangle^i_{|\mathbf{v}|}}{\langle f_i\rangle^i_{|\mathbf{v}|}} \approx \frac{\langle|\mathbf{v}|S_i\rangle^i_{|\mathbf{v}|}}{\langle S_i\rangle^i_{|\mathbf{v}|}}\,, \quad (2.132)$$

$$\tilde{\nu}_{ii} = \frac{\langle\nu_{ii}(|\mathbf{v}|^{-3})f_i\rangle^i_{|\mathbf{v}|}}{\langle f_i\rangle^i_{|\mathbf{v}|}} \approx \frac{\langle\nu_{ii}(|\mathbf{v}|^{-3})S_i\rangle^i_{|\mathbf{v}|}}{\langle S_i\rangle^i_{|\mathbf{v}|}}\,, \quad (2.133)$$

where the right most terms express the ion source function S_i based approximations, which are, in general, easy to evaluate.

Finally, we can write the *one energy group BGK ion transport equation*

$$\frac{1}{|\tilde{\mathbf{v}}|_i}\frac{\partial I_i}{\partial t} + \mathbf{n}\cdot\nabla_{\mathbf{x}}I_i = \frac{5\,q_i}{m_i}\frac{\langle|\mathbf{v}|^{-1}S_i\rangle^i_{|\mathbf{v}|}}{\langle|\mathbf{v}|S_i\rangle^i_{|\mathbf{v}|}}\mathbf{n}\cdot\mathbf{E}\,I_i + \tilde{k}_i\left(\langle S_i\rangle^i_{|\mathbf{v}|} - I_i\right)\,, \quad (2.134)$$

which results from (2.131) when divided by $|\tilde{\mathbf{v}}|_i$ (2.132) and where $\tilde{k}_i = \frac{\tilde{\nu}_{ii}}{|\tilde{\mathbf{v}}|_i}$ is the extinction coefficient and $\tilde{\sigma}_e = \frac{\tilde{\nu}_{\sigma e}}{|\tilde{\mathbf{v}}|}$ is the scattering coefficient and the term $\frac{\langle |\mathbf{v}|^{-1} f_i \rangle_{|\mathbf{v}|}^i}{\langle |\mathbf{v}| f_i \rangle_{|\mathbf{v}|}^i}$ accompanying the electric field was simplified by using the source function S_i approximation.

Application of the Nonlocal BGK Electron and Ion Transport Model

The nonlocal electron transport model is defined in the Eulerian frame by equation (2.127) and the nonlocal ion transport model is defined in the Eulerian frame by equation (2.134), where the quantities I_e (2.122) and I_i (2.130) can be interpreted as one energy group specific intensities representing the entire spectrum of electron and ion energies, nevertheless, they keep the important information about the angular distribution.

The electron source function S_e, the mean ionization $\bar{Z}$, the ion source function S_i, and the electric field $\mathbf{E}$ can be also expressed in the Lagrangian frame moving with the fluid velocity $\mathbf{u}$. Since in the case of electrons the specific intensity transport velocity is characterized by $|\mathbf{v}|_e$, the convective derivative $\frac{1}{|\tilde{\mathbf{v}}|}\frac{\mathrm{d}I_e}{\mathrm{d}t} = \frac{1}{|\tilde{\mathbf{v}}|}\frac{\partial I_e}{\partial t} + \frac{\mathbf{u}}{|\tilde{\mathbf{v}}|}\nabla_{\mathbf{x}}I_e$ [65] has to be applied. The same transformation has to be also applied in the case of ions.

The *one energy group BGK electron and ion transport equations* in the Lagrangian frame resulting from (2.127, 2.134) then take the following form

$$\frac{1}{|\tilde{\mathbf{v}}|_e}\frac{\mathrm{d}I_e}{\mathrm{d}t} + \left(\mathbf{n} - \frac{\mathbf{u}}{|\tilde{\mathbf{v}}|_e}\right) \cdot \nabla_{\mathbf{x}}I_e = \frac{5\,q_e}{m_e}\frac{\langle |\mathbf{v}|^{-1}S_e \rangle_{|\mathbf{v}|}^e}{\langle |\mathbf{v}|S_e \rangle_{|\mathbf{v}|}^e}\mathbf{n}\cdot\mathbf{E}\,I_e + \frac{n_i}{|\tilde{\mathbf{v}}|_e n_e}\frac{\mathrm{d}\bar{Z}}{\mathrm{d}t}\langle S_e \rangle_{|\mathbf{v}|}^e$$
$$+ \tilde{k}_e\left(\langle S_e \rangle_{|\mathbf{v}|}^e - I_e\right) + \tilde{\sigma}_e\left(\bar{I}_e - I_e\right), \qquad (2.135)$$

$$\frac{1}{|\tilde{\mathbf{v}}|_i}\frac{\mathrm{d}I_i}{\mathrm{d}t} + \left(\mathbf{n} - \frac{\mathbf{u}}{|\tilde{\mathbf{v}}|_i}\right) \cdot \nabla_{\mathbf{x}}I_i = \frac{5\,q_i}{m_i}\frac{\langle |\mathbf{v}|^{-1}S_i \rangle_{|\mathbf{v}|}^i}{\langle |\mathbf{v}|S_i \rangle_{|\mathbf{v}|}^i}\mathbf{n}\cdot\mathbf{E}\,I_i + \tilde{k}_i\left(\langle S_i \rangle_{|\mathbf{v}|}^i - I_i\right).$$
$$(2.136)$$

If we choose the source functions S_e and S_i to be represented by the Maxwellian velocity distribution of a moving fluid

$$f_M^e(\mathbf{x}, t, |\mathbf{v}|, \mathbf{n}) = n_e\left(\frac{m_e}{2\pi k_B T_e}\right)^{\frac{3}{2}}\exp\left(-\frac{m_e|\mathbf{v}|^2|\mathbf{n} - \frac{\mathbf{u}}{|\mathbf{v}|}|^2}{2k_B T_e}\right), \qquad (2.137)$$

$$f_M^i(\mathbf{x}, t, |\mathbf{v}|, \mathbf{n}) = n_i\left(\frac{m_i}{2\pi k_B T_e}\right)^{\frac{3}{2}}\exp\left(-\frac{m_i|\mathbf{v}|^2|\mathbf{n} - \frac{\mathbf{u}}{|\mathbf{v}|}|^2}{2k_B T_i}\right), \qquad (2.138)$$

where T_e and T_i are electron and ion temperatures, one can observe, that the term $\mathbf{n} - \frac{\mathbf{u}}{|\mathbf{v}|}$, which is similar to the terms $\mathbf{n} - \frac{\mathbf{u}}{|\mathbf{v}|_e}$ of (2.135) and $\mathbf{n} - \frac{\mathbf{u}}{|\mathbf{v}|_i}$ of (2.136), increases the complexity of the nonlocal transport problem. However, the Maxwellian velocity distributions (2.137) and (2.138) degenerate into an appropriate isotropic source function since the transport velocity takes over the fluid velocity. For simplicity, we will always consider that

$$|\tilde{\mathbf{v}}|_e \gg |\mathbf{u}|, \quad |\tilde{\mathbf{v}}|_i \gg |\mathbf{u}|, \qquad (2.139)$$

which assures that $\mathbf{n} - \frac{\mathbf{u}}{|\mathbf{v}|}$ can be approximated by $\mathbf{n}$ in (2.135, 2.136, 2.137, 2.138).

Based on definitions (2.124, 2.125, 2.126, 2.132, 2.133), we show explicit values of the uniform electron transport velocity $|\tilde{\mathbf{v}}|_e$, the uniform electron-ion collision frequency $\tilde{\nu}_{ei}$, the uniform scattering frequency $\tilde{\nu}_{\sigma_e}$, the uniform ion transport velocity $|\tilde{\mathbf{v}}|_i$, and the uniform ion-ion collision frequency $\tilde{\nu}_{ii}$ to be

$$|\tilde{\mathbf{v}}|_e \approx \frac{\langle |\mathbf{v}| f_M^e \rangle_{|\mathbf{v}|}^e}{\langle f_M^e \rangle_{|\mathbf{v}|}^e} \approx \frac{8}{3\sqrt{\pi}} \sqrt{\frac{2k_B T_e}{m_e}} \approx 2.13\,|\mathbf{v}_{T_e}|\,, \tag{2.140}$$

$$\tilde{\nu}_{ei} \approx \frac{\langle \nu_{ei}(|\mathbf{v}|^{-3}) f_M^e \rangle_{|\mathbf{v}|}^e}{\langle f_M^e \rangle_{|\mathbf{v}|}^e} = \bar{\nu}_{ei} |\mathbf{v}_{T_e}|^3 \frac{\sqrt{\pi}}{4} \left(\frac{m_e}{2k_B T_e} \right)^{\frac{3}{2}} \approx 0.16\,\bar{\nu}_{ei}\,, \tag{2.141}$$

$$\tilde{\nu}_{\sigma_e} \approx \frac{\langle \nu_{\sigma_e}(|\mathbf{v}|^{-3}) f_M^e \rangle_{|\mathbf{v}|}^e}{\langle f_M^e \rangle_{|\mathbf{v}|}^e} = \bar{\nu}_{\sigma_e} |\mathbf{v}_{T_e}|^3 \frac{\sqrt{\pi}}{4} \left(\frac{m_e}{2k_B T_e} \right)^{\frac{3}{2}} \approx 0.16\,\bar{\nu}_{\sigma_e}\,, \tag{2.142}$$

$$|\tilde{\mathbf{v}}|_i \approx \frac{\langle |\mathbf{v}| f_M^i \rangle_{|\mathbf{v}|}^i}{\langle f_M^i \rangle_{|\mathbf{v}|}^i} \approx \frac{8}{3\sqrt{\pi}} \sqrt{\frac{2k_B T_i}{m_i}} \approx 2.13\,|\mathbf{v}_{T_i}|\,, \tag{2.143}$$

$$\tilde{\nu}_{ii} \approx \frac{\langle \nu_{ii}(|\mathbf{v}|^{-3}) f_M^i \rangle_{|\mathbf{v}|}^i}{\langle f_M^i \rangle_{|\mathbf{v}|}^i} = \bar{\nu}_{ii} |\mathbf{v}_{T_i}|^3 \frac{\sqrt{\pi}}{4} \left(\frac{m_i}{2k_B T_i} \right)^{\frac{3}{2}} \approx 0.16\,\bar{\nu}_{ii}\,, \tag{2.144}$$

where the above quantities are expressed with respect to the electron thermal velocity magnitude $|\mathbf{v}_{T_e}| = \sqrt{\frac{k_B T_e}{m_e}}$, the ion thermal velocity magnitude $|\mathbf{v}_{T_i}| = \sqrt{\frac{k_B T_i}{m_i}}$, and the electron-ion thermal collision, the ion-ion thermal collision and scattering frequencies $\bar{\nu}_{ei}$, $\bar{\nu}_{ii}$, and $\bar{\nu}_{\sigma_e}$ [3], respectively.

Finally, we write the **nonlocal BGK electron and ion transport model** in Lagrangian frame

$$\frac{1}{|\tilde{\mathbf{v}}|_e} \frac{\mathrm{d}I_e}{\mathrm{d}t} + \mathbf{n} \cdot \nabla_{\mathbf{x}} I_e = \frac{q_e}{k_B T_H^e} \mathbf{n} \cdot \mathbf{E}\, I_e + n_i \frac{\mathrm{d}\bar{Z}}{\mathrm{d}t} \frac{3}{8\pi} k_B T_e$$
$$+ \tilde{k}_e \left(\left(\frac{n_e}{\pi^{\frac{3}{2}}} \frac{\sqrt{2}k_B^{\frac{3}{2}}}{\sqrt{m_e}} \right) T_e^{\frac{3}{2}} - I_e \right) + \tilde{\sigma}_e \left(\bar{I}_e - I_e \right)\,, \tag{2.145}$$

$$\frac{1}{|\tilde{\mathbf{v}}|_i} \frac{\mathrm{d}I_i}{\mathrm{d}t} + \mathbf{n} \cdot \nabla_{\mathbf{x}} I_i = \frac{q_i}{k_B T_H^i} \mathbf{n} \cdot \mathbf{E}\, I_i + \tilde{k}_i \left(\left(\frac{n_i}{\pi^{\frac{3}{2}}} \frac{\sqrt{2}k_B^{\frac{3}{2}}}{\sqrt{m_i}} \right) T_i^{\frac{3}{2}} - I_i \right)\,, \tag{2.146}$$

which results from equations (2.135) and (2.136), where we used $S_e = f_M^e$ (2.137) and $S_i = f_M^i$ (2.138) following the assumption (2.139). We also used T_H^e and T_H^i, which are the kinetic temperatures of electrons and ions, respectively, and will be defined further in this section. An important observation about the electron transport model (2.145) is, that its asymptotic behavior gives a diffusive heat flux $\mathbf{q}_{BGK} \approx 0.4 \mathbf{q}_{SH}$ from the previous section, which supports the range of validity of our model. A detailed description of the diffusion asymptotic can be found in Appendix A.4.

An important property of the proposed nonlocal BGK electron transport model (2.145) reads

$$\tilde{\lambda}_e = \frac{1}{\tilde{k}_e} = \frac{|\tilde{\mathbf{v}}|_e}{\tilde{\nu}_{ei}} \approx \frac{2.13|\mathbf{v}_{T_e}|}{0.16\bar{\nu}_{ei}} = \frac{128}{3\pi} \bar{\lambda}_e \approx 13.6 \bar{\lambda}_e\,, \tag{2.147}$$

which states, that the nonlocal BGK electron transport model mean free path $\tilde{\lambda}_e$ related to the electron distribution is of one order of magnitude larger than the usual mean free path $\bar{\lambda}_e$, which is related to the thermal velocity of electrons. An equivalent relation

holds also for the proposed nonlocal BGK ion transport model (2.146) i.e.

$$\tilde{\lambda}_i = \frac{1}{\tilde{k}_i} = \frac{|\tilde{\mathbf{v}}|_i}{\tilde{\nu}_{ii}} \approx \frac{2.13|\mathbf{v}_{T_i}|}{0.16\bar{\nu}_{ii}} = \frac{128}{3\pi}\bar{\lambda}_{ii} \approx 13.6\bar{\lambda}_i \,, \tag{2.148}$$

where $\bar{\lambda}_i$ is the usual ion mean free path, which is related to the thermal velocity of ions.

Many of the above formulas were obtained by using the following Gauss integrals

$$\langle |\mathbf{v}|^{-3} f_M \rangle_{|\mathbf{v}|} = \frac{nm}{\pi^{\frac{3}{2}}} \frac{\sqrt{\pi}}{8} \,, \tag{2.149}$$

$$\langle |\mathbf{v}|^{-1} f_M \rangle_{|\mathbf{v}|} = \frac{3}{8} \frac{n}{\pi} k_B T \,, \tag{2.150}$$

$$\langle f_M \rangle_{|\mathbf{v}|} = \frac{n}{\pi^{\frac{3}{2}}} \frac{\sqrt{2} k_B^{\frac{3}{2}}}{\sqrt{m}} T^{\frac{3}{2}} \,, \tag{2.151}$$

$$\langle |\mathbf{v}| f_M \rangle_{|\mathbf{v}|} = \frac{n}{\pi^{\frac{3}{2}}} \frac{15\sqrt{\pi}}{8} \frac{k_B^2}{m} T^2 \,, \tag{2.152}$$

where n is the density of given particles, m is the mass of given particle, T is the temperature of given particles distribution and the operator $\langle \rangle_{|\mathbf{v}|}$ is equivalent to (2.121) in the case of electrons or (2.129) in the case of ions, and f_M corresponds to (2.137) in the case of electrons and to (2.138) in the case of ions. In equations (2.140, 2.143), the exact value $\frac{15\sqrt{\pi}}{16}$ was approximated by the value $\frac{8}{3\sqrt{\pi}}$, which reflects the result of (2.150).

This section can be closed by defining an approximate temperature of transported electrons and ions, which are represented by the quantities I_e and I_i. Even though the velocity distribution of electrons can, in principle, be absolutely random, the experimental experience indicates, that the distribution approaches the Maxwell-Boltzmann distribution. In the case of ions, the velocity distribution is even closer to the Maxwell-Boltzmann distribution. This allows us to define electron and ion kinetic temperatures as

$$T_H^e = \frac{m_e \pi}{k_B} \left(\frac{\int_{4\pi} I_e \, \mathrm{d}\omega}{4\pi n_e m_e \sqrt{2}} \right)^{\frac{2}{3}} \,, \tag{2.153}$$

$$T_H^i = \frac{m_i \pi}{k_B} \left(\frac{\int_{4\pi} I_i \, \mathrm{d}\omega}{4\pi n_i m_i \sqrt{2}} \right)^{\frac{2}{3}} \,, \tag{2.154}$$

which is a result of (2.151) further integrated over all solid angles, where $\mathrm{d}\omega = \sin(\phi)\mathrm{d}\phi\mathrm{d}\theta$.

In principal, we formulated our nonlocal BGK transport model (2.145, 2.146) in such a way, that the energy transport is treated directly through I_e and I_i. However, the particle transport, i.e. electron and ion densities, need to be evaluated as well. The electron and ion density change due to the nonlocal transport can be expressed as

$$\frac{\mathrm{d}n_e}{\mathrm{d}t} = \frac{2}{3\,k_B\,T_H^e} \left(\frac{q_e}{k_B\,T_H^e} \mathbf{q}_H^e \cdot \mathbf{E} - \nabla_{\mathbf{x}} \cdot \mathbf{q}_H^e \right) + n_i \frac{\mathrm{d}\bar{Z}}{\mathrm{d}t} \,, \tag{2.155}$$

$$\frac{\mathrm{d}n_i}{\mathrm{d}t} = \frac{2}{3\,k_B\,T_H^i} \left(\frac{q_i}{k_B\,T_H^i} \mathbf{q}_H^i \cdot \mathbf{E} - \nabla_{\mathbf{x}} \cdot \mathbf{q}_H^i \right) \,, \tag{2.156}$$

which is based on the statistical distribution approach, i.e. that the change of number

of particles can be obtained by dividing the change of energy by mean particle energy. Equation (2.155) was obtained from (2.145) by dividing the I_e related terms by the mean particle energy $\frac{3}{2} k_B T_H^e$ and by dividing the $\bar{Z}$ related term by the mean thermal energy $\frac{3}{2} k_B T_e$. Equation (2.156) was obtained from (2.146) by dividing the I_i related terms by the mean particle energy $\frac{3}{2} k_B T_H^i$. Any term related to $\tilde{k}_e, \tilde{\sigma}_e, \tilde{k}_i$, i.e related to collisions, in (2.145, 2.146) by definition cancels out, since collisions do not produce particles.

Since we know, that in plasma the charge density ρ^q change is governed by the relation

$$\frac{\mathrm{d}\rho^q}{\mathrm{d}t} = \frac{\mathrm{d}}{\mathrm{d}t} \left(q_i n_i + q_e n_e \right) = e \frac{\mathrm{d}}{\mathrm{d}t} \left(\bar{Z} n_i - n_e \right) , \qquad (2.157)$$

where e is positive charge related to one electron, we can see, that based on equations (2.155) and (2.156) the charge density change due to nonlocal transport reads

$$\frac{\mathrm{d}\rho^q}{\mathrm{d}t} = \frac{2 \bar{Z} e}{3 k_B T_H^i} \left(\frac{\bar{Z} e}{k_B T_H^i} \mathbf{q}_H^i \cdot \mathbf{E} - \nabla_\mathbf{x} \cdot \mathbf{q}_H^i \right) + \frac{2 e}{3 k_B T_H^e} \left(\nabla_\mathbf{x} \cdot \mathbf{q}_H^e - \frac{e}{k_B T_H^e} \mathbf{q}_H^e \cdot \mathbf{E} \right) . \qquad (2.158)$$

The heat fluxes due to electron and ion transport are given by explicit formulas

$$\mathbf{q}_H^e = \int_{4\pi} \mathbf{n} I_e \, \mathrm{d}\omega , \qquad (2.159)$$

$$\mathbf{q}_H^i = \int_{4\pi} \mathbf{n} I_i \, \mathrm{d}\omega , \qquad (2.160)$$

where the integration over all solid angles $\mathrm{d}\omega = \sin(\phi)\mathrm{d}\phi\mathrm{d}\theta$ is performed.

It is worth mentioning, that the energy flux hydrodynamic closure (2.75) is well described by (2.159) in the case of electrons and by (2.160) in the case of ions, when the velocity assumption (2.139) holds. The nonlocal transport treatment does not provide any term directly describing the viscous flux hydrodynamic closure (2.74). Nevertheless, the viscosity effect is usually less important in plasma physics in general.

We provide an approximate expression of the anisotropic effect due to viscosity as

$$\mathbf{g}_H^e = \frac{\tilde{k}_e + \tilde{\sigma}_e}{|\tilde{\mathbf{v}}|_e} \int_{4\pi} \mathbf{n} I_e \, \mathrm{d}\omega , \qquad (2.161)$$

$$\mathbf{g}_H^i = \frac{\tilde{k}_i}{|\tilde{\mathbf{v}}|_i} \int_{4\pi} \mathbf{n} I_i \, \mathrm{d}\omega , \qquad (2.162)$$

where $\mathbf{g}_H^e$ and $\mathbf{g}_H^i$ are the momentum source terms due to viscosity to be applied in hydrodynamics. The above approximations originate from the radiation transport treatment presented in [6] and are valid when the velocity assumption (2.139) holds.

2.4 Radiative Transfer

So far the description of plasma relied on the fluid equations continuum model. Nevertheless, under the condition of high-temperature plasma, which is the case of laser-heated plasmas, generation of radiation field due to plasma fluid photon emission becomes an important physical phenomenon. The effect of radiation added to the total energy density and momentum of the system through radiation energy density, radiation energy flux, and its contribution to the fluid pressure. It is necessary to define these quantities for radiation and describe the way radiation couples to the plasma.

2.4.1 The Specific Intensity and Equation of Radiation Transfer

The radiation field, seen as a fluid of photons, is, in general, a function of position and time, where at any given position poses distribution in both direction and energy of photons. As in [2], we define the *specific intensity* $I(\mathbf{x}, t, \mathbf{n}, \nu)[erg/cm^2/s/Hz/sr]$ of radiation at position $\mathbf{x}$ and time t, traveling in direction $\mathbf{n}$ with frequency ν, to be such that amount of energy transported by radiation of frequencies $(\nu, \nu + \mathrm{d}\nu)$ across an oriented surface element $\mathrm{d}\mathbf{S}$, in a time $\mathrm{d}t$, into a solid angle $\mathrm{d}\omega$ around $\mathbf{n}$, is

$$\mathrm{d}E = I(\mathbf{x}, t, \mathbf{n}, \nu)\,\mathbf{n} \cdot \mathrm{d}\mathbf{S}\mathrm{d}\omega\mathrm{d}\nu\mathrm{d}t\,. \tag{2.163}$$

The *photon distribution function* f_R is defined such that $f_R(\mathbf{x}, t, \mathbf{p})\mathrm{d}^3x\mathrm{d}^3p$ is the number of photons per volume d^3x at $(\mathbf{x}, t)$ with momenta within $(\mathbf{p}, \mathbf{p} + \mathrm{d}\mathbf{p})$, where $\mathbf{p} = \frac{h\nu}{c}\mathbf{n}$ ($h\nu$ is photon energy). Using the momentum space defined in spherical coordinates where $\mathrm{d}^3p = p^2\mathrm{d}p\mathrm{d}\omega = \left(\frac{h\nu}{c}\right)^2\frac{h}{c}\mathrm{d}\nu\mathrm{d}\omega$, we find that the number of photons can be equally expressed as

$$\frac{I(\mathbf{x}, t, \mathbf{n}, \nu)}{h\nu c}\,\mathrm{d}^3x\mathrm{d}\nu\mathrm{d}\omega = \frac{h^3\nu^2}{c^3}f_R(\mathbf{x}, t, \mathbf{n}, \nu)\,\mathrm{d}^3x\mathrm{d}\nu\mathrm{d}\omega\,, \tag{2.164}$$

where we used that $\mathrm{d}^3x = c\mathrm{d}t\mathrm{d}S$ and counted number of photons instead of their energy on the left hand side of (2.164). Since the distribution function f_R is relativistically invariant, the explicit relation of the specific intensity to f_R is of great use in co-moving frame coordinates formulation.

The *monochromatic radiation energy density* ϵ_R^ν at frequency ν is the number density of photons at that frequency, summed over all solid angles, times their energy $h\nu$, which according to (2.164) reads

$$\epsilon_R^\nu = \frac{1}{c}\int_{4\pi} I\,\mathrm{d}\omega\,. \tag{2.165}$$

The *monochromatic radiation flux* $\mathbf{q}_R^\nu$ is a vector such that $\mathbf{q}_R^\nu \cdot \mathrm{d}\mathbf{S}$ gives the net rate of radiant energy flow per unit frequency interval, at frequency ν, across the element surface $\mathrm{d}\mathbf{S}$. The net number of photons flux crossing $\mathrm{d}\mathbf{S}$ per unit time and frequency interval from all solid angles and multiplied by the photon energy $h\nu$ gives the energy flux

$$\mathbf{q}_R^\nu = \int_{4\pi} \mathbf{n}\,I\,\mathrm{d}\omega\,. \tag{2.166}$$

The net rate of radiative momentum transport across $\mathrm{d}\mathbf{S}$ at frequency ν is $\frac{1}{c}\mathbf{q}_R^\nu \cdot \mathrm{d}\mathbf{S}$, since the momentum of a photon with energy $h\nu$ is $\frac{h\nu}{c}$. Then, the *radiation pressure tensor* described as radiative momentum transport per unit frequency interval, at frequency ν, across surface perpendicular to each of the coordinate axis and integrated over all

solid angles is defined as

$$\mathbf{P}_R^\nu = \frac{1}{c} \int_{4\pi} \mathbf{n} \otimes \mathbf{n} \, I \, \mathrm{d}\omega \,. \tag{2.167}$$

The principal task of this section it the formulation of the *transfer equation*, which determines how radiation is transported through plasma and is the equivalent of the Boltzmann equation for photons. Then, the specific intensity of traveling photons at frequency ν along the direction $\mathbf{n}$ is governed by the equation

$$\frac{1}{c} \frac{\partial I}{\partial t} + \left. \frac{\partial I}{\partial s} \right|_{\mathbf{n}} = j^\nu - k^\nu I \,, \tag{2.168}$$

where s is the path length and $\left. \frac{\partial I}{\partial s} \right|_{\mathbf{n}}$ is the derivative of I with respect to the path length s along the ray direction $\mathbf{n}$. Since photons travel with the velocity equal to the speed of light, we can observe, that the left hand side of (2.168) describes the transport (advection) of the photon energy propagating in the direction $\mathbf{n}$. Terms on the right hand side are plasma *emissivity* $j^\nu [erg/cm^3/s/Hz/sr]$ and *opacity* $k^\nu [1/cm]$. The meaning of the right hand side of (2.168) is the rate of change of photon intensity at point $\mathbf{x}$ at time t due to positive contribution of photon emission $j^\nu \mathrm{d}\nu \mathrm{d}\omega$ and negative contribution $-k^\nu I \mathrm{d}\nu \mathrm{d}\omega$. When (2.168) is seen as the Boltzmann transport equation for photons, its right hand side resembles to collision operators in section 2.2.2, especially to the BGK form (2.46). Its resemblance resides in that $\frac{1}{k^\nu} = \lambda^\nu$, where $\lambda^\nu [cm]$ is the *monochromatic photon mean free path* corresponding to the photon frequency ν.

The collision operator of the nonlocal model of radiation transport (2.168) has to be further extended by assuming the *scattering* of photons by plasma background. After being thermally emitted (due to j^ν), the photon may be scattered out of its direction many times before being absorbed by plasma (due to k^ν) and converted back into the internal energy of plasma.

The *mean intensity* is defined as the average of the specific intensity over all solid angles as

$$\bar{I}(\mathbf{x}, t, \nu) = \frac{1}{4\pi} \int_{4\pi} I \, \mathrm{d}\omega \,. \tag{2.169}$$

The transfer equation of photons with extended collision operator by scattering reads

$$\frac{1}{c} \frac{\partial I}{\partial t} + \left. \frac{\partial I}{\partial s} \right|_{\mathbf{n}} = j^\nu + \sigma^\nu \bar{I} - (k^\nu + \sigma^\nu) \, I \,, \tag{2.170}$$

where $\sigma^\nu [1/cm]$ is the *scattering coefficient* of photons with frequency ν. An important property of using mean intensity is that such an isotropic operator conserves number of photons being scattered.

2.4.2   Moments of the Transfer Equation

The physical meaning of the zero-order and first-order moments of the transfer equation (2.170) resemble to the moments applied in section 2.2.3, i.e. the energy and momentum equations.

We define the specific intensity $I(\mathbf{x}, \phi, \theta, \nu)$ to be a function of position vector $\mathbf{x}$, which can be, in general, expressed in a general curvilinear coordinate system, spherical coordinates ϕ and θ, where ϕ and θ are the polar and azimuthal angles (see Fig. 2.1) describe the direction $\mathbf{n}$ of traveling photons, and frequency ν representing the magnitude of photon momentum $\frac{h\nu}{c}$.

The derivative with respect to the path length along the direction $\mathbf{n}$, i.e. the operator $\frac{\partial}{\partial s}\big|_{\mathbf{n}}$ of (2.170), then takes a specific form with respect to the coordinate system used.

The 1D Slab Geometry Transfer Equation

In the Cartesian coordinates the position vector is defined as $\mathbf{x} = (x, y, z)$, where the coordinate axis vectors are constant (non-curvilinear). The slab geometry implies a reduced dependence of the specific intensity $I(\mathbf{x}(z), t, \mathbf{n}(\phi), \nu)$, and the resulting form of the *slab transfer equation* reads [2]

$$\frac{1}{c}\frac{\partial I}{\partial t} + \cos(\phi)\frac{\partial I}{\partial z} = j^\nu + \sigma^\nu \bar{I} - (k^\nu + \sigma^\nu)\, I\,, \tag{2.171}$$

which represents a 4D problem, i.e. the solution of (2.171) depends on t, z, ϕ and ν.

The integration over all solid angles of photon directions applied to (2.171) leads to the zero-order moment equation [2]

$$\frac{\partial \epsilon_R^\nu}{\partial t} + \frac{\partial \mathbf{q}_z^\nu}{\partial z} = \int_0^{2\pi}\int_0^\pi j^\nu + \sigma^\nu \bar{I} - (k^\nu + \sigma^\nu)\, I \sin(\phi)\mathrm{d}\phi\mathrm{d}\theta\,, \tag{2.172}$$

where the definitions of monochromatic radiation energy density ϵ^ν (2.165) and monochromatic radiation energy flux $\mathbf{q}^\nu$ (2.166) were used.

In order to clarify the relation between the spatial coordinate system, in this case the Cartesian coordinate system, and the directional coordinate system, which is always spherical coordinate system see Fig. 2.1. The reference axis z corresponds to the direction $\mathbf{n}(0)$.

The 1D Spherically Symmetric Geometry Transfer Equation

In spherical coordinates the position vector is defined as $\mathbf{x} = (r, \tilde{\phi}, \tilde{\theta})$, where the coordinate axis vectors change according to the position dependence on $(\tilde{\phi}, \tilde{\theta})$, i.e. system is curvilinear. The spherically symmetric geometry implies a reduced dependence of the specific intensity $I(\mathbf{x}(r), t, \mathbf{n}(\phi), \nu)$, and the resulting form of the *spherically symmetric transfer equation* reads

$$\frac{1}{c}\frac{\partial I}{\partial t} + \cos(\phi)\frac{\partial I}{\partial r} - \frac{\sin(\phi)}{r}\frac{\partial I}{\partial \phi} = j^\nu + \sigma^\nu \bar{I} - (k^\nu + \sigma^\nu)\, I\,, \tag{2.173}$$

which represents a 4D problem, i.e. the solution of (2.173) depends on t, r, ϕ and ν.

The integration over all solid angles of photon directions applied to (2.173) leads to the zero-order moment equation [2]

$$\frac{\partial \epsilon_R^\nu}{\partial t} + \frac{1}{r^2}\frac{\partial \left(r^2\, \mathbf{q}_r^\nu\right)}{\partial r} = \int_0^{2\pi}\int_0^\pi j^\nu + \sigma^\nu \bar{I} - (k^\nu + \sigma^\nu)\, I \sin(\phi)\mathrm{d}\phi\mathrm{d}\theta\,, \tag{2.174}$$

where the definitions of monochromatic radiation energy density ϵ^ν (2.165) and monochromatic radiation energy flux $\mathbf{q}^\nu$ (2.166) were used.

In order to clarify the relation between the spatial coordinate system, in this case spherical coordinate system, and the directional coordinate system, which is always spherical coordinate system see Fig. 2.1. The reference axis of symmetry is chosen to be aligned with the z axis and corresponds to the transport direction $\mathbf{n}(0)$.
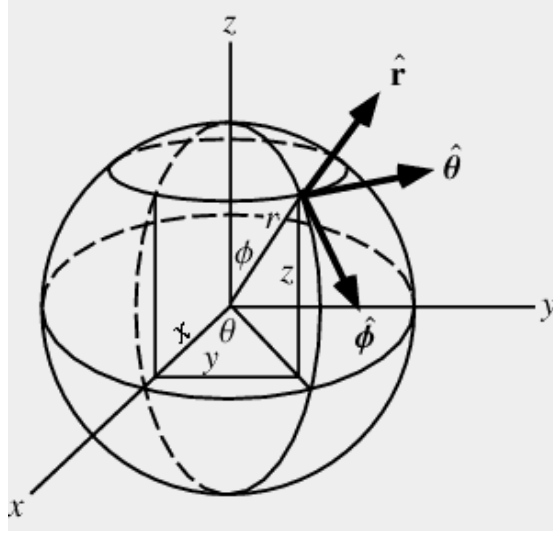
FIGURE 2.1: Graphical interpretation of the orthonormal curvilinear basis of spherical coordinates system [66].

It is worth mentioning that the origin of the derivative with respect to ϕ in (2.173) is not obvious. The reader may refer to [2] for a better understanding.

The 2D Axis Symmetric Geometry Transfer Equation

In cylindrical coordinates the position vector is defined as $\mathbf{x} = (r, \tilde{\theta}, z)$, where the coordinate axis vectors change according to the position dependence on $(\tilde{\theta})$, i.e. system is curvilinear. The axis symmetric geometry implies a reduced dependence of the specific intensity $I(\mathbf{x}(r, z), t, \mathbf{n}(\phi, \theta), \nu)$, and the resulting form of the *axis symmetric transfer equation* reads [2]

$$\frac{1}{c}\frac{\partial I}{\partial t} + \sin(\phi)\left(\cos(\theta)\frac{\partial I}{\partial r} - \frac{\sin(\theta)}{r}\frac{\partial I}{\partial \theta}\right) + \cos(\phi)\frac{\partial I}{\partial z} = j^\nu + \sigma^\nu \bar{I} - (k^\nu + \sigma^\nu) I\,, \quad (2.175)$$

which represents a 6D problem, i.e. the solution of (2.175) depends on t, r, z, ϕ, θ and ν.

The integration over all solid angles of photon directions applied to (2.175) leads to the zero-order moment equation [2]

$$\frac{\partial \epsilon_R^\nu}{\partial t} + \frac{1}{r}\frac{\partial\left(r\,\mathbf{q}_r^\nu\right)}{\partial r} + \frac{\partial \mathbf{q}_z^\nu}{\partial z} = \int_0^{2\pi}\int_0^\pi j^\nu + \sigma^\nu \bar{I} - (k^\nu + \sigma^\nu) I \sin(\phi)\mathrm{d}\phi\mathrm{d}\theta\,, \quad (2.176)$$

where the definitions of monochromatic radiation energy density ϵ^ν (2.165) and monochromatic radiation energy flux $\mathbf{q}^\nu$ (2.166) were used.

In order to clarify the relation between the spatial coordinate system, in this case cylindrical coordinate system, and the directional coordinate system, which is always spherical coordinate system see Fig. 2.1. The reference plane of the cylindrical symmetry is chosen to be given by the x and z axes, which correspond to the transport directions $\mathbf{n}(\pi/2, 0)$ and $\mathbf{n}(0, 0)$ (see Fig. 2.2).

It is worth mentioning that the origin of the derivative with respect to θ in (2.175) is not obvious. The reader may refer to [2] for a better understanding.
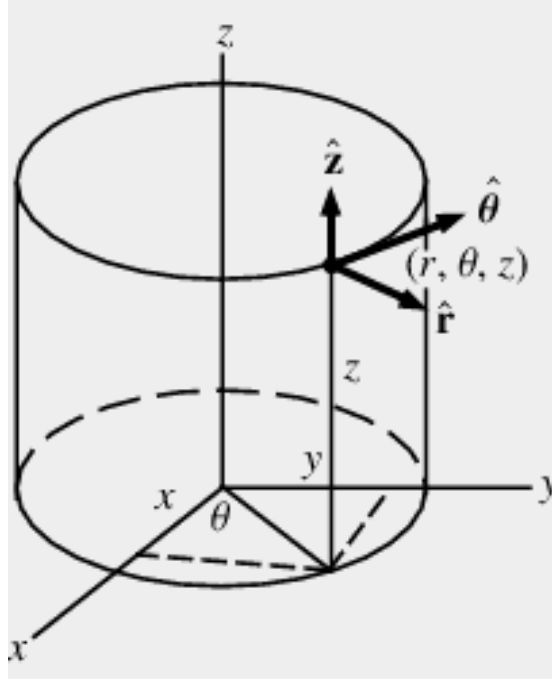
FIGURE 2.2: Graphical interpretation of the orthonormal curvilinear basis of cylindrical coordinates system [67].

Monochromatic Radiation Energy and Momentum Equations

We have already shown the zero-order moment of the transfer equation for different geometries, i.e. the slab geometry (2.171), spherically symmetric geometry (2.173), and axis symmetric geometry (2.175). Independent of the coordinate system used, the zero-order moment of the latter mentioned transfer equations (2.172, 2.174, 2.176) lead to the *energy equation* of the radiation field

$$\frac{\partial \epsilon_R^\nu}{\partial t} + \nabla \cdot \mathbf{q}_R^\nu = \int_{4\pi} j^\nu + \sigma^\nu \bar{I} - (k^\nu + \sigma^\nu) I d\omega \,, \tag{2.177}$$

where $\nabla \cdot$ refers to the divergence operator defined with respect to the coordinate system and the monochromatic radiation energy density ϵ_R^ν and monochromatic radiation energy flux $\mathbf{q}_R^\nu$ were defined in(2.165) and (2.166), respectively.

The first-order moment, in particular the $\frac{\mathbf{n}}{c}$ moment, leads to the *momentum equation* of the radiation field

$$\frac{1}{c^2} \frac{\partial \mathbf{q}_R^\nu}{\partial t} + \nabla \cdot \mathbf{P}_R^\nu = \int_{4\pi} \frac{\mathbf{n}}{c} \left(j^\nu + \sigma^\nu \bar{I} - (k^\nu + \sigma^\nu) I \right) d\omega \,. \tag{2.178}$$

where the monochromatic radiation pressure tensor $\mathbf{P}_R^\nu$ was defined in (2.167).

It is worth mentioning that right hand sides of (2.177) and (2.178) are nothing else than energy and momentum exchange due to collisions with plasma, more precisely with electron specie of plasma. Thus, we write

$$g_R^\nu = -\int_{4\pi} j^\nu + \sigma^\nu \bar{I} - (k^\nu + \sigma^\nu) I d\omega \approx k^\nu c \epsilon_R^\nu - 4\pi j^\nu \,, \tag{2.179}$$

$$\mathbf{g}_R^\nu = -\int_{4\pi} \frac{\mathbf{n}}{c} \left(j^\nu + \sigma^\nu \bar{I} - (k^\nu + \sigma^\nu) I \right) d\omega \approx \frac{k^\nu + \sigma^\nu}{c} \mathbf{q}_R^\nu \,. \tag{2.180}$$

where g_R^ν is the energy exchange term between plasma electrons and radiation field photons at the frequency ν, and $\mathbf{g}_R^\nu$ is the momentum exchange term between plasma electrons and radiation field photons at the frequency ν. The right most terms of (2.179) and (2.180) arise when the emission coefficient j^ν, scattering coefficient σ^ν, and opacity coefficient k^ν are approximated as being isotropic.

In the end, we write the *monochromatic radiation equations*

$$\frac{\partial \epsilon_R^\nu}{\partial t} + \nabla \cdot \mathbf{q}_R^\nu \;=\; 4\pi j^\nu - k^\nu c \epsilon_R^\nu\,, \tag{2.181}$$

$$\frac{1}{c^2}\frac{\partial \mathbf{q}_R^\nu}{\partial t} + \nabla \cdot \mathbf{P}_R^\nu \;=\; -\frac{k^\nu + \sigma^\nu}{c}\,\mathbf{q}_R^\nu\,. \tag{2.182}$$

where the isotropic approximation of j^ν, σ^ν and k^ν in (2.177, 2.178) applies.

2.4.3 Equations of Radiation Hydrodynamics

In section 2.2.5, the two temperature single-fluid hydrodynamic model in Lagrangian frame is defined. Even though we described the continuum equations to be used for the fluid model of plasma in a very detail, such a model of laser-heated plasmas is still missing a very important physical phenomenon the *plasma-radiation coupling*.

A straightforward way to include such a coupling is to treat the radiation field (photons) as another specie and apply the collisional terms according to (2.179) and (2.180). This leads to the plasma fluid model extended by the radiation coupling

$$\frac{\mathrm{d}\rho}{\mathrm{d}t} \;=\; -\rho \nabla_{\mathbf{x}} \cdot \mathbf{u}\,, \tag{2.183}$$

$$\rho \frac{\mathrm{d}\mathbf{u}}{\mathrm{d}t} \;=\; -\nabla_{\mathbf{x}}\,(p_i + p_e) + \nabla_{\mathbf{x}} \cdot (\sigma_i + \sigma_e) + \mathbf{g}_R\,, \tag{2.184}$$

$$\rho \frac{\partial \tilde{\varepsilon}_i}{\partial T_i}\frac{\mathrm{d}T_i}{\mathrm{d}t} \;=\; -\rho \frac{\partial \tilde{\varepsilon}_i}{\partial \rho}\frac{\mathrm{d}\rho}{\mathrm{d}t} - p_i \nabla_{\mathbf{x}} \cdot \mathbf{u} + \sigma_i : \nabla_{\mathbf{x}}\mathbf{u} - \nabla_{\mathbf{x}} \cdot \mathbf{q}_i + \tilde{g}_{i|e}\,, \tag{2.185}$$

$$\rho \frac{\partial \tilde{\varepsilon}_e}{\partial T_e}\frac{\mathrm{d}T_e}{\mathrm{d}t} \;=\; -\rho \frac{\partial \tilde{\varepsilon}_e}{\partial \rho}\frac{\mathrm{d}\rho}{\mathrm{d}t} - p_e \nabla_{\mathbf{x}} \cdot \mathbf{u} + \sigma_e : \nabla_{\mathbf{x}}\mathbf{u} - \nabla_{\mathbf{x}} \cdot \mathbf{q}_e - \tilde{g}_{i|e} + g_R - \mathbf{u} \cdot \mathbf{g}_R\,. \tag{2.186}$$

where the coupling terms g_R and $\mathbf{g}_R$ must be integrated over the entire spectra of frequency

$$g_R \;=\; \int_0^\infty k^\nu c \epsilon_R^\nu - 4\pi j^\nu \,\mathrm{d}\nu\,, \tag{2.187}$$

$$\mathbf{g}_R \;=\; \int_0^\infty \frac{k^\nu + \sigma^\nu}{c}\,\mathbf{q}_R^\nu \,\mathrm{d}\nu\,, \tag{2.188}$$

i.e. collisions with photons at any frequency has to be included.

Another way is to substitute the energy exchange term $g_R = -\frac{\mathrm{d}\epsilon_R}{\mathrm{d}t} - \nabla \cdot \mathbf{q}_R$ in (2.186) following equations (2.177, 2.179, 2.187), where we define the *radiation energy density* ϵ_R and the *radiation flux* $\mathbf{q}_R$ as

$$\epsilon_R \;=\; \int_0^\infty \epsilon_R^\nu \,\mathrm{d}\nu\,, \tag{2.189}$$

$$\mathbf{q}_R \;=\; \int_0^\infty \mathbf{q}_R^\nu \,\mathrm{d}\nu\,, \tag{2.190}$$

where the contribution from any frequency adds to the radiation field quantities.

We will refer to the following model as the *equations of radiation hydrodynamics*, which describes two temperature single-fluid model including the inherent plasma-radiation coupling. The model comprises the following equations

$$\frac{\mathrm{d}\rho}{\mathrm{d}t} = -\rho\nabla\cdot\mathbf{u}\,, \tag{2.191}$$

$$\rho\frac{\mathrm{d}\mathbf{u}}{\mathrm{d}t} = -\nabla\left(p_i + p_e\right) + \nabla\cdot\left(\sigma_i + \sigma_e\right) + \mathbf{g}_R\,, \tag{2.192}$$

$$\rho\frac{\partial\tilde{\varepsilon}_i}{\partial T_i}\frac{\mathrm{d}T_i}{\mathrm{d}t} = -\rho\frac{\partial\tilde{\varepsilon}_i}{\partial\rho}\frac{\mathrm{d}\rho}{\mathrm{d}t} - p_i\nabla\cdot\mathbf{u} + \sigma_i : \nabla\mathbf{u} - \nabla\cdot\mathbf{q}_i + \tilde{g}_{i|e}\,, \tag{2.193}$$

$$\rho\frac{\partial\tilde{\varepsilon}_e}{\partial T_e}\frac{\mathrm{d}T_e}{\mathrm{d}t} + \frac{\mathrm{d}\epsilon_R}{\mathrm{d}t} = -\rho\frac{\partial\tilde{\varepsilon}_e}{\partial\rho}\frac{\mathrm{d}\rho}{\mathrm{d}t} - p_e\nabla\cdot\mathbf{u} + \sigma_e : \nabla\mathbf{u} - \nabla\cdot\left(\mathbf{q}_e + \mathbf{q}_R\right) - \tilde{g}_{i|e} - \mathbf{u}\cdot\mathbf{g}_R\,, \tag{2.194}$$

where equation (2.194) can be seen as the equation of "total energy" of electrons and radiation, which treats the evolution of electron temperature T_e and radiation energy density ϵ_R inherently.

In order to solve the radiation hydrodynamic model (2.191–2.194), the *radiation hydrodynamics closure*

$$\mathrm{cl}_{RadHydro} = \left(\frac{\partial\tilde{\varepsilon}_i}{\partial T_i}, \frac{\partial\tilde{\varepsilon}_e}{\partial T_e}, \frac{\partial\tilde{\varepsilon}_i}{\partial\rho}, \frac{\partial\tilde{\varepsilon}_e}{\partial\rho}, p_i, p_e, \sigma_i, \sigma_e, \mathbf{q}_i, \mathbf{q}_e, \tilde{g}_{i|e}, \epsilon_R, \mathbf{q}_R, \mathbf{g}_R\right)\,, \tag{2.195}$$

has to be provided, which is an extension of the two temperature single-fluid hydrodynamic closure (2.94) by the radiation field quantities radiation energy ϵ_R (2.189), radiation flux $\mathbf{q}_R$ (2.190), and radiation-plasma momentum exchange term $\mathbf{g}_R$ (2.188).

2.5   Radiation Transport Models

In principle, there is two different approaches to model the radiation transport used in the literature. First one is the approach based on the moments of the fundamental radiation transfer equation (2.170). In general, just the first two moments equations (2.181, 2.182) are considered, and form a widely used model using emissivity j, opacity k, and scattering coefficient σ as plasma parameters. Also higher moments could be applied, but the first two are widely used and considered to be sufficient [68]. Second one is the approach based on a direct solution of the radiation transfer equation (2.170), which is the one we apply in our nonlocal transport hydrodynamic model. The advantage of the latter approach is its first principle equation background, however, its solution addresses a 7D full phase space problem. This is not the case of the former approach, which relies only on time and spatial coordinates.

Anyway, both models have to obey the diffusion asymptotic with respect to the electron temperature, which is in a greater detail described in Appendix A.4.

2.5.1   Spherical Harmonics Approximations

As we have mentioned already before, the first two moments equations (2.181, 2.182) are widely used to model radiation transport. In these, ε_R^ν and $\mathbf{q}_R^\nu$ are the unknowns, i.e. radiation energy density, and radiation flux, respectively. In principle, there is one more unknown, and that is the radiation pressure tensor $\mathbf{P}_R^\nu$, which is defined in (2.167). The way $\mathbf{P}_R^\nu$ is treated addresses the following radiation transport models.

The Radiation Diffusion Approximation

First, we describe by far the most used radiation transport model nowadays. It consists in approximating the specific radiation intensity by the zero and first order term of Legendre polynomials, i.e.

$$\tilde{I} = I_0 + \mu \, I_1 \,, \tag{2.196}$$

where $\mu = \cos(\phi)$ refers to the projection of transport direction $\mathbf{n}(\phi)$ into z axis, which represents the axis of symmetry.

In the case of the approximate specific radiation intensity (2.196), the comparison of the radiation energy (2.165) and the radiation pressure tensor (2.167) gives a very important relation

$$\mathbf{P}_R^\nu = \frac{c}{3}\mathbf{I}\varepsilon_R^\nu \,, \tag{2.197}$$

where $\mathbf{I}$ is a unit matrix. The relation (2.197) is very often called P_1 closure.

If we take the stationary form of radiation momentum equation (2.182) and we apply (2.197), we obtain the following approximation of the radiation flux

$$\mathbf{q}_R^\nu = -\frac{c}{3}\frac{1}{k+\sigma}\nabla\varepsilon \,. \tag{2.198}$$

Finally, the *radiation diffusion model* reads

$$\frac{\partial \varepsilon_R^\nu}{\partial t} - \nabla \cdot \left(\frac{c}{3}\frac{1}{k+\sigma^\nu}\nabla\varepsilon_R^\nu \right) = 4\pi j^\nu - k^\nu \, c\varepsilon_R^\nu \,, \tag{2.199}$$

which was obtained by inserting the radiation flux (2.198) in the radiation energy equation (2.181). Since we used the monochromatic equations (2.181, 2.182), the radiation

diffusion equation (2.199) has to be adapted as

$$\frac{\partial \varepsilon_R^g}{\partial t} - \nabla \cdot \left(\frac{c}{3} \frac{1}{k_R^g + \sigma} \nabla \varepsilon_R^g \right) = 4\pi j^g - k_P^g c \varepsilon_R^g, \tag{2.200}$$

where the index g refers to a wide group (interval) of frequencies. The opacities k_P^g and k_R^g are the mean Planck and the mean Rosseland opacity. They differ in the their weighting-over-frequencies model and the main distinction is that the mean Rosseland opacity refers to the diffusive approach [6]. It is worth mentioning that the model (2.200) inherently treats the transport velocity to be infinite in the optically thin limit $k_R \ll 1$ due to the negligence of the time derivative in the definition (2.198).

The P_1 approximation

In the previous section we defined the P1 closure (2.197). Its name is not a coincidence, because the *P1 model*

$$\frac{\partial \varepsilon_R^g}{\partial t} + \nabla \cdot \mathbf{q}_R^g = 4\pi j^g - k_P^g \varepsilon_R^g, \tag{2.201}$$

$$\frac{1}{c} \frac{\partial \mathbf{q}_R^g}{\partial t} + \frac{c}{3} \nabla \varepsilon_R^g = -(k_P^g + \sigma^g) \mathbf{q}_R^g, \tag{2.202}$$

is obtained from the one group form of the radiation field equations (2.181, 2.182) by directly applying the latter closure (2.197). On the first sight the radiation diffusion model (2.200) and (2.201, 2.202) originate from the same approximation (2.197), however, the latter is less diffusive due to the exclusive use of the mean Planck opacity and proper time derivative in (2.202). This treatment also keeps the propagation velocity to be finite even in the optically thin limit $k_P \ll 1$.

Nevertheless the P_1 approximation provides the propagation velocity $c\sqrt{3}/3 \approx 0.577c$ rather than the correct value of c [6] in this case.

The $P_{1/3}$ approximation

The problem of inaccurate propagation velocity in the optically thin limit was addressed in [68]. It was proposed a combination of one third of (2.202) and two thirds of (2.198), thus giving the momentum equation

$$\frac{1}{3c} \frac{\partial \mathbf{q}_R^g}{\partial t} + \frac{c}{3} \nabla \varepsilon_R^g = -(k_P^g + \sigma) \mathbf{q}_R^g, \tag{2.203}$$

which provides the appropriate propagation velocity c, and is called the $P_{1/3}$ approximation. The latter method has been analyzed in [69]. It was shown that both P_1 and $P_{1/3}$ are first order methods in the optically thick limit [70].

The Variable Eddington Factor Method

All the models above are based on the specific radiation intensity approximation (2.196), which inherently indicates an insufficient treatment of highly anisotropic radiation transport. Solution of such an inconsistency can be addressed by modifying the closure relation (2.197) as

$$\mathbf{P}_R^g = \mathbf{I} f^g c \varepsilon_R^g, \tag{2.204}$$

where the coefficient f is called Variable Eddington Factor approximation (VEF). According to proposed models [61, 71] f^g spans the interval $(1/3, 1)$, which corresponds to the low anisotropy models (2.200–2.203) and to the free streaming wave limit at the extremes of the interval, respectively. Unfortunately, an important class of states where $f^g < 1/3$ are inherently excluded. In order to recover these states the value of f^g can be obtained by solving the radiation transport equation (2.170), which keeps the necessary information about radiation field anisotropy. However, once solved the equation (2.170) we do not need to solve (2.200) neither (2.201–2.203).

2.5.2 The Nonlocal BGK Radiation Transport Model

The transfer equation (2.170) can be reformulated into the BGK form

$$\frac{1}{c}\frac{\partial I_p^\nu}{\partial t} + \mathbf{n}\cdot\nabla I_p^\nu = k_p^\nu\left(I_S - I_p^\nu\right) + \sigma_p^\nu\left(\bar{I}_p^\nu - I_p^\nu\right), \tag{2.205}$$

where the photon source at frequency ν is given as $j^\nu = k_p^\nu I_S$ and the transfer operator $\mathbf{n}\cdot\nabla$ refers to a general operator $\frac{\partial}{\partial s}|_\mathbf{n}$.

The angular mean of the specific intensity I_p is defined as

$$\bar{I}_p^\nu(\mathbf{x}, t) = \frac{1}{4\pi}\int_{4\pi} I_p^\nu(\mathbf{x}, t, \mathbf{n})\mathrm{d}\omega. \tag{2.206}$$

We define the *total radiation intensity operator* for a quantity g as

$$\langle g\rangle_\nu = \int_0^\infty g\,\mathrm{d}\nu, \tag{2.207}$$

which brings up definition of the *total radiation intensity*

$$I_p(\mathbf{x}, t, \mathbf{n}) = \langle I_p^\nu(\mathbf{x}, t, \mathbf{n})\rangle_\nu, \tag{2.208}$$

which can be interpreted as a one energy transport group specific intensity representing the entire spectrum of photon energies, nevertheless, it keeps the information about the angular distribution of photons.

The application of the $\langle\rangle_\nu$ operator to the BGK transfer equation (2.205) leads to

$$\frac{1}{c}\frac{\partial\langle I_p^\nu\rangle_\nu}{\partial t} + \mathbf{n}\cdot\nabla\langle I_p^\nu\rangle_\nu = \left(\langle k_p^\nu I_S\rangle_\nu - \langle k_p^\nu I_e^\nu\rangle_\nu\right) + \left(\langle\sigma_p^\nu\bar{I}_p\rangle\nu - \langle\sigma_p^\nu I_p^\nu\rangle_\nu\right). \tag{2.209}$$

The BGK model requires a unique opacity and scattering coefficients. These are expressed based on the form of (2.209) as the following

$$\bar{k}_p = \frac{\langle k_p^\nu I_p^\nu\rangle_\nu}{\langle I_p^\nu\rangle_\nu} \approx \frac{\langle k_p^\nu I_S\rangle_\nu}{\langle I_S\rangle_\nu}, \tag{2.210}$$

$$\bar{\sigma}_p = \frac{\langle\sigma_p^\nu I_e^\nu\rangle_\nu}{\langle I_p^\nu\rangle_\nu} \approx \frac{\langle\sigma_p^\nu I_S\rangle_\nu}{\langle I_S\rangle_\nu}, \tag{2.211}$$

where the right most terms express the radiation source function I_S based approximations, which are, in general, easy to evaluate.

Based on the form of (2.209) and definitions (2.210, 2.211) we write the BGK radiation transport equation

$$\frac{1}{c}\frac{\partial I_p}{\partial t} + \mathbf{n} \cdot \nabla I_p = \bar{k}_p \left(\langle I_S \rangle_\nu - I_p \right) + \bar{\sigma}_p \left(\bar{I}_p - I_p \right) , \qquad (2.212)$$

where the *mean total radiation intensity* is defined as

$$\bar{I}_p(\mathbf{x}, t) = \langle \bar{I}_p^\nu(\mathbf{x}, t) \rangle_\nu . \qquad (2.213)$$

In order to address the plasma background, we define the source function I_S to be the Planck photon energy distribution

$$I_B(\mathbf{x}, t, \mathbf{n}, \nu) = \frac{2h\nu^3}{c^2} \frac{1}{\exp\left(\frac{h\nu}{k_B T_R}\right) - 1} , \qquad (2.214)$$

where for the Planck distribution holds

$$\langle I_B \rangle_\nu = a T_R^4 , \qquad (2.215)$$

where $a = \frac{\sigma}{\pi}$, σ being the Stefan-Boltzmann constant, T_R is the energetic radiation temperature of the equilibrium distribution (2.214), which is under the condition of local thermodynamic equilibrium equal to the electron plasma temperature, i.e. $T_R = T_e$. Consequently, the *gray-body BGK radiation transport equation in Eulerian frame* reads

$$\frac{1}{c}\frac{\partial I_p}{\partial t} + \mathbf{n} \cdot \nabla I_p = \bar{k}_p \left(a T_e^4 - I_p \right) + \bar{\sigma}_p \left(\bar{I}_p - I_p \right) . \qquad (2.216)$$

If we use $\frac{1}{c}\frac{d}{dt} = \frac{1}{c}\frac{\partial}{\partial t} + \frac{\mathbf{u}}{c}\nabla \approx \frac{1}{c}\frac{\partial}{\partial t}$ since $c \gg |\mathbf{u}|$ [65], we obtain the *gray-body BGK radiation transport equation in Lagrangian frame*

$$\frac{1}{c}\frac{d I_p}{dt} + \mathbf{n} \cdot \nabla I_p = \bar{k}_p \left(a T_e^4 - I_p \right) + \bar{\sigma}_p \left(\bar{I}_p - I_p \right) , \qquad (2.217)$$

where the quantities T_e, $\bar{k}_p$, and $\bar{\sigma}_p$ are defined in the Lagrangian frame.

The BGK model requires a unique opacity and scattering coefficients. These are expressed based on the form of (2.209) as the following

$$\bar{k}_p \quad \approx \quad \frac{\langle k_p^\nu I_B \rangle_\nu}{\langle I_B \rangle_\nu} , \qquad (2.218)$$

$$\bar{\sigma}_p \quad \approx \quad \frac{\langle \sigma_p^\nu I_B \rangle_\nu}{\langle I_B \rangle_\nu} . \qquad (2.219)$$

In the case of radiation, the transport velocity is always equal to the speed of light c.

2.6   The Nonlocal Transport Hydrodynamic Model

The *laser-heated plasma nonlocal transport hydrodynamic model* describes two temperature single-fluid model including laser-plasma coupling, radiation-plasma coupling, and transported electrons-plasma coupling. The model comprises the following equations

$$
\frac{\mathrm{d}\rho}{\mathrm{d}t} = -\rho\nabla\cdot\mathbf{u}\,, \tag{2.220}
$$

$$
\rho\frac{\mathrm{d}\mathbf{u}}{\mathrm{d}t} = -\nabla\left(p_i + p_e\right) + \rho^q\left(\mathbf{E} + \mathbf{u}\times\mathbf{B}\right) + \mathbf{g}_R + \mathbf{g}_H\,, \tag{2.221}
$$

$$
\rho\frac{\partial\varepsilon_i}{\partial T_i}\frac{\mathrm{d}T_i}{\mathrm{d}t} = -\rho\frac{\partial\varepsilon_i}{\partial\rho}\frac{\mathrm{d}\rho}{\mathrm{d}t} - p_i\nabla\cdot\mathbf{u} + G_{ie}\left(T_e - T_i\right)\,, \tag{2.222}
$$

$$
\rho\frac{\partial\varepsilon_e}{\partial T_e}\frac{\mathrm{d}T_e}{\mathrm{d}t} + \frac{\mathrm{d}\epsilon_R}{\mathrm{d}t} = -\rho\frac{\partial\varepsilon_e}{\partial\rho}\frac{\mathrm{d}\rho}{\mathrm{d}t} - p_e\nabla\cdot\mathbf{u} - \nabla\cdot\left(\mathbf{q}_H + \mathbf{q}_R\right) - G_{ie}\left(T_e - T_i\right)
$$
$$
-\mathbf{u}\cdot\left(\mathbf{g}_R + \mathbf{g}_H\right) + Q_{\mathrm{IB}}\,, \tag{2.223}
$$

where (2.220) represents the conservation of the single-fluid mass, (2.221) are the single-fluid momentum equations with the contributions of radiation and transported electrons momentum exchange $\mathbf{g}_R$ and $\mathbf{g}_H$, respectively, (2.222) is the energy equation of ions comprising the ion-electron exchange term based on G_{ie}, and equation (2.223) can be seen as the energy equation of electrons and radiation, comprising the electron specie (bounded plus free transported electrons) and the radiation field while the radiation and electron transport effect is coupled in an inherent way. Here we use the electron heat flux notation $\mathbf{q}_H$. The term Q_{IB} stands for the laser-plasma coupling due to inverse-bremsstrahlung mechanism. The appearance of the electromagnetic force in equation (2.221) suggests that the single-fluid need not to be quasi-neutral, nevertheless the charge density will always tend to be small $\rho^q \approx 0$.

In order to solve the radiation hydrodynamic model (2.220, 2.221, 2.222, 2.223), the *nonlocal transport hydrodynamic closure*

$$
\mathrm{cl}_{NonlocalHydro} = \left(\frac{\partial\varepsilon_i}{\partial T_i}, \frac{\partial\varepsilon_e}{\partial T_e}, \frac{\partial\varepsilon_i}{\partial\rho}, \frac{\partial\varepsilon_e}{\partial\rho}, p_i, p_e, G_{ie}, \epsilon_R, \mathbf{q}_R, \mathbf{g}_R, \mathbf{q}_H, \mathbf{g}_H\right)\,, \tag{2.224}
$$

has to be provided, which is an extension of the two temperature single-fluid hydrodynamic closure (2.94) completed by the radiation energy density ϵ_R radiation flux $\mathbf{q}_R$ radiation-plasma momentum exchange term $\mathbf{g}_R$, electron heat flux $\mathbf{q}_H$, and transported electrons-plasma momentum exchange term $\mathbf{g}_H$.

We would like to stress that our proposed two temperature single-fluid nonlocal transport hydrodynamic model can be distinguished by several properties. Firstly, a special treatment of the specific internal energy of ions and electrons is applied, since we track separately the time evolution of its density and temperature dependent parts as

$$
\frac{\mathrm{d}\varepsilon}{\mathrm{d}t} = \frac{\partial\varepsilon}{\partial T}\frac{\mathrm{d}T}{\mathrm{d}t} + \frac{\partial\varepsilon}{\partial\rho}\frac{\mathrm{d}\rho}{\mathrm{d}t}\,, \tag{2.225}
$$

for both ions and electrons. This approach allows a better insight into the processes of entropy production during the evolution of plasmas. Secondly, not like the local diffusion treatment of the electron heat flux $\mathbf{q}_H$ [10] with a flux limiter [72] widely used in the majority of hydro codes, as in [73, 74], we directly implement a kinetic solution of the electron transport, naturally nonlocal, which defines the heat flux. Furthermore, the electron temperature T_e refers to bound electrons, while the free transported

electrons can possess a different temperature. However, these temperatures naturally equilibrate when the electron mean free path is sufficiently short and plasma achieves a local thermal equilibrium. This effect of localization can be seen in the asymptotic approximation (A.29), where $\tilde{I}_e^{(0)}$ is the dominant isotropic term representing thermal equilibrium. An overall description of the nonlocal electron transport model is presented in the next section.

In what follows, we provide a general formula of each closure term of (2.224). The equation of state related properties are defined as

$$\frac{\partial \varepsilon_i}{\partial T_i} = -T_i \left(\frac{\partial^2 f_i}{\partial T_i^2} \right)_\rho, \qquad \frac{\partial \varepsilon_i}{\partial \rho} = \left(\frac{\partial f_i}{\partial \rho} \right)_{T_i} - T_i \left(\frac{\partial}{\partial T_i} \left(\frac{\partial f_i}{\partial \rho} \right)_{T_i} \right)_\rho, \qquad (2.226)$$

$$\frac{\partial \varepsilon_e}{\partial T_e} = -T_e \left(\frac{\partial^2 f_e}{\partial T_e^2} \right)_\rho, \qquad \frac{\partial \varepsilon_e}{\partial \rho} = \left(\frac{\partial f_e}{\partial \rho} \right)_{T_e} - T_e \left(\frac{\partial}{\partial T_e} \left(\frac{\partial f_e}{\partial \rho} \right)_{T_e} \right)_\rho, \qquad (2.227)$$

$$p_i = \rho^2 \left(\frac{\partial f_i}{\partial \rho} \right)_{T_i}, \qquad p_e = \rho^2 \left(\frac{\partial f_e}{\partial \rho} \right)_{T_e}, \qquad (2.228)$$

where $f_i(\rho, T_i)$ and $f_e(\rho, T_e)$ are Helmholtz free energies for both ions and electrons. The f_i and f_e functions are provided by the equation of state libraries, QEOS [75, 76], BADGER [77], and SESAME [78, 79, 80]. The energy exchange closure is defined as $G_{ie} = \rho \frac{\partial \varepsilon_i}{\partial \rho} \nu_{ie}$, where ν_{ie} is the ion-electron collision frequency [3].

Terms related to the radiation transport are defined as

$$\epsilon_R = \frac{1}{c} \int_{4\pi} I_p \, d\omega, \qquad (2.229)$$

$$\mathbf{q}_R = \int_{4\pi} \mathbf{n} I_p \, d\omega, \qquad (2.230)$$

$$\mathbf{g}_R = \frac{\bar{k}_p + \bar{\sigma}_p}{c} \int_{4\pi} \mathbf{n} I_p \, d\omega \qquad (2.231)$$

where c is speed of light, $\bar{k}_p$ mean Planck opacity, $\bar{\sigma}_p$ scattering coefficient and I_p is the one energy group radiation intensity, which is a fundamental quantity to describe the radiation transport.

Terms related to the electron transport are defined as

$$\mathbf{q}_H = \int_{4\pi} \mathbf{n} I_e \, d\omega, \qquad (2.232)$$

$$\mathbf{g}_H = \frac{\tilde{k}_e + \tilde{\sigma}_e}{|\tilde{\mathbf{v}}|} \int_{4\pi} \mathbf{n} I_e \, d\omega \qquad (2.233)$$

where $\tilde{k}_e$ is the inverse of electron mean free path, $\tilde{\sigma}_p$ scattering coefficient, $|\tilde{\mathbf{v}}|$ the mean transport velocity, and I_e is the one energy group electron intensity, which is a fundamental quantity to describe the electron transport.

element	a	r	s
Be^4	0.2	1.284	-2.83
C^6	1.35	1.063	-2.38
O^8	22.1	1.023	-1.8
Al^{13}	34.2	1.48	-2.41
Ti^{22}	85.84	1.44	-2.08
Fe^{26}	89.97	1.38	-2.13
Cu^{29}	100.8	1.35	-2.12
Mo^{42}	315.9	1.31	-1.56
Sn^{50}	328.6	1.23	-1.59
Ba^{56}	324.0	1.24	-1.64
Au^{79}	666.0	1.16	-1.23

TABLE 2.1: The scaling law for the mean opacity as a function of density and temperature powers $\bar{k}_p[1/cm] = a\,T^s[keV]\,\rho^r[g/cm^3]$ for different materials.

2.6.1 The Nonlocal Radiation Transport Closure

In section 2.5.2 we have defined the BGK radiation transport model in Lagrangian frame (2.217), which is an appropriate model for radiation transport related to the hydrodynamics equations (2.220–2.223) and reads

$$\frac{1}{c}\frac{\mathrm{d}I_p}{\mathrm{d}t} + \mathbf{n} \cdot \nabla I_p = \bar{k}_p\left(aT_e^4 - I_p\right) + \bar{\sigma}_p\left(\bar{I}_p - I_p\right) , \qquad (2.234)$$

where $\bar{k}_p$ and $\bar{\sigma}_p$ are the mean Planck opacity and the mean scattering coefficients, respectively.

The mean opacity (2.218) and the mean scattering coefficients (2.219) can be evaluated with respect to density ρ and temperature T. The evaluation is based on collision radiative (CR) atomic codes calculations [7].

In the case of hydrodynamic model description of plasma, a quantitative scaling law for the mean opacities as a function of density and temperature powers represents an appropriate alternative to a detailed spectral description. Such a scaling law for the mean opacities of different materials can be found in Table 2.1 [81].

2.6.2 The Nonlocal Electron Transport Closure

In section 2.3.3 we defined the BGK radiation transport model in Lagrangian frame (2.145), which is an appropriate model for electron transport related to the hydrodynamics equations (2.220–2.223) and reads

$$\frac{1}{|\tilde{\mathbf{v}}|_e}\frac{\mathrm{d}I_e}{\mathrm{d}t} + \mathbf{n} \cdot \nabla I_e = \left(\frac{q_e}{k_B T_e}\mathbf{n} \cdot \mathbf{E}\right)I_e + n_i\frac{\mathrm{d}\bar{Z}}{\mathrm{d}t}\frac{3}{8\pi}k_B\,T_e$$

$$+ \tilde{k}_e\left(\left(\frac{n_e}{\pi^{\frac{3}{2}}}\frac{\sqrt{2}k_B^{\frac{3}{2}}}{\sqrt{m_e}}\right)T_e^{\frac{3}{2}} - I_e\right) + \tilde{\sigma}_e\left(\bar{I}_e - I_e\right) , \quad (2.235)$$

where $|\tilde{\mathbf{v}}|_e = 2.13 v_{T_e}$ is the uniform electron transport velocity, $\tilde{k}_e = \frac{\tilde{\nu}_e}{|\tilde{\mathbf{v}}|} = \frac{1}{\tilde{\lambda}_e} \approx \frac{1}{13.6\lambda_{T_e}}$ the inverse to the uniform electron mean free path, where λ_{T_e} is the mean free path of

electron moving with thermal velocity v_{T_e}, and $\tilde{\sigma}_e = \frac{\tilde{\nu}_{\sigma_e}}{|\tilde{\mathbf{v}}|}$ the uniform scattering coefficient of electrons. The uniform property means a unique value to be used for entire energy spectra and all these quantities are described in section 2.3.3. $\mathbf{E}$ is the electric field intensity and $\bar{I}_e$ is the angular mean value of electron intensity.

The nonlocal BGK electron transport model describes the processes of generation, transport, and collisions (thermalization and isotropization) of transported electrons. Every particular process can be related to a specific term of (2.235), i.e. transport (advection) of electrons is governed by the term

$$\frac{1}{|\tilde{\mathbf{v}}|}\frac{\mathrm{d}I_e}{\mathrm{d}t} + \mathbf{n}\cdot\nabla I_e\,, \tag{2.236}$$

the process of generation resides in the source/sink of electrons due to ionization/recombination

$$n_i\frac{\mathrm{d}\bar{Z}}{\mathrm{d}t}\frac{3}{8\pi}k_B\,T_e \tag{2.237}$$

scattering (the idostropization part of collisions) is described by a simple collision operator

$$\tilde{\sigma}_e\left(\bar{I}_e - I_e\right)\,, \tag{2.238}$$

thermalization comprises two parts: absorption, which takes a linear form

$$-\tilde{k}_e I_e\,, \tag{2.239}$$

and its inverse, the reemission of thermal electrons, given as

$$\tilde{k}_e\left(\frac{n_e}{\pi^{\frac{3}{2}}}\frac{\sqrt{2}k_B^{\frac{3}{2}}}{\sqrt{m_e}}\right)T_e^{\frac{3}{2}}\,, \tag{2.240}$$

and last but not least is the acceleration term

$$\left(\frac{q_e}{k_B T_e}\mathbf{n}\cdot\mathbf{E}\right)I_e\,. \tag{2.241}$$

In principle, term 2.241 is more effective on slower electrons due to its inverse dependence on T_e, thus it acts a source of return current electrons in the case of multi-group approach.

The relevant two-temperature equation of state library resides in the model which assumes that there are one ion population and two electron populations: a free (transported) electrons and electrons still bound to the parent nucleus. In general, the free electrons can have a different temperature than the bound electrons, nevertheless, these temperatures equilibrate due to electron-ion collisions. Such a model includes charge screening and Coulomb interactions between free electrons, bound electrons and ions. We prefer that $\frac{1}{|\tilde{\mathbf{v}}|}\frac{\mathrm{d}I_e}{\mathrm{d}t}$ is explicitly set to zero in (2.235) and the corresponding change of free electrons energy is included in the term

$$\frac{\mathrm{d}\varepsilon_e}{\mathrm{d}t} = \frac{\partial\varepsilon_e}{\partial T_e}\frac{\mathrm{d}T_e}{\mathrm{d}t} + \frac{\partial\varepsilon_e}{\partial\rho}\frac{\mathrm{d}\rho}{\mathrm{d}t}\,, \tag{2.242}$$

of (2.223), where ε_e comprises free electrons and bound electrons energy parts, i.e. $\varepsilon_e = \varepsilon_e^{free} + \varepsilon_e^{bound}$. This treatment is especially important in the case of dense plasma in order to not under-predict the electron energy and pressure [82].

The electron transport model (2.235) captures the key features of nonlocal electron transport, while obeying the diffusion asymptotic given by SH model with an acceptable error as has been stated in section 2.3.3 and as is described in more detail in Appendix A.4.

2.6.3   Maxwell Equations for Nonlocal Transport Hydrodynamics

So far we have not touched the problem of the Maxwell's equations role in the nonlocal transport hydrodynamic model. A simple approximation of a electrostatic electric field intensity has been introduced in section 2.6.2. Nevertheless, we aim to include also the magnetic field effect, which brings more physics into our laser-heated plasma model.

As in [83] we assume the charge density ρ^q to be distributed over three-dimensional domain Ω with a surface boundary Γ and an outwardly directed surface normal direction $\mathbf{n}$. The domain Ω is filled with a multi-material specified at any position $\mathbf{x}$ by the values of the electromagnetic material properties σ, ε and μ, the electrical conductivity, the electric permittivity and the magnetic permeability, respectively.

The Maxwell's equations in terms of the electric field intensity $\mathbf{E}$ and the magnetic flux density $\mathbf{B}$ consist of Maxwell-Ampere's and Maxwell-Faraday's laws

$$\varepsilon \frac{\partial \mathbf{E}}{\partial t} = \nabla \times \frac{1}{\mu}\mathbf{B} - \sigma\mathbf{E}\,, \quad \frac{\partial \mathbf{B}}{\partial t} = -\nabla \times \mathbf{E}\,,$$

and of Maxwell-Gauss's and Maxwell-Thomson's laws

$$\nabla \cdot \varepsilon\mathbf{E} = \rho^q\,, \quad \nabla \cdot \mathbf{B} = 0\,,$$

where we used Ohm's law $\mathbf{j} = \sigma\mathbf{E}$ in the Maxwell-Ampere equation.

We impose the *good conductor approximation* condition

$$\varepsilon\frac{\partial \mathbf{E}}{\partial t} \ll \sigma\mathbf{E}\,, \tag{2.243}$$

thus neglecting the effect of the displacement current. Such a simplification leads to the diffusion description

$$\frac{\partial \mathbf{B}}{\partial t} = -\nabla \times \frac{1}{\sigma}\nabla \times \frac{1}{\mu}\mathbf{B}\,, \tag{2.244}$$

of electromagnetic field, rather than the electromagnetic waves description.

The electric field intensity $\mathbf{E}$ can be expressed in its potential form

$$\mathbf{E} = -\nabla\phi - \frac{\partial \mathbf{A}}{\partial t} = \mathbf{E}^{irr} + \mathbf{E}^{ind}\,, \tag{2.245}$$

where $\mathbf{E}^{irr} = -\nabla\phi$ is the irrotational component of $\mathbf{E}$ and $\mathbf{E}^{ind} = -\frac{\partial \mathbf{A}}{\partial t}$ is the induced eddy current component of $\mathbf{E}$ due to a time varying magnetic vector potential $\mathbf{A}$.

We enforce the gauge condition

$$\nabla \cdot \varepsilon\mathbf{A} = 0\,, \tag{2.246}$$

which is equivalent to the condition

$$\nabla \cdot \varepsilon\mathbf{E}^{ind} = 0\,. \tag{2.247}$$

Based on (2.243), (2.245), and (2.247), the *Maxwell's equations for nonlocal transport hydrodynamics* in Eulerian frame take the following form

$$\nabla \cdot \varepsilon \nabla \phi \;=\; \rho^q, \tag{2.248}$$

$$\sigma \mathbf{E}^{ind} \;=\; \nabla \times \frac{1}{\mu} \mathbf{B} + \sigma \nabla \phi, \tag{2.249}$$

$$\frac{\partial \mathbf{B}}{\partial t} \;=\; -\nabla \times \mathbf{E}^{ind}. \tag{2.250}$$

The solution $\mathbf{E} = -\nabla \phi + \mathbf{E}^{ind}$ and $\mathbf{B}$ than contribute to the nonlocal electron transport model (2.235) and to the hydrodynamic momentum equation (2.221).

Even though the induced fields $\mathbf{E}^{ind}$ and $\mathbf{B}$ may be important in the laser-heated plasma, the implementation of numerical methods to solve the system (2.248–2.250) would be too computationally demanding. Also, one of the aims of the nonlocal transport hydrodynamic model (2.220–2.223, 2.235, 2.234) is to address the deviation from the quasi-neutrality of plasma due to the nonlocal transport. We propose to employ the electrostatic description

$$\nabla \cdot \varepsilon \nabla \phi \;=\; \rho^q, \tag{2.251}$$

$$\mathbf{E} \;=\; -\nabla \phi, \tag{2.252}$$

should be a sufficient approximation to model electromagnetic contribution to hydrodynamics. The quantity of charge density ρ^q is governed by equation (2.158).

Chapter 3

Numerics

In this section we derive and discuss a finite element-based numerical approximation scheme for the nonlocal BGK radiation and electron transport equations (2.234, 2.235) and energy equations of ions and electrons (2.222, 2.223) in slab, spherically symmetric and axis-symmetric geometries.

In general, we can call the model a transport coupled problem, where we need to solve a kinetic like transport problem represented by the BGK transport equation and its coupling to the energy equations, which are also solved.

In order to make clear how the nonlocal transport contributes to the laser-heated plasma model presented in section 2.6, we need to rewrite equations (2.234–2.223). In principle, the energy equations describe the evolution of the ion temperature T_i and the electron temperature T_e, where the radiation field represented by the intensity I_p and the transported electrons represented by the intensity I_e contribute significantly (if not, then the transport can be neglected). Since the radiation and electron transport are modeled in the same manner, we will consider only one specie of particles in this chapter. Thus, we can introduce the *nonlocal transport coupled problem* model

$$a_i \frac{\mathrm{d}T_i}{\mathrm{d}t} = G_{ie}(T_e - T_i) + P_i \,, \tag{3.1}$$

$$a_e \frac{\mathrm{d}T_e}{\mathrm{d}t} + \int_{4\pi} \frac{1}{c}\frac{\mathrm{d}I}{\mathrm{d}t} + \mathbf{n} \cdot \nabla I \mathrm{d}\omega = G_{ie}(T_i - T_e) + P_e \,, \tag{3.2}$$

$$\frac{1}{c}\frac{\mathrm{d}I}{\mathrm{d}t} + \mathbf{n} \cdot \nabla I = (\mathbf{n} \cdot \mathbf{S} + S_A)\, T_e + S_b - (\kappa + \mathbf{n} \cdot \mathbf{\Upsilon})\, I + \sigma \bar{I} \,, \tag{3.3}$$

where temperatures $T_i(t, \mathbf{x})$ and $T_e(t, \mathbf{x})$, and the intensity $I(t, \mathbf{n}, \mathbf{x})$ are primary variables. Ion heat capacity a_i, electron heat capacity a_e, ion-electron exchange rate G_{ie}, external source of ion energy P_i (hydrodynamic effect), external source of electron energy P_e (hydrodynamic plus laser effect), transport velocity c of given particles, extinction coefficient $\kappa = k + \sigma$, anisotropic extinction coefficient $\mathbf{\Upsilon}$, scattering coefficient σ, anisotropic source part $\mathbf{S}$ and isotropic source parts S_A and S_b are all functions of time t and position $\mathbf{x}$. The mean intensity $\bar{I}$ is defined as

$$\bar{I} = \frac{1}{4\pi} \int_{4\pi} I \, \mathrm{d}\omega \,. \tag{3.4}$$

The appropriate way to write the operation $\mathbf{n} \cdot \nabla I$ should be $\frac{\partial I}{\partial s}\big|_{\mathbf{n}}$ which is the derivative of I with respect to the path length s along the ray direction $\mathbf{n}$ defined in section 2.4.1. In this form, the definition is correct for any coordinate system. However, we will write the corresponding transport operator explicitly with respect to the coordinate system used in the following text. The integral term on the right hand side of (3.2)

then corresponds to the energy density change and energy flux divergence of the transported particles energy. These quantities are defined in (2.229, 2.230) in the case of radiation and in (2.232) in the case of electrons, where we do not consider the electrons energy change.

Our interest aims to Lagrangian numerical methods for the problem (3.1-3.3), where the equations are discretized and solved on a generally unstructured computational mesh that moves with the fluid velocity $\mathbf{u}$. The Lagrangian definition of transport equation (3.3) is a general form of radiation and electron transport equations (2.234, 2.235).

3.1 The Discontinuous Galerkin Bhatnagar–Gross–Krook Transport and Temperatures (DG-BGK&Ts) Scheme

The name discrete-ordinates or S_N is often used for short-characteristic methods used to solve the problem of transport of particles. The pioneering work done by Pomraning [84] brought this method to public at an early stage. The problems associated with inaccuracy and negative solutions vanished through the use of the discontinuous finite element method [85, 86]. The originally proposed strategy of obtaining the solution to the transport equation (3.3) resided in sweeping the intensity I along a set of discrete directions (ordinates). A further progress in acceleration of such sweeping methods was presented in [87, 88]. The modern form of the discontinuous finite element method is referred as the discontinuous Galerkin (DG) method [89, 90, 91], which offers a high-order discretization and computational efficiency capabilities [92, 93, 94].

Our aim is to define a high-order finite element scheme, which provides a full discretization of the problem (3.1–3.3) , i.e. a discretization, which treats time, direction, and spatial dimensions. We define a multidimensional domain

$$\Omega_{t,\mathbf{n},\mathbf{x}} = \Delta t \times \Omega_{\mathbf{n}} \times \Omega_{\mathbf{x}} \,, \tag{3.5}$$

where Δt is the time domain (a reasonably short time interval), the angular domain $\Omega_{\mathbf{n}} = (\Delta\theta \times \Delta\phi)$ spans over the all directions in spherical coordinates (see Fig. 2.1) represented by $\Delta\theta = (0, 2\pi)$ and $\Delta\phi = (0, \pi)$, and $\Omega_{\mathbf{x}}$ refers to a general continuous spatial domain. A simpler domain which does not include angular dimensions is defined as

$$\Omega_{t,\mathbf{x}} = \Delta t \times \Omega_{\mathbf{x}} \,. \tag{3.6}$$

In principle, we can observe that the transport equation's (3.3) main contribution to the electron temperature equation (3.2) is the divergence of vector flux of energy (we assume that the energy exchange term is minor). Mathematical models describing the evolution of scalar quantity based on the divergence of a vector flux quantity have been widely used in continuum mechanics. Actually, a new numerical approach called mixed finite element method [95, 96] was born to provide an accurate and stable solution of the latter model.

We propose a similar strategy to solve the model of nonlocal transport coupled problem (3.1–3.3) based on the Galerkin variational principle of a mixed problem

$$\int_{\Omega_{t,\mathbf{n},\mathbf{x}}} \Psi \left[\frac{1}{c} \frac{\mathrm{d}I}{\mathrm{d}t} + \mathbf{n} \cdot \nabla I + (\kappa + \mathbf{n} \cdot \mathbf{\Upsilon}) I - \sigma \bar{I} - ((\mathbf{n} \cdot \mathbf{S} + S_A) T_e + S_b) \right] \mathrm{d}\Omega_{t,\mathbf{n},\mathbf{x}} = 0,$$

$$\forall \Psi \in L_I^2, \qquad (3.7)$$

$$\int_{\Omega_{t,\mathbf{x}}} \Xi \left[a_e \frac{\mathrm{d}T_e}{\mathrm{d}t} + \int_{4\pi} \frac{1}{\tilde{v}} \frac{\mathrm{d}I}{\mathrm{d}t} + \mathbf{n} \cdot \nabla I \mathrm{d}\omega - G_{ie}(T_i - T_e) - P_e \right] \mathrm{d}\Omega_{t,\mathbf{x}} = 0,$$

$$\forall \Xi \in L_{T_e}^2, \qquad (3.8)$$

$$\int_{\Omega_{t,\mathbf{x}}} \tilde{\Xi} \left[a_i \frac{\mathrm{d}T_i}{\mathrm{d}t} - G_{ie}(T_e - T_i) - P_i \right] \mathrm{d}\Omega_{t,\mathbf{x}} = 0,$$

$$\forall \tilde{\Xi} \in L_{T_i}^2, \qquad (3.9)$$

where the test functions Ψ belongs to the functional space L_I^2, which lies on the computational domain $\Omega_{t,\mathbf{n},\mathbf{x}}$ defined in (3.5), the test functions Ξ belongs to the functional space $L_{T_e}^2$, which lies on the computational domain $\Omega_{t,\mathbf{x}}$ defined in (3.6), and the test functions $\tilde{\Psi}$ belongs to the functional space $L_{T_i}^2$, which lies on the computational domain $\Omega_{t,\mathbf{x}}$ defined in (3.6). The mixed problem resides in that the test functions $\Xi, \tilde{\Xi}$ possess a different polynomial order and that Ψ not only possesses a different polynomial order but also refers to a vector quantity due to its span over the directions.

At this point we should stress that the above variational principle applies to the entire computational domain $\Omega_{t,\mathbf{x}}$, which is spatially discretized by an, in general unstructured, mesh and a subsequent time-level discretization in the time domain. What follows is a one element discretization, which is finally applied in the DG-BGK&Ts solver in order to obtain a computationally efficient solution of the problem (3.7–3.9).

The Discontinuous Galerkin BGK Transport Scheme

In order to find the unknown I which solves (3.3), we use the strong form discontinuous Galerkin (DG) variational principle on a functional space L_I^e, which lies on the computational domain $\Omega_{t,\mathbf{n},\mathbf{x}}^e$ defined on one element of the computational mesh. The spatial part of the latter domain possesses a Lipschitz continuous boundary Γ with a normal vector $\mathbf{n}_\Gamma$.

The discontinuous Galerkin variational form reads

$$\int_{\Omega_{t,\mathbf{n},\mathbf{x}}^e} \Psi \left[\frac{1}{c} \frac{\mathrm{d}I}{\mathrm{d}t} + \mathbf{n} \cdot \nabla I + (\kappa + \mathbf{n} \cdot \mathbf{\Upsilon}) I - \sigma \bar{I} - ((\mathbf{n} \cdot \mathbf{S} + S_A) T_e + S_b) \right] \mathrm{d}\Omega_{\mathbf{x}}^e \mathrm{d}\Omega_{\mathbf{n}} \mathrm{d}\Omega_t$$

$$= \int_{\Omega_t} \int_{\Omega_{\mathbf{n}}} \int_{\Gamma} \Psi \left[(\mathbf{F} - \mathbf{F}^*) \cdot \mathbf{n}_\Gamma \right] \mathrm{d}\Gamma \mathrm{d}\Omega_{\mathbf{n}} \mathrm{d}\Omega_t, \forall \Psi \in L_I^e, \quad (3.10)$$

where, in accordance with the strong discontinuous Galerkin principle, we applied the divergence theorem firstly to the term $\Psi \mathbf{n} \cdot \nabla I$, when the numerical flux appeared, and secondly to the term $-I\mathbf{n} \cdot \nabla \Psi$, which results in the fluxes difference $(\mathbf{F} - \mathbf{F}^*)$ on the right hand side of (3.10).

In our particular case, we use the natural flux of the form

$$\mathbf{F} = \mathbf{n}I, \qquad (3.11)$$

and we choose the upwind numerical flux

$$\mathbf{F}^* = \begin{cases} \mathbf{n}(\theta,\phi)I\,, & \mathbf{n}(\theta,\phi) \cdot \mathbf{n}_\Gamma(\mathbf{x}) \geq 0 \\ \mathbf{n}(\theta,\phi)\tilde{I}\,, & \mathbf{n}(\theta,\phi) \cdot \mathbf{n}_\Gamma(\mathbf{x}) < 0 \end{cases}, \tag{3.12}$$

where $\mathbf{n}_\Gamma$ is the outward normal to Γ. The meaning of the numerical flux definition (3.12) is that the outgoing flux is represented by the cell internal quantity I and the incoming flux is given by an external quantity $\tilde{I}$, which is provided by the adjacent cells.

A direct consequence of definitions (3.11) and (3.12) leads to the explicit form of the right hand side of (3.10) to be

$$RHS = \int_{\Omega_t} \int_{\Omega_\mathbf{n}} \int_{\Gamma_{\mathbf{n}\cdot\mathbf{n}_\Gamma<0}} \Psi\left[(I - \tilde{I})\mathbf{n}(\theta,\phi)\cdot\mathbf{n}_\Gamma(\mathbf{x})\right]\,\mathrm{d}\Gamma\mathrm{d}\Omega_\mathbf{n}\mathrm{d}\Omega_t\,, \forall\Psi\in L_I^e\,, \tag{3.13}$$

where $\Gamma_{\mathbf{n}\cdot\mathbf{n}_\Gamma<0}$ means the part of boundary Γ where the projection of the transport direction $\mathbf{n}$ into the surface normal $\mathbf{n}_\Gamma$ is less than zero, i.e. $\mathbf{n}\cdot\mathbf{n}_\Gamma < 0$.

The Systematic Discretization of I, T_e, and T_i

The finite element form of time, angular, and space (Lagrangian) discretization is based on the discontinuous Galerkin high-order finite element method. The high-order finite element method naturally resides on construction of robust discrete bases and consequent matrices. Moreover, we aim to discretize the problem defined in multiple dimensions which are, by definition, of different nature, i.e. time vs. angular discretization vs. spatial discretization in the case of the unknown I. In order to keep the discretization process clear, we adopt a systematic construction of the scheme while treating the different dimensions as separated as possible.

One of the properties of every finite element is its domain of definition. We define a multidimensional element domain

$$\Omega_{t,\mathbf{n},\mathbf{x}}^e = \Delta t \times \Omega_\mathbf{n} \times \Omega_\mathbf{x}^e\,, \tag{3.14}$$

where Δt and $\Omega_\mathbf{n}$ are the same as in (3.5), and a simpler domain

$$\Omega_{t,\mathbf{x}}^e = \Delta t \times \Omega_\mathbf{x}^e\,, \tag{3.15}$$

where $\Omega_\mathbf{x}^e$ is a finite spatial domain represented by one cell of the computational Lagrangian mesh. One can observe, that $\Omega_\mathbf{x}^e$ is a local domain of each of the mesh cells, while Δt and $\Omega_\mathbf{n}$ are global domains.

In order to define the discretization of unknowns I, T_e, and T_i, we start with the lowest order discretization represented by the constant basis (a column vector)

$$\omega^0 = [1]^T\,, \tag{3.16}$$

which possesses only one degree of freedom. This basis is not used to discretize any of the unknowns, nevertheless, assists in many steps of the scheme construction.

The set of bases written as the column vectors

$$\omega_t = [\omega_0(t),..,\omega_{N_t}(t)]^T\,, \quad \omega_\theta = [\omega_1(\theta),..,\omega_{N_\theta}(\theta)]^T\,, \quad \omega_\phi = [\omega_1(\phi),..,\omega_{N_\phi}(\phi)]^T\,. \tag{3.17}$$

represents discretization of the time dimension t, the angle dimension θ, and the angle dimension ϕ, where θ and ϕ are angular components of spherical coordinates. The

numbers N_t, N_θ, and N_ϕ determine the number of degrees of freedom corresponding to dimensions t, θ, ϕ. The main feature of the bases of (3.17) is that they depend only on one variable, i.e. these are 1D bases.

In the case of spatial discretization, we use a set of three different bases, i.e. for intensity I, electron temperature T_e and ion temperature T_i. These bases are represented by the column vectors

$$\psi = [\psi_1(\mathbf{x}), .., \psi_{N_I}(\mathbf{x})]^T, \quad \xi = [\xi_1(\mathbf{x}), .., \xi_{N_{T_e}}(\mathbf{x})]^T, \quad \tilde{\xi} = [\tilde{\xi}_1(\mathbf{x}), .., \tilde{\xi}_{N_{T_i}}(\mathbf{x})]^T. \quad (3.18)$$

where $\mathbf{x} \in \Omega_{\mathbf{x}}^e$ and N_I, N_{T_e}, and N_{T_i} are the numbers of degrees of freedom corresponding to spatial discretization of each of the quantities I, T_e, and T_i. In the contrary to (3.17), the bases of (3.18) depend on up to three variables, in general, noted x_1, x_2, x_3.

The discretization of the unknowns I, T_e, and T_i of the system (3.7, 3.8, 3.9) are then constructed in the manner to work on the domain $\Omega_{t,\mathbf{n},\mathbf{x}}$ (3.5) in the case of I and on the domain $\Omega_{t,\mathbf{x}}$ (3.6) in the case of T_e and T_i, and are defined as

$$I(t, \mathbf{n}(\theta, \phi), \mathbf{x}) = \mathbf{\Psi}^T(t, \mathbf{n}(\theta, \phi), \mathbf{x}) \cdot \mathbf{I}, \quad T_e(t, \mathbf{x}) = \mathbf{\Xi}^T(t, \mathbf{x}) \cdot \mathbf{T}_e, \quad T_i(t, \mathbf{x}) = \tilde{\mathbf{\Xi}}^T(t, \mathbf{x}) \cdot \mathbf{T}_i, \quad (3.19)$$

which defines the discrete representations $\mathbf{I}$, $\mathbf{T}_e$, and $\mathbf{T}_i$, and where the interpolation bases are constructed as

$$\mathbf{\Psi} = \omega_t \otimes \omega_\theta \otimes \omega_\phi \otimes \psi, \quad \mathbf{\Xi} = \omega_t \otimes \xi, \quad \tilde{\mathbf{\Xi}} = \omega_t \otimes \tilde{\xi}, \quad (3.20)$$

i.e. using the elementary basis of (3.17, 3.18) and $\otimes$ is the tensor product. Based on the finite bases (3.20), we can define the discrete forms of the functional spaces used in (3.7–3.9) , i.e. $L_I^e(\mathbf{\Psi})$ which comprises the solutions $\mathbf{I}$, $L_{T_e}^e(\mathbf{\Xi})$ which comprises the solutions $\mathbf{T}_e$, and $L_{T_i}^e(\tilde{\mathbf{\Xi}})$ which comprises the solutions $\mathbf{T}_i$.

The definition (3.20) determines the number of degree of freedom of each of the unknowns, i.e. the discrete representation $\mathbf{I}$ possesses $\tilde{N}_I = (N_t + 1) \cdot N_\theta \cdot N_\phi \cdot N_I$ degrees of freedom, the discrete representation $\mathbf{T}_e$ possesses $\tilde{N}_{T_e} = (N_t + 1) \cdot N_{T_e}$ degrees of freedom, and the discrete representation $\mathbf{T}_i$ possesses $\tilde{N}_{T_i} = (N_t + 1) \cdot N_{T_i}$ degrees of freedom.

It is worth noting, that the basis ω_t in (3.17) is indexed from zero, referring to the zero time level (the initial condition). Consequently, the discrete unknown $\mathbf{I}$ consists of the first $N_\theta \cdot N_\phi \cdot N_I$ components referring to the initial time of Δt and of the "real" unknown $N_t \cdot N_\theta \cdot N_\phi \cdot N_I$ components. We define them as

$$\mathbf{I}^0 = [I_1, .., I_{N_\theta \cdot N_\phi \cdot N_I}]^T, \quad (3.21)$$

$$\mathbf{I}^1 = [I_{N_\theta \cdot N_\phi \cdot N_I + 1}, .., I_{(N_t+1) \cdot N_\theta \cdot N_\phi \cdot N_I}]^T. \quad (3.22)$$

Since we use the same time discretization for the discrete unknowns $\mathbf{T}_e$ and $\mathbf{T}_i$, we also define the initial condition part and the "real" unknown part as

$$\mathbf{T}_e^0 = [T_{e_1}, .., T_{e_{N_{T_e}}}]^T, \quad (3.23)$$

$$\mathbf{T}_e^1 = [T_{e_{(N_{T_e}+1)}}, .., T_{e_{(N_t+1) \cdot N_{T_e}}}]^T, \quad (3.24)$$

of the discrete unknown $\mathbf{T}_e$ and the same parts of the discrete unknown $\mathbf{T}_i$ are

$$\mathbf{T}_i^0 = [T_{i_1}, .., T_{i_{N_{T_i}}}]^T, \quad (3.25)$$

$$\mathbf{T}_i^1 = [T_{i_{(N_{T_i}+1)}}, .., T_{i_{(N_t+1) \cdot N_{T_i}}}]^T. \quad (3.26)$$

The definitions (3.21–3.26) allow us to write the explicit form of the discrete representations of our problem as

$$\mathbf{I} = [\mathbf{I}^{0T}, \mathbf{I}^{1T}]^{T}, \quad \mathbf{T}_{e} = [\mathbf{T}_{e}^{0T}, \mathbf{T}_{e}^{1T}]^{T}, \quad \mathbf{T}_{i} = [\mathbf{T}_{i}^{0T}, \mathbf{T}_{i}^{1T}]^{T}. \tag{3.27}$$

As can be seen in (3.20), the process of construction of our discrete scheme might be very challenging, since the number of dimensions goes up to six in case of the discrete unknown $\mathbf{I}$, i.e. $t + \theta + \phi + x_1 + x_2 + x_3$. In order to employ a systematic concept of discretization of a multi-dimensional problem, we remind some tensor product $\otimes$ operations which apply to any two basis of (3.17–3.18).

The first example is the tensor product operation on the basis of the time discretization ω_t and on the basis of the spatial discretization (of $\mathbf{T}_e$) ξ, which performs as

$$\omega_t \otimes \xi = [\omega_1(t)\,\xi_1(\mathbf{x}), .., \omega_1(t)\,\xi_{N_{T_e}}(\mathbf{x}), .., \omega_{N_t}(t)\,\xi_1(\mathbf{x}), .., \omega_{N_t}(t)\,\xi_{N_{T_e}}(\mathbf{x})]^{T}, \tag{3.28}$$

an results in a $N_t \cdot N_{T_e}$ column vector.

The second example is the tensor product operation on the transpose to the basis of the time discretization ω_t^T and on the transpose to the basis of the spatial discretization (of $\mathbf{T}_e$) ξ^T, which performs as

$$\omega_t^T \otimes \xi^T = [\omega_1(t)\,\xi_1(\mathbf{x}), .., \omega_1(t)\,\xi_{N_{T_e}}(\mathbf{x}), .., \omega_{N_t}(t)\,\xi_1(\mathbf{x}), .., \omega_{N_t}(t)\,\xi_{N_{T_e}}(\mathbf{x})], \tag{3.29}$$

and results in a $N_t \cdot N_{T_e}$ row vector.

The third example is the tensor product operation on the time basis and its transpose ω_t and ω_t^T giving The third example is the tensor product operation on the basis of the time discretization ω_t and on the transpose to the basis of the time discretization ω_t^T, which performs as

$$\omega_t \otimes \omega_t^T = \begin{bmatrix} \omega_1(t)\,\omega_1(t) & .. & \omega_1(t)\,\omega_{N_t}(t) \\ : & & : \\ \omega_{N_t}(t)\,\omega_1(t) & .. & \omega_{N_t}(t)\,\omega_{N_t}(t) \end{bmatrix}, \tag{3.30}$$

and the result is a $N_t \times N_t$ matrix.

The use of the operations (3.28–3.30) prove to be extremely useful in the construction of our DG-BGK&Ts scheme. In particular, the product of $\mathbf{\Psi}$ and $\mathbf{\Psi}^T$ bases gives a $\tilde{N}_I \times \tilde{N}_I$ matrix

$$\mathbf{\Psi} \otimes \mathbf{\Psi}^T = \left(\omega_t \otimes \omega_t^T\right) \otimes \left(\omega_\theta \otimes \omega_\theta^T\right) \otimes \left(\omega_\phi \otimes \omega_\phi^T\right) \otimes \left(\psi \otimes \psi^T\right), \tag{3.31}$$

which can be written as a product of matrices corresponding to separate dimensions.

A similar result holds for the product of $\mathbf{\Psi}$ and $\mathbf{\Xi}^T$ bases, which gives

$$\mathbf{\Psi} \otimes \mathbf{\Xi}^T = \left(\omega_t \otimes \omega_t^T\right) \otimes \left(\omega_\theta \otimes \omega_\phi\right) \otimes \left(\psi \otimes \xi^T\right), \tag{3.32}$$

a $\tilde{N}_I \times \tilde{N}_{T_e}$ matrix, and the product of $\mathbf{\Xi}$ and $\mathbf{\Psi}^T$ bases, which gives

$$\mathbf{\Xi} \otimes \mathbf{\Psi}^T = \left(\omega_t \otimes \omega_t^T\right) \otimes \left(\omega_\theta^T \otimes \omega_\phi^T\right) \otimes \left(\xi \otimes \psi^T\right) = \left(\mathbf{\Psi} \otimes \mathbf{\Xi}^T\right)^{T}, \tag{3.33}$$

a $\tilde{N}_{T_e} \times \tilde{N}_I$ matrix and it is the transpose to (3.32). The product of $\mathbf{\Xi}$ and $\mathbf{\Xi}^T$ bases gives

$$\mathbf{\Xi} \otimes \mathbf{\Xi}^T = \left(\omega_t \otimes \omega_t^T\right) \otimes \left(\xi \otimes \xi^T\right), \tag{3.34}$$

a $\tilde{N}_{T_e} \times \tilde{N}_{T_e}$ matrix. The product of $\tilde{\Xi}$ and $\tilde{\Xi}^T$ bases gives

$$\tilde{\Xi} \otimes \tilde{\Xi}^T = \left(\omega_t \otimes \omega_t^T\right) \otimes \left(\tilde{\xi} \otimes \tilde{\xi}^T\right) , \tag{3.35}$$

a $\tilde{N}_{T_i} \times \tilde{N}_{T_i}$ matrix. Finally, the product of Ξ and $\tilde{\Xi}^T$ bases gives

$$\Xi \otimes \tilde{\Xi}^T = \left(\omega_t \otimes \omega_t^T\right) \otimes \left(\xi \otimes \tilde{\xi}^T\right) , \tag{3.36}$$

a $\tilde{N}_{T_e} \times \tilde{N}_{T_i}$ matrix, which is the transpose to the product of $\tilde{\Xi}$ and Ξ^T bases, i.e.

$$\tilde{\Xi} \otimes \Xi^T = \left(\omega_t \otimes \omega_t^T\right) \otimes \left(\tilde{\xi} \otimes \xi^T\right) . \tag{3.37}$$

The advantage of the property of separation of problem dimensions represented in (3.31–3.37) resides not only in its simple formulation on the paper, however, more importantly, it allows us to discretize the problem treating the dimensions t, θ, ϕ, and $\mathbf{x}$ in a separate way.

In general, we aim to discretize the slab, the spherically symmetric, and the axisymmetric geometries. All of the discretizations of the unknowns I, T_e, and T_i (3.19, 3.20) use the same discretization basis ω_t for the time dimension t. Even more, it can be seen that the discretization of the angular dimensions θ and ϕ is also independent of the spatial dimensions $\mathbf{x}$. Being so, we define the very complete part of the finite element discretization process related to time and angular dimensions first, and then we show how to treat each of spatial geometries in a separate section.

The Discretization of t, θ, and ϕ Dimensions

In this section we show finite element matrices related to time t, angle θ , and angle ϕ dimensions. Even though it is a little beforehand, since we have not defined the discrete forms of the variational problem (3.7–3.9), the following set of matrices will prove to be useful in later sections.

The finite element matrix is constructed by using a test function space basis and a trial basis. In general, every such matrix will be denoted as

$$\mathbf{B}_{\mathbf{x},x_i}^{f,g} , \tag{3.38}$$

where $\mathbf{B}$ is the matrix name, f is the discretized unknown and refers to the test basis, g is a contributing unknown and refers to the trial basis, and $\mathbf{x}$ represent coordinate system the test and trial bases are defined on (x_i points to a specific variable of $\mathbf{x}$). In general, the most important label is the coordinate system and other labels are very often omitted.

The set of needed matrices related to the time dimension is

$$\mathbf{D}_t = \int_{\Delta t} \omega_t \otimes \frac{\mathrm{d}\omega_t^T}{\mathrm{d}t}\, \mathrm{d}t , \tag{3.39}$$

$$\mathbf{M}_t = \int_{\Delta t} \omega_t \otimes \omega_t^T\, \mathrm{d}t , \tag{3.40}$$

$$\mathbf{M}_t^0 = \int_{\Delta t} \omega_t \otimes \omega^{0T}\, \mathrm{d}t , \tag{3.41}$$

where $\mathbf{D}_t$ refers to the distributional derivative with respect to time t, $\mathbf{M}_t$ is the so-called time mass matrix, and $\mathbf{M}_t^0$ is the contracted time mass matrix.

The lowest order time discretization is called backward Euler method, which comprises the zero time level and the final time level unknowns. Its particular form of the time matrices (3.39, 3.40, 3.41) read

$$\tilde{\mathbf{D}}_t = \begin{bmatrix} -\frac{1}{\Delta t} & 0 \\ 0 & \frac{1}{\Delta t} \end{bmatrix}, \quad \tilde{\mathbf{M}}_t = \begin{bmatrix} 0 & 0 \\ 0 & 1 \end{bmatrix}, \quad \tilde{\mathbf{M}}_t^0 = \begin{bmatrix} 0 \\ 1 \end{bmatrix}. \tag{3.42}$$

The backward Euler method will be the cornerstone of our scheme in laser-heated plasmas simulation due to its stability.

As the time bases, the bases related to dimensions θ and ϕ of (3.17) are used to discretize the unknown $\mathbf{I}$ independently of the spatial discretization. We define a necessary set of matrices to be used in the DG-BGK&Ts construction.

The set of matrices related to θ dimension reads

$$\mathbf{M}_\theta = \int_0^\pi \omega_\theta \otimes \omega_\theta^T \, \mathrm{d}\theta, \tag{3.43}$$

$$\mathbf{M}_{\cos(\theta)} = \int_0^\pi \omega_\theta \otimes \omega_\theta^T \cos(\theta) \, \mathrm{d}\theta, \tag{3.44}$$

$$\mathbf{D}_{\sin(\theta)} = \int_0^\pi \omega_\theta \otimes \frac{\mathrm{d}\omega_\theta^T}{\mathrm{d}\theta} \sin(\theta) \, \mathrm{d}\theta, \tag{3.45}$$

where $\mathbf{M}_\theta$ is the θ mass matrix, $\mathbf{M}_{\cos(\theta)}$ is the cosine θ projection matrix, and $\mathbf{D}_{\sin(\theta)}$ refers to the distributional derivative with respect to θ projected by sine function. The contracted versions of the latter matrices follow

$$\mathbf{M}_\theta^{0T} = \int_0^\pi \omega^0 \otimes \omega_\theta^T \, \mathrm{d}\theta, \tag{3.46}$$

$$\mathbf{M}_{\cos(\theta)}^{0T} = \int_0^\pi \omega^0 \otimes \omega_\theta^T \cos(\theta) \, \mathrm{d}\theta, \tag{3.47}$$

$$\mathbf{D}_{\sin(\theta)}^{0T} = \int_0^\pi \omega^0 \otimes \frac{\mathrm{d}\omega_\theta^T}{\mathrm{d}\theta} \sin(\theta) \, \mathrm{d}\theta. \tag{3.48}$$

The set of matrices related to ϕ dimension reads

$$\mathbf{M}_\phi = \int_0^\pi \omega_\phi \otimes \omega_\phi^T \sin(\phi) \, \mathrm{d}\phi, \tag{3.49}$$

$$\mathbf{M}_{\cos(\phi)} = \int_0^\pi \omega_\phi \otimes \omega_\phi^T \cos(\phi) \sin(\phi) \, \mathrm{d}\phi, \tag{3.50}$$

$$\mathbf{D}_{\sin(\phi)} = \int_0^\pi \omega_\phi \otimes \frac{\mathrm{d}\omega_\phi^T}{\mathrm{d}\phi} \sin(\phi) \, \mathrm{d}\phi, \tag{3.51}$$

$$\mathbf{M}_{\sin(\phi)} = \int_0^\pi \omega_\phi \otimes \omega_\phi^T \sin(\phi) \sin(\phi) \, \mathrm{d}\phi, \tag{3.52}$$

where $\mathbf{M}_\phi$ is the ϕ mass matrix, $\mathbf{M}_{\cos(\phi)}$ is the cosine ϕ projection matrix, $\mathbf{M}_{\sin(\phi)}$ is the sine ϕ projection matrix, and $\mathbf{D}_{\sin(\phi)}$ refers to the distributional derivative with respect to ϕ projected by sine function. The contracted versions of the latter matrices

follow

$$\mathbf{M}_\phi^{0T} = \int_0^\pi \omega^0 \otimes \omega_\phi^T \sin(\phi)\,\mathrm{d}\phi\,, \tag{3.53}$$

$$\mathbf{M}_{\cos(\phi)}^{0T} = \int_0^\pi \omega^0 \otimes \omega_\phi^T \cos(\phi)\sin(\phi)\,\mathrm{d}\phi\,, \tag{3.54}$$

$$\mathbf{D}_{\sin(\phi)}^{0T} = \int_0^\pi \omega^0 \otimes \frac{\mathrm{d}\omega_\phi^T}{\mathrm{d}\phi}\sin(\phi)\,\mathrm{d}\phi\,, \tag{3.55}$$

$$\mathbf{M}_{\sin(\phi)}^{0T} = \int_0^\pi \omega^0 \otimes \omega_\phi^T \sin(\phi)\sin(\phi)\,\mathrm{d}\phi\,, \tag{3.56}$$

In (3.43–3.48) we integrate over $\theta \in (0,\pi)$ instead of the entire azimuthal range $(0, 2\pi)$, since we expect a symmetry of I such that

$$I(t, \theta, \phi, \mathbf{x}) = I(t, 2\pi - \theta, \phi, \mathbf{x})\,, \tag{3.57}$$

which is the case of the slab, the spherically symmetric, and the axis symmetric geometries. Let the discrete form of the mean intensity (3.4) owing the symmetry (3.57) be a relevant example

$$\bar{I} = \frac{1}{4\pi} \int_0^{2\pi} \int_0^\pi I(\theta, \phi) \sin(\phi)\mathrm{d}\phi\mathrm{d}\theta =$$

$$\frac{1}{4\pi} \left(\int_0^\pi \int_0^\pi I(\theta, \phi) \sin(\phi)\mathrm{d}\phi\mathrm{d}\theta - \int_\pi^0 \int_0^\pi I(2\pi - \theta, \phi) \sin(\phi)\mathrm{d}\phi\mathrm{d}\theta \right) =$$

$$\frac{2}{4\pi} \int_0^\pi \int_0^\pi \omega_t^T \otimes \omega_\theta^T \otimes \omega_\phi^T \otimes \psi^T \sin(\phi)\mathrm{d}\phi\mathrm{d}\theta \cdot \mathbf{I} = \left[\omega_t^T \otimes \frac{1}{2\pi} \mathbf{M}_\theta^{0T} \otimes \mathbf{M}_\phi^{0T} \otimes \psi^T \right] \cdot \mathbf{I}\,, \tag{3.58}$$

where we used (3.19). The right most term of (3.58) will serve as a basis to the construction of an energy conservative form of the discrete scattering operator.

3.1.1 The 1D Slab DG-BGK&Ts Scheme

The slab geometry provides a simple function dependence on one coordinate. We choose to work in the z axis of the Cartesian coordinate system in space and in spherical coordinate system of transport directions, where the reference axis is given by the latter z axis (see Fig. 2.1).

In what follows, we show the strategy of one element partial discretization of the equations of transport (3.7), electron temperature (3.8), and ion temperature (3.9) in subsequent sections. Either I, T_e, and T_i unknown functions are piecewise continuous in space and continuous in time polynomials. The unknown I is continuous in directions.

The last section explains the method of solution on the entire computational domain which is the critical point of computational efficiency.

The 1D Slab Geometry DG-BGK Transport Scheme

In the Cartesian coordinates the position vector is defined as $\mathbf{x} = (x, y, z)$, where the coordinate axis vectors are constant (non-curvilinear). The slab geometry implies a reduced dependence of the specific intensity $I(t, \mathbf{n}(\phi), \mathbf{x}(z))$, and the resulting form of

the *slab transfer equation* reads

$$\frac{1}{c}\frac{\mathrm{d}I}{\mathrm{d}t} + \cos(\phi)\frac{\partial I}{\partial z} = (\cos(\phi)S_z + S_A)\,T_e + S_b - (\kappa + \cos(\phi)\Upsilon_z)\,I + \sigma\bar{I}\,, \qquad (3.59)$$

which represents a 3D problem, i.e. the solution I of (3.59) depends on t, ϕ and z. All the coefficients

$$c, \kappa, \Upsilon_z, \sigma, S_z, S_A, S_b\,, \qquad (3.60)$$

depend, in general, on time t and position z.

The discrete form of the discontinuous Galerkin variation principle (3.10, 3.13) in the case of the 1D slab geometry uses the discretization of I and T_e (3.19) where the bases $\boldsymbol{\Psi}$ and $\boldsymbol{\Xi}$ of (3.20) are defined on the spatial domain using the coordinate system $\mathbf{x} = \mathbf{x}(z)$, in particular, the bases ψ and ξ of (3.18) depend on z.

The *discrete 1D slab geometry variational form* of the discontinuous Galerkin BGK transport equation (3.59) reads

$$\int_{\Delta t}\int_0^{2\pi}\int_0^\pi\int_{\Delta z}\boldsymbol{\Psi}\otimes\left[\left(\frac{1}{c}\frac{\mathrm{d}\boldsymbol{\Psi}^T}{\mathrm{d}t} + \cos(\phi)\frac{\partial\boldsymbol{\Psi}^T}{\partial z} + (\kappa + \cos(\phi)\Upsilon_z)\boldsymbol{\Psi}^T\right.\right.$$

$$\left.\left. - \frac{\sigma}{4\pi}\int\boldsymbol{\Psi}^T\sin(\phi)\mathrm{d}\phi\mathrm{d}\theta\right)\cdot\mathbf{I} - \left((\cos(\phi)S_z + S_A)\,\boldsymbol{\Xi}^T\cdot\mathbf{T}_e + S_b\right)\right]\mathrm{d}z\sin(\phi)\mathrm{d}\phi\mathrm{d}\theta\mathrm{d}t =$$

$$\int_{\Delta t}\int_0^{2\pi}\int_0^\pi\int_{\Gamma_{\mathbf{n}\cdot\mathbf{n}_\Gamma<0}}\boldsymbol{\Psi}\otimes\left[\left(\boldsymbol{\Psi}^T\cdot\mathbf{I} - \tilde{\boldsymbol{\Psi}}^T\cdot\tilde{\mathbf{I}}\right)\cos(\phi)n_{\Gamma_z}\right]\mathrm{d}\Gamma_z\sin(\phi)\mathrm{d}\phi\mathrm{d}\theta\mathrm{d}t\,, \quad (3.61)$$

where Δz is the spatial domain of the element and where $\Gamma_{\mathbf{n}\cdot\mathbf{n}_\Gamma<0}$ means the part of boundary Γ where the projection of the transport direction $\mathbf{n}$ into the surface normal $\mathbf{n}_\Gamma$ is less than zero, i.e. $\mathbf{n}\cdot\mathbf{n}_\Gamma = \cos(\phi)n_{\Gamma_z} < 0$.

If one uses the property (3.31), the right hand side of (3.61) can be written as

$$\mathbf{M}_t\otimes\mathbf{M}_\theta\otimes\boldsymbol{\Gamma}_z^-\cdot\mathbf{I} - \mathbf{M}_t\otimes\mathbf{M}_\theta\otimes\left(\tilde{\boldsymbol{\Gamma}}_z^-\cdot\tilde{\mathbf{I}}\right)$$

where we used the t and θ matrices (3.40, 3.43) and the remaining matrices are defined, i.e. the internal DG matrix $\boldsymbol{\Gamma}_z^-$ as

$$\boldsymbol{\Gamma}_z^- = \int_0^\pi\int_{\Gamma_{\mathbf{n}\cdot\mathbf{n}_\Gamma<0}}\left(\omega_\phi\otimes\omega_\phi^T\right)\otimes\left(\psi\otimes\psi^T\right)(\cos(\phi)n_{\Gamma_z})\sin(\phi)\,\mathrm{d}\Gamma\mathrm{d}\phi\,, \qquad (3.62)$$

and the external DG matrix $\tilde{\boldsymbol{\Gamma}}_z^-$ trough the term

$$\mathbf{M}_t\otimes\mathbf{M}_\theta\otimes\left(\tilde{\boldsymbol{\Gamma}}_z^-\cdot\tilde{\mathbf{I}}\right)_\Gamma = \mathbf{M}_t\otimes\mathbf{M}_\theta\otimes$$

$$\sum_{adj}\left[\int_0^\pi\int_{\Gamma_{\mathbf{n}\cdot\mathbf{n}_\Gamma<0}^{adj}}\left(\omega_\phi\otimes\omega_\phi^T\right)\otimes\left(\psi\otimes\tilde{\psi}_{adj}^T\right)\left(\cos(\phi)n_{\Gamma_z^{adj}}\right)\sin(\phi)\,\mathrm{d}\Gamma^{adj}\mathrm{d}\phi\right]\cdot\tilde{\mathbf{I}}^{adj}\,, \quad (3.63)$$

where adj refers to all adjacent cells, i.e. Γ^{adj} corresponds to the part of the boundary Γ shared with an adjacent cell, where the discretization is $\tilde{I} = \left(\omega_t\otimes\omega_\theta\otimes\omega_\phi\otimes\tilde{\psi}_{adj}\right)^T\cdot\tilde{\mathbf{I}}$.

In the same way as we constructed (3.63), we can apply the products $\boldsymbol{\Psi}\otimes\boldsymbol{\Psi}^T$ of (3.31) and $\boldsymbol{\Psi}\otimes\boldsymbol{\Xi}^T$ of (3.32) wherever they appear in (3.61), which leads to the *1D slab*

geometry DG-BGK scheme formulation

$$
\begin{aligned}
\Bigg[\frac{1}{c}\mathbf{D}_t \otimes \mathbf{M}_\theta \otimes \mathbf{M}_\phi \otimes \mathbf{M}_z^I &+ \mathbf{M}_t \otimes \mathbf{M}_\theta \otimes \mathbf{M}_{\cos(\phi)} \otimes \mathbf{D}_{z,z}^I \\
&+ \kappa \mathbf{M}_t \otimes \mathbf{M}_\theta \otimes \mathbf{M}_\phi \otimes \mathbf{M}_z^I + \Upsilon_z \mathbf{M}_t \otimes \mathbf{M}_\theta \otimes \mathbf{M}_{\cos(\phi)} \otimes \mathbf{M}_z^I \\
&- \frac{\sigma}{4\pi}\mathbf{M}_t \otimes \left(\mathbf{M}_\theta^0 \otimes 2\mathbf{M}_\theta^{0T}\right) \otimes \left(\mathbf{M}_\phi^0 \otimes \mathbf{M}_\phi^{0T}\right) \otimes \mathbf{M}_z^I - \mathbf{M}_t \otimes \mathbf{M}_\theta \otimes \boldsymbol{\Gamma}_z^- \Bigg] \cdot \mathbf{I} = \\
\Big[S_z \mathbf{M}_t \otimes \mathbf{M}_\theta^0 \otimes \mathbf{M}_{\cos(\phi)}^0 &\otimes \mathbf{M}_z^{I,Te} + S_A \mathbf{M}_t \otimes \mathbf{M}_\theta^0 \otimes \mathbf{M}_\phi^0 \otimes \mathbf{M}_z^{I,Te} \Big] \cdot \mathbf{T}_e + S_b \mathbf{M}_t^0 \otimes \mathbf{M}_\theta^0 \otimes \mathbf{M}_\phi^0 \otimes \mathbf{M}_z^{I,0} \\
&- \mathbf{M}_t \otimes \mathbf{M}_\theta \otimes \left(\tilde{\boldsymbol{\Gamma}}_z^- \cdot \tilde{\mathbf{I}}\right)_\Gamma, \quad (3.64)
\end{aligned}
$$

where apart from the already defined t, θ, and ϕ matrices (3.39–3.41, 3.43, 3.46, 3.49, 3.50, 3.53, 3.54), we define the spatial discretization matrices

$$
\mathbf{M}_z^I = \int_{\Delta z} \psi(z) \otimes \psi(z)^T \, \mathrm{d}z, \tag{3.65}
$$

$$
\mathbf{D}_{z,z}^I = \int_{\Delta z} \psi(z) \otimes \frac{\partial \psi(z)^T}{\partial z} \, \mathrm{d}z \tag{3.66}
$$

$$
\mathbf{M}_z^{I,Te} = \int_{\Delta z} \psi(z) \otimes \xi(z)^T \, \mathrm{d}z, \tag{3.67}
$$

$$
\mathbf{M}_z^{I,0} = \int_{\Delta z} \psi(z) \otimes \omega_0^T \, \mathrm{d}z. \tag{3.68}
$$

The main goal of the 1D slab geometry DG-BGK scheme (3.64) of the transport equation (3.59) resides in finding the linear dependence of the unknown $\mathbf{I}$ on the unknown $\mathbf{T}_e$ [97, 98, 99, 100, 51, 50] as

$$
\mathbf{I} = \mathbf{A}_z \cdot \mathbf{T}_e + \mathbf{b}_z, \tag{3.69}
$$

which can be directly obtained from (3.64) after some straightforward algebraic operations. It is worth mentioning, that the adjacent cells discretization $\tilde{\mathbf{I}}$ is absorbed in the $\mathbf{b}_z$ vector.

As was stated before, we want to make use of the lowest order backward Euler time discretization. The *1D slab geometry backward Euler DG-BGK scheme* can be obtained by using the backward Euler time matrices (3.42) in (3.64), thus giving

$$
\begin{aligned}
\Bigg[\frac{1}{c\Delta t}\mathbf{M}_\theta \otimes \mathbf{M}_\phi \otimes \mathbf{M}_z^I &+ \mathbf{M}_\theta \otimes \mathbf{M}_{\cos(\phi)} \otimes \mathbf{D}_{z,z}^I + \kappa \mathbf{M}_\theta \otimes \mathbf{M}_\phi \otimes \mathbf{M}_z^I + \\
\Upsilon_z \mathbf{M}_\theta \otimes \mathbf{M}_{\cos(\phi)} \otimes \mathbf{M}_z^I &- \frac{\sigma}{4\pi}\left(\mathbf{M}_\theta^0 \otimes 2\mathbf{M}_\theta^{0T}\right) \otimes \left(\mathbf{M}_\phi^0 \otimes \mathbf{M}_\phi^{0T}\right) \otimes \mathbf{M}_z^I - \mathbf{M}_\theta \otimes \boldsymbol{\Gamma}_z^- \Bigg] \cdot \mathbf{I}^1 = \\
\Big[S_z \mathbf{M}_\theta^0 \otimes \mathbf{M}_{\cos(\phi)}^0 &\otimes \mathbf{M}_z^{I,Te} + S_A \mathbf{M}_\theta^0 \otimes \mathbf{M}_\phi^0 \otimes \mathbf{M}_z^{I,Te} \Big] \cdot \mathbf{T}_e^1 + S_b \mathbf{M}_\theta^0 \otimes \mathbf{M}_\phi^0 \otimes \mathbf{M}_z^{I,0} \\
&- \mathbf{M}_\theta \otimes \left(\tilde{\boldsymbol{\Gamma}}_z^- \cdot \tilde{\mathbf{I}}_1\right)_\Gamma + \frac{1}{c\Delta t}\mathbf{M}_\theta \otimes \mathbf{M}_\phi \otimes \mathbf{M}_z^I \cdot \mathbf{I}^0, \quad (3.70)
\end{aligned}
$$

where the discretization $\mathbf{I}$ has been divided into its explicit part $\mathbf{I}^0$ and its implicit part

$\mathbf{I}^1$ according to (3.21) and (3.22), respectively. The scheme also uses only the implicit part of the unknown $\mathbf{T}_e$, i.e. $\mathbf{T}_e^1$ defined in (3.24).

In the case of the backward Euler scheme (3.70), we can explicitly write

$$\mathbf{A}_z \;=\; \mathbf{L}_z^{-1} \cdot \left[\mathbf{M}_{\cos(\phi)}^0 \otimes S_z \mathbf{M}_z^{I,Te} + \mathbf{M}_\phi^0 \otimes S_A \mathbf{M}_z^{I,Te} \right], \tag{3.71}$$

$$\mathbf{b}_z \;=\; \mathbf{L}_z^{-1} \cdot \left[\mathbf{M}_\phi^0 \otimes S_b \mathbf{M}_z^{I,0} - \left(\tilde{\mathbf{\Gamma}}_z^- \cdot \tilde{\mathbf{I}}_1 \right)_\Gamma + \frac{1}{c\Delta t} \mathbf{M}_\phi \otimes \mathbf{M}_z^I \cdot \mathbf{I}_0 \right], \tag{3.72}$$

which includes the inversion of the element matrix

$$\mathbf{L}_z = \left[\mathbf{M}_\phi \otimes \frac{1}{c\Delta t} \mathbf{M}_z^I + \mathbf{M}_{\cos(\phi)} \otimes \mathbf{D}_{z,z}^I + \mathbf{M}_\phi \otimes \kappa \mathbf{M}_z^I + \right.$$

$$\left. \mathbf{M}_{\cos(\phi)} \otimes \mathbf{\Upsilon}_z \mathbf{M}_z^I - \left(\mathbf{M}_\phi^0 \otimes \mathbf{M}_\phi^{0T} \right) \otimes \frac{\sigma}{2} \mathbf{M}_z^I - \mathbf{\Gamma}_z^- \right]. \tag{3.73}$$

Finally, we can write the backward Euler solution to (3.59) as a linear function of the unknown $\mathbf{T}_e$ [51, 50]

$$\mathbf{I}^1 = \mathbf{A}_z \cdot \mathbf{T}_e^1 + \mathbf{b}_z, \tag{3.74}$$

where the linear coefficient $\mathbf{A}_z$ and the constant vector $\mathbf{b}_z$ are defined in (3.71) and (3.72), respectively.

It was opted at the beginning of this section that all the coefficients of (3.60) depend, in general, on time t and position z. Nevertheless, when used in the schemes (3.64) and (3.70), we need to put some restrictions on the form of the latter coefficients.

In the case of the backward Euler scheme (3.70) any time dependence of (3.60) cannot be included by definition. The best option is to use their mean values over Δt. However, the dependence on z can be enforced in the finite element matrices construction, e.g. the spatial dependence of the extinction coefficient κ can be included as

$$\kappa \mathbf{M}_z^I = \int_{\Delta z} \psi(z) \otimes \psi(z)^T \kappa(z) \, \mathrm{d}z,$$

which appears in (3.73) and other coefficients of (3.60) can be treated in the exactly same manner.

The approach to be used in the case of the scheme (3.64) is equivalent, while we impose the condition of separable dependence on time and on space of coefficients (3.60). We show an example of the extinction coefficient κ, which needs to be written as $\kappa(t,z) = g(t)f(z)$. Then, the inclusion of the latter dependence reads

$$\kappa \mathbf{M}_t \otimes \mathbf{M}_\theta \otimes \mathbf{M}_\phi \otimes \mathbf{M}_z^I = \int_{\Delta t} \omega_t \otimes \omega_t^T g(t) \, \mathrm{d}t \otimes \mathbf{M}_\theta \otimes \mathbf{M}_\phi \otimes \int_{\Delta z} \psi(z) \otimes \psi(z)^T f(z) \, \mathrm{d}z,$$

which can be directly used in (3.64). The treatment of other coefficients of (3.60) simply follows the example above.

It is worth mentioning that the spatial discretization matrices (3.65–3.68) are integrated over a 1D interval Δz, which is a simple quadrature rule operation using a mapping based on the Δz scaling. One can observe, that the boundary matrices $\mathbf{\Gamma}_z^-$ (3.62)

and $\tilde{\mathbf{\Gamma}}_z^-$ (3.63) can also be written separated as

$$
\mathbf{\Gamma}_z^- = \sum_{F=+,-} \int_0^\pi \omega_\phi \otimes \omega_\phi^T \left(\cos(\phi) n_{\Gamma_z^F} \right) \sin(\phi)\, \mathrm{d}\phi \otimes \int_{\Gamma^F} \psi(z) \otimes \psi(z)^T\, \mathrm{d}\Gamma^F \,,
$$

$$
\tilde{\mathbf{\Gamma}}_z^- = \sum_{F=+,-} \int_0^\pi \omega_\phi \otimes \omega_\phi^T \left(\cos(\phi) n_{\Gamma_z^F} \right) \sin(\phi)\, \mathrm{d}\phi \otimes \int_{\Gamma^F} \psi(z) \otimes \tilde{\psi}^F(z)^T\, \mathrm{d}\Gamma^F \,,
$$

since neither of the normals n_{Γ_z} and $n_{\Gamma_z^{adj}}$ depends on the position z. In the slab geometry, the boundary Γ consists of two parts Γ^+ and Γ^-, which represented by constant vectors $\mathbf{n}_{\Gamma^+} = [0,0,n_{\Gamma_z^+} = 1]^T$ and $\mathbf{n}_{\Gamma^-} = [0,0,n_{\Gamma_z^-} = -1]^T$. In the definitions above, the integration over the angle ϕ applies only where $\cos(\phi)n_{\Gamma_z^F} < 0$. A special attention must be paid when evaluating the mass boundary $\int_{\Gamma^F} \psi(z) \otimes \tilde{\psi}^F(z)^T\, \mathrm{d}\Gamma^F$ since the neighbor element basis $\tilde{\psi}^F$ is used.

The 1D Slab Geometry DG-T_e Electron Temperature Scheme

The slab geometry implies a reduced dependence of the electron temperature $T_e(t,\mathbf{x}(z))$, and the resulting form of the *slab electron temperature equation* reads

$$
a_e \frac{\mathrm{d}T_e}{\mathrm{d}t} + G_{ie}T_e + \int_0^{2\pi} \int_0^\pi \left(\frac{1}{c}\frac{\mathrm{d}I}{\mathrm{d}t} + \cos(\phi)\frac{\partial I}{\partial z} \right) \sin(\phi)\mathrm{d}\phi\mathrm{d}\theta = P_e + G_{ie}T_i \,, \qquad (3.75)
$$

which represents a 3D problem, i.e. the solution T_e of (3.75) depends on t, z and ϕ due to $\mathbf{I}$. All the coefficients

$$
c, a_e, G_{ie}, P_e \,, \qquad (3.76)
$$

depend, in general, on time t and position z.

The discrete form of the discontinuous Galerkin variation principle (3.8) in the case of the 1D slab geometry uses the discretization of T_e, I, and T_i (3.19) where the bases $\mathbf{\Xi}$, $\mathbf{\Psi}$, and $\tilde{\mathbf{\Xi}}$ of (3.20) are defined on the spatial domain using the coordinate system $\mathbf{x} = \mathbf{x}(z)$, in particular, the bases ξ, ψ, and $\tilde{\xi}$ of (3.18) depend on z.

The *discrete 1D slab geometry variational form* of the discontinuous Galerkin electron temperature equation (3.75) reads

$$
\int_{\Delta t} \int_{\Delta z} \mathbf{\Xi} \otimes \left[\left(a_e \frac{\mathrm{d}\mathbf{\Xi}^T}{\mathrm{d}t} + G_{ie}\mathbf{\Xi}^T \right) \cdot \mathbf{T}_e + \right.
$$

$$
\left. \left(\int_0^{2\pi} \int_0^\pi \left(\frac{1}{c}\frac{\mathrm{d}\mathbf{\Psi}^T}{\mathrm{d}t} + \cos(\phi)\frac{\partial \mathbf{\Psi}^T}{\partial z} \right) \sin(\phi)\mathrm{d}\phi\mathrm{d}\theta \right) \cdot \mathbf{I} - P_e - G_{ie}\tilde{\mathbf{\Xi}}^T \cdot \mathbf{T}_i \right] \mathrm{d}z\mathrm{d}t = 0 \,,
$$

$$
(3.77)
$$

where Δz is the spatial domain of the element.

We can apply the products $\mathbf{\Xi} \otimes \mathbf{\Xi}^T$ of (3.34), $\mathbf{\Xi} \otimes \mathbf{\Psi}^T$ of (3.33), and $\mathbf{\Xi} \otimes \tilde{\mathbf{\Xi}}^T$ of (3.36) wherever they appear in (3.77), which leads to the *1D slab geometry DG-T_e scheme*

formulation

$$\left[a_e\mathbf{D}_t \otimes \mathbf{M}_z^{Te} + G_{ie}\mathbf{M}_t \otimes \mathbf{M}_z^{Te}\right] \cdot \mathbf{T}_e - P_e\mathbf{M}_t^0 \otimes \mathbf{M}_z^{Te,0} - G_{ie}\mathbf{M}_t \otimes \mathbf{M}_z^{Te,T_i} \cdot \mathbf{T}_i$$

$$+ \left[\frac{1}{c}\mathbf{D}_t \otimes 2\mathbf{M}_\theta^0 \otimes \mathbf{M}_\phi^0 \otimes \mathbf{M}_z^{Te,I} + \mathbf{M}_t \otimes 2\mathbf{M}_\theta^0 \otimes \mathbf{M}_{\cos(\phi)}^0 \otimes \mathbf{D}_{z,z}^{Te,I}\right] \cdot \mathbf{I} = 0, \quad (3.78)$$

where apart from the already defined t, θ, and ϕ matrices (3.39–3.41, 3.46, 3.53, 3.54) we define the spatial discretization matrices

$$\mathbf{M}_z^{Te} = \int_{\Delta z} \xi \otimes \xi^T \, \mathrm{d}z, \quad (3.79)$$

$$\mathbf{M}_z^{Te,I} = \int_{\Delta z} \xi \otimes \psi^T \, \mathrm{d}z = \mathbf{M}_z^{I,Te}{}^T, \quad (3.80)$$

$$\mathbf{D}_{z,z}^{Te,I} = \int_{\Delta z} \xi \otimes \frac{\partial \psi^T}{\partial z} \, \mathrm{d}z \quad (3.81)$$

$$\mathbf{M}_z^{Te,0} = \int_{\Delta z} \xi \otimes \omega_0^T \, \mathrm{d}z, \quad (3.82)$$

$$\mathbf{M}_z^{Te,T_i} = \int_{\Delta z} \xi \otimes \tilde{\xi}^T \, \mathrm{d}z. \quad (3.83)$$

Now, the linear function solution (3.69) can be justified. The latter has the form $\mathbf{I} = \mathbf{A}_z \cdot \mathbf{T}_e + \mathbf{b}_z$, which when plugged in (3.78) provides the *1D slab geometry DG-T_e electron temperature scheme*

$$\left[a_e\mathbf{D}_t \otimes \mathbf{M}_z^{Te} + G_{ie}\mathbf{M}_t \otimes \mathbf{M}_z^{Te}\right] \cdot \mathbf{T}_e - P_e\mathbf{M}_t^0 \otimes \mathbf{M}_z^{Te,0} - G_{ie}\mathbf{M}_t \otimes \mathbf{M}_z^{Te,T_i} \cdot \mathbf{T}_i +$$

$$\left[\frac{1}{c}\mathbf{D}_t \otimes 2\mathbf{M}_\theta^0 \otimes \mathbf{M}_\phi^0 \otimes \mathbf{M}_z^{Te,I} + \mathbf{M}_t \otimes 2\mathbf{M}_\theta^0 \otimes \mathbf{M}_{\cos(\phi)}^0 \otimes \mathbf{D}_{z,z}^{Te,I}\right] \cdot (\mathbf{A}_z \cdot \mathbf{T}_e + \mathbf{b}_z) = 0,$$

$$(3.84)$$

which is apparently a problem of the unknown $\mathbf{T}_e$ and the unknown $\mathbf{T}_i$. Nevertheless, the former unknown $\mathbf{I}$ is implicitly coupled via the matrix $\mathbf{A}_z$ and the vector $\mathbf{b}_z$.

As was stated before, we want to make use of the lowest order backward Euler time discretization. The *1D slab geometry backward Euler DG-T_e scheme* can be obtained by using the backward Euler time matrices (3.42) in (3.84), thus giving

$$\left[\frac{a_e}{\Delta t}\mathbf{M}_z^{Te} + G_{ie}\mathbf{M}_z^{Te}\right] \cdot \mathbf{T}_e^1 - P_e\mathbf{M}_z^{Te,0} - G_{ie}\mathbf{M}_z^{Te,T_i} \cdot \mathbf{T}_i^1 +$$

$$\left[2\mathbf{M}_\theta^0 \otimes \left(\mathbf{M}_\phi^0 \otimes \frac{1}{c\Delta t}\mathbf{M}_z^{Te,I} + \mathbf{M}_{\cos(\phi)}^0 \otimes \mathbf{D}_{z,z}^{Te,I}\right)\right] \cdot (\mathbf{A}_z \cdot \mathbf{T}_e^1 + \mathbf{b}_z) =$$

$$\frac{a_e}{\Delta t}\mathbf{M}_z^{Te} \cdot \mathbf{T}_e^0 + 2\mathbf{M}_\theta^0 \otimes \mathbf{M}_\phi^0 \otimes \frac{1}{c\Delta t}\mathbf{M}_z^{Te,I} \cdot \mathbf{I}^0, \quad (3.85)$$

where each of the discretizations $\mathbf{T}_e$ and $\mathbf{I}$ have been divided into its explicit part, i.e. $\mathbf{T}_e^0$ and $\mathbf{I}^0$, respectively, and its implicit part, i.e. $\mathbf{T}_e^1$ and $\mathbf{I}^1$ respectively, according to (3.23, 3.24) and (3.21, 3.22), respectively. The scheme also uses only the implicit part of

the unknown $\mathbf{T}_i$, i.e. $\mathbf{T}_i^1$ defined in (3.26). The matrix $\mathbf{A}_z$ and the vector $\mathbf{b}_z$ are defined in (3.71) and (3.72).

It was opted at the beginning of this section that all the coefficients of (3.76) depend, in general, on time t and position z. Nevertheless, when used in the schemes (3.84) and (3.85), we need to put some restrictions on the form of the latter coefficients.

In the case of the backward Euler scheme (3.85) any time dependence of (3.76) cannot be included by definition. The best option is to use their mean values over Δt. However, the dependence on z can be enforced in the finite element matrices construction, e.g. the spatial dependence of the heat capacity coefficient a_e can be included as

$$a_e \mathbf{M}_z^{Te} = \int_{\Delta z} \xi(z) \otimes \xi(z)^T a_e(z) \, \mathrm{d}z \,,$$

which appears in (3.85) and other coefficients of (3.76) can be treated in the exactly same manner.

The approach to be used in the case of the scheme (3.84) is equivalent, while we impose the condition of separable dependence on time and on space of coefficients (3.76). We show an example of the heat capacity coefficient a_e, which needs to be written as $a_e(t, z) = g(t)f(z)$. Then, the inclusion of the latter dependence reads

$$a_e \mathbf{D}_t \otimes \mathbf{M}_z^{Te} = \int_{\Delta t} \omega_t \otimes \frac{\mathrm{d}\omega_t^T}{\mathrm{d}t} g(t) \, \mathrm{d}t \otimes \int_{\Delta z} \xi(z) \otimes \xi(z)^T f(z) \, \mathrm{d}z \,,$$

which can be directly used in (3.84). The treatment of other coefficients of (3.76) simply follows the example above.

The 1D Slab Geometry DG-T_i Electron Temperature Scheme

The slab geometry implies a reduced dependence of the ion temperature $T_i(t, \mathbf{x}(z))$, and the resulting form of the *slab ion temperature equation* reads

$$a_i \frac{\mathrm{d}T_i}{\mathrm{d}t} + G_{ie}T_i = P_i + G_{ie}T_e \,, \tag{3.86}$$

which represents a 2D problem, i.e. the solution T_i of (3.86) depends on t, z. All the coefficients

$$a_i, G_{ie}, P_i \,, \tag{3.87}$$

depend, in general, on time t and position z.

The discrete form of the discontinuous Galerkin variation principle (3.9) in the case of the 1D slab geometry uses the discretization of T_i, and T_e (3.19) where the bases $\tilde{\boldsymbol{\Xi}}$, and $\boldsymbol{\Xi}$ of (3.20) are defined on the spatial domain using the coordinate system $\mathbf{x} = \mathbf{x}(z)$, in particular, the bases $\tilde{\xi}$, and ξ of (3.18) depend on z.

The *discrete 1D slab geometry variational form* of the discontinuous Galerkin ion temperature equation (3.86) reads

$$\int_{\Delta t} \int_{\Delta z} \tilde{\boldsymbol{\Xi}} \otimes \left[\left(a_i \frac{\mathrm{d}\tilde{\boldsymbol{\Xi}}^T}{\mathrm{d}t} + G_{ie}\tilde{\boldsymbol{\Xi}}^T \right) \cdot \mathbf{T}_i - P_i - G_{ie}\boldsymbol{\Xi}^T \cdot \mathbf{T}_e \right] \mathrm{d}z\mathrm{d}t = 0 \,, \tag{3.88}$$

where Δz is the spatial domain of the element.

We can apply the products $\tilde{\Xi} \otimes \tilde{\Xi}^T$ of (3.35), and $\tilde{\Xi} \otimes \Xi^T$ of (3.37) wherever they appear in (3.88), which leads to the *1D slab geometry DG-T_i scheme* formulation

$$\left[a_i \mathbf{D}_t \otimes \mathbf{M}_z^{T_i} + G_{ie} \mathbf{M}_t \otimes \mathbf{M}_z^{T_i} \right] \cdot \mathbf{T}_i - G_{ie} \mathbf{M}_t \otimes \mathbf{M}_z^{T_i, T_e} \cdot \mathbf{T}_e = P_i \mathbf{M}_t^0 \otimes \mathbf{M}_z^{T_i, 0}, \quad (3.89)$$

where apart from the already defined t matrices (3.39–3.41), we define the spatial discretization matrices

$$\mathbf{M}_z^{T_i} = \int_{\Delta z} \tilde{\xi} \otimes \tilde{\xi}^T \, \mathrm{d}z, \tag{3.90}$$

$$\mathbf{M}_z^{T_i, 0} = \int_{\Delta z} \tilde{\xi} \otimes \omega_0^T \, \mathrm{d}z, \tag{3.91}$$

$$\mathbf{M}_z^{T_i, T_e} = \int_{\Delta z} \tilde{\xi} \otimes \xi^T \, \mathrm{d}z = \mathbf{M}_z^{T_e, T_i \, T}. \tag{3.92}$$

As was stated before, we want to make use of the lowest order backward Euler time discretization. The *1D slab geometry backward Euler DG-T_i scheme* can be obtained by using the backward Euler time matrices (3.42) in (3.89), thus giving

$$\left[\frac{a_i}{\Delta t} \mathbf{M}_z^{T_i} + G_{ie} \mathbf{M}_z^{T_i} \right] \cdot \mathbf{T}_i^1 - G_{ie} \mathbf{M}_z^{T_i, T_e} \cdot \mathbf{T}_e^1 = P_i \mathbf{M}_z^{T_i, 0} + \frac{a_i}{\Delta t} \mathbf{M}_z^{T_i} \cdot \mathbf{T}_i^0, \tag{3.93}$$

where the discretization $\mathbf{T}_i$ has been divided into its explicit part $\mathbf{T}_i^0$ and its implicit part $\mathbf{T}_i^1$ according to (3.25, 3.26). The scheme also uses only the implicit part of the unknown $\mathbf{T}_e$, i.e. $\mathbf{T}_e^1$ defined in (3.24).

It was opted at the beginning of this section that all the coefficients of (3.87) depend, in general, on time t and position z. Nevertheless, when used in the schemes (3.89) and (3.93), we need to put some restrictions on the form of the latter coefficients.

In the case of the backward Euler scheme (3.93) any time dependence of (3.87) cannot be included by definition. The best option is to use their mean values over Δt. However, the dependence on z can be enforced in the finite element matrices construction, e.g. the spatial dependence of the heat capacity coefficient a_i can be included as

$$a_i \mathbf{M}_z^{T_i} = \int_{\Delta z} \tilde{\xi}(z) \otimes \tilde{\xi}(z)^T a_i(z) \, \mathrm{d}z,$$

which appears in (3.93) and other coefficients of (3.87) can be treated in the exactly same manner.

The approach to be used in the case of the scheme (3.89) is equivalent, while we impose the condition of separable dependence on time and on space of coefficients (3.87). We show an example of the heat capacity coefficient a_i, which needs to be written as $a_i(t, z) = g(t) f(z)$. Then, the inclusion of the latter dependence reads

$$a_i \mathbf{D}_t \otimes \mathbf{M}_z^{T_i} = \int_{\Delta t} \omega_t \otimes \frac{\mathrm{d}\omega_t^T}{\mathrm{d}t} g(t) \, \mathrm{d}t \otimes \int_{\Delta z} \tilde{\xi}(z) \otimes \tilde{\xi}(z)^T f(z) \, \mathrm{d}z,$$

which can be directly used in (3.89). The treatment of other coefficients of (3.87) simply follows the example above.

3.1.2   The 1D Spherically Symmetric DG-BGK&Ts Scheme

The spherically symmetric geometry provides a simple function dependence on one spatial coordinate. The change of spatial coordinate is referred to the z axis of the Cartesian coordinate system in space and in spherical coordinate system of transport directions, where the reference axis is given by the latter z axis (see Fig. 2.1).

In what follows, we show the strategy of one element partial discretization of the equations of transport (3.7), electron temperature (3.8), and ion temperature (3.9) in subsequent sections. Either I, T_e, and T_i unknown functions are piecewise continuous in space and continuous in time polynomials. The unknown I is continuous in directions.

The last section explains the method of solution on the entire computational domain which is the critical point of computational efficiency.

The 1D Spherically Symmetric Geometry DG-BGK Transport Scheme

In spherical coordinates the position vector is defined as $\mathbf{x} = (r, \tilde{\phi}, \tilde{\theta})$, where the coordinate axis vectors change according to the position dependence on $(\tilde{\phi}, \tilde{\theta})$, i.e. system is curvilinear. The spherically symmetric geometry implies a reduced dependence of the specific intensity $I(t, \mathbf{n}(\phi), \mathbf{x}(r))$, and the resulting form of the *spherically symmetric transfer equation* reads

$$\frac{1}{c}\frac{\mathrm{d}I}{\mathrm{d}t} + \cos(\phi)\frac{\partial I}{\partial r} - \frac{\sin(\phi)}{r}\frac{\partial I}{\partial \phi} = (\cos(\phi)S_r + S_A)\,T_e + S_b - (\kappa + \cos(\phi)\Upsilon_r)\,I + \sigma\bar{I}\,, \quad (3.94)$$

which represents a 3D problem, i.e. the solution I of (3.94) depends on t, ϕ and r. All the coefficients

$$c, \kappa, \Upsilon_r, \sigma, S_r, S_A, S_b\,, \quad (3.95)$$

depend, in general, on time t and position r.

The discrete form of the discontinuous Galerkin variation principle (3.10, 3.13) in the case of the 1D slab geometry uses the discretization of I and T_e (3.19) where the bases $\mathbf{\Psi}$ and $\mathbf{\Xi}$ of (3.20) are defined on the spatial domain using the coordinate system $\mathbf{x} = \mathbf{x}(r)$, in particular, the bases ψ and ξ of (3.18) depend on r.

The *discrete 1D spherically symmetric geometry variational form* of the discontinuous Galerkin BGK transport equation (3.94) reads

$$\int_{\Delta t}\int_0^{2\pi}\int_0^\pi\int_{\Delta r}\mathbf{\Psi}\otimes\left[\left(\frac{1}{c}\frac{\mathrm{d}\mathbf{\Psi}^T}{\mathrm{d}t} + \cos(\phi)\frac{\partial\mathbf{\Psi}^T}{\partial r} - \frac{\sin(\phi)}{r}\frac{\partial\mathbf{\Psi}^T}{\partial\phi} + (\kappa + \cos(\phi)\Upsilon_r)\mathbf{\Psi}^T\right.\right.$$

$$\left.\left. - \frac{\sigma}{4\pi}\int\mathbf{\Psi}^T\sin(\phi)\mathrm{d}\phi\mathrm{d}\theta\right)\cdot\mathbf{I} - ((\cos(\phi)S_r + S_A)\,\mathbf{\Xi}^T\cdot\mathbf{T}_e + S_b)\right]r\mathrm{d}r\sin(\phi)\mathrm{d}\phi\mathrm{d}\theta\mathrm{d}t =$$

$$\int_{\Delta t}\int_0^{2\pi}\int_0^\pi\int_{\Gamma_{\mathbf{n}\cdot\mathbf{n}_\Gamma<0}}\mathbf{\Psi}\otimes\left[\left(\mathbf{\Psi}^T\cdot\mathbf{I} - \tilde{\mathbf{\Psi}}^T\cdot\tilde{\mathbf{I}}\right)\cos(\phi)n_{\Gamma_r}\right]\mathrm{d}\Gamma_r\sin(\phi)\mathrm{d}\phi\mathrm{d}\theta\mathrm{d}t\,, \quad (3.96)$$

where Δr is the spatial domain of the element and where $\Gamma_{\mathbf{n}\cdot\mathbf{n}_\Gamma<0}$ means the part of boundary Γ where the projection of the transport direction $\mathbf{n}$ into the surface normal $\mathbf{n}_\Gamma$ is less than zero, i.e. $\mathbf{n}\cdot\mathbf{n}_\Gamma = \cos(\phi)n_{\Gamma_r} < 0$.

Since the procedure of obtaining the discrete scheme representing the solution of transport problem in the spherically symmetric geometry is rather tedious, we show directly the backward Euler solution to (3.94) as a linear function of the unknown $\mathbf{T}_e$

[51, 50]

$$\mathbf{I}^1 = \mathbf{A}_r \cdot \mathbf{T}_e^1 + \mathbf{b}_r \,, \tag{3.97}$$

where the linear coefficient $\mathbf{A}_r$ and the constant vector $\mathbf{b}_r$ are defined as

$$\mathbf{A}_r = \mathbf{L}_r^{-1} \cdot \left[\mathbf{M}_{\cos(\phi)}^0 \otimes S_r \mathbf{M}_r^{I,T_e} + \mathbf{M}_\phi^0 \otimes S_A \mathbf{M}_r^{I,T_e} \right], \tag{3.98}$$

$$\mathbf{b}_r = \mathbf{L}_r^{-1} \cdot \left[\mathbf{M}_\phi^0 \otimes S_b \mathbf{M}_r^{I,0} - \left(\tilde{\mathbf{\Gamma}}_r^- \cdot \tilde{\mathbf{I}}_1 \right)_\Gamma + \frac{1}{c\Delta t} \mathbf{M}_\phi \otimes \mathbf{M}_r^I \cdot \mathbf{I}_0 \right], \tag{3.99}$$

which includes the inversion of the element matrix

$$\mathbf{L}_r = \left[\mathbf{M}_\phi \otimes \frac{1}{c\Delta t} \mathbf{M}_r^I + \mathbf{M}_{\cos(\phi)} \otimes \mathbf{D}_{r,r}^I - \mathbf{D}_{\sin(\phi)} \otimes \mathbf{M}_{r/r}^I + \mathbf{M}_\phi \otimes \kappa \mathbf{M}_r^I + \right.$$

$$\left. \mathbf{M}_{\cos(\phi)} \otimes \Upsilon_r \mathbf{M}_r^I - \left(\mathbf{M}_\phi^0 \otimes \mathbf{M}_\phi^{0T} \right) \otimes \frac{\sigma}{2} \mathbf{M}_r^I - \mathbf{\Gamma}_r^- \right]. \tag{3.100}$$

The reader should refer to Appendix B.1.1 in order to see details about the construction of the scheme above.

The 1D Spherically Symmetric Geometry DG-T_e Temperature Scheme

The spherically symmetric geometry implies a reduced dependence of the electron temperature $T_e(t, \mathbf{x}(r))$, and the resulting form of the *spherically symmetric electron temperature equation* reads

$$a_e \frac{\mathrm{d}T_e}{\mathrm{d}t} + \int_0^{2\pi} \int_0^\pi \left(\frac{1}{c} \frac{\mathrm{d}I}{\mathrm{d}t} + \cos(\phi) \frac{\partial I}{\partial r} - \frac{\sin(\phi)}{r} \frac{\partial I}{\partial \phi} \right) \sin(\phi) \mathrm{d}\phi \mathrm{d}\theta + G_{ie} T_e = P_e + G_{ie} T_i \,, \tag{3.101}$$

which represents a 3D problem, i.e. the solution T_e of (3.101) depends on t, r and ϕ due to I. All the coefficients

$$c, a_e, G_{ie}, P_e \,, \tag{3.102}$$

depend, in general, on time t and position r.

The discrete form of the discontinuous Galerkin variation principle (3.8) in the case of the 1D spherically symmetric geometry uses the discretization of T_e, I, and T_i (3.19) where the bases $\mathbf{\Xi}$, $\mathbf{\Psi}$, and $\tilde{\mathbf{\Xi}}$ of (3.20) are defined on the spatial domain using the coordinate system $\mathbf{x} = \mathbf{x}(r)$, in particular, the bases ξ, ψ, and $\tilde{\xi}$ of (3.18) depend on r.

The *discrete 1D spherically symmetric geometry variational form* of the discontinuous Galerkin electron temperature equation (3.101) reads

$$\int_{\Delta t} \int_{\Delta r} \mathbf{\Xi} \otimes \left[\left(a_e \frac{\mathrm{d}\mathbf{\Xi}^T}{\mathrm{d}t} + G_{ie}\mathbf{\Xi}^T \right) \cdot \mathbf{T}_e + \right.$$

$$\left(\int_0^{2\pi} \int_0^\pi \left(\frac{1}{c} \frac{\mathrm{d}\mathbf{\Psi}^T}{\mathrm{d}t} + \cos(\phi) \frac{\partial \mathbf{\Psi}^T}{\partial r} - \frac{\sin(\phi)}{r} \frac{\partial \mathbf{\Psi}^T}{\partial \phi} \right) \sin(\phi) \mathrm{d}\phi \mathrm{d}\theta \right) \cdot \mathbf{I}$$

$$\left. - P_e - G_{ie}\tilde{\mathbf{\Xi}}^T \cdot \mathbf{T}_i \right] r \mathrm{d}r \mathrm{d}t = 0 \,, \tag{3.103}$$

where Δr is the spatial domain of the element.

As in the case of the 1D slab geometry, we define the *1D spherically symmetric geometry backward Euler DG-T_e scheme*

$$\left[\frac{a_e}{\Delta t}\mathbf{M}_r^{Te} + G_{ie}\mathbf{M}_r^{Te}\right] \cdot \mathbf{T}_e^1 - P_e\mathbf{M}_r^{Te,0} - G_{ie}\mathbf{M}_r^{Te,T_i} \cdot \mathbf{T}_i^1 +$$

$$\left[2\mathbf{M}_\theta^0 \otimes \left(\mathbf{M}_\phi^0 \otimes \frac{1}{c\Delta t}\mathbf{M}_r^{Te,I} + \mathbf{M}_{\cos(\phi)}^0 \otimes \mathbf{D}_{r,r}^{Te,I} - \mathbf{D}_{\sin(\phi)}^0 \otimes \mathbf{M}_{r/r}^{Te,I}\right)\right] \cdot \left(\mathbf{A}_r \cdot \mathbf{T}_e^1 + \mathbf{b}_r\right) =$$

$$\frac{a_e}{\Delta t}\mathbf{M}_r^{Te} \cdot \mathbf{T}_e^0 + 2\mathbf{M}_\theta^0 \otimes \mathbf{M}_\phi^0 \otimes \frac{1}{c\Delta t}\mathbf{M}_r^{Te,I} \cdot \mathbf{I}^0, \quad (3.104)$$

where each of the discretizations $\mathbf{T}_e$ and $\mathbf{I}$ have been divided into its explicit part, i.e. $\mathbf{T_e^0}$ and $\mathbf{I^0}$, respectively, and its implicit part, i.e. $\mathbf{T}_e^1$ and $\mathbf{I}^1$ respectively, according to (3.23, 3.24) and (3.21, 3.22), respectively. The scheme also uses only the implicit part of the unknown $\mathbf{T}_i$, i.e. $\mathbf{T}_i^1$ defined in (3.26). The matrix $\mathbf{A}_r$ and the vector $\mathbf{b}_r$ are defined in (3.98) and (3.99).

The reader should refer to Appendix B.1.2 in order to see details about the construction of the scheme above, where the definition of time discretization is defined in its general form.

The 1D Spherically Symmetric Geometry DG-T_i Temperature Scheme

The spherically symmetric geometry implies a reduced dependence of the ion temperature $T_i(t, \mathbf{x}(r))$, and the resulting form of the *spherically symmetric ion temperature equation* reads

$$a_i\frac{\mathrm{d}T_i}{\mathrm{d}t} + G_{ie}T_i = P_i + G_{ie}T_e, \quad (3.105)$$

which represents a 2D problem, i.e. the solution T_i of (3.105) depends on t and r. All the coefficients

$$a_i, G_{ie}, P_i, \quad (3.106)$$

depend, in general, on time t and position r.

The discrete form of the discontinuous Galerkin variation principle (3.9) in the case of the 1D spherically symmetric geometry uses the discretization of T_i, and T_e (3.19) where the bases $\tilde{\mathbf{\Xi}}$, and $\mathbf{\Xi}$ of (3.20) are defined on the spatial domain using the coordinate system $\mathbf{x} = \mathbf{x}(r)$, in particular, the bases $\tilde{\xi}$, and ξ of (3.18) depend on r.

The *discrete 1D spherically symmetric geometry variational form* of the discontinuous Galerkin ion temperature equation (3.105) reads

$$\int_{\Delta t}\int_{\Delta r} \tilde{\mathbf{\Xi}} \otimes \left[\left(a_i\frac{\mathrm{d}\tilde{\mathbf{\Xi}}^T}{\mathrm{d}t} + G_{ie}\tilde{\mathbf{\Xi}}^T\right) \cdot \mathbf{T}_i - P_i - G_{ie}\mathbf{\Xi}^T \cdot \mathbf{T}_e\right] r\mathrm{d}r\mathrm{d}t = 0, \quad (3.107)$$

where Δr is the spatial domain of the element.

The *1D spherically symmetric geometry backward Euler DG-T_i scheme* is defined as

$$\left[\frac{a_i}{\Delta t}\mathbf{M}_r^{T_i} + G_{ie}\mathbf{M}_r^{T_i}\right] \cdot \mathbf{T}_i^1 - G_{ie}\mathbf{M}_r^{T_i,T_e} \cdot \mathbf{T}_e^1 = P_i\mathbf{M}_r^{T_i,0} + \frac{a_i}{\Delta t}\mathbf{M}_r^{T_i} \cdot \mathbf{T}_i^0, \quad (3.108)$$

where the discretization $\mathbf{T}_i$ has been divided into its explicit part $\mathbf{T}_i^0$ and its implicit part $\mathbf{T}_i^1$ according to (3.25, 3.26). The scheme also uses only the implicit part of the unknown $\mathbf{T}_e$, i.e. $\mathbf{T}_e^1$ defined in (3.24).

The reader should refer to Appendix B.1.3 in order to see details about the construction of the scheme above, where the definition of time discretization is defined in its general form.

3.1.3 The 2D Axisymmetric DG-BGK&Ts Scheme

The axisymmetric geometry provides a functional dependence on two spatial coordinates r and z. We choose to work in the xz plane of the Cartesian coordinate system (see Fig. 2.2) in space and in spherical coordinate system of transport directions, where the reference axis is given by the z axis (see Fig. 2.1).

In what follows, we show the strategy of one element partial discretization of the equations of transport (3.7), electron temperature (3.8), and ion temperature (3.9) in subsequent sections. Either I, T_e, and T_i unknown functions are piecewise continuous in space and continuous in time polynomials. The unknown I is continuous in directions.

The last section explains the method of solution on the entire computational domain which is the critical point of computational efficiency.

The 2D Axisymmetric Geometry DG-BGK Transport Scheme

In cylindrical coordinates the position vector is defined as $\mathbf{x} = (r, \tilde{\theta}, z)$, where the coordinate axis vectors change according to the position dependence on $(\tilde{\theta})$, i.e. system is curvilinear. The axisymmetric geometry implies a reduced dependence of the specific intensity $I(t, \mathbf{n}(\phi, \theta), \mathbf{x}(r, z))$, and the resulting form of the *axisymmetric transfer equation* reads

$$\frac{1}{c}\frac{\mathrm{d}I}{\mathrm{d}t} + \sin(\phi)\left(\cos(\theta)\frac{\partial I}{\partial r} - \frac{\sin(\theta)}{r}\frac{\partial I}{\partial \theta}\right) + \cos(\phi)\frac{\partial I}{\partial z} =$$
$$(\sin(\phi)\cos(\theta)S_r + \cos(\phi)S_z + S_A)\,T_e + S_b - (\kappa + \sin(\phi)\cos(\theta)\Upsilon_r + \cos(\phi)\Upsilon_z)\,I + \sigma\bar{I}\,,$$
$$(3.109)$$

which represents a 5D problem, i.e. the solution I of (3.109) depends on t, ϕ, θ and r, z. All the coefficients

$$c, \kappa, \Upsilon_r, \Upsilon_z, \sigma, S_r, S_z, S_A, S_b\,, \qquad (3.110)$$

depend, in general, on time t and position r, z.

The discrete form of the discontinuous Galerkin variation principle (3.10, 3.13) in the case of the 2D axisymmetric geometry uses the discretization of I and T_e (3.19) where the bases $\boldsymbol{\Psi}$ and $\boldsymbol{\Xi}$ of (3.20) are defined on the spatial domain using the coordinate system $\mathbf{x} = \mathbf{x}(r, z)$, in particular, the bases ψ and ξ of (3.18) depend on r and z.

The *discrete 2D axisymmetric geometry variational form* of the discontinuous Galerkin BGK transport equation (3.109) reads

$$\int_{\Delta t}\int_0^{2\pi}\int_0^{\pi}\int_{\Omega_{rz}}\boldsymbol{\Psi}\otimes\left[\left(\frac{1}{c}\frac{\mathrm{d}\boldsymbol{\Psi}^T}{\mathrm{d}t} + \sin(\phi)\left(\cos(\theta)\frac{\partial\boldsymbol{\Psi}^T}{\partial r} - \frac{\sin(\theta)}{r}\frac{\partial\boldsymbol{\Psi}^T}{\partial \theta}\right) + \cos(\phi)\frac{\partial\boldsymbol{\Psi}^T}{\partial z}\right.\right.$$

$$+ (\kappa + \sin(\phi)\cos(\theta)\Upsilon_r + \cos(\phi)\Upsilon_z)\boldsymbol{\Psi}^T - \frac{\sigma}{4\pi}\int\boldsymbol{\Psi}^T\sin(\phi)\mathrm{d}\phi\mathrm{d}\theta\bigg)\cdot\mathbf{I}$$

$$\left.- \left((\sin(\phi)\cos(\theta)S_r + \cos(\phi)S_z + S_A)\,\boldsymbol{\Xi}^T\cdot\mathbf{T}_e + S_b\right)\right]r\mathrm{d}\Omega_{rz}\sin(\phi)\mathrm{d}\phi\mathrm{d}\theta\mathrm{d}t =$$

$$\int_{\Delta t}\int_0^{2\pi}\int_0^{\pi}\int_{\Gamma_{\mathbf{n}\cdot\mathbf{n}_\Gamma<0}}\boldsymbol{\Psi}\otimes\left[\left(\boldsymbol{\Psi}^T\cdot\mathbf{I} - \tilde{\boldsymbol{\Psi}}^T\cdot\tilde{\mathbf{I}}\right)(\sin(\phi)\cos(\theta)n_{\Gamma_r} + \cos(\phi)n_{\Gamma_z})\right]$$

$$\mathrm{d}\Gamma_{rz}\sin(\phi)\mathrm{d}\phi\mathrm{d}\theta\mathrm{d}t\,, \quad (3.111)$$

where Ω_{rz} is a general spatial domain of the element and $\Gamma_{\mathbf{n}\cdot\mathbf{n}_\Gamma < 0}$ means the part of boundary Γ_{rz} (in general curvilinear) where the projection of the transport direction $\mathbf{n}$ into the surface normal $\mathbf{n}_\Gamma$ is less than zero, i.e. $\mathbf{n}\cdot\mathbf{n}_\Gamma = \sin(\phi)\cos(\theta)n_{\Gamma_r} + \cos(\phi)n_{\Gamma_z} < 0$.

Since the procedure of obtaining the discrete scheme representing the solution of transport problem in the spherically symmetric geometry is rather tedious, we show directly the backward Euler solution to (3.109) as a linear function of the unknown $\mathbf{T}_e$ having the following form

$$\mathbf{I}^1 = \mathbf{A}_{rz} \cdot \mathbf{T}_e^1 + \mathbf{b}_{rz}, \tag{3.112}$$

where the linear coefficient $\mathbf{A}_{rz}$ and the constant vector $\mathbf{b}_{rz}$ are defined as

$$\begin{aligned}
\mathbf{A}_{rz} &= \mathbf{L}_{rz}^{-1} \cdot \Big[\mathbf{M}_{\cos(\theta)}^0 \otimes \mathbf{M}_{\sin(\phi)}^0 \otimes S_r \mathbf{M}_{rz}^{I,Te} + \mathbf{M}_\theta^0 \otimes \mathbf{M}_{\cos(\phi)}^0 \otimes S_z \mathbf{M}_{rz}^{I,Te} \\
&\quad + \mathbf{M}_\theta^0 \otimes \mathbf{M}_\phi^0 \otimes S_A \mathbf{M}_{rz}^{I,Te} \Big],
\end{aligned} \tag{3.113}$$

$$\mathbf{b}_{rz} = \mathbf{L}_{rz}^{-1} \cdot \left[\mathbf{M}_\theta^0 \otimes \mathbf{M}_\phi^0 \otimes S_b \mathbf{M}_{rz}^{I,0} - \left(\tilde{\mathbf{\Gamma}}_{rz}^- \cdot \tilde{\mathbf{I}}_1 \right)_\Gamma + \frac{1}{c\Delta t} \mathbf{M}_\theta \otimes \mathbf{M}_\phi \otimes \mathbf{M}_{rz}^I \cdot \mathbf{I}_0 \right], \tag{3.114}$$

which includes the inversion of the element matrix

$$\begin{aligned}
\mathbf{L}_{rz} = \Big[&\mathbf{M}_\theta \otimes \mathbf{M}_\phi \otimes \frac{1}{c\Delta t} \mathbf{M}_{rz}^I + \mathbf{M}_{\cos(\theta)} \otimes \mathbf{M}_{\sin(\phi)} \otimes \mathbf{D}_{rz,r}^I - \mathbf{D}_{\sin(\theta)} \otimes \mathbf{M}_{\sin(\phi)} \otimes \mathbf{M}_{rz/r}^I \\
&+ \mathbf{M}_\theta \otimes \mathbf{M}_{\cos(\phi)} \otimes \mathbf{D}_{rz,z}^I + \mathbf{M}_\theta \otimes \mathbf{M}_\phi \otimes \kappa \mathbf{M}_{rz}^I + \mathbf{M}_{\cos(\theta)} \otimes \mathbf{M}_{\sin(\phi)} \otimes \Upsilon_r \mathbf{M}_{rz}^I + \\
&\mathbf{M}_\theta \otimes \mathbf{M}_{\cos(\phi)} \otimes \Upsilon_z \mathbf{M}_{rz}^I - \left(\mathbf{M}_\theta^0 \otimes 2\mathbf{M}_\theta^{0T} \right) \otimes \left(\mathbf{M}_\phi^0 \otimes \mathbf{M}_\phi^{0T} \right) \otimes \frac{\sigma}{4\pi} \mathbf{M}_{rz}^I - \mathbf{\Gamma}_{rz}^- \Big]. \tag{3.115}
\end{aligned}$$

The reader should refer to Appendix B.2.1 in order to see details about the construction of the scheme above.

It is worth mentioning that the spatial discretization matrices are integrated over Ω_{rz} which can be, in general, a curvilinear 2D domain. This makes the quadrature rule used to evaluate the scheme matrices exceptionally more complex and a special curvilinear mapping must be adopted [101, 102].

The 2D Axisymmetric Geometry DG-$\mathbf{T}_e$ Temperature Scheme

The axisymmetric geometry implies a reduced dependence of the electron temperature $T_e(t, \mathbf{x}(r, z))$, and the resulting form of the *axisymmetric electron temperature equation* reads

$$\begin{aligned}
a_e \frac{\mathrm{d}T_e}{\mathrm{d}t} + \int_0^{2\pi} \int_0^\pi \left(\frac{1}{c}\frac{\mathrm{d}I}{\mathrm{d}t} + \sin(\phi)\left(\cos(\theta)\frac{\partial I}{\partial r} - \frac{\sin(\theta)}{r}\frac{\partial I}{\partial \theta} \right) + \cos(\phi)\frac{\partial I}{\partial z} \right) \sin(\phi)\mathrm{d}\phi\mathrm{d}\theta \\
+ G_{ie}T_e = P_e + G_{ie}T_i, \quad (3.116)
\end{aligned}$$

which represents a 5D problem, i.e. the solution T_e of (3.116) depends on t, r, z and ϕ, θ due to I. All the coefficients

$$c, a_e, G_{ie}, P_e, \tag{3.117}$$

depend, in general, on time t and position r, z.

The discrete form of the discontinuous Galerkin variation principle (3.8) in the case of the 2D axisymmetric geometry uses the discretization of T_e, I, and T_i (3.19) where the bases $\boldsymbol{\Xi}$, $\boldsymbol{\Psi}$, and $\tilde{\boldsymbol{\Xi}}$ of (3.20) are defined on the spatial domain using the coordinate system $\mathbf{x} = \mathbf{x}(r, z)$, in particular, the bases ξ, ψ, and $\tilde{\xi}$ of (3.18) depend on r and z.

The *discrete 2D axisymmetric geometry variational form* of the discontinuous Galerkin electron temperature equation (3.116) reads

$$
\int_{\Delta t} \int_{\Omega_{rz}} \boldsymbol{\Xi} \otimes \left[\left(a_e \frac{\mathrm{d}\boldsymbol{\Xi}^T}{\mathrm{d}t} + G_{ie}\boldsymbol{\Xi}^T \right) \cdot \mathbf{T}_e + \left(\int_0^{2\pi} \int_0^{\pi} \left(\frac{1}{c}\frac{\mathrm{d}\boldsymbol{\Psi}^T}{\mathrm{d}t} + \right. \right. \right.
$$
$$
\sin(\phi) \left(\cos(\theta)\frac{\partial \boldsymbol{\Psi}^T}{\partial r} - \frac{\sin(\theta)}{r}\frac{\partial \boldsymbol{\Psi}^T}{\partial \theta} \right) + \cos(\phi)\frac{\partial \boldsymbol{\Psi}^T}{\partial z} \right) \sin(\phi)\mathrm{d}\phi\mathrm{d}\theta \right) \cdot \mathbf{I}
$$
$$
\left. - P_e - G_{ie}\tilde{\boldsymbol{\Xi}}^T \cdot \mathbf{T}_i \right] r\mathrm{d}\Omega_{rz}\mathrm{d}t = 0\,, \quad (3.118)
$$

where Ω_{rz} is a general spatial domain of the element.

As in the case of the slab geometry, we define the *2D axisymmetric geometry backward Euler DG-T_e scheme*

$$
\left[\frac{a_e}{\Delta t}\mathbf{M}_{rz}^{T_e} + G_{ie}\mathbf{M}_{rz}^{T_e} \right] \cdot \mathbf{T}_e^1 - P_e\mathbf{M}_{rz}^{T_e,0} - G_{ie}\mathbf{M}_{rz}^{T_e,T_i} \cdot \mathbf{T}_i^1 + \left[2\mathbf{M}_\theta^0 \otimes \mathbf{M}_\phi^0 \otimes \frac{1}{c\Delta t}\mathbf{M}_{rz}^{T_e,I} \right.
$$
$$
\left. + 2\mathbf{M}_{\cos(\theta)}^0 \otimes \mathbf{M}_{\sin(\phi)}^0 \otimes \mathbf{D}_{rz,r}^{T_e,I} - 2\mathbf{D}_{\sin(\theta)}^0 \otimes \mathbf{M}_{\sin(\phi)}^0 \otimes \mathbf{M}_{rz/r}^{T_e,I} + 2\mathbf{M}_\theta^0 \otimes \mathbf{M}_{\cos(\phi)}^0 \otimes \mathbf{D}_{rz,z}^{T_e,I} \right]
$$
$$
\cdot \left(\mathbf{A}_{rz} \cdot \mathbf{T}_e^1 + \mathbf{b}_{rz} \right) = \frac{a_e}{\Delta t}\mathbf{M}_{rz}^{T_e} \cdot \mathbf{T}_e^0 + 2\mathbf{M}_\theta^0 \otimes \mathbf{M}_\phi^0 \otimes \frac{1}{c\Delta t}\mathbf{M}_{rz}^{T_e,I} \cdot \mathbf{I}^0\,, \quad (3.119)
$$

where each of the discretizations $\mathbf{T}_e$ and $\mathbf{I}$ have been divided into its explicit part, i.e. $\mathbf{T_e^0}$ and $\mathbf{I^0}$, respectively, and its implicit part, i.e. $\mathbf{T}_e^1$ and $\mathbf{I}^1$ respectively, according to (3.23, 3.24) and (3.21, 3.22), respectively. The scheme also uses only the implicit part of the unknown $\mathbf{T}_i$, i.e. $\mathbf{T}_i^1$ defined in (3.26). The matrix $\mathbf{A}_{rz}$ and the vector $\mathbf{b}_{rz}$ are defined in (3.113) and (3.114).

The reader should refer to Appendix B.2.2 in order to see details about the construction of the scheme above, where the definition of time discretization is defined in its general form.

The 2D Axisymmetric Geometry DG-T_i Temperature Scheme

The axisymmetric geometry implies a reduced dependence of the ion temperature $T_i(t, \mathbf{x}(r, z))$, and the resulting form of the *axisymmetric ion temperature equation* reads

$$
a_i \frac{\mathrm{d}T_i}{\mathrm{d}t} + G_{ie}T_i = P_i + G_{ie}T_e\,, \quad (3.120)
$$

which represents a 3D problem, i.e. the solution T_i of (3.120) depends on t and r, z. All the coefficients

$$
a_i, G_{ie}, P_i\,, \quad (3.121)
$$

depend, in general, on time t and position r, z.

The discrete form of the discontinuous Galerkin variation principle (3.9) in the case of the 2D axisymmetric geometry uses the discretization of T_i, and T_e (3.19) where the bases $\tilde{\Xi}$, and Ξ of (3.20) are defined on the spatial domain using the coordinate system $\mathbf{x} = \mathbf{x}(r, z)$, in particular, the bases $\tilde{\xi}$, and ξ of (3.18) depend on r and z.

The *discrete 2D axisymmetric geometry variational form* of the discontinuous Galerkin ion temperature equation (3.120) reads

$$\int_{\Delta t} \int_{\Omega_{rz}} \tilde{\Xi} \otimes \left[\left(a_i \frac{\mathrm{d}\tilde{\Xi}^T}{\mathrm{d}t} + G_{ie}\tilde{\Xi}^T \right) \cdot \mathbf{T}_i - P_i - G_{ie}\Xi^T \cdot \mathbf{T}_e \right] r \mathrm{d}\Omega_{rz} \mathrm{d}t = 0 \,, \qquad (3.122)$$

where Ω_{rz} is a general spatial domain of the element.

The *2D axisymmetric geometry backward Euler DG-T_i scheme* is defined as

$$\left[\frac{a_i}{\Delta t}\mathbf{M}_{rz}^{T_i} + G_{ie}\mathbf{M}_{rz}^{T_i} \right] \cdot \mathbf{T}_i^1 - G_{ie}\mathbf{M}_{rz}^{T_i, T_e} \cdot \mathbf{T}_e^1 = P_i \mathbf{M}_{rz}^{T_i, 0} + \frac{a_i}{\Delta t}\mathbf{M}_{rz}^{T_i} \cdot \mathbf{T}_i^0 \,, \qquad (3.123)$$

where the discretization $\mathbf{T}_i$ has been divided into its explicit part $\mathbf{T}_i^0$ and its implicit part $\mathbf{T}_i^1$ according to (3.25, 3.26). The scheme also uses only the implicit part of the unknown $\mathbf{T}_e$, i.e. $\mathbf{T}_e^1$ defined in (3.24).

The reader should refer to Appendix B.2.3 in order to see details about the construction of the scheme above, where the definition of time discretization is defined in its general form.

3.1.4 Solver of the DG-BGK&Ts scheme

In the 1D slab geometry, the transport equation (3.3) and its variational form (3.7) can
be solved by the linear function

$$\mathbf{I}^1 = \mathbf{A}_z \cdot \mathbf{T}_e^1 + \mathbf{b}_z(\tilde{\mathbf{I}}_1)\,, \tag{3.124}$$

defined by (3.74), where we use the backward Euler discretization in time. The electron
temperature equation (3.2) and its variational form (3.8) can be solved by the scheme

$$\left[\frac{a_e}{\Delta t}\mathbf{M}_z^{Te} + G_{ie}\mathbf{M}_z^{Te}\right] \cdot \mathbf{T}_e^1 - G_{ie}\mathbf{M}_z^{Te,Ti} \cdot \mathbf{T}_i^1 +$$

$$\left[2\mathbf{M}_\theta^0 \otimes \left(\mathbf{M}_\phi^0 \otimes \frac{1}{c\Delta t}\mathbf{M}_z^{Te,I} + \mathbf{M}_{\cos(\phi)}^0 \otimes \mathbf{D}_{z,z}^{Te,I}\right)\right] \cdot \mathbf{I}^1$$

$$= P_e\mathbf{M}_z^{Te,0} + \frac{a_e}{\Delta t}\mathbf{M}_z^{Te} \cdot \mathbf{T}_e^0 + 2\mathbf{M}_\theta^0 \otimes \mathbf{M}_\phi^0 \otimes \frac{1}{c\Delta t}\mathbf{M}_z^{Te,I} \cdot \mathbf{I}^0\,, \tag{3.125}$$

defined by (3.85), where we have kept the dependence on $\mathbf{I}^1$. The ion temperature
equation (3.1) and its variational form (3.9) can be solved by the scheme defined by
(3.93).

When observed in more detail, the scheme (3.93) solving the ion equation is com-
pletely localized within one element. This means, the solution of ion temperature $\mathbf{T}_i$
can be obtained by a small matrix inversion applied mesh-element-wise. However,
this is not the case of the solution (3.124). More precisely, the intensity $\mathbf{I}^1$ can be eval-
uated in every element of mesh, nevertheless, its solution always depend on $\tilde{\mathbf{I}}_1$, which
are the degree of freedom $\mathbf{I}^1$ of neighboring elements. This makes the scheme to have
a full matrix and its inversion is computationally demanding.

In order to improve the scheme's complexity, we insert the solution (3.124) directly
into the electron temperature equation (3.125). This leads to the elimination of the un-
known $\mathbf{I}^1$ and we get the temperature (electron and ion) scheme (3.85) which with
the ion scheme (3.93) provides a complete discretization of the problem (3.1–3.3).

Nevertheless, we still have the connection between neighboring elements by means
of $\mathbf{b}_z(\tilde{\mathbf{I}}_1)$ of (3.124). The optimal way would be to use (3.124) recursively

$$\mathbf{I}^1 = \mathbf{A}_z \cdot \mathbf{T}_e^1 + \mathbf{b}_z(\tilde{\mathbf{A}}_z \cdot \tilde{\mathbf{T}}_e^1 + \tilde{\mathbf{b}}_z(\tilde{\tilde{\mathbf{I}}}_1)) = \ldots \tag{3.126}$$

where we used the linear function scheme (3.124) of the neighboring degrees of free-
dom $\tilde{\mathbf{I}}_1$, which could be also applied to $\tilde{\tilde{\mathbf{I}}}_1$ and so on. This recursive approach would
eventually finished with a full matrix scheme for the temperatures unknowns. We
choose to avoid this recursive construction and we used an iterative approach, where
the DG-BGK&Ts scheme represented by the electron temperature part (3.85) and the ion
temperature part (3.93) is evaluated with explicit values of $\tilde{\mathbf{I}}_1$. These values are updated
after every iteration with the scheme (3.124). The loop runs until the temperature un-
knowns converge. This approach results to be very effective in the case of laser-heated
plasma simulations, where the number of iterations was usually kept under ten.

In the 1D spherically symmetric geometry, the transport equation (3.3) and its vari-
ational form (3.7) can be solved by the scheme (3.97). The electron temperature equa-
tion (3.2) and its variational form (3.8) can be solved by the scheme (3.104) and the ion
temperature equation (3.1) and its variational form (3.9) can be solved by the scheme

defined by (3.108). The same definition is done in the 2D axisymmetric geometry. The transport equation (3.3) and its variational form (3.7) can be solved by the scheme (3.112). The electron temperature equation (3.2) and its variational form (3.8) can be solved by the scheme (3.119) and the ion temperature equation (3.1) and its variational form (3.9) can be solved by the scheme defined by (3.123). In every geometry, we use the same strategy of iterative approach as in the 1D slab geometry case.

3.2   The Hydrodynamics and DG-BGK&Ts Scheme Coupling

So far, we have been treating the construction of the DG-BGK&Ts scheme in the numeric part of this work. Nevertheless, a big portion of section 2 is dedicated to the hydrodynamic model, which, as desired, contains nonlocal transport of energy. In order to make our DG-BGK&Ts scheme a self consistent unit within the laser-heated plasma simulation, we show a strategy of how the scheme will be coupled to any external Lagrangian hydro code. In principal, the only necessary quantities needed from the hydro code output are the increment of specific internal energy $\Delta\varepsilon$ and the average fluid velocity $\mathbf{u}$ related to the fluid time evolution over the interval Δt (in the case of explicit hydrodynamic scheme given by the Courant-Friedrichs-Lewy condition [103]).

Let us introduce the simplest hydrodynamic model represented by Euler equations of conservation of mass, momentum, and specific internal energy having the form

$$\frac{\mathrm{d}\rho}{\mathrm{d}t} = -\rho\nabla\cdot\mathbf{u}, \tag{3.127}$$

$$\rho\frac{\mathrm{d}\mathbf{u}}{\mathrm{d}t} = -\nabla(p+q) + \mathbf{g}, \tag{3.128}$$

$$\rho\frac{\mathrm{d}\varepsilon}{\mathrm{d}t} = -(p+q)\nabla\cdot\mathbf{u} - \mathbf{u}\cdot\mathbf{g} + Q_{\mathrm{IB}}, \tag{3.129}$$

where additional terms $\mathbf{g}$ and Q_{IB} related to external force (source of momentum due to collisions with transported particles) and external source of energy (deposited laser energy), respectively, were applied to accommodate the model (3.127, 3.128, 3.129) to laser-heated plasma simulations. One more extra term appeared aside the thermodynamic force represented by the artificial viscosity q, thus imposing an additional artificial force leading to numeric stability in simulation of the shock-wave phenomenon [104, 105]. The hydrodynamic model (3.127, 3.128, 3.129) can be solved by well tested numerical schemes, either staggered grid [106, 101, 107, 108, 109, 110, 111] or cell centered [112] methods. Our DG-BGK&Ts scheme then requires the following quantities

$$\frac{\mathrm{d}\bar{\varepsilon}}{\mathrm{d}t} = \frac{\Delta\varepsilon}{\Delta t}, \quad \bar{\mathbf{u}} = \frac{\int_{\Delta t}\mathbf{u}\mathrm{d}t}{\Delta t}, \tag{3.130}$$

which are provided by the hydrodynamic numerical schemes mentioned above.

Since this work aims to use the two temperature single fluid hydrodynamic model, the specific internal energy, pressure, and viscosity of (3.128, 3.129) comprise the ion and electron components, i.e. $\varepsilon = \varepsilon_i + \varepsilon_e$, $p = p_i + p_e$, and $q = q_i + q_e$. Very important quantities are the individual thermodynamic power given by either electrons or ions. These can be extracted from (3.129) as

$$(p_i+q_i)\nabla\cdot\mathbf{u} = -\frac{p_i+q_i}{p+q}\left(\rho\frac{\mathrm{d}\bar{\varepsilon}}{\mathrm{d}t} + \bar{\mathbf{u}}\cdot\mathbf{g} - Q_{\mathrm{IB}}\right), \tag{3.131}$$

$$(p_e+q_e)\nabla\cdot\mathbf{u} = -\frac{p_e+q_e}{p+q}\left(\rho\frac{\mathrm{d}\bar{\varepsilon}}{\mathrm{d}t} + \bar{\mathbf{u}}\cdot\mathbf{g} - Q_{\mathrm{IB}}\right), \tag{3.132}$$

where the mean values of (3.130) were used. Details about the two temperature single fluid model can be found in section 2.2.5.

If one compares the ion and electron energy equations (3.1, 3.2) defined in the introduction of section 3.1 with corresponding nonlocal transport hydrodynamic equations (2.222, 2.223) defined in section 2.6, the yet unknown explicit terms of the DG-BGK&Ts

scheme can be determined, i.e. the ion and electron heat capacities enter the scheme as

$$a_i = \rho \frac{\partial \varepsilon_i}{\partial T_i}, \tag{3.133}$$

$$a_e = \rho \frac{\partial \varepsilon_e}{\partial T_e}, \tag{3.134}$$

and a little bit more elaborated quantities representing the source of heat of ions and electrons result to be

$$P_i = \frac{p_i + q_i}{p + q} \left(\rho \frac{\mathrm{d}\bar{\varepsilon}}{\mathrm{d}t} + \bar{\mathbf{u}} \cdot (\mathbf{g}_R + \mathbf{g}_H) - Q_{\mathrm{IB}} \right) - \rho \frac{\partial \varepsilon_i}{\partial \rho} \frac{\mathrm{d}\rho}{\mathrm{d}t}, \tag{3.135}$$

$$P_e = \frac{p_e + q_e}{p + q} \left(\rho \frac{\mathrm{d}\bar{\varepsilon}}{\mathrm{d}t} + \bar{\mathbf{u}} \cdot (\mathbf{g}_R + \mathbf{g}_H) - Q_{\mathrm{IB}} \right) - \rho \frac{\partial \varepsilon_e}{\partial \rho} \frac{\mathrm{d}\rho}{\mathrm{d}t} - \mathbf{u} \cdot (\mathbf{g}_R + \mathbf{g}_H) + Q_{\mathrm{IB}}, \tag{3.136}$$

where the momentum sources $\mathbf{g}_R$ and $\mathbf{g}_H$ due to collisions of the transported photons and electrons with the bulk plasma fluid are taken as explicit numbers.

The Application of the DG-BGK&Ts scheme to Nonlocal Transport Hydrodynamics

In section 2.6 we defined a complete hydrodynamic model to be used to simulate the laser-heated plasma problem. Assuming that the hydrodynamic part has provided us with necessary quantities $\frac{\mathrm{d}\bar{\varepsilon}}{\mathrm{d}t}$ and $\bar{\mathbf{u}}$ of (3.130), we can focus directly on the nonlocal transport model represented by the energy (2.222, 2.223) and transport (2.234, 2.235) equations.

The appropriate nonlocal transport model to which the DG-BGK&Ts scheme discretization is applied then reads

$$a_i \frac{\mathrm{d}T_i}{\mathrm{d}t} + G_{ie}(T_i - T_e) = P_i, \tag{3.137}$$

$$a_e \frac{\mathrm{d}T_e}{\mathrm{d}t} + G_{ie}(T_e - T_i) = P_e - \int_{4\pi} \left(\frac{1}{c} \frac{\mathrm{d}I_p}{\mathrm{d}t} + \mathbf{n} \cdot \nabla I_p + \mathbf{n} \cdot \nabla I_e \right) \mathrm{d}\omega, \tag{3.138}$$

$$\frac{1}{c} \frac{\mathrm{d}I_p}{\mathrm{d}t} + \mathbf{n} \cdot \nabla I_p = S_A^p T_e + S_b^p - \left(\bar{k}_p + \bar{\sigma}_p \right) I_p + \bar{\sigma}_p \bar{I}_p, \tag{3.139}$$

$$\mathbf{n} \cdot \nabla I_e = S_A^e T_e + S_b^e - \left(\tilde{k}_e + \tilde{\sigma}_e + \mathbf{n} \cdot \mathbf{\Upsilon}_e \right) I_e + \tilde{\sigma}_e \bar{I}_e, \tag{3.140}$$

where a_i, a_e, P_i, and P_e were defined in (3.133–3.136), the extinction and the scattering coefficients of photons $\bar{k}_p$ and $\bar{\sigma}_p$ were defined in section 2.6.1, and the extinction and the scattering coefficient of electrons $\tilde{k}_e$ and $\tilde{\sigma}_e$ were defined in section 2.6.2.

Apparently, the nonlocal radiation and electron transport equations (3.139, 3.140) represent a specific form of the BGK transport equation defined in section 3.1, where the photon source function based on (2.234) has the form

$$S_A^p = 4\bar{k}_p a \left(T_e^0 \right)^3, \tag{3.141}$$

$$S_b^P = -3\bar{k}_p a \left(T_e^0 \right)^4, \tag{3.142}$$

and the electron source function based on (2.235), or more precisely, obtained from (2.240, 2.237) has the following form

$$S_A^e = \frac{3 n_i k_B}{8\pi} \frac{\mathrm{d}\bar{Z}}{\mathrm{d}t} + \tilde{k}_e \left(\frac{3}{2} \frac{n_e}{\pi^{\frac{3}{2}}} \frac{\sqrt{2} k_B^{\frac{3}{2}}}{\sqrt{m_e}} \right) (T_e^0)^{\frac{1}{2}} , \qquad (3.143)$$

$$S_b^e = -\tilde{k}_e \left(\frac{1}{2} \frac{n_e}{\pi^{\frac{3}{2}}} \frac{\sqrt{2} k_B^{\frac{3}{2}}}{\sqrt{m_e}} \right) (T_e^0)^{\frac{3}{2}} , \qquad (3.144)$$

where $\frac{\mathrm{d}\bar{Z}}{\mathrm{d}t}$ is the ionization change rate provided by the equation of state. The very last term results from (2.241) and reads

$$\boldsymbol{\Upsilon} = \frac{q\mathbf{E}}{k_B T_e^0} , \qquad (3.145)$$

where the electric field intensity $\mathbf{E}$ must be provided, e.g. as proposed in section 2.6.3.

The value T_e^0 refers to a reference temperature of Taylor series expansion used to obtain the linear form of the radiation and electron sources (3.141, 3.142) and (3.143, 3.144).

The application of the DG-BGK&Ts scheme resides in application of the transport scheme (3.74) to the photon and electron transport equations (3.139) and (3.140) as

$$\mathbf{I}_p^1 = \mathbf{A}_z^p \cdot \mathbf{T}_e^1 + \mathbf{b}_z^p(\tilde{\mathbf{I}}_1) \qquad (3.146)$$

$$\mathbf{I}_e^1 = \mathbf{A}_z^e \cdot \mathbf{T}_e^1 + \mathbf{b}_z^e(\tilde{\mathbf{I}}_1) , \qquad (3.147)$$

where the coefficients $\mathbf{A}_z^p, \mathbf{b}_z^p, \mathbf{A}_z^e, \mathbf{b}_z^e$ are finally used in the electron temperature scheme (3.85), where both intensities (3.147) and (3.147) are used according to (3.138). These solutions correspond to the 1D slab geometry. In the case of 1D spherically symmetric and 2D axisymmetric geometries the transport schemes (3.97) and (3.112) and the electron temperature schemes (3.104) and (3.119) should be used.

The implementation of the latter strategy to solve equations (3.137–3.140) has been developed and further presented at several conferences [113, 114, 115, 116, 117, 118].

3.3   Numerical Tests

A numerical scheme itself is a theoretical concept which aims to be applied to some computations. In order to prepare the DG-BGK&T method to be used in practice, we coded the appropriate parts of the scheme and benchmarked its capabilities on several test cases against the appropriate analytical solutions. In the following text we are using the notation used in [101, 107], the original work using the MFEM finite element library [102] for Lagrangian hydrodynamics. When using Qn, we refer to the n*th* order polynomial basis of finite element used for discretization of the intensity I, the unknown of the DG-BGK transport scheme; when using QnQm we refer to the n*th* order finite element basis of intensity and m*th* order finite element basis used for discretization of the temperature T. For example we use Q3Q2, which means a bi-cubic polynomial basis of intensity and bi-quadratic polynomial basis of temperature. The notation I[Qn] and T[QnQm] then stand for the numerical solution of intensity and temperature using the appropriate discretization.

The first test focuses on the transport scheme only, where the temperature dependent source function is supposed to be static, i.e. does not change in time. This brings the advantage that we can find an analytical solution. Furthermore, we can find solutions of any mode of transport, i.e. free-streaming, non-local or diffusive. The idea of the second test case is to demonstrate the asymptotic behavior when approaching the diffusive transport limit. According to our knowledge, it is not common for transport numerical schemes to approximate diffusion in an appropriate way. In other words, we want to stress the importance of the higher order scheme for both intensity and temperature because with the low-order scheme the diffusive heat conduction limit is not recovered.

3.3.1   The Exact Steady Transport Test of DG-BGK Transport Scheme

The slab geometry implies that the source function and the boundary condition depend only on one coordinate; in our case, on z coordinate. We define $\mu = \cos(\phi)$ where ϕ is the spherical polar angle, i.e. the angle between the intensity direction **n** and z-axis. We apply the zero boundary condition, i.e. $I(z_0, \mu) = 0$ and the steady state is represented by $\frac{\partial I}{\partial t} = 0$. Consequently, we obtain a simplified form of (3.3), an ordinary differential equation [100]

$$\mu \frac{\mathrm{d}I(z,\mu)}{\mathrm{d}z} = k\left(f(z) - I(z,\mu)\right), \tag{3.148}$$

where the constant $k = \lambda^{-1}$ is the inverse of the particle mean free path, also called absorptivity, and $f(z)$ is an explicit source function. We can find a formal solution of (3.148) as [6]

$$I(z,\mu,z_0) = \int_{z_0}^{z} f(\tilde{z}) \exp\left(\frac{k}{\mu}(\tilde{z} - z)\right) \frac{k}{\mu} \,\mathrm{d}\tilde{z}. \tag{3.149}$$

In our particular case, we use the source function
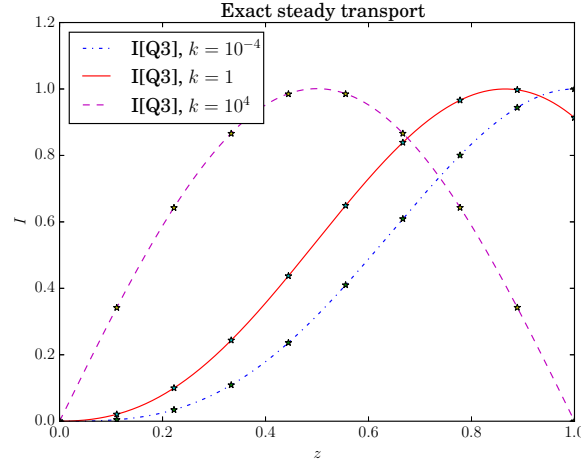
$$f(z) = \sin(\pi z), \tag{3.150}$$

FIGURE 3.1: Numerical steady state solution to (3.148) calculated using quadrilateral element Q3. Photons are generated by the static source function $\sin(\pi z)$ and travel in the direction from left to right. We show three different values of $k = 10^{-4}, 1, 10^4$, which correspond to free-streaming, nonlocal and diffusive transport, respectively. The normalized exact solution is represented with lines and corresponding numerical approximation with stars. The maximum value of I in case of $k = 10^{-4}, 1, 10^4$ are $I_{max} = 7.2 \cdot 10^{-9}, 0.51, 1$, respectively. The maximum value reflects the weakness of source function due to small k. Table 3.1 shows quantitative errors and convergence order of our method.

defined on the interval $z \in (0, 1)$. The corresponding solution of (3.149) reads

$$I(z, \mu, z_0) = \exp\left(\frac{k(z_0 - z)}{\mu}\right) \left(\frac{k\pi\mu\cos(\pi z_0)}{\mu^2\pi^2 + k^2} - \frac{k^2\sin(\pi z_0)}{\mu^2\pi^2 + k^2}\right) +$$
$$\frac{k^2}{\mu^2\pi^2 + k^2}\left(\sin(\pi z) - \frac{\mu\pi}{k}\cos(\pi z)\right) . \quad (3.151)$$

In order to find a numerical solution of (3.148) with $\mu = \cos(\pi/4)$, we used the DG-BGK scheme (3.70).

The scheme has been iterated until the steady solution was obtained. The iteration was stopped when the relative change of the L1 norm of I was less than 10^{-15}. Fig. 3.1 shows numerical results of the steady state solution of (3.148) calculated using quadrilateral elements Q1 and Q3. Photons are generated by the static source function $1 - \cos(z)$ and travel in the direction from left to right. Table 3.1 shows quantitative errors and convergence order of our method.

The intensity I is generated by the source function $\sin(\pi z)$, and photons travel in the direction from left to right. We show three different values of $k = 10^{-4}, 1, 10^4$. One can observe that in the diffusive case the intensity aligns with the source function $\sin(\pi z)$, which is in agreement with (3.151) evaluated for $k = 10^4$. Table 3.1 shows errors and convergence order of our method. We used the $L1$ norm errors of computed intensity compared to the analytic solution (3.151) with $\mu = \cos(\pi/4)$.

The test shows that our method is high-order accurate for values $k \in (10^{-4}, 10^4)$. This is equivalent to the range of Knudsen number $K_n = \lambda/L \in (10^4, 10^{-4})$ since

element	cells	$E_{L1}^{k=10^{-4}}$	$q_{L1}^{k=10^{-4}}$	$E_{L1}^{k=1}$	$q_{L1}^{k=1}$	$E_{L1}^{k=10^4}$	$q_{L1}^{k=10^4}$
I[Q1]	10	2.7e-07		2.3e-03	0.0	8.3e-03	
I[Q1]	20	4.9e-08	2.5	4.3e-04	2.4	1.6e-03	2.4
I[Q1]	40	1.2e-08	2.0	1.1e-04	2.0	3.7e-04	2.1
I[Q1]	80	2.9e-09	2.0	2.6e-05	2.0	9.0e-05	2.1
I[Q2]	10	4.6e-09		4.1e-05	0.0	3.5e-07	
I[Q2]	20	4.1e-10	3.5	3.5e-06	3.5	5.2e-08	2.8
I[Q2]	40	4.5e-11	3.2	4.0e-07	3.2	1.2e-08	2.1
I[Q2]	80	5.4e-12	3.1	4.7e-08	3.1	2.8e-09	2.1
I[Q3]	10	7.3e-11		2.6e-07	0.0	2.3e-06	
I[Q3]	20	2.8e-12	4.7	8.4e-09	5.0	1.0e-07	4.5
I[Q3]	40	1.5e-13	4.2	4.3e-10	4.3	5.6e-09	4.2
I[Q3]	80	8.9e-15	4.1	2.4e-11	4.1	3.3e-10	4.1

TABLE 3.1: Steady state test errors and convergence order. Our method proves to be high-order accurate for values $k \in (10^{-4}, 10^4)$ covering transparent, non-local and diffusive transport regimes in plasma.

the characteristic length of the system is $L = 1$, i.e. half period of the source function $\sin(\pi z)$. The range of Knudsen number is large enough to cover conditions of any specific transport, i.e. the transparent-like free streaming in the case of $k = 10^{-4}$, the typically nonlocal transport represented by $k = 1$, and the diffusion-like regime corresponding to $k = 10^4$.

We are particularly interested in the diffusive condition when $k \gg 1$. In that case, the first term of (3.151) behaves as $\exp(-z/\mu k)$ and is immediately damped. The second term tends to $\sin(\pi z) - \frac{\mu \pi}{k} \cos(\pi z)$ which is nothing else than the asymptotic formula $I \approx f - \mu/k \frac{df}{dz}$ corresponding to the diffusion of the BGK operator described in [6]. In order to discuss the numerical results, we consider $k = 10^4$. The anisotropic part of (3.151), i.e. the term provoking energy transport, gives approximately

$$-\frac{k^2}{\mu^2 \pi^2 + k^2} \frac{\mu \pi}{k} \cos(\pi z) \approx 1\text{e-}4 \,, \tag{3.152}$$

for $k = 10^4, \mu = \cos(\pi/4)$. We can conclude that in the case of the diffusive regime, the second-order element Q1 is not efficient because it gives an error 9.0e-5 on 80 cells spatial resolution, which is of the same order as the diffusive term (3.152); meanwhile, the error 2.3e-6 on 10 cells spatial resolution obtained by the fourth-order element Q3 is in order of percents of (3.152), i.e. it satisfies the diffusion regime even on such a rough spatial resolution.

3.3.2 The Multi-Group Diffusion Test of DG-BGK&Ts Scheme

The previous numerical test demonstrated that the transport scheme is high-order accurate for any value of extinction coefficient k, i.e. it is also consistent with the diffusive asymptotic of the BGK equation (3.3). This is an extremely important property. The accuracy is not a question of the transport scheme only, it is also crucial that the temperature scheme demonstrates accuracy in the case of diffusion.

One can define a simple model of energy transport. The temperature dependent source $k\sigma T$, where k^{-1} is the particle mean free path and σ a material constant, generates energetic particles, e.g. photons. These are transported with velocity c and reabsorbed within the travel distance of k^{-1}, thus producing a temperature profile evolution due to the energy transport. We also want to represent two groups of energetic particles with different mean free paths $k_{g_1}^{-1}, k_{g_2}^{-1}$, where g_j represents an energetic group.

The model equations based on (3.3, 3.2) are

$$\frac{1}{c}\frac{\partial I_{g_j}}{\partial t} + \mathbf{n}\cdot\nabla I_{g_j} = k_{g_j}\left(\sigma T - I_{g_j}\right), \qquad (3.153)$$

$$C_v\frac{\partial T}{\partial t} + \sum_{j=1,2}\int_{4\pi}\left(\frac{1}{c}\frac{\partial I_{g_j}}{\partial t} + \mathbf{n}\cdot\nabla I_{g_j}\right)\mathbf{dn}\Delta_{g_j} = 0, \qquad (3.154)$$

where the two-group intensity (I_{g_1}, I_{g_2}) represent the transported particles, c is speed of light, C_v is the heat capacity, and Δ_g is an energetic group weight.

It is not easy to find an analytic solution to such a self-consistent system. The solution can be found in the case of two asymptotic behaviors $k \to 0$ and $k \to \infty$. The solution to the first asymptotic is trivial since there are no particles generated and, consequently, the energy flux is zero. In order to find the solution to the second asymptotic, one way is to apply the Hilbert expansion in a small parameter k^{-1} [46]. This leads to the local approximation of (3.153) as

$$I_{g_j} = \sigma T - \frac{\sigma}{k_{g_j}}\mathbf{n}\cdot\nabla T + O(k_{g_j}^{-2}) \approx \sigma T - \frac{\sigma}{k_{g_j}}\mathbf{n}\cdot\nabla T, \qquad (3.155)$$

where we have kept the terms to the first order only. When we use (3.155) in (3.154), the following model equation arises

$$\left(C_v + \frac{4\pi}{c}(\Delta_{g_1} + \Delta_{g_2})\sigma\right)\frac{\partial T}{\partial t} \approx \frac{4\pi}{3}(\Delta_{g_1}k_{g_1}^{-1} + \Delta_{g_2}k_{g_2}^{-1})\sigma\frac{\partial^2 T}{\partial z^2}, \qquad (3.156)$$

where we imposed the condition $\nabla \cdot \nabla T = \frac{\partial^2 T}{\partial z^2}$, i.e. that T depends only on z (due to slab geometry), and k_{g_1}, k_{g_2}, and σ are constant. Equation (3.156) is the usual local formulation of transport, the heat equation.

In [5] the following analytic solution to the linear heat equation (3.156) is presented

$$T(z,t) = \frac{Q}{\sqrt{4\pi\kappa t}}\exp\left(-\frac{z^2}{4\kappa t}\right), \qquad (3.157)$$

where Q is the amount of energy in the system and

$$\kappa = \frac{\frac{4\pi}{3}(\Delta_{g_1}k_{g_1}^{-1} + \Delta_{g_2}k_{g_2}^{-1})\sigma}{C_v + \frac{4\pi}{c}(\Delta_{g_1} + \Delta_{g_2})\sigma}, \qquad (3.158)$$

is the heat conductivity.

We expect the transport DG-BGK scheme (3.70) approximates accurately (3.155), i.e. the diffusive asymptotic, if $k_{g_1} \approx k_{g_2} \gg 1$. If so, we expect the scheme (3.85) to bring the numerical solution converging to the solution of (3.156), i.e. the solution (3.157). In
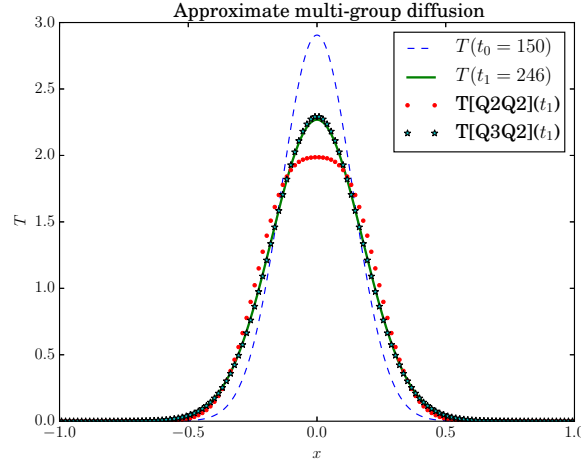
FIGURE 3.2: The multi-group diffusion test results.

order to test this property, we choose the following simulation parameters

$$C_v = \sigma = 2.4 \cdot 10^{11}, c = 3 \cdot 10^{10}, Q = 1, \tag{3.159}$$

and we let the computational domain span the interval $x \in (-1, 1)$. Since we are focused on the multi-group diffusion, we put the following values

$$k_{g_1} = 10^5, k_{g_2} = 1.25 \cdot 10^4, \Delta_{g_1} = 0.5, \Delta_{g_2} = 0.125, \tag{3.160}$$

where the group absorptivity k_{g_1} and k_{g_2} meet the diffusive value of the Knudsen number $K_n = \frac{1}{k_{g_j}L} \approx 10^{-5}$, and where $L = 2$ is the computational domain length. It is also worth noting that both groups are of the same importance in the diffusion conductivity (3.158), since $\Delta_{g_1} k_{g_1}^{-1} = \Delta_{g_2} k_{g_2}^{-1}$.

cells	32	64	128	256	512
T[Q1Q1]	2.2e-01 [5]	2.4e-01 (-0.1)	2.3e-01 (0.0)	2.3e-01 (0.0)	2.3e-01 (0.0)
T[Q2Q2]	8.7e-02 [4]	9.5e-02 (-0.1)	9.8e-02 (-0.0)	9.6e-02 (0.0)	9.1e-02 (0.1)
T[Q3Q2]	1.2e-01 [4]	5.7e-02 (1.1)	1.0e-02 (2.5)	1.3e-03 (2.9)	–
T[Q3Q3]	7.6e-02 [4]	4.6e-02 (0.7)	9.8e-03 (2.2)	1.3e-03 (2.9)	–
T[Q4Q4]	2.9e-02 [4]	9.6e-03 (1.6)	1.3e-03 (2.9)	–	–
T[Q5Q5]	2.3e-03 [4]	8.2e-05 (4.8)	–	–	–
T[Q6Q6]	1.7e-04 [4]	–	–	–	–

TABLE 3.2: The relative L_1-error calculated at $t_1 = 246$ of discretizations QnQm to the solution (3.157) are shown. In the first column we also present number of iterations $[\gamma]$ of the DG-BGK&Ts scheme to converge, and in other columns we show the rate of convergence (q) of the scheme. We can see that the solutions T[Q1Q1] and T[Q2Q2] do not converge. Any higher order approximation does.

The computation starts from the analytical solution (3.157) at time $t_0 = 150$ and evolves till the final time $t_1 = 246$. In Fig. 3.2 we present the exact solution (3.157) to the linear heat wave equation (3.154) in the initial time $t_0 = 150$ (blue dashed line) and

in the final time $t_1 = 246$ (green continuous line). Numerical solutions T[Q2Q2] and T[Q3Q2] are figured using red dots and green stars, respectively. It can be seen that the discretization Q3Q2 performs much better than the discretization Q2Q2, which is also demonstrated in Table 3.2 and Table 3.3. . Table 3.2 and Table 3.3 show results of

cells	32	64	128	256	512
T[Q1Q1]	5.6e-01 [5]	6.1e-01 (-0.1)	6.3e-01 (-0.0)	6.2e-01 (0.0)	6.1e-01 (0.0)
T[Q2Q2]	2.2e-01 [4]	2.7e-01 (-0.3)	2.8e-01 (-0.1)	2.8e-01 (0.0)	2.6e-01 (0.1)
T[Q3Q2]	2.7e-01 [4]	1.4e-01 (1.0)	2.5e-02 (2.5)	3.2e-03 (3.0)	–
T[Q3Q3]	1.9e-01 [4]	1.3e-01 (0.6)	2.8e-02 (2.2)	3.9e-03 (2.9)	–
T[Q4Q4]	7.5e-02 [4]	2.6e-02 (1.6)	3.6e-03 (2.8)	–	–
T[Q5Q5]	5.5e-03 [4]	2.3e-04 (4.6)	–	–	–
T[Q6Q6]	4.1e-04 [4]	–	–	–	–

TABLE 3.3: The absolute L_0-error calculated at $t_1 = 246$ of discretizations QnQm to the solution (3.157) are shown. In the first column we also present number of iterations $[\gamma]$ of the DG-BGK&Ts scheme to converge, and in other columns we show the rate of convergence (q) of the scheme. We can see that the solutions T[Q1Q1] and T[Q2Q2] do not converge. Any higher order approximation does.

several high order approximations. Our analysis has shown that the scheme based on Q1Q1 discretization does not approximate the solution (3.157). Actually, the solution T[Q1Q1] stays static aligned to the initial solution. This shows that higher order approximation is necessary in order to model diffusive-like transport. In case of higher order schemes, the decreasing error was appropriately reflected by the order of approximation used; except for Q2Q2, which approximates the physical principle of diffusion but does not converge when discretization is refined. This drawback was cured when we improved the discretization order of I, i.e. we used the discretization Q3Q2, which performs better then Q2Q2. It is also worth noting that we have encountered an interesting behavior of the scheme, which is that the combinations Q(n+1)Qn seem to be more stable in simulations. A similar behavior was observed in [95, 96], which will serve as a basis for our future analysis.

The evolution of the solution (3.157) from the time $t_0 = 150$ to the time $t_1 = 246$ can be found in Fig. 3.2. The numerical solution of the approximation Q3Q2 clearly outperforms the approximation Q2Q2 and provides a reasonable accuracy for 128 cells discretization.

One should be aware that our DG-BGK&Ts scheme does not use any kind of diffusion operator, i.e. it uses the model equations (3.153, 3.154). Still, the relative errors in Table 3.2 and in Table 3.3 prove the scheme is precisely accurate in the diffusive regime.

The Multi-Group Laser Absorption Test of DG-BGK&Ts Scheme

The numerical results of the multi-group diffusion test presented in the previous section were obtained by solving the transport model (3.153, 3.154). It is worth mentioning that these equations solve a complete nonlocal transport coupled problem with two different groups of photons and electron temperature.

In order to show an extended application, we redefine equation (3.154) to include a source of energy deposited by a laser as the following

$$C_v \frac{\partial T}{\partial t} + \sum_{j=1,2} \int_{4\pi} \left(\frac{1}{c} \frac{\partial I_{g_j}}{\partial t} + \mathbf{n} \cdot \nabla I_{g_j} \right) \mathrm{d}\mathbf{n} \Delta_{g_j} = Q_L , \qquad (3.161)$$

where Q_L is a constant source of energy and g_1 and g_2 correspond to two groups of photons, which possess different extinction coefficients $k_1 = 1\mathrm{e}{-4}$ and $k_2 = 1\mathrm{e}4$. The spatial distribution of laser source pattern can be seen in Fig. 3.3. Apparently, we present a 2D simulation in the Cartesian coordinate system, where the transport of two group of photons leads to nonlocal transport of energy deposited by the laser.
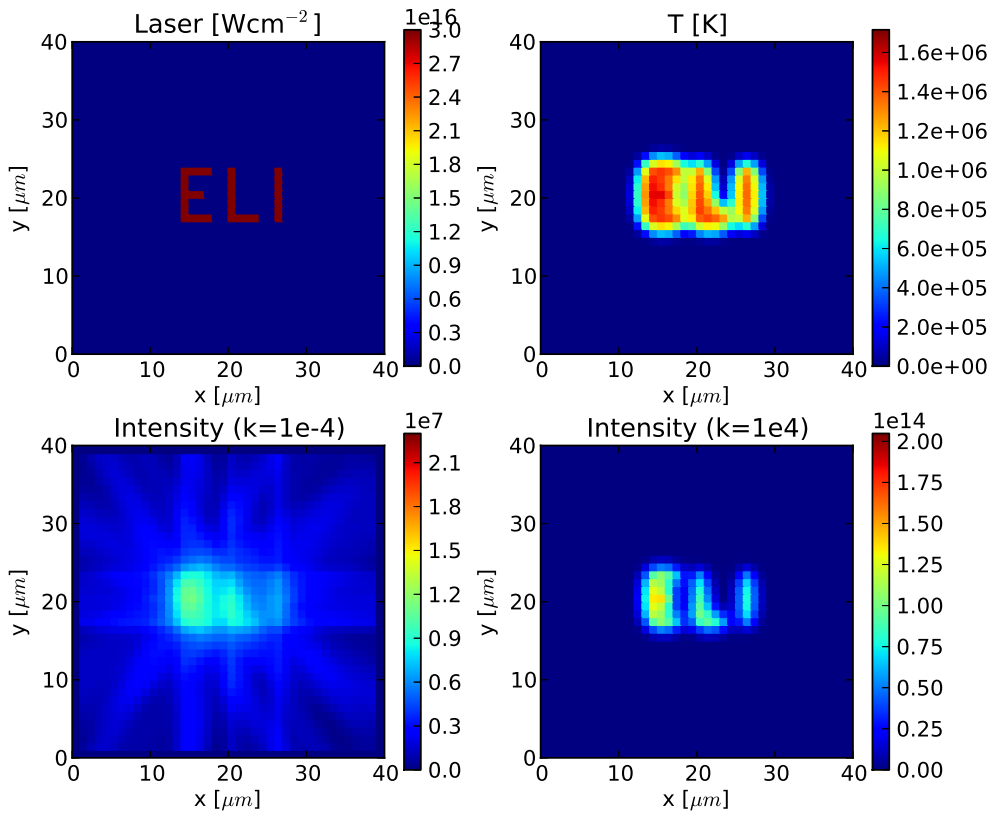
FIGURE 3.3: Simulation results in time 300 ps after the laser source was turned on.

The results of simulation are shown in Fig. 3.3. The top-left figure shows the absorption of laser energy in a sharp-shaped word ELI (Extreme Light Infrastructure [119]). The top-right figure shows how the energy spreads in time. The bottom-left and bottom-right figures show the distribution of intensity of long-path-transport and short-path-transport (diffusive) photons described by the extinction coefficient $k = 1\mathrm{e}{-4}$ and $k = 1\mathrm{e}4$, respectively. Obviously, this simulation cannot be compared to an analytical solution, however, it shows the capability of solving a complicated spatial geometry of the source of energy in 2D.

Chapter 4

Simulations of Laser-Heated Plasmas

As a part of this work we developed a nonlocal transport hydrodynamic code Plasma Euler and Transport Equation (PETE), which was used as the simulation tool. PETE is based on our nonlocal transport hydrodynamic model presented in section 2.6, where the Euler equations are solved by using the staggered grid scheme [106] and the non-local transport equations for electrons and radiation are solved by our proposed high-order finite element DG-BGK&Ts scheme presented in section 3.1. The necessary equation of state closure was provided by the SESAME tables [78, 79, 80] further complemented by opacities given as in [81].

The actual implementation of PETE consists of one dimensional hydrodynamic solver coupled to the slab geometry DG-BGK&Ts scheme, which discretizes one dimension in space and one dimension in transport directions. Even though the latter geometry is rather simple, we used a higher order angular (ϕ) discretization Q3 in order to address the transport anisotropy, and a higher order spatial (z) discretization Q3Q2 in order to capture appropriately the diffusive regime of the energy transport. In the case of time discretization we used the simplest backward Euler scheme, which provides the most stable calculations.

4.1   L4 Beamline Prepulse

The project Extreme Light Infrastructure (ELI) [119] is a part of the European plan to build a new generation of large research facilities selected by the European Strategy Forum for Research Infrastructures (ESFRI). The main goal of ELI is to create the latest laser equipment in the world. Research projects aiming to investigate the interaction of light with matter at intensities being 10 times higher than those currently achievable in the facilities around the world have started the first phase.

The facility will make available high-brightness multi-TW ultrashort laser pulses at kHz repetition rate, PW 10 Hz repetition rate pulses, and kilojoule nanosecond pulses for generation of 10 PW peak power. The most powerful laser referred as 10 PW was named Krakatit and, in general, is labeled L4. It is based on the solid-state Nd:glass laser technology using the chirped pulse amplification (CPA) [121], where the stretched and subsequently amplified pulse undergoes a final step compression in time as shown in Fig. 4.1. The use of mixed Nd:glass CPA laser providing spectral bandwidth allows for effective pulse compression [122], and thus, the peak power of 10 PW. A schematic depiction of the L4 beamline can be seen in Fig. 4.2, where the principal laser pulse can reach the energy of 1.5 kJ, which should be compressed into the interval of less than 150 fs. In principle, the laser pulse will deliver a power $P = \frac{E}{\Delta t} = \frac{1500 \text{J}}{150 \times 10^{-15} \text{s}} = 10$ PW. An auxiliary 150 J pulse can be used to accompany the main pulse. Both pulses
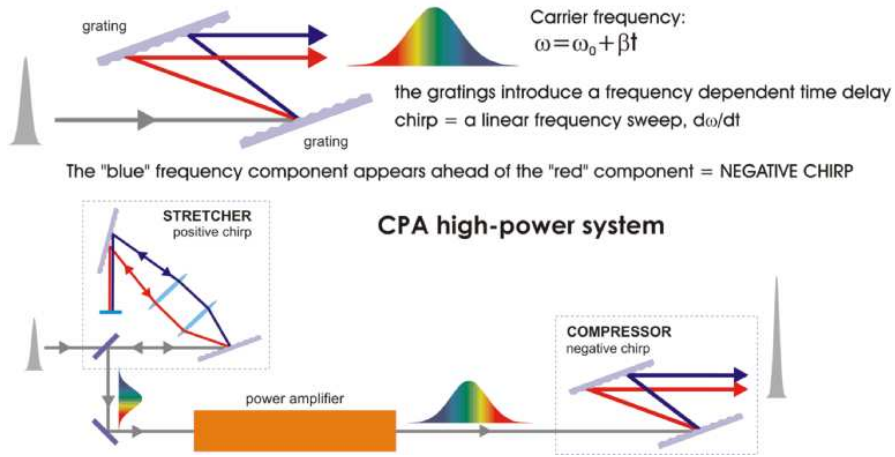
FIGURE 4.1: A schematic depiction [120] of linear CPA concept to obtain a high power laser pulse is shown. The concept of the frequency chirp shown on the top is used to stretch the seed pulse, which is subsequently amplified and again compressed by applying the negative chirp.

can also operate in an uncompressed long ns range. In the future, an optical parametric chirped pulse amplification (OPCPA) [123, 124] technique could be adopted, which will possibly offer an extremely short high energy laser pulse.

The extreme power of the L4 beamline is better expressed in terms of laser intensity, which actually addresses the laser-matter interaction phenomena. Usually, the laser intensity of approximately 10^{16} W/cm^2 is considered to be a maximum limit for hydrodynamic model to be valid. It is well known, that in the case of laser intensities surpassing 10^{18} W/cm^2 the regime of classical physics breaks down and principals of relativity must be applied. In any case, the proposed experiments to be realized on the L4 beamline go well above the relativistic laser intensity limit possibly reaching intensities of 10^{24} W/cm^2, which far beyond the hydrodynamic limit. However, in the latter case, the high intensity laser pulse is unavoidably accompanied by a prepulse, which, in the case of 10 PW, must be considered with a special care in experimental settings. According to [120], the L4 beamline will generate a 10 ns laser pedestal, which should be kept within the contrast of 10^{-11} with respect to the high intensity pulse. In principle, the effects of laser prepulse lead to several scenarios due to the early laser pedestal. The preplasma creation at the front side of the target is always observed once the prepulse intensity exceeds the limit of plasma creation being approximately 10^9 W/cm^2. In the case of higher prepulse intensity the laser pulse launches a shock which propagates inside the target, while a higher intensity implies a faster propagation velocity of the shock. Yet another effect can occur and that is when the shock breaks out at the rear side of the target, which produces a long plasma profile [125, 126, 127, 128].

All of the latter effects lead to a specific preplasma profile and its variation can alter the final outcome of the high intensity pulse interaction with matter (preplasma). In general, we aim to characterize such a preplasma profile by doing a set of hydrodynamic simulations of the L4 beamline prepulse specified above. We believe that our nonlocal hydrodynamic model presented in section 2.6 covers all relevant aspects of physics, and so, brings a beneficial insight into the preplasma creation to be present in the future experiments at the L4 beamline.
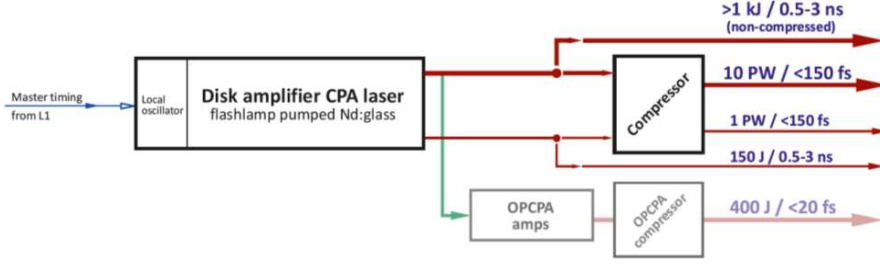
FIGURE 4.2: A scheme of the L4 beamline [120] is shown. In principle, the main kilojoule pulse can deliver the power of 10 PW. An auxiliary 150 J pulse can accompany the main pulse. Both pulses can also operate in an uncompressed long ns range, as is shown. The shaded line including OPCPA technique could possibly offer an extremely short high energy laser pulse, though this is a future concept only nowadays.

4.1.1 Interaction configuration

The compressed laser beam is transported into the experimental chamber and appropriately focused to the location of a target, which leads to a laser-matter interaction followed by the creation of plasma. The following configuration of the L4 beamline will be considered

$$\lambda = 1.057\mu\text{m}, E = 1.5\text{kJ}, \text{FWHM} = 150\text{fs}, d_1 = 11.29\mu\text{m}, d_2 = 3.57\mu\text{m}, d_3 = 1.13\mu\text{m}, \tag{4.1}$$

where λ is the Nd:glass laser pulse wave length, E is the laser pulse energy, the full-width-half-maximum (FWHM) refers to the effective time duration of the high intensity laser pulse, and d_1, d_2, and d_3 are the focal spot diameters corresponding to focal spot surfaces 10^{-6}cm^2, 10^{-7}cm^2, and 10^{-8}cm^2. Thus, the corresponding intensities generated by the 10 PW L4 beamline are

$$I_1 = 10^{22}\text{W/cm}^2, I_2 = 10^{23}\text{W/cm}^2, I_3 = 10^{24}\text{W/cm}^2. \tag{4.2}$$

With respect to the maximum intensities (4.2) and the expected contrast 10^{-11}, we assume a flat laser pulse of duration 10 ns with a constant prepulse intensities $I_1^{pp} = 10^{11}\text{W/cm}^2, I_2^{pp} = 10^{12}\text{W/cm}^2, I_3^{pp} = 10^{13}\text{W/cm}^2$ [120]. The prepulses will interact with a massive solid target of thickness of 100 μm.

In order to address a broad range of possible applications, we will use three different materials: hydrogen (H, Z=1), plastic (CH, Z=3.5), and iron (Fe, Z=26), where Z is the atomic number. This will help us to better understand the relation between the material target characterized by varied atomic number Z and corresponding physical regime, which dominates the preplasma dynamics in hydrodynamic simulations.

4.1.2 Simulation results

A set of hydrodynamic simulations has been carried out in order to predict the effects of the prepulse corresponding to the L4 beamline.

We model the experimental situation when a constant laser prepulse of duration 10 ns is incident normally on hydrogen, plastic, and iron massive 100 μm thick targets, while the prepulse is due to the finite 10^{-11} contrast of the L4 beamline configured as (4.1, 4.2). This leads to nine different simulations, where, as a result, the responses of three different material targets to three different laser intensities are characterized.
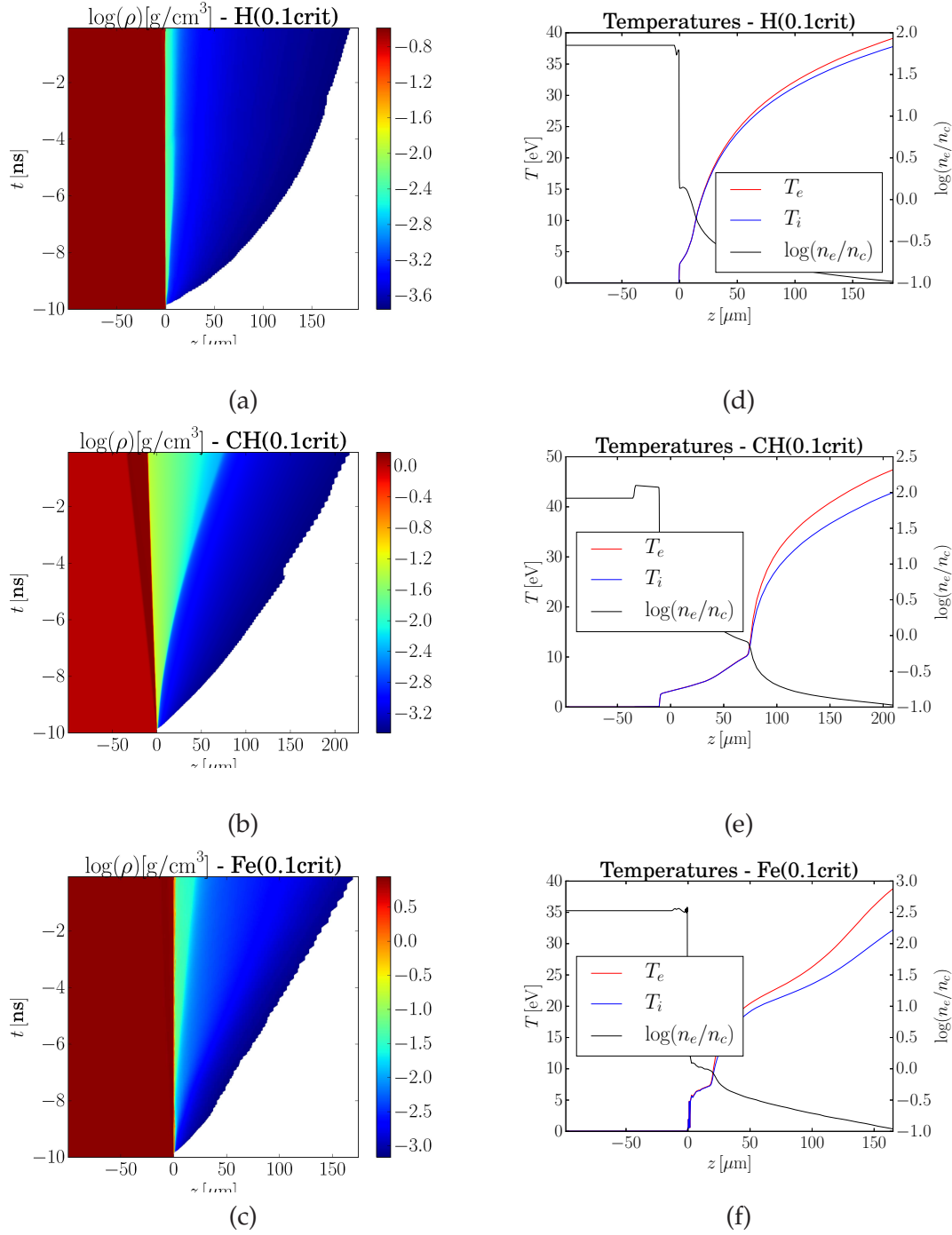
(a)

(d)
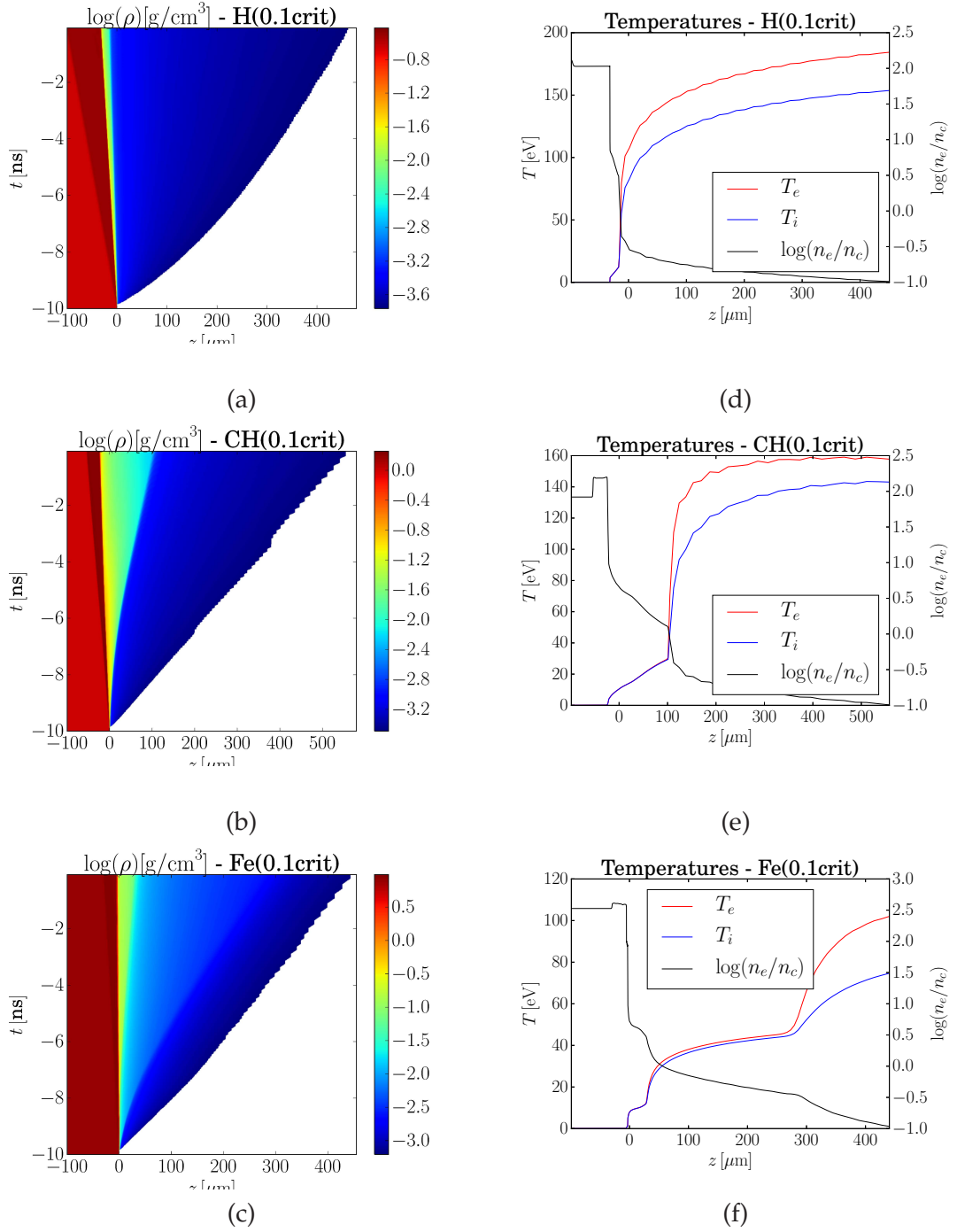

(b)

(e)

(c)

(f)

FIGURE 4.3: The region corresponding to the electron density $n_e \geq 0.1 n_c$ in the case of the prepulse intensity $10^{11} \mathrm{W/cm^2}$ (corresponding to the maximum intensity $10^{22} \mathrm{W/cm^2}$) is shown. Figure (a), (b), and (c) show how the plasma density profile evolves during the 10 ns prepulse of the L4 laser beam in the case of hydrogen, plastic, and iron targets, repsectively. Profiles of electron and ion temperatures and electron density normalized to critical density of the L4 laser beam are shown in figures (d), (e), and (f) at the time corresponding to 100 ps before the arrival of the high intensity pulse.
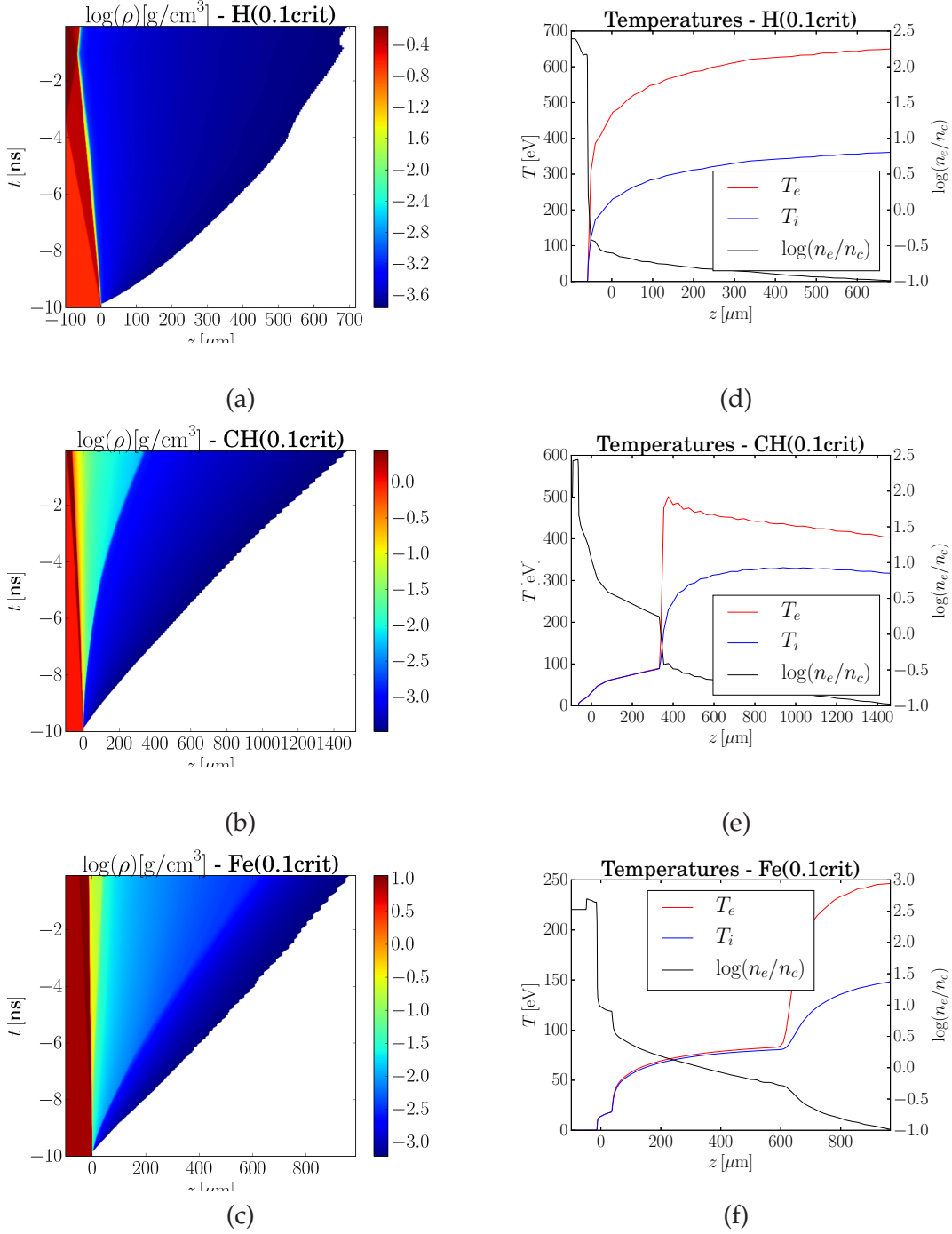
(a)

(d)

(b)

(e)

(c)

(f)

FIGURE 4.4: The region corresponding to the electron density $n_e \geq 0.1 n_c$ in the case of the prepulse intensity 10^{12}W/cm^2 (corresponding to the maximum intensity 10^{23}W/cm^2) is shown. Figure (a), (b), and (c) show how the plasma density profile evolves during the 10 ns prepulse of the L4 laser beam in the case of hydrogen, plastic, and iron targets, repsectively. Profiles of electron and ion temperatures and electron density normalized to critical density of the L4 laser beam are shown in figures (d), (e), and (f) at the time corresponding to 100 ps before the arrival of the high intensity pulse.

(a)

(b)

(c)

(d)

(e)

(f)

FIGURE 4.5: The region corresponding to the electron density $n_e \geq 0.1 n_c$ in the case of the prepulse intensity 10^{13}W/cm^2 (corresponding to the maximum intensity 10^{24}W/cm^2) is shown. Figure (a), (b), and (c) show how the plasma profile corresponding to the latter density range evolves during the 10 ns prepulse of the L4 laser beam in the case of hydrogen, plastic, and iron targets, repsectively. Profiles of electron and ion temperatures and electron density normalized to critical density of the L4 laser beam are shown in figures (d), (e), and (f) at the time corresponding to 100 ps before the arrival of the high intensity pulse.

In order to address a relevant interaction region, we show the plasma with density higher than 0.1 of the critical density n_c, which refers to a characteristic depth of plasma, where the high intensity laser pulse encounters a strong response of preplasma.

In Fig. 4.3 we can see how the created plasma evolves during the 10 ns prepulse of a constant intensity $10^{11}\mathrm{W/cm^2}$ in the case of hydrogen, plastic, and iron targets. The corresponding profiles of electron and ion temperatures and electron density normalized to critical density are shown at the time corresponding to 100 ps before the arrival of the high intensity pulse. Equivalent results of hydrogen, plastic, and iron targets in the case of the prepulse of a constant intensity $10^{12}\mathrm{W/cm^2}$ are shown in Fig. 4.4, and last but not least are the equivalent results of hydrogen, plastic, and iron targets in the case of the prepulse of a constant intensity $10^{13}\mathrm{W/cm^2}$, which are shown in Fig. 4.5.

In general, we can conclude that the $0.1 \ n_c$ region of created preplasma will expand approximately 200 μm in the case of the lowest intensity ($10^{11}\mathrm{W/cm^2}$) prepulse. What is quite surprising is that the expansion length vary just a little with respect to different Z materials, i.e. 180 μm in the case of hydrogen, 205 μm in the case of plastic, and 165 μm in the case of iron. One should notice the faster expansion of plastic then of hydrogen, even though, plastic is much heavier. Quite similar tendency of preplasma expansion can be found in the case of prepulse of the intensity $10^{12}\mathrm{W/cm^2}$. The 0.1 n_c region of created preplasma will expand 460 μm in the case of hydrogen, 540 μm in the case of plastic, and 430 μm in the case of iron, which is approximately 500 μm with a small variation with respect to atomic number Z. Finally, in the case of the highest intensity ($10^{13}\mathrm{W/cm^2}$) prepulse, we can observe the expansion length to be 670 μm in the case of hydrogen, 1450μm in the case of plastic, and 930μm in the case of iron. As in the previous cases, expansion of the plastic target overtakes the hydrogen target. Further more, we can see, that in the case of the prepulse of the intensity $10^{13}\mathrm{W/cm^2}$ the expansion scale length varies with respect to atomic number Z.

Apart from the temperature and density profiles, we are also interested in energy fluxes, which are responsible for the plasma dynamics. We distinguish between three different fluxes of energy, which are used in the nonlocal transport hydrodynamic model presented in section 2.6. These are the hydrodynamic flux $\mathbf{q}_{Hydro} = p\mathbf{v}$, where p is the total pressure and $\mathbf{v}$ is the fluid velocity, then nonlocal radiation flux $\mathbf{q}_{Rad}$ obtained from the nonlocal radiation transport equation (2.234), and nonlocal electron heat flux $\mathbf{q}_{Heat}$ obtained from the nonlocal electron transport equation (2.235). In principle, hydrodynamic flux is the essential energy carrier in plasma fluid. However, under certain circumstances, the effect of $\mathbf{q}_{Hydro}$ can be overtaken by particle transport as electrons or photons.

In Fig. 4.6 which corresponds to the prepulse intensity $10^{11}\mathrm{W/cm^2}$, it can be seen, that in the case of hydrogen the radiation flux is almost negligible, which is due to low Z. However, the heat flux competes with the hydrodynamic flux and surpasses it close to the critical density. In the case of plastic, the radiation flux takes over both the hydrodynamic flux and the heat flux, however, in the region deeper then the critical density the heat flux dominates and a several tens of microns thick layer can be observed as the effect of the heat flux in Fig. 4.6(b). In the case of iron, the hydrodynamic flux is negligible. Due to the high Z of iron the radiation flux dominates almost everywhere except of a thin precursor resulting from the heat flux in the region close to the critical density. In the case of the prepulse intensity $10^{12}\mathrm{W/cm^2}$, the tendency of the energy fluxes competition is quite similar, however, the radiation flux is more dominant in the case of plastic and iron, and in the case of hydrogen the hydrodynamic fluxes is

the one who dominates, which is shown in Fig. 4.7. Again, there is a thin precursor due to the heat flux in the case of hydrogen. Last but not least is the case of the prepulse intensity 10^{13}W/cm^2. In Fig. 4.8 we can see the tendency of increasing dominance of the hydrodynamic flux in the case of hydrogen and of increasing dominance of the radiation flux in the case of plastic. In the case of iron the radiation flux plays the dominant role, nevertheless, the effect of the heat flux precursor is getting more significant. One should note, that in the case of iron the radiation flux closely approaches the magnitude of the laser energy flux $|\mathbf{q}_{Laser}|$, i.e. the target is cooled down due to the radiation transport significantly.

In order to conclude, we will remind the definition of the Knudsen number. It is defined as $K_n = \frac{\tilde{\lambda}}{L}$, where $\tilde{\lambda}$ is the mean free path of a particle and $L = \frac{T_e}{|\nabla_{\mathbf{x}} T_e|}$ is the characteristic temperature length scale of plasma usually related to the transport of energy. The plasma background is considered to be reaching the diffusive asymptotic of particle transport if $K_n < 10^{-2}$. In the case of $K_n > 10^{-2}$ the particle transport is non-local, which reaches the transparent/ballistic transport regime if $K_n \gg 10^{-2}$. The main advantage of the nonlocal transport hydrodynamic model is that there is no physical limitation of the transport models used, i.e. the usually used flux limiters (with ad hoc coefficients) in the case of SH electron transport or the radiation diffusion transport do not need to be applied, since we solve directly the appropriate forms (2.234, 2.234) of the Boltzmann transport equation. Further more, using the flux limiters is a very rough physical assumption, since the resulting fluxes do not obey any transport model.

If we observe the bottom part of figures 4.6, 4.7, and 4.8, we can see an important observation. Radiation and heat fluxes contribute significantly only in the regions where K_n^e and K_n^p are larger than 10^{-2}. This means, that the energy flux due to electron and photon transport plays an important role exclusively inthese regions of the non-local regime. On the other hand side, it is almost negligible when K_n^e and K_n^p are smaller then 10^{-2}. An important outcome of the latter is, that the usual diffusion models also contribute the most in regions where K_n^e and K_n^p are larger than 10^{-2}, because the flux is a linear function of the mean free path λ (A.22). However, the diffusive flux (A.22) overestimates the actual electron heat flux and must undertake a rough action of the flux limiter. Our experience with the SH electron model in the hydrodynamic simulations of laser-heated plasma confirms that the major contribution in hydrodynamic simulations of flux is localized where, actually, the flux limiter takes action.

Physical reliability is the main reason why we prefer to use a more complicated and computationally more demanding nonlocal model in the case of laser-heated plasmas.
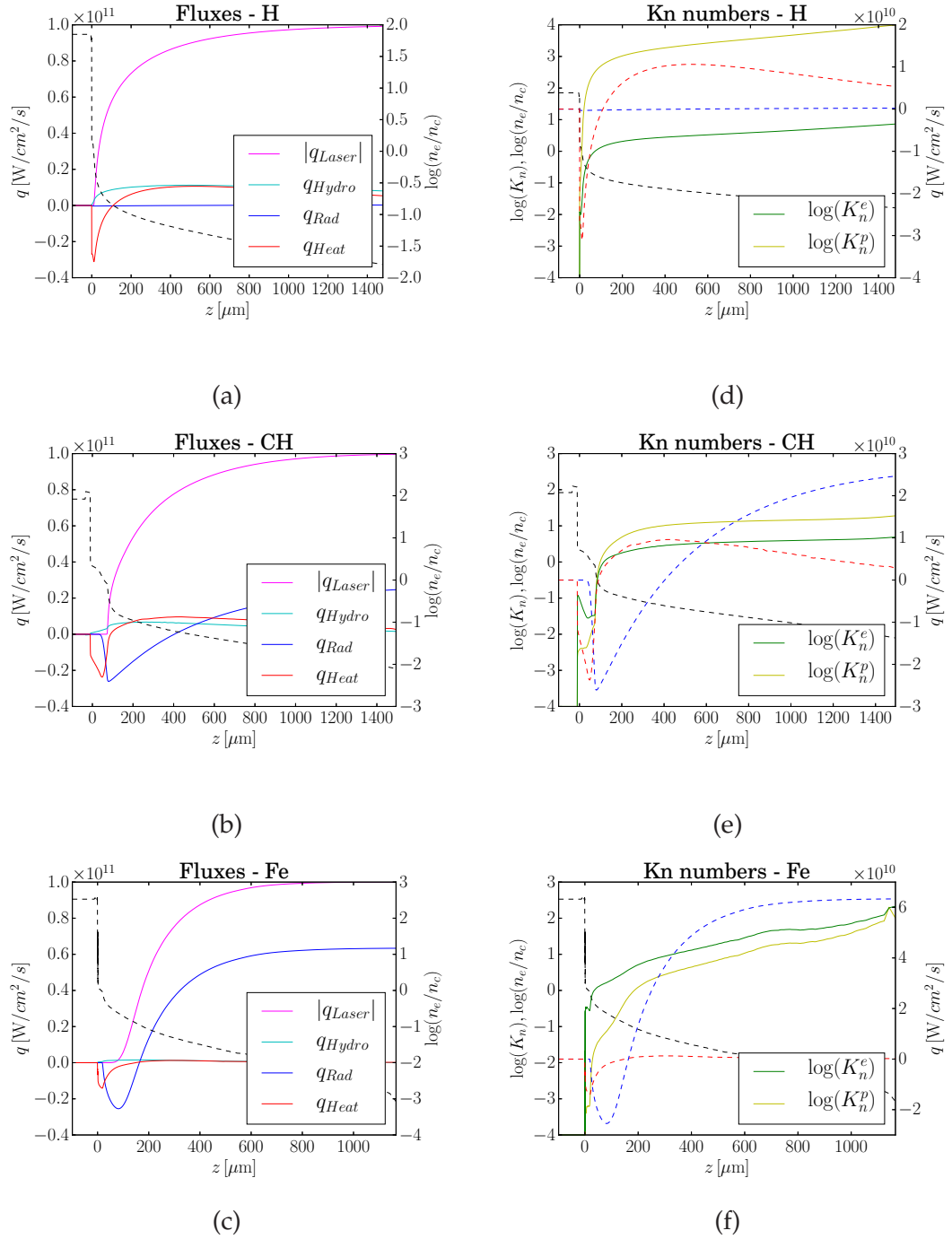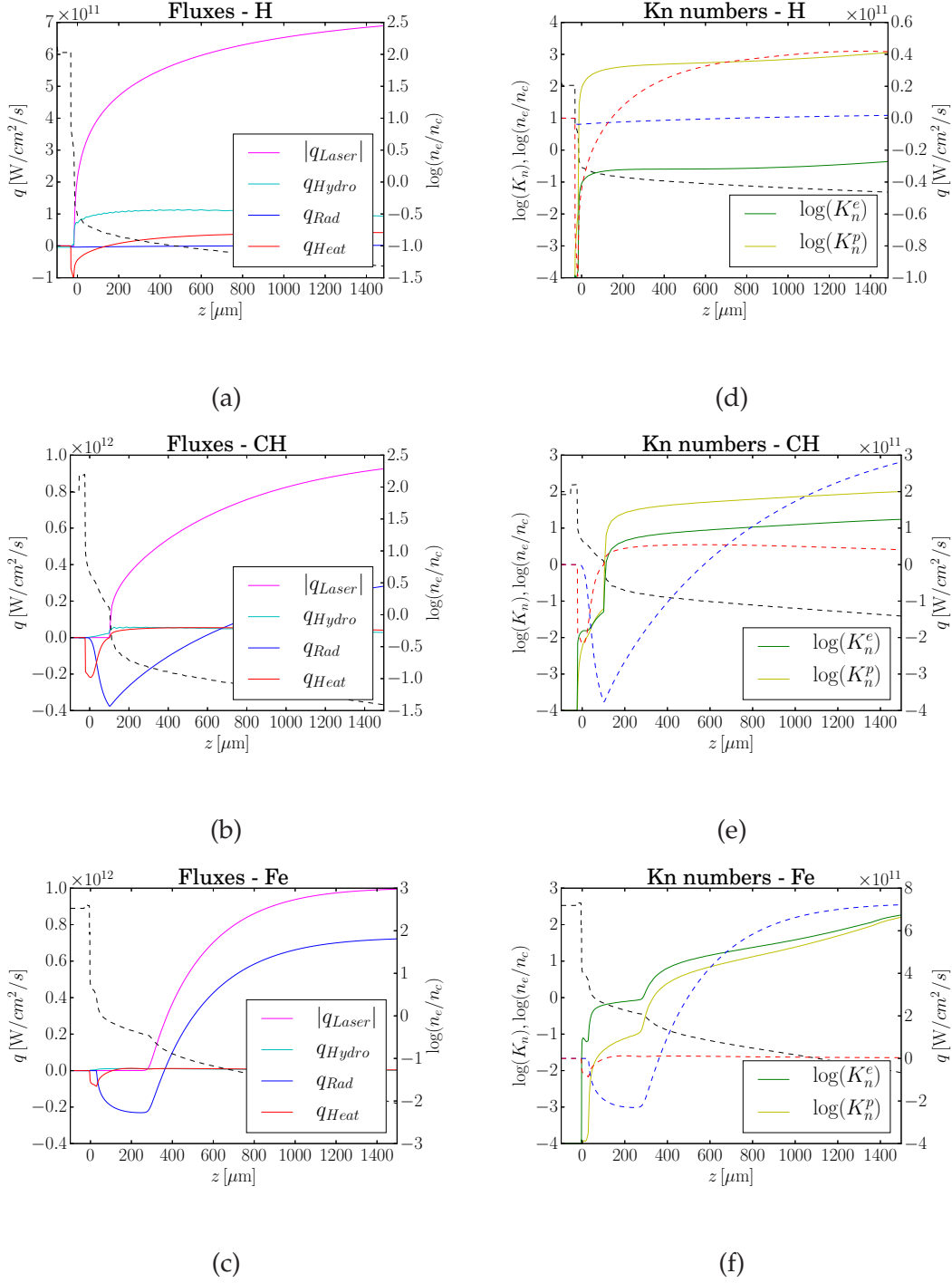
FIGURE 4.6: Effective competition between hydrodynamic, radiation, and electron heat energy fluxes accompanied by laser in hydrogen, plastic, and iron targets at the time of 100 ps before arrival of the maximum intensity 10^{22}W/cm^2 is shown. The corresponding information about electrons and photons Knudsen numbers show figures (d), (e), and (f). The laser energy flux $\mathbf{q}_{Laser}$ goes from right to left. Black, red, and blue dashed lines correspond to the electron density to the critical density ratio, the electron heat flux, and the radiation heat flux, respectively.

(a)

(d)

(b)

(e)

(c)

(f)

FIGURE 4.7: Effective competition between hydrodynamic, radiation, and electron heat energy fluxes accompanied by laser in hydrogen, plastic, and iron targets at the time of 100 ps before arrival of the maximum intensity 10^{23}W/cm^2 is shown. The corresponding information about electrons and photons Knudsen numbers show figures (d), (e), and (f). The laser energy flux $\mathbf{q}_{Laser}$ goes from right to left. Black, red, and blue dashed lines correspond to the electron density to the critical density ratio, the electron heat flux, and the radiation heat flux, respectively.
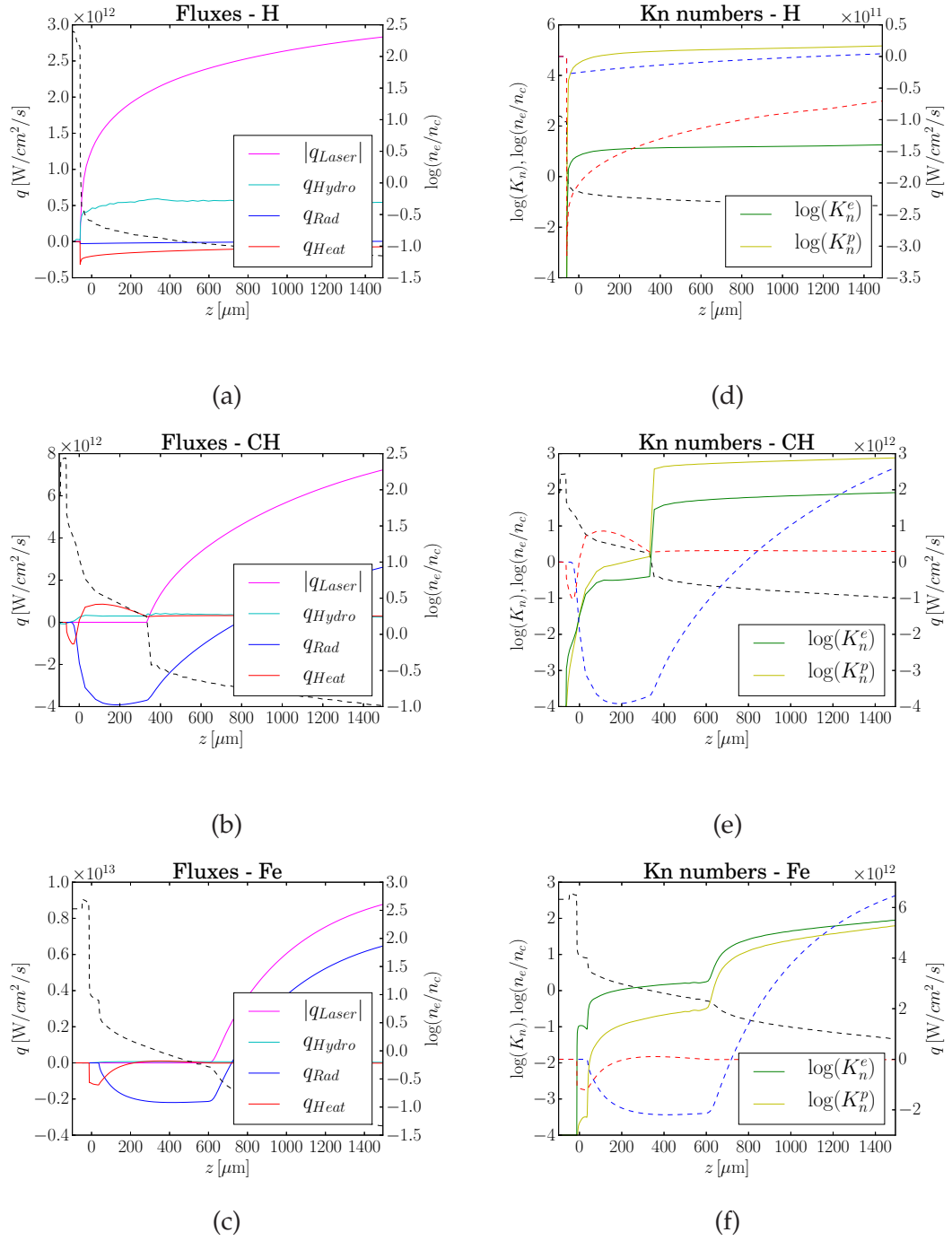
FIGURE 4.8: Effective competition between hydrodynamic, radiation, and electron heat energy fluxes accompanied by laser in hydrogen, plastic, and iron targets at the time of 100 ps before arrival of the maximum intensity 10^{24}W/cm^2 is shown. The corresponding information about electrons and photons Knudsen numbers show figures (d), (e), and (f). The laser energy flux $\mathbf{q}_{Laser}$ goes from right to left. Black, red, and blue dashed lines correspond to the electron density to the critical density ratio, the electron heat flux, and the radiation heat flux, respectively.

4.2   Warm Dense Foam EOS Experiments at OMEGA

Warm dense matter (WDM) is a unique state of dense plasmas present in many astrophysical objects, e.g. large gaseous planets, brown dwarfs, crusts of old stars and others [129]. It is also a transient state during heating of solid materials to high temperatures. It is naturally created when laser irradiates and consequently heats up solid targets or during massive material compression like implosion of deuterium-tritium-fuel pellets during ICF implosions [130].

At moderately high temperatures around 1-100 eV, material solid densities, and pressures above 1 Mbar the plasma is created both by collisional and pressure ionization thus resulting in a system where ions are strongly correlated and the electron population is partially or fully degenerate. It is obviously far from the model of Boltzmann gas based on binary collisions. Such a high correlation makes the theoretical description of WDM very challenging [131]. A detailed knowledge of the equation of state of light elements such as carbon is however essential to understanding of many processes in material sciences, in the efficient ICF strategy, or in the formation and structure of the massive astrophysical objects [132].
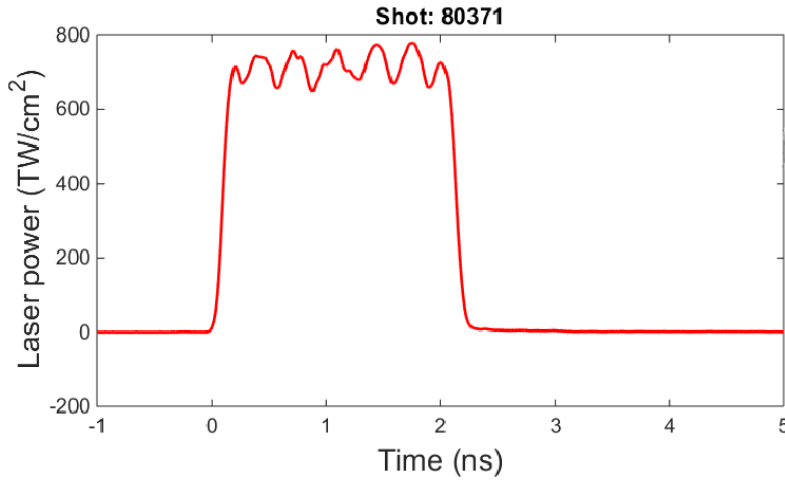

FIGURE 4.9: The composite time profile of laser used in the experiment at OMEGA facility, which consists of fourteen particular laser beams which stacked together provided an almost flat 2 ns laser drive of intensity 7.5×10^{14} W/cm^2 is shown [133].

In recent years interesting experimental and theoretical work on carbon has been fueled by a rich supply of unique phases, material properties, and atomic structure. A good example of theoretical work on this subject are extensive studies using quantum molecular dynamics (QMD) simulations to describe the EOS and microscopic properties of warm dense carbon and hydrocarbons including shock-compressed polymers [134] and diamond [131, 135]. The EOS and electrical conductivity of shock-compressed ICF ablators containing plastic has been studied in [136]. The first principles simulations have been used to obtain an extensive phase diagram and EOS of carbon [137]. Progress has also been made in experimental study of properties of dense states in carbon. Different compression schemes are possible based on the laser-driven shocks in solid targets [138, 139].

Here, we aim to do a theoretical study of a dynamically compressed low density carbon foam based on the experiment at OMEGA laser facility [133]. Such foams are

used in various laser experiment applications, in particular in ICF research [140]. Results of our hydrodynamic simulation of the generated shock and its velocity are used to clarify the experimental results obtained in [133].

4.2.1 Experimental results

The experiments were performed at the 60-beam OMEGA laser facility at the Laboratory for Laser Energetics (LLE) at the University of Rochester, NY [141]. Fourteen beams were frequency-tripled to give wavelength of 351 nm and then used to drive a strong shock in planar targets through ablation from a plastic CH layer. Each laser beam had a square temporal pulse profile with 1 ns duration. The final drive was created by stacking these pulses in time and through phase plate detuning that provided an almost flat drive with intensity 7.5×10^{14} W/cm^2. The resulting time profile of approximately 2 ns long drive when the fourteen beams (450 J beam^{-1}) were all overlapped in time is shown in Fig. 4.9.

The main target consists of several different material planar layers arranged to form a cylinder with 600 μm diameter. The subsequent structure of layers consists of 25 μm thick CH ablator, 3 μm thick Au radiation shield, 70 μm thick Al pusher, followed by a 300 μm thick CH foam. The CH foam was a porous polystyrene made by the hipe process where the mass density was ≈ 0.15 g/cm^3 [139, 133].
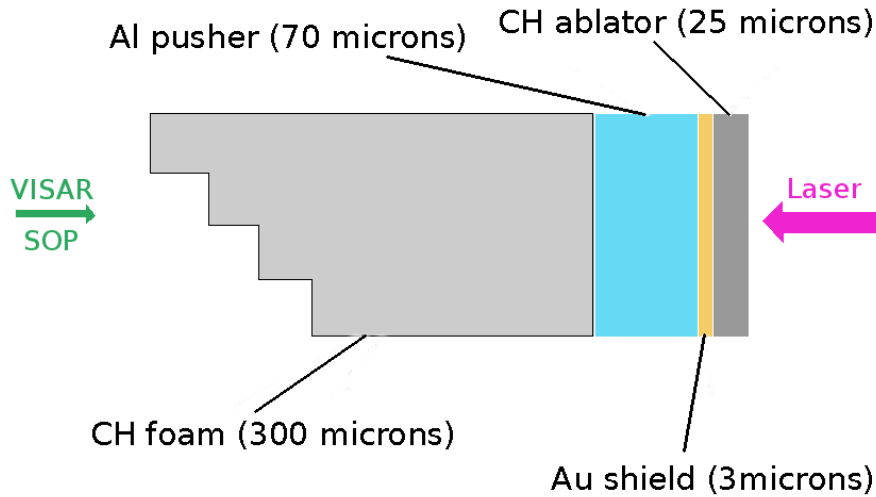

FIGURE 4.10: A scheme of a multi-layered target used in the WDFEOS experiment is shown. The main target consists of 25 μm thick CH ablator, 3 μm thick Au radiation shield, 70 μm thick Al pusher, followed by a 300 μm thick CH foam with the mass density of 0.15 g/cm^3. The rear side of the target is manufactured with three 40 μm steps in order to capture breakouts of the shock.

In the case of the 0.15 g/cm^3 plastic foam, standard techniques as velocity interferometry (VISAR) [142] or streaked optical pyrometry (SOP) [143] cannot provide a movie of propagating shocks, since the used foam is opaque to the visible light. In order to address this difficulty, the target was manufactured with three steps of thickness of 40 μm at the rear side as shown in Fig. 4.10. These steps are used to measure breakout times of the shock, which actually can be measured with both VISAR and

SOP techniques. The corresponding VISAR and SOP breakout measurements of laser-driven shock in the plastic foam are shown in Fig. 4.11.

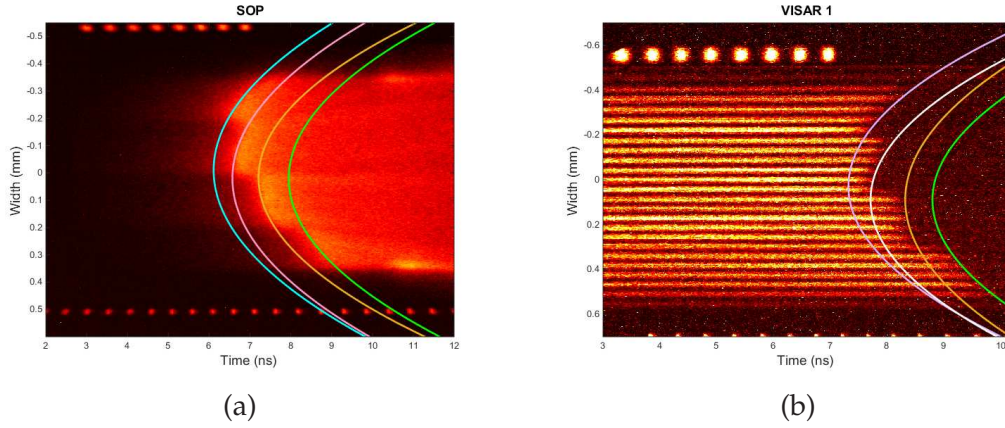(a)   (b)

FIGURE 4.11: Experimental breakout measurements from the shot 80371. Figure (a) shows the measured output from the SOP diagnostic and figure (b) shows the measured output from the VISAR diagnostic used at OMEGA facility.

Apart from the VISAR and SOP diagnostics the novel x-ray Thomson scattering (XRTS) technique to measure electron temperature was used to probe the shocked plastic foam [133]. The signal of XRTS was then fitted with the XRS code [144] to obtain the electron temperature to be ranging between 20 and 30 eV [133]. Based on predictions from QMD [145], SESAME 7593 [146] and FPEOS [147] equation of state tables for polystyrene, the measured shock velocities of 60-70 km/s correspond to a shocked density of 0.6-0.7 g/cm^3 [133], which reaches $\approx 5 \times$ compression. The details of these measurements are described in [133].
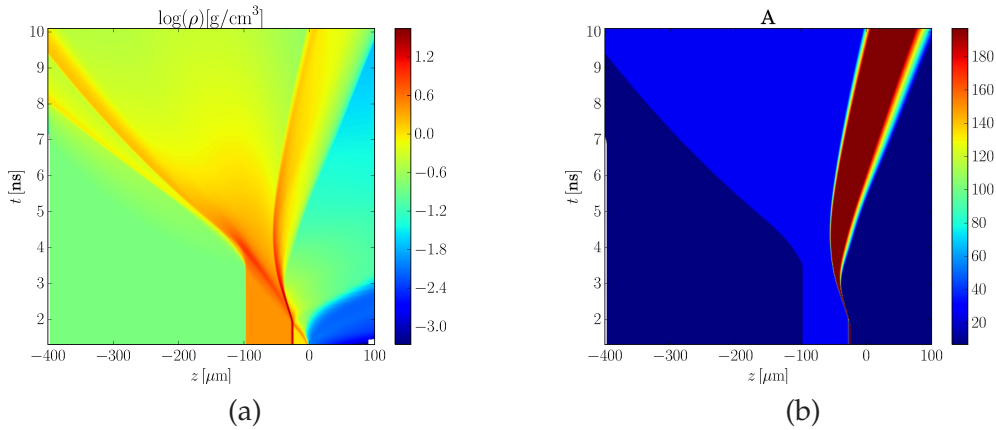

(a)   (b)

FIGURE 4.12: Figure (a) shows how the plasma density profile evolves during approximately 10 ns after the flat pulse was triggered. Figure (b) shows the atomic number, so material regions can be easily distinguished. The rainbow effect present in figure (b) is due to the image interpolation. No material mixing occurs.

From Fig. 4.11 can be seen, that the first and the last breakouts measured by SOP correspond to times 6.1 ns and 8.1 ns, which gives an approximate shock velocity 60 km/s. In the case of VISAR the first and the last breakouts correspond to times 7.2 ns

and 8.9 ns, which gives an approximate shock velocity 70 km/s. However, the first breakout observed by SOP occurs more than 1 ns before the first breakout observed by VISAR despite the fact that the shock velocity measured by VISAR is greater than the shock velocity measured by SOP. We will to provide a physical explanation to the latter discrepancy through the analysis of our hydrodynamic simulations.

4.2.2 Simulation results

In order to simulate the laser-driven shock in low density plastic foam described in the experiment above, we use our nonlocal hydrodynamic code PETE. The corresponding numerical parameters of the DG-BGK&Ts scheme was presented at the beginning of this chapter.

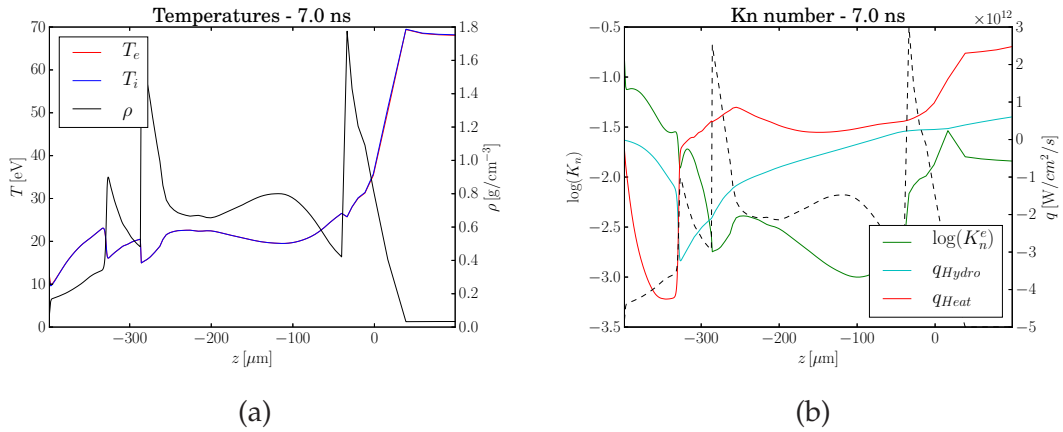(a)   (b)

FIGURE 4.13: Figure (a) shows the line-out of the plasma density, electron and ion temperatures profiles at time 7 ns (refer to Fig. 4.12). Figure (b) shows corresponding profiles of hydrodynamic energy flux $\mathbf{q}_{Hydro} = p\mathbf{v}$ and electron heat flux $\mathbf{q}_{Heat}$. As a measure of nonlocality the electron Knudsen number K_n^e is also shown.

Fig. 4.12 presents the results of a hydrodynamic simulation when the pulse shown in Fig. 4.9 of laser radiation of wavelength $\lambda = 351$ nm and maximum intensity 7.5×10^{14} W/cm^2 is incident normally on the target shown in Fig. 4.10. The front surface of the multi-layer target is placed to the origin of z axis and extends to the left, where the foam layer is placed in the interval $z \in (-100\mu\text{m}, -400\mu\text{m})$.

Fig. 4.12(a) shows how the plasma density profile evolves during approximately 10 ns after the laser pulse was triggered. Several shocks can be observed. Since the multi layer target was used, Fig. 4.12(b) shows the atomic number of plasma ion fluid, so each material regions can be easily distinguished. Three different materials can be identified: plastic ($A \approx 12$) present as the ablative and the foam layers, aluminum ($A \approx 27$) present as the pusher layer, and gold ($A \approx 197$) present as a thin shield layer.

Fig. 4.13(a) shows the plasma density, electron and ion temperatures profiles corresponding to the time 7 ns lineout of Fig. 4.12. Fig. 4.13(b) shows corresponding profiles of the electron heat flux $\mathbf{q}_{Heat}$, the hydrodynamic flux $\mathbf{q}_{Hydro}$, and the electron Knudsen number K_n^e. The electron heat flux results from the model (2.235) and the hydrodynamic flux is defined as $\mathbf{q}_{Hydro} = p\mathbf{v}$, where p is the plasma fluid pressure and $\mathbf{v}$ the plasma fluid velocity. The electron Knudsen number is defined as $K_n^e = \frac{\lambda_e}{L}$, where λ_e is the electron mean free path and $L = \frac{T_e}{|\nabla_{\mathbf{x}} T_e|}$ is the characteristic scale length of plasma. The plasma background is considered to be reaching the heat diffusion

transport if $K_n^e < 10^{-2}$. It is worth mentioning that the electron heat flux is obviously in the nonlocal regime of transport in the region of the plastic foam according to Fig. 4.13(b).

We can also see that the electron temperature is around 15-25 eV in the region of shocked foam and the corresponding density is between 0.5-0.9 g/cm^2, which corresponds closely to experimentally measured results of 20-30 eV and 0.6-0.7 g/cm^2 presented in [133]. It should be mentioned that we use the same equation of state of plastic foam as in [133], i.e. SESAME 7593 [146].
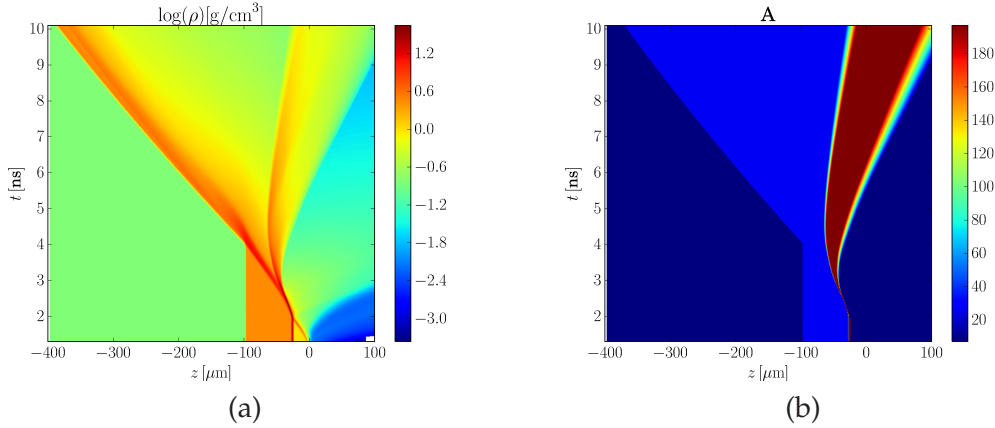

FIGURE 4.14: *Diffusive regime.* Figure (a) shows how the plasma density profile evolves during approximately 10 ns after the flat pulse was triggered. Figure (b) shows the atomic number, so material regions can be easily distinguished. The rainbow effect present in figure (b) is due to the image interpolation. No material mixing occurs.

In order to analyze the effect of energy transport nonlocality, we decided to run the same laser-driven shock simulation where we artificially reduced the electron mean free path to be 10 × smaller, thus we made the transport to be more diffusive. The corresponding results are shown in Fig. 4.14 and at time 7ns in Fig. 4.15. The shock velocity decreased and, more importantly, the electron temperature is around few eV in the region of shocked foam and the corresponding density is between 2.7-3.3 g/cm^2, which does not reflect the experimental results at all. The nonlocal transport hydrodynamic model presented in section 2.6 thus plays a crucial role in order to predict the results of laser-driven shocked plastic foam.

Let us compare the nonlocal transport hydrodynamic simulation results with the SOP and VISAR results presented in the previous section. Fig. 4.16 shows the time evolution of density and temperature profiles.

Firstly, we analyze the results related to VISAR, which is designed to reflect a jump in the density profile. In order to simplify the analysis of the shock velocity, in Fig. 4.16(a) we show the range between the Al pusher and plastic foam interface and the first manufactured step at the rear side of the target shown in Fig. 4.10. This corresponds to the first breakout of the shock. The first shock breakout time can be easily seen on the left edge of Fig. 4.16(a) corresponding to the time 6.3 ns. Then, we show the entire range of the plastic foam layer in Fig. 4.16(b). This corresponds to the last breakout of the shock. The last shock breakout time can be easily seen on the left edge of Fig. 4.16(b) corresponding to the time 8.0 ns. Consequently, the simulated mean shock velocity is approximately 70 km/s, which is in a great agreement with the VISAR experimental results.
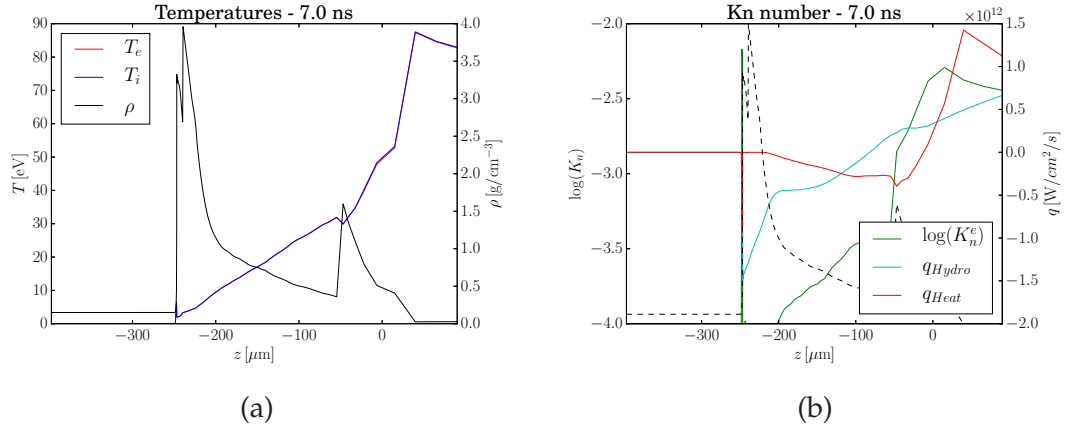
(a)

(b)

FIGURE 4.15: *Diffusive regime*. Figure (a) shows a line-out of the plasma density, electron and ion temperatures profiles at the time 7 ns of Fig. 4.14. Figure (b) shows corresponding profiles of hydrodynamic energy flux $\mathbf{q}_{Hydro} = p\mathbf{v}$ and electron heat flux $\mathbf{q}_{Heat}$. As a measure of nonlocality the electron Knudsen number K_n^e is also shown.

Secondly, we analyze the results related to SOP, which is designed to capture a relatively high temperature on the target rear side. In order to simplify the analysis of the shock velocity, in Fig. 4.16(c) we show the range between the Al pusher and plastic foam interface and the first manufactured step at the rear side of the target shown in Fig. 4.10. The first temperature breakout time can be easily seen on the left edge of Fig. 4.16(c) corresponding to the time 5.0 ns. Then, we show the entire range of the plastic foam layer in Fig. 4.16(d). The last temperature breakout time can be easily seen on the left edge of Fig. 4.16(d) corresponding to the time 7.0 ns. Consequently, the simulated mean velocity of the preheat caused by nonlocal electron transport is approximately 60 km/s, which is in a great agreement with the SOP experimental results.

According to our simulations the observed breakouts in Fig. 4.11(a) are related to the temperature breakouts due to the electron transport preheat. This theory is also supported by the profile of mass density of compressed plastic foam shown in Fig. 4.13, where the contribution of the nonlocal heat flux is essential. We are also well aware of the early occurrence of all the breakouts being about 1 ns earlier then in the experimental results. This could be the 1D effect of channeling during the plasma ablation stage of the experiment. In any case we believe that our nonlocal transport hydrodynamic model can reveal some important physical concepts, which are difficult to discover on a pure experimental basis.
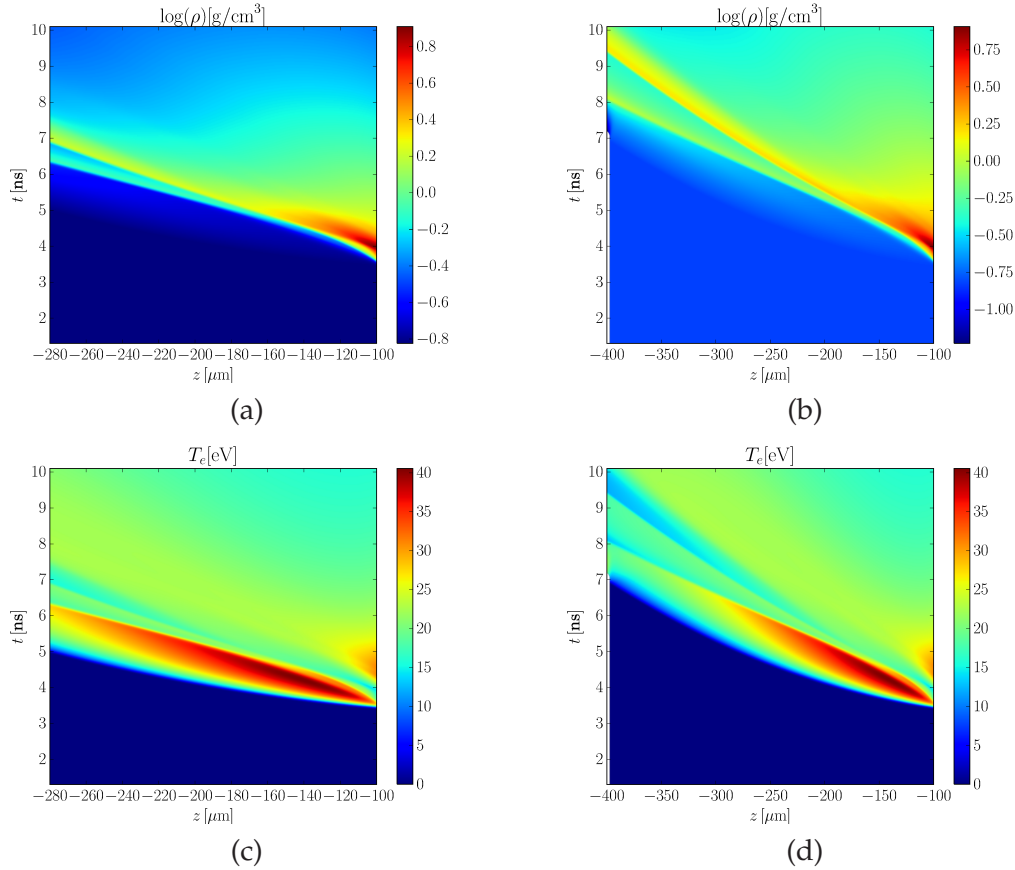
FIGURE 4.16: Simulation results of density and temperature profiles evolution in the plastic foam layer. The jump in density shown in figures (a) and (b) can be related to the experimental results of VISAR shown in Fig. 4.11(b). The preheat precursor surpassing the shock propagation in the plastic foam layer shown in figures (c) and (d) can be related to the experimental results of SOP shown in Fig. 4.11(a). The first shock breakout can be easily seen on the left edge of figure (a) corresponding to the time 6.3 ns. The last shock breakout can be easily seen on the left edge of figure (b) corresponding to the time 8.0 ns. The first temperature breakout can be easily seen on the left edge of figure (c) corresponding to the time 5.0 ns. The last temperature breakout can be easily seen on the left edge of figure (d) corresponding to the time 7.0 ns.

Chapter 5

Conclusions

The hydrodynamic model approximation is still the dominant approach for modeling plasmas under various conditions in high energy density physics (HEDP), e.g. laser-heated plasmas. It is based on conservation laws of mass, momentum and energy representing macroscopic properties of plasma, which are further accompanied by the equation of state closure which aims to include necessary microscopic properties of plasma. The proper description of plasma exhibiting a high anisotropy in motion of its constituents (electrons and ions) must necessarily include the transport closure. Nowadays, the majority of hydrodynamic codes relies on the Spitzer-Harm (SH) heat flux transport closure, which is a version of the Chapman-Enskog small parameter expansion method adapted for plasmas. The popularity of this exceptional mathematical approach resides in its simplicity and a strong theoretical background. However, this theory prescribes clearly the range of validity of the SH model with respect to the mean free path of plasma particles, and unfortunately, conditions reached in current laser-heated plasma experiments very often leak outside the domain of validity of the SH model, thus leading to the loss of predictive capability of hydrodynamic simulations.

A remedy to this situation may reside in a more fundamental approach based on first-principle concepts. Such a method would reside in the solution of the Boltzmann transport equation representing plasma particles by a distribution function. This method is referred to as the kinetic approach and provides a complete dynamics of plasma, i.e. describes both macroscopic and microscopic properties of ions and electrons (or other particles) by modeling their transport and collisions. However, the computational cost of the numerical solution corresponding to the kinetic approach would be prohibitive with respect to the time, space, and energy scales of experiments, and its model of binary collisions is valid only for fluids of low or intermediate densities.

As a result of an extensive analysis of the concepts of hydrodynamics and kinetics, we concluded that an appropriate strategy would be a combination of the latter concepts, while the simplicity and the efficiency would be inherited from hydrodynamics on the one hand side, and the first principle concept of transport anisotropy resulting from kinetics would be also kept on the other hand side. The nonlocal transport hydrodynamic model presented in the chapter devoted to physics provides a possible solution to this problem. We believe that the properties of the BGK transport equation makes it an ideal candidate to represent kinetic effects in hydrodynamics, since the BGK collision operator itself depends on the density and temperature, which are the primary variables in the hydrodynamic model. Consequently, our nonlocal transport hydrodynamic model results to be a self-consistent method describing the plasma fluid. It is further extended by the effect of the radiation transport. It is not a coincidence that we use the same transport equation based on the BGK collision operator in the case of transport of photons. In principle, the formulation of the nonlocal BGK

electron and ion transport model was inspired by the concept of the radiation transport equation from the beginning.

Obviously, the application of the nonlocal BGK transport model provides a significant improvement in plasma description with respect to the traditional diffusion transport models for electrons, ions, and photons, while no extra treatment as flux-limiting is necessary due to the fact that mean free path of particles embodies the relevant physics into the model of transport. The nonlocal transport hydrodynamic model possesses also an advantage over the pure kinetic approach, which lies in the inherent use of the equation of state, since kinetics manifestly fails in the case of high density intermediate temperature plasmas, where the concept of hydrodynamics is the only valid model.

In spite of the simple form of the BGK transport equation, its solution belongs to seven-dimensional phase space and is exceptionally challenging. In the chapter devoted to numerics, we have demonstrated the properties of our proposed DG-BGK&Ts scheme on two academic examples. As its name indicates, we use the discontinuous Galerkin high-order finite element discretization, which is constructed to solve the BGK transport equation problem in up to 7D. The main reason for using the high-order method is that additional degrees of freedom per computational element increase the accuracy and robustness of simulations compared to low-order methods, which have historically been used. A direct consequence can be observed in the academic example of the diffusive regime of transport, which can be numerically recovered only if we apply a higher order finite element method. The latter emphasizes the importance of the nonlocal transport hydrodynamic model, which provides a reliable bridge between kinetics and traditionally used diffusive hydrodynamics.

The theoretical concept of the DG-BGK&Ts scheme has been implemented into our Plasma Euler and Transport Equations code PETE, which takes as its basis the nonlocal transport hydrodynamic model including the BGK kinetics of electrons and photons. The actual implementation of PETE consists of one dimensional hydrodynamic staggered grid solver coupled to the slab geometry DG-BGK&Ts scheme, the SESAME equation of state, and is completed by the mean Planck opacities.

Bearing in mind that the accuracy of the high-order discretization ensures an appropriate transport solution with respect to any mean free path of electrons or photons, we performed a set of simulations to analyze the effect of the nonlocal energy transport in laser-heated plasma experiments.

We did a theoretical study of the prepulse plasma generation on the future most intense laser in the world, the L4 beamline at the Extreme Light Infrastructure (ELI) facility. As a result we could describe the most important effects driving the plasma expansion and address the importance of the nonlocal energy transport. Based on the Knudsen number analysis we can conclude, that the main contribution of the energy transport occurs in regions, where the transport regime is far from being diffusive. Consequently, we propose to analyze in more detail a same set of simulations based on the traditional SH electron transport and address its physical reliability.

In the second case, we did a set of simulations related to the warm dense foam equation of state experiments at the OMEGA laser facility at the Laboratory for Laser Energetics (LLE) at the University of Rochester, NY. The original task has been to clarify the experimental results obtained, which indicated a slight uncertainty in measurements. The simulation results of laser-heated plasma experiment were compared to the relevant experimental data reproducing them surprisingly well. For instance, simulation results were in a good agreement with experimentally measured mass density and electron temperature of the shocked plastic foam. A similar match could be found

between the simulated and measured shock velocities. We observe a purely nonlocal effect in the form of a significant preheat surpassing the propagating shock in our simulations. This effect was originally addressed as uncertain in the experimental results and our simulation provides a reasonable explanation.

Encouraged by the successful nonlocal transport hydrodynamic model implementation and, even more, by the good match between simulation and experimental results, we aim to continue in the development of the PETE code and extend it into higher dimensions. Since the high-order methods have greater FLOP/byte ratios, meaning that more time is spent on floating point operations compared to memory transfer, we expect our DG-BGK&Ts scheme to perform optimally in parallel computing. Even though the parallel implementation of the scheme is not an easy task, it is a crucial step in order to perform serious laser-heated plasma simulations in multi-dimensions. We believe that, since the DG-BGK&Ts scheme code inherits from the massively parallelized MFEM library [102] developed at the Lawrence Livermore National Laboratory, we will succeed.

Appendix A

Diffusive transport

In [47] the following form of the Boltzmann transport equation of electrons in laser-heated plasma was proposed

$$\frac{\partial f_e}{\partial t} + \mathbf{v} \cdot \nabla_{\mathbf{x}} f_e + \frac{q_e}{m_e} \mathbf{E} \cdot \nabla_{\mathbf{v}} f_e = C_{ee}(f_e, f_e) + C_{ei}(f_e, f_i) + I_{IB}(\mathbf{E}_L, f_e) , \qquad \text{(A.1)}$$

where f_e and f_i are the distribution functions of electrons and ions, respectively, q_e and m_e mass and charge of electron, $\mathbf{E}$ is a plasma generated electric field, and $\mathbf{E}_L$ is an electric field related to laser. Apart from the transport operator in the phase space placed on the left-hand side of (A.1), we can also identify collision operators, namely collisions among electrons them selves C_{ee} and collisions among electrons and ions C_{ei}, and the last term describes the inverse-bremsstrahlung heating I_{IB} of electrons due to the absorption of laser energy. Also a ponderomotive laser field pressure effect could be included, but we do not consider it in this work.

The classical diffusive approximation to the deterministic transport of electrons in laser-heated plasma is presented in this section. The most frequently used such an approximation introduced by Spitzer and Harm [10, 48] is based on the expansion in a small parameter further combined with the P_1 anisotropy approximation. We further show the diffusive regime of our proposed nonlocal BGK electron transport (2.145) presented in section 2.3.3.

A.1   The Spitzer-Harm Approximation in Laser-Heated Plasma

An appropriate analysis related to the diffusive approach to transport is based on the combination of the Hilbert expansion in a small parameter λ and the angular Legendre polynomials expansion [52]

$$f_e = \sum_{i=0}^{\infty} f_i \lambda^i \sum_k f_k P_k(cos(\phi)) = f_e^{(0)} + f_e^{(1)} \lambda \cos(\phi) + f_e^{(2)} \lambda + f_e^{(3)} \cos(\phi) + O(\lambda^2, \cos^2(\phi)) ,$$

$$\text{(A.2)}$$

where ϕ is the polar angle (see Fig. 2.1) with respect to z-axis, and the right hand side of (A.2) shows its explicit series to the second order. We will use the notation $\cos(\phi) = \mu$.

In order to work with equation (A.1), we need to define its right hand side explicitly [52]

$$C_{ei}(f_e, f_i) + C_{ee}(f_e, f_e) = \nu_{ei}\nabla_{\mathbf{v}}\left(\frac{1}{|\mathbf{v}|}\left(\mathbf{I} - \frac{\mathbf{v}\otimes\mathbf{v}}{|\mathbf{v}|^2}\right)\nabla_{\mathbf{v}}f_e\right) = \frac{\nu_{ei}}{2}\frac{\partial}{\partial\mu}(1-\mu^2)\frac{\partial f_e}{\partial\mu}\,,$$
(A.3)

$$I_{IB}(\mathbf{E}_L, f_e) = \frac{\nu_{ei}|\mathbf{v}_L|^2|\mathbf{v}|}{6}\frac{\partial}{\partial|\mathbf{v}|}\left(\frac{g}{|\mathbf{v}|}\frac{\partial f_e}{\partial|\mathbf{v}|}\right)\,,$$
(A.4)

where $\mathbf{v}$ is the electron velocity, $\mathbf{v}_L = \frac{e\,\mathbf{E}_L}{m_e\,\omega_0}$ is the quiver velocity of an electron accelerated by the laser field $\mathbf{E}_L$, $g = (1+\omega_0^{-2}\nu_{ei}^2(|\mathbf{v}|))$ is the resonant function, and

$$\nu_{ei} = n_i\frac{Z^2\,e^4}{(4\,\pi\,\epsilon_0)^2}\frac{4\,\pi}{m_e^2}\frac{\ln\Lambda}{|\mathbf{v}|^3}\,,$$
(A.5)

is the electron-ion collision frequency [3] and ω_0 is the frequency of the laser. The collision operator (A.3) considers electron-ion collisions to be dominant over electron-electron collisions [4]. The right-most term shows its formulation in spherical coordinates [52], which is also the case of formulation of the inverse-bremsstrahlung operator (A.4) [47, 148].

It is convenient to define the electron mean free path

$$\lambda = \frac{\nu_{ei}}{|\mathbf{v}|}\,,$$
(A.6)

since the electron transport equation (A.1) can be formulated as

$$\frac{1}{|\mathbf{v}|}\frac{\partial f_e}{\partial t} + \mathbf{n}\cdot\nabla_{\mathbf{x}}f_e + \frac{q_e}{|\mathbf{v}|\,m_e}\mathbf{E}\cdot\nabla_{\mathbf{v}}f_e = \frac{1}{\lambda}\left(\frac{1}{2}\frac{\partial}{\partial\mu}(1-\mu^2)\frac{\partial f_e}{\partial\mu} + \frac{|\mathbf{v}_L|^2|\mathbf{v}|^2}{6}\frac{\partial}{\partial|\mathbf{v}|}\frac{g}{|\mathbf{v}|}\frac{\partial f_e}{\partial|\mathbf{v}|}\right)\,,$$
(A.7)

where we made use of (A.3, A.4, A.6).

It is extremely difficult to solve (A.7) analytically, however, it is satisfactory to find an approximate axis-symmetric solution as

$$\tilde{f}_e = f_e^{(0)} + f_e^{(1)}\lambda\mu\,,$$
(A.8)

which reflects a small spatial deviation with respect to λ and a small anisotropy effect given by μ from the dominant term $f_e^{(0)}$, which is homogeneous in space and isotropic in angle.

When we insert $\tilde{f}_e$ (A.8) in the place of f_e in (A.7), we obtain

$$\frac{1}{|\mathbf{v}|}\frac{\partial\left(f_e^{(0)} + f_e^{(1)}\lambda\mu\right)}{\partial t} + \mathbf{n}\cdot\nabla_{\mathbf{x}}\left(f_e^{(0)} + f_e^{(1)}\lambda\mu\right) + \frac{q_e}{|\mathbf{v}|\,m_e}\mathbf{E}\cdot\nabla_{\mathbf{v}}\left(f_e^{(0)} + f_e^{(1)}\lambda\mu\right) =$$
$$\frac{1}{\lambda}\left(\frac{1}{2}\frac{\partial}{\partial\mu}(1-\mu^2)\frac{\partial\left(f_e^{(0)} + f_e^{(1)}\lambda\mu\right)}{\partial\mu} + \frac{|\mathbf{v}_L|^2|\mathbf{v}|^2}{6}\frac{\partial}{\partial|\mathbf{v}|}\frac{g}{|\mathbf{v}|}\frac{\partial\left(f_e^{(0)} + f_e^{(1)}\lambda\mu\right)}{\partial|\mathbf{v}|}\right)\,,$$
(A.9)

which is the fundamental equation of the diffusive transport.

The following two equations

$$\frac{\partial}{\partial\mu}(1-\mu^2)\frac{\partial f_e^{(0)}}{\partial\mu} + \frac{|\mathbf{v}_L|^2|\mathbf{v}|^2}{3}\frac{\partial}{\partial|\mathbf{v}|}\frac{g}{|\mathbf{v}|}\frac{\partial f_e^{(0)}}{\partial|\mathbf{v}|} = 0, \tag{A.10}$$

$$\frac{1}{2}\frac{\partial}{\partial\mu}(1-\mu^2)\frac{\partial f_e^{(1)}}{\partial\mu}\mu = \mu\left(\frac{\partial f_e^{(0)}}{\partial z} - \frac{q_e E_z}{|\mathbf{v}|\,m_e}\frac{\partial f_e^{(0)}}{\partial|\mathbf{v}|}\right), \tag{A.11}$$

result from the search for terms corresponding to λ^0, i.e. zero order (A.10), and λ^1, i.e. first order (A.11), equalities. In equation (A.11) we used $\nabla_{\mathbf{v}}f_e^{(0)} = -\mathbf{n}\frac{\partial f_e^{(0)}}{\partial|\mathbf{v}|}$, which is true for isotropic function $f_e^{(0)}$ [2].

When the collision operator on the left hand side of equation (A.11) is evaluated, the solution

$$f_e^{(1)} = -\left(\frac{\partial f_e^{(0)}}{\partial z} - \frac{q_e E_z}{|\mathbf{v}|\,m_e}\frac{\partial f_e^{(0)}}{\partial|\mathbf{v}|}\right), \tag{A.12}$$

is obtained in a straightforward way searching for terms corresponding to μ^1.

At first we discuss the case when $\mathbf{E}_L = 0$, i.e. the inverse-bremsstrahlung operator in equations (A.1, A.7), but most importantly in (A.10) is neglected. Then, the most natural distribution function of electrons satisfying (A.10) is the Maxwellian velocity distribution [39]

$$f_e^{(0)} = \frac{n_e}{\left(\pi\,\frac{2\,k_B\,T_e}{m_e}\right)^{\frac{3}{2}}}\exp\left(-\frac{m_e|\mathbf{v}|^2}{2\,k_B\,T_e}\right), \tag{A.13}$$

where m_e, n_e and T_e are electron mass, density and temperature, and k_B is the Boltzmann constant.

Now, based on the explicit formulas

$$\nabla_{\mathbf{x}}f_e^{(0)} = \left(\frac{\nabla_{\mathbf{x}}n_e}{n_e} + \left(\frac{m_e\,|\mathbf{v}|^2}{2\,k_B\,T_e} - \frac{3}{2}\right)\frac{\nabla_{\mathbf{x}}T_e}{T_e}\right)f_e^{(0)}, \tag{A.14}$$

$$\frac{\partial f_e^{(0)}}{\partial|\mathbf{v}|} = \frac{|\mathbf{v}|\,m_e}{k_B\,T_e}\,f_e^{(0)}, \tag{A.15}$$

the approximate solution of (A.7) takes the form

$$\tilde{f}_e = \frac{n_e}{\left(\pi\,\frac{2\,k_B\,T_e}{m_e}\right)^{\frac{3}{2}}}\exp\left(-\frac{m_e|\mathbf{v}|^2}{2\,k_B\,T_e}\right)$$

$$\left(1 - \mathbf{n}\cdot\lambda\left(\left(\frac{\nabla_{\mathbf{x}}n_e}{n_e} + \left(\frac{m_e\,|\mathbf{v}|^2}{2\,k_B\,T_e} - \frac{3}{2}\right)\frac{\nabla_{\mathbf{x}}T_e}{T_e}\right) - \frac{q_e\mathbf{E}}{k_B\,T_e}\right)\right), \tag{A.16}$$

which was obtained by inserting (A.13) into (A.12) and into the expansion based approximate solution (A.8). Yet unknown electric field $\mathbf{E}$ in (A.16) can be obtained in a self-consistent manner by enforcing a zero electron flux, a condition also known as quasi-neutrality. This corresponds to the condition

$$\int_{4\pi}\int_{|\mathbf{v}|}|\mathbf{v}|\mathbf{n}\tilde{f}_e|\mathbf{v}|^2\,\mathrm{d}|\mathbf{v}|\,\mathrm{d}\mathbf{n} = \mathbf{0}, \tag{A.17}$$

which leads to the following dependence of the electric field on the thermodynamic variables

$$\mathbf{E} = \frac{k_B T_e}{q_e} \left(\frac{\nabla_{\mathbf{x}} n_e}{n_e} + \frac{5}{2} \frac{\nabla_{\mathbf{x}} T_e}{T_e} \right). \tag{A.18}$$

In order to conclude, the electron distribution function satisfying the electron transport equation (A.7) takes the form

$$\tilde{f}_e = \frac{n_e}{\left(\pi \frac{2 k_B T_e}{m_e} \right)^{\frac{3}{2}}} \exp \left(-\frac{m_e |\mathbf{v}|^2}{2 k_B T_e} \right) \left(1 - D \left(\frac{m_e |\mathbf{v}|^2}{2 k_B T_e} \right) \right), \tag{A.19}$$

where the transport function reads

$$D(w) = \lambda \, (w - 4) \, \frac{\mathbf{n} \cdot \nabla_{\mathbf{x}} T_e}{T_e}. \tag{A.20}$$

The form of (A.19) follows the notation used in the original work of Spitzer and Harm (SH) [10] and reflects the results of the Lorentz gas approximation [53, 54, 55]. The commonly used term SH transport refers more precisely to the work [48], where the transport function $D(w)$ was further extended by the electron-electron collision operator, which had to be solved numerically. The latter concludes, that the mean free path of electrons should be adjusted as

$$\lambda_{SH} = \frac{0.24 \bar{Z} + 0.058}{1 + 0.24 \bar{Z}} \lambda, \tag{A.21}$$

with respect to the mean ionization $\bar{Z}$.

Last, but not least, is the SH formulation of the electron heat flux, which provides the transport closure to the hydrodynamic system. This formulation can be directly evaluated by integrating the distribution function (A.19) over the velocity space as

$$\mathbf{q}_{SH} = \int_{4\pi} \int_{|\mathbf{v}|} |\mathbf{v}| \mathbf{n} |\mathbf{v}|^2 \tilde{f}_e |\mathbf{v}|^2 \, \mathrm{d}|\mathbf{v}| \mathrm{d}\mathbf{n} = -\frac{256 n_e}{\sqrt{8\pi}} \frac{k_B^{\frac{3}{2}}}{\sqrt{m_e}} \bar{\lambda}_{SH} \sqrt{T_e} \nabla_{\mathbf{x}} T_e, \tag{A.22}$$

where the thermal mean free path is given by

$$\bar{\lambda}_{SH} = \frac{0.24 \bar{Z} + 0.058}{1 + 0.24 \bar{Z}} \bar{\lambda} = \frac{0.24 \bar{Z} + 0.058}{1 + 0.24 \bar{Z}} \frac{n_i Z^2 e^4}{(4 \pi \epsilon_0)^2} \frac{m_e^2 v_{T_e}^4}{4 \pi \ln \Lambda}, \tag{A.23}$$

reflecting the electrons with thermal velocity $v_{T_e} = \sqrt{\frac{k_B T_e}{m_e}}$. It is also interesting to consider the effect of the electric field (A.18). When (A.22) is evaluated using (A.16), while $\mathbf{E} = \mathbf{0}$, the resulting flux is 3.5 times larger than (A.22).

It is worth mentioning that in the case of $\nabla_{\mathbf{x}} n_e \neq \mathbf{0}$ the electric field (A.18) is not aligned to the axis of symmetry given by the temperature gradient and the theory is not precise. The effect of density profile influence has been investigated in [149].

Now, we consider the case when (A.10) is solved by a super-Gaussian distribution function due to the effect of inverse-bremsstrahlung, which is produced by applied laser intensity $\mathbf{E}_L$. The super-Gaussian function depends on the parameter m [148, 149] as

$$f_e^{(0)} = \tilde{C} \frac{n_e}{(\tilde{\alpha} T_e)^{\frac{3}{2}}} \exp \left(-\frac{|\mathbf{v}|^m}{(\tilde{\alpha} T_e)^{\frac{m}{2}}} \right), \tag{A.24}$$

where $\tilde{\alpha} = \frac{2\,k_B}{m_e}\frac{3}{2}\frac{\Gamma(3/m)}{\Gamma(5/m)}$ and $\tilde{C} = \frac{m}{4\pi\,\Gamma(3/m)}$. The parameter lies in $m \in (2,5)$ and is governed by the laser field $\mathbf{E}_L$. In case of weak laser field $m \to 2$ and the super-Gaussian (A.24) degenerates to the usual Maxwell-Boltzmann distribution (A.13).

The generalization of super-Gaussian (A.24) distribution implies

$$\mathbf{E} = \frac{m_e\,\tilde{\alpha}T_e}{m\,q_e}\frac{\Gamma\left(\frac{8}{m}\right)}{\Gamma\left(\frac{m+6}{m}\right)}\left(\frac{\nabla_{\mathbf{x}}n_e}{n_e} + \frac{5}{2}\frac{\nabla_{\mathbf{x}}T_e}{T_e}\right), \qquad (A.25)$$

and finally, the electron distribution function satisfying the electron transport equation (A.7) with the effect of absorbed laser energy takes the form

$$\tilde{f}_e = \tilde{C}\frac{n_e}{(\tilde{\alpha}T_e)^{\frac{3}{2}}}\exp\left(-\frac{|\mathbf{v}|^m}{(\tilde{\alpha}T)^{\frac{m}{2}}}\right)\left(1 - D\left(\frac{|\mathbf{v}|}{(\tilde{\alpha}T_e)^{\frac{1}{2}}}\right)\right), \qquad (A.26)$$

where the transport function reads

$$D(w) = \lambda\Bigg(\left(1 - \frac{\Gamma\left(\frac{8}{m}\right)}{\Gamma\left(\frac{m+6}{m}\right)}\,w^{m-2}\right)\frac{\mathbf{n}\cdot\nabla_{\mathbf{x}}n_e}{n_e}$$
$$+ \left(\frac{m}{2}\,w^m - \frac{5}{2}\frac{\Gamma\left(\frac{8}{m}\right)}{\Gamma\left(\frac{m+6}{m}\right)}\,w^{m-2} - \frac{3}{2}\right)\frac{\mathbf{n}\cdot\nabla_{\mathbf{x}}T_e}{T_e}\Bigg). \qquad (A.27)$$

Also the dependence $m(\mathbf{x})$ could have been taken into account in (A.27). Such an approach can be found in [150].

A.2   Diffusion Asymptotic of the Nonlocal BGK Electron Transport Model

Even though our proposed electron transport model presented in section 2.3.3 aims to appropriately describe the transport of energy on the range of long distances, i.e. the nonlocal regime of transport, it must also respect the classical SH diffusion asymptotic described in the previous section.

The following equation

$$\mathbf{n}\cdot\nabla_{\mathbf{x}}\left(I_e^{(0)} + I_e^{(1)}\tilde{\lambda}_e\mu\right) - \frac{q_e}{k_BT_e}\mathbf{n}\cdot\mathbf{E}\cdot\left(I_e^{(0)} + I_e^{(1)}\tilde{\lambda}_e\mu\right) =$$
$$\frac{1}{\tilde{\lambda}_e}\left(\left(\frac{n_e}{\pi^{\frac{3}{2}}}\frac{\sqrt{2}k_B^{\frac{3}{2}}}{\sqrt{m_e}}\right)T_e^{\frac{3}{2}} - \left(I_e^{(0)} + I_e^{(1)}\tilde{\lambda}_e\mu\right)\right) - \frac{\alpha}{\tilde{\lambda}_e}I_e^{(1)}\tilde{\lambda}_e\mu, \quad (A.28)$$

was obtained from (2.145) without time derivatives by introducing an approximate solution of the electron specific intensity

$$\tilde{I}_e = I_e^{(0)} + I_e^{(1)}\tilde{\lambda}_e\mu, \qquad (A.29)$$

which reflects a small spatial deviation with respect to $\tilde{\lambda}_e$ and a small anisotropy effect given by μ from the dominant term $I_e^{(0)}$, which is homogeneous in space and isotropic in angle. The approximate solution (A.29) follows the strategy of (A.8) while both originate from (A.2). The right most term of (A.28) corresponds to the electron scattering

of (2.145). Since the scattering naturally contributes to the mean free path of electrons, it can be characterized as scaling to $\tilde{\lambda}_e$ trough a scaling factor $\alpha = \tilde{\sigma}_e \tilde{\lambda}_e$.

Like in the previous section, equation (A.28) is a basis for the search of zero and first order terms in a small parameter, represented by $\tilde{\lambda}_e$ (2.147). The following two equations

$$I_e^{(0)} = \left(\frac{n_e}{\pi^{\frac{3}{2}}} \frac{\sqrt{2} k_B^{\frac{3}{2}}}{\sqrt{m_e}} \right) T_e^{\frac{3}{2}}, \tag{A.30}$$

$$-(1-\alpha)I_e^{(1)}\mu = \mu \left(\frac{\partial I_e^{(0)}}{\partial z} - \frac{q_e E_z}{k_B T_e} I_e^{(0)} \right), \tag{A.31}$$

result from the search for terms corresponding to $\tilde{\lambda}_e^0$, i.e. zero order (A.30), and $\tilde{\lambda}_e^1$, i.e. first order (A.31), equalities.

The approximate solution (A.29) takes the form

$$\tilde{I}_e = \frac{n_e \sqrt{2}}{\pi^{\frac{3}{2}}} \frac{k_B^{\frac{3}{2}}}{\sqrt{m_e}} T_e^{\frac{3}{2}} \left(1 - \frac{\tilde{\lambda}_e}{1+\alpha} \mathbf{n} \cdot \left(\frac{\nabla_{\mathbf{x}} n_e}{n_e} + \frac{3}{2} \frac{\nabla_{\mathbf{x}} T_e}{T_e} - \frac{q_e}{k_B T_e} \mathbf{E} \right) \right), \tag{A.32}$$

which was obtained by expressing $I_e^{(0)}$ and $I_e^{(1)}$ from equations (A.30, A.31).

At last, we evaluate the electron heat flux corresponding to the diffusion asymptotic solution (A.32) as

$$\mathbf{q}_{BGK}^e = \int_{4\pi} \mathbf{n} \tilde{I}_e \mathbf{dn} = -\frac{256\sqrt{2} n_e}{3\pi^{\frac{3}{2}}} \frac{k_B^{\frac{3}{2}}}{\sqrt{m_e}} \frac{\bar{\lambda}_{T_e}}{1+\alpha} \sqrt{T_e} \nabla_{\mathbf{x}} T_e, \tag{A.33}$$

where we used relation $\tilde{\lambda}_e = \frac{128}{3\pi} \bar{\lambda}_{T_e}$ (2.147), where $\bar{\lambda}_{T_e}$ is the thermal mean free path (A.23). It is necessary to comment, that we omitted the gradient of density, i.e. $\nabla_{\mathbf{x}} n_e = 0$, and the electric field, i.e. $\mathbf{E} = 0$ in (A.33). The argument for omitting the electric field is based on quasi-neutrality condition in the diffusion regime and that we use the Poisson electrostatic model (2.251, 2.252) for $\mathbf{E}$.

An observation between (A.22) and (A.33) gives that $\mathbf{q}_{BGK}^e \approx 0.4 \mathbf{q}_{SH}$. That is an acceptable error of the electron transport in the diffusion regime. One should also notice, that we do not use $\bar{\lambda}_{SH}$ as in (A.22), since the effect of electron-electron collisions is reflected by the scaling coefficient α.

A.3 Diffusion Asymptotic of the Nonlocal BGK Ion Transport Model

Even though our proposed ion transport model presented in section 2.3.3 aims to appropriately describe the transport of energy on the range of rather long distances, i.e. the nonlocal regime of transport, it also obeys diffusion asymptotic when appropriate.

The following equation

$$\mathbf{n} \cdot \nabla_{\mathbf{x}} \left(I_i^{(0)} + I_i^{(1)} \tilde{\lambda}_i \mu \right) - \frac{q_i}{k_B T_i} \mathbf{n} \cdot \mathbf{E} \cdot \left(I_i^{(0)} + I_i^{(1)} \tilde{\lambda}_i \mu \right) =$$

$$\frac{1}{\tilde{\lambda}_i} \left(\left(\frac{n_i}{\pi^{\frac{3}{2}}} \frac{\sqrt{2} k_B^{\frac{3}{2}}}{\sqrt{m_i}} \right) T_i^{\frac{3}{2}} - \left(I_i^{(0)} + I_i^{(1)} \tilde{\lambda}_i \mu \right) \right) , \quad \text{(A.34)}$$

was obtained from (2.146) without time derivatives by introducing an approximate solution of the electron specific intensity

$$\tilde{I}_i = I_i^{(0)} + I_i^{(1)} \tilde{\lambda}_i \mu , \quad \text{(A.35)}$$

which reflects a small spatial deviation with respect to $\tilde{\lambda}_i$ and a small anisotropy effect given by μ from the dominant term $I_i^{(0)}$, which is homogeneous in space and isotropic in angle. The approximate solution (A.35) originates from (A.2).

Since the ion asymptotic equation (A.34) resembles to equation (A.28) with $\alpha = 0$, we can proceed to the ion heat flux evaluation as

$$\mathbf{q}_{BGK}^i = \int_{4\pi} \mathbf{n} \tilde{I}_i d\mathbf{n} = -\frac{256\sqrt{2} n_i}{3\pi^{\frac{3}{2}}} \frac{k_B^{\frac{3}{2}}}{\sqrt{m_i}} \bar{\lambda}_{T_i} \sqrt{T_i} \nabla_{\mathbf{x}} T_e , \quad \text{(A.36)}$$

where we used relation $\tilde{\lambda}_i = \frac{128}{3\pi} \bar{\lambda}_{T_i}$ (2.148), where $\bar{\lambda}_{T_i}$ is the thermal mean free path of ions.

A.4 Diffusion Asymptotic of the Nonlocal BGK Radiation Transport Model

In section 2.5.2 we presented a standard model of radiation transport. In order to extend the understanding about the transport of photons, its diffusion asymptotic should be also described.

The following equation

$$\mathbf{n} \cdot \nabla_{\mathbf{x}} \left(I_p^{(0)} + I_p^{(1)} \tilde{\lambda}_p \mu \right) = \frac{1}{\lambda_p} \left(a T_e^4 - \left(I_p^{(0)} + I_p^{(1)} \lambda_p \mu \right) \right) - \frac{\alpha}{\lambda_p} I_p^{(1)} \lambda_p \mu , \quad \text{(A.37)}$$

was obtained from (2.217) without time derivatives by introducing an approximate solution of the radiation specific intensity

$$\tilde{I}_p = I_p^{(0)} + I_p^{(1)} \lambda_p \mu , \quad \text{(A.38)}$$

which reflects a small spatial deviation with respect to λ_p and a small anisotropy effect given by μ from the dominant term $I_p^{(0)}$, which is homogeneous in space and isotropic in angle. The approximate solution (A.38) originates from (A.2).

Since the radiation asymptotic equation (A.37) resembles to equation (A.28) with $\mathbf{E} = \mathbf{0}$ and different dependence on T_e, we can write the approximate solution (A.38) as

$$\tilde{I}_p = a T_e^4 \left(1 - \frac{4\lambda_p}{T_e} \mathbf{n} \cdot \nabla_{\mathbf{x}} T_e \right) . \quad \text{(A.39)}$$

Then, we can proceed to the radiation heat flux evaluation as

$$\mathbf{q}^p_{BGK} = \int_{4\pi} \mathbf{n}\tilde{I}_p \mathbf{dn} = -\frac{16\pi}{3}\lambda_p T_e^3 \nabla_{\mathbf{x}} T_e \,, \tag{A.40}$$

where we used relation $\lambda_p = \frac{1}{\bar{k}_p}\bar{k}_p$ being the mean Planck opacity (2.218). In astrophysics, the mean Planck opacity is very often substituted in (A.40) by the mean Rosseland opacity [6].

Appendix B

Details of the DG-BGK&Ts Scheme

B.1 The 1D Spherically Symmetric DG-BGK&Ts Scheme

B.1.1 The DG-BGK Transport Scheme

In spherical coordinates the position vector is defined as $\mathbf{x} = (r, \tilde{\phi}, \tilde{\theta})$, where the coordinate axis vectors change according to the position dependence on $(\tilde{\phi}, \tilde{\theta})$, i.e. system is curvilinear. The spherically symmetric geometry implies a reduced dependence of the specific intensity $I(t, \mathbf{n}(\phi), \mathbf{x}(r))$, and the resulting form of the *spherically symmetric transfer equation* reads

$$\frac{1}{c}\frac{\mathrm{d}I}{\mathrm{d}t} + \cos(\phi)\frac{\partial I}{\partial r} - \frac{\sin(\phi)}{r}\frac{\partial I}{\partial \phi} = (\cos(\phi)S_r + S_A)\ T_e + S_b - (\kappa + \cos(\phi)\Upsilon_r)\ I + \sigma\bar{I}, \quad \text{(B.1)}$$

which represents a 3D problem, i.e. the solution I of (B.1) depends on t, ϕ and r. All the coefficients

$$c, \kappa, \Upsilon_r, \sigma, S_r, S_A, S_b, \quad \text{(B.2)}$$

depend, in general, on time t and position r.

The discrete form of the discontinuous Galerkin variation principle (3.10, 3.13) in the case of the 1D spherically symmetric geometry uses the discretization of I and T_e (3.19) where the bases $\boldsymbol{\Psi}$ and $\boldsymbol{\Xi}$ of (3.20) are defined on the spatial domain using the coordinate system $\mathbf{x} = \mathbf{x}(r)$, in particular, the bases ψ and ξ of (3.18) depend on r.

The *discrete 1D spherically symmetric geometry variational form* of the discontinuous Galerkin BGK transport equation (B.1) reads

$$\int_{\Delta t}\int_0^{2\pi}\int_0^{\pi}\int_{\Delta r} \boldsymbol{\Psi} \otimes \left[\left(\frac{1}{c}\frac{\mathrm{d}\boldsymbol{\Psi}^T}{\mathrm{d}t} + \cos(\phi)\frac{\partial\boldsymbol{\Psi}^T}{\partial r} - \frac{\sin(\phi)}{r}\frac{\partial\boldsymbol{\Psi}^T}{\partial\phi} + (\kappa + \cos(\phi)\Upsilon_r)\boldsymbol{\Psi}^T\right.\right.$$

$$\left.\left. - \frac{\sigma}{4\pi}\int\boldsymbol{\Psi}^T\sin(\phi)\mathrm{d}\phi\mathrm{d}\theta\right)\cdot\mathbf{I} - \left((\cos(\phi)S_r + S_A)\ \boldsymbol{\Xi}^T\cdot\mathbf{T}_e + S_b\right)\right]r\mathrm{d}r\sin(\phi)\mathrm{d}\phi\mathrm{d}\theta\mathrm{d}t =$$

$$\int_{\Delta t}\int_0^{2\pi}\int_0^{\pi}\int_{\Gamma_{\mathbf{n}\cdot\mathbf{n}_\Gamma<0}} \boldsymbol{\Psi} \otimes \left[\left(\boldsymbol{\Psi}^T\cdot\mathbf{I} - \tilde{\boldsymbol{\Psi}}^T\cdot\tilde{\mathbf{I}}\right)\cos(\phi)n_{\Gamma_r}\right]\mathrm{d}\Gamma_r\sin(\phi)\mathrm{d}\phi\mathrm{d}\theta\mathrm{d}t, \quad \text{(B.3)}$$

where Δr is the spatial domain of the element and where $\Gamma_{\mathbf{n}\cdot\mathbf{n}_\Gamma<0}$ means the part of boundary Γ where the projection of the transport direction $\mathbf{n}$ into the surface normal $\mathbf{n}_\Gamma$ is less than zero, i.e. $\mathbf{n}\cdot\mathbf{n}_\Gamma = \cos(\phi)n_{\Gamma_r} < 0$.

If one uses the property (3.31), the right hand side of (B.3) can be written as

$$\mathbf{M}_t \otimes \mathbf{M}_\theta \otimes \boldsymbol{\Gamma}_r^- \cdot \mathbf{I} - \mathbf{M}_t \otimes \mathbf{M}_\theta \otimes \left(\tilde{\boldsymbol{\Gamma}}_r^- \cdot \tilde{\mathbf{I}}\right)$$

where we used the t and θ matrices (3.40, 3.43) and the remaining matrices are defined, i.e. the internal DG matrix $\mathbf{\Gamma}_r^-$ as

$$\mathbf{\Gamma}_r^- = \int_0^\pi \int_{\Gamma_{\mathbf{n}\cdot\mathbf{n}_\Gamma < 0}} \left(\omega_\phi \otimes \omega_\phi^T\right) \otimes \left(\psi \otimes \psi^T\right) (\cos(\phi)n_{\Gamma_r})\, r\, \sin(\phi)\mathrm{d}\Gamma \mathrm{d}\phi\,, \qquad \text{(B.4)}$$

and the external DG matrix $\tilde{\mathbf{\Gamma}}_r^-$ trough the term

$$\mathbf{M}_t \otimes \mathbf{M}_\theta \otimes \left(\tilde{\mathbf{\Gamma}}_r^- \cdot \tilde{\mathbf{I}}\right)_\Gamma = \mathbf{M}_t \otimes \mathbf{M}_\theta \otimes$$
$$\sum_{adj} \left[\int_0^\pi \int_{\Gamma_{\mathbf{n}\cdot\mathbf{n}_\Gamma < 0}^{adj}} \left(\omega_\phi \otimes \omega_\phi^T\right) \otimes \left(\psi \otimes \tilde{\psi}_{adj}^T\right) \left(\cos(\phi)n_{\Gamma_r^{adj}}\right) \sin(\phi)\, r\, \mathrm{d}\Gamma^{adj} \mathrm{d}\phi \right] \cdot \tilde{\mathbf{I}}^{adj}\,,$$
$$\text{(B.5)}$$

where adj refers to all adjacent cells, i.e. Γ^{adj} corresponds to the part of the boundary Γ shared with an adjacent cell, where the discretization is $\tilde{I} = \left(\omega_t \otimes \omega_\theta \otimes \omega_\phi \otimes \tilde{\psi}_{adj}\right)^T \cdot \tilde{\mathbf{I}}$.

In the same way as we constructed (B.5), we can apply the products $\mathbf{\Psi} \otimes \mathbf{\Psi}^T$ of (3.31) and $\mathbf{\Psi} \otimes \mathbf{\Xi}^T$ of (3.32) wherever they appear in (B.3), which leads to the *1D spherically symmetric geometry DG-BGK scheme* formulation

$$\left[\frac{1}{c}\mathbf{D}_t \otimes \mathbf{M}_\theta \otimes \mathbf{M}_\phi \otimes \mathbf{M}_r^I + \mathbf{M}_t \otimes \mathbf{M}_\theta \otimes \mathbf{M}_{\cos(\phi)} \otimes \mathbf{D}_{r,r}^I - \mathbf{M}_t \otimes \mathbf{M}_\theta \otimes \mathbf{D}_{\sin(\phi)} \otimes \mathbf{M}_{r/r}^I \right.$$
$$+ \kappa\mathbf{M}_t \otimes \mathbf{M}_\theta \otimes \mathbf{M}_\phi \otimes \mathbf{M}_r^I + \Upsilon_z \mathbf{M}_t \otimes \mathbf{M}_\theta \otimes \mathbf{M}_{\cos(\phi)} \otimes \mathbf{M}_r^I$$
$$\left. - \frac{\sigma}{4\pi}\mathbf{M}_t \otimes \left(\mathbf{M}_\theta^0 \otimes 2\mathbf{M}_\theta^{0T}\right) \otimes \left(\mathbf{M}_\phi^0 \otimes \mathbf{M}_\phi^{0T}\right) \otimes \mathbf{M}_r^I - \mathbf{M}_t \otimes \mathbf{M}_\theta \otimes \mathbf{\Gamma}_r^- \right] \cdot \mathbf{I} =$$
$$\left[S_r\mathbf{M}_t \otimes \mathbf{M}_\theta^0 \otimes \mathbf{M}_{\cos(\phi)}^0 \otimes \mathbf{M}_r^{I,Te} + S_A\mathbf{M}_t \otimes \mathbf{M}_\theta^0 \otimes \mathbf{M}_\phi^0 \otimes \mathbf{M}_r^{I,Te} \right] \cdot \mathbf{T}_e + S_b\mathbf{M}_t^0 \otimes \mathbf{M}_\theta^0 \otimes \mathbf{M}_\phi^0 \otimes \mathbf{M}_r^{I,0}$$
$$- \mathbf{M}_t \otimes \mathbf{M}_\theta \otimes \left(\tilde{\mathbf{\Gamma}}_r^- \cdot \tilde{\mathbf{I}}\right)_\Gamma\,, \quad \text{(B.6)}$$

where apart from the already defined t, θ, and ϕ matrices (3.39, 3.40, 3.41, 3.43, 3.46, 3.49, 3.50, 3.51, 3.53, 3.54), we define the spatial discretization matrices

$$\mathbf{M}_r^I = \int_{\Delta r} \psi(r) \otimes \psi(r)^T r\, \mathrm{d}r\,, \qquad \text{(B.7)}$$

$$\mathbf{D}_{r,r}^I = \int_{\Delta r} \psi(r) \otimes \frac{\partial\psi(r)^T}{\partial r} r\, \mathrm{d}r \qquad \text{(B.8)}$$

$$\mathbf{M}_{r/r}^I = \int_{\Delta r} \psi(r) \otimes \psi(r)^T \mathrm{d}r\,, \qquad \text{(B.9)}$$

$$\mathbf{M}_r^{I,Te} = \int_{\Delta r} \psi(r) \otimes \xi(r)^T r\, \mathrm{d}r\,, \qquad \text{(B.10)}$$

$$\mathbf{M}_r^{I,0} = \int_{\Delta r} \psi(r) \otimes \omega_0^T r\, \mathrm{d}r\,, \qquad \text{(B.11)}$$

The main goal of the 1D spherically symmetric geometry DG-BGK scheme (B.6) of the transport equation (B.1) resides in finding the linear dependence of the unknown $\mathbf{I}$

on the unknown $\mathbf{T}_e$ [97, 98, 100, 51, 50] as

$$\mathbf{I} = \mathbf{A}_r \cdot \mathbf{T}_e + \mathbf{b}_r \,, \tag{B.12}$$

which can be directly obtained from (B.6) after some straightforward algebraic operations. It is worth mentioning, that the adjacent cells discretization $\tilde{\mathbf{I}}$ is absorbed in the $\mathbf{b}_r$ vector.

As was stated before, we want to make use of the lowest order backward Euler time discretization. The *1D spherically symmetric geometry backward Euler DG-BGK scheme* can be obtained by using the backward Euler time matrices (3.42) in (B.6), thus giving

$$\left[\frac{1}{c\Delta t}\mathbf{M}_\theta \otimes \mathbf{M}_\phi \otimes \mathbf{M}_r^I + \mathbf{M}_\theta \otimes \mathbf{M}_{\cos(\phi)} \otimes \mathbf{D}_{r,r}^I - \mathbf{M}_\theta \otimes \mathbf{D}_{\sin(\phi)} \otimes \mathbf{M}_{r/r}^I + \kappa\mathbf{M}_\theta \otimes \mathbf{M}_\phi \otimes \mathbf{M}_r^I + \right.$$

$$\left. \Upsilon_r\mathbf{M}_\theta \otimes \mathbf{M}_{\cos(\phi)} \otimes \mathbf{M}_r^I - \frac{\sigma}{4\pi}\left(\mathbf{M}_\theta^0 \otimes 2\mathbf{M}_\theta^{0T}\right) \otimes \left(\mathbf{M}_\phi^0 \otimes \mathbf{M}_\phi^{0T}\right) \otimes \mathbf{M}_r^I - \mathbf{M}_\theta \otimes \mathbf{\Gamma}_r^- \right] \cdot \mathbf{I}^1 =$$

$$\left[S_r\mathbf{M}_\theta^0 \otimes \mathbf{M}_{\cos(\phi)}^0 \otimes \mathbf{M}_r^{I,Te} + S_A\mathbf{M}_\theta^0 \otimes \mathbf{M}_\phi^0 \otimes \mathbf{M}_r^{I,Te} \right] \cdot \mathbf{T}_e + S_b\mathbf{M}_\theta^0 \otimes \mathbf{M}_\phi^0 \otimes \mathbf{M}_r^{I,0}$$

$$- \mathbf{M}_\theta \otimes \left(\tilde{\mathbf{\Gamma}}_r^- \cdot \tilde{\mathbf{I}}_1\right)_\Gamma + \frac{1}{c\Delta t}\mathbf{M}_\theta \otimes \mathbf{M}_\phi \otimes \mathbf{M}_r^I \cdot \mathbf{I}^0 \,, \quad \text{(B.13)}$$

where the discretization $\mathbf{I}$ has been divided into its explicit part $\mathbf{I}^0$ and its implicit part $\mathbf{I}^1$ according to (3.21) and (3.22), respectively. The scheme also uses only the implicit part of the unknown $\mathbf{T}_e$, i.e. $\mathbf{T}_e^1$ defined in (3.24).

In the case of the backward Euler scheme (B.13), we can explicitly write

$$\mathbf{A}_r = \mathbf{L}_r^{-1} \cdot \left[\mathbf{M}_{\cos(\phi)}^0 \otimes S_r\mathbf{M}_r^{I,Te} + \mathbf{M}_\phi^0 \otimes S_A\mathbf{M}_r^{I,Te} \right] \,, \tag{B.14}$$

$$\mathbf{b}_r = \mathbf{L}_r^{-1} \cdot \left[\mathbf{M}_\phi^0 \otimes S_b\mathbf{M}_r^{I,0} - \left(\tilde{\mathbf{\Gamma}}_r^- \cdot \tilde{\mathbf{I}}_1\right)_\Gamma + \frac{1}{c\Delta t}\mathbf{M}_\phi \otimes \mathbf{M}_r^I \cdot \mathbf{I}_0 \right] \,, \tag{B.15}$$

which includes the inversion of the element matrix

$$\mathbf{L}_r = \left[\mathbf{M}_\phi \otimes \frac{1}{c\Delta t}\mathbf{M}_r^I + \mathbf{M}_{\cos(\phi)} \otimes \mathbf{D}_{r,r}^I - \mathbf{D}_{\sin(\phi)} \otimes \mathbf{M}_{r/r}^I + \mathbf{M}_\phi \otimes \kappa\mathbf{M}_r^I + \right.$$

$$\left. \mathbf{M}_{\cos(\phi)} \otimes \Upsilon_r\mathbf{M}_r^I - \left(\mathbf{M}_\phi^0 \otimes \mathbf{M}_\phi^{0T}\right) \otimes \frac{\sigma}{2}\mathbf{M}_r^I - \mathbf{\Gamma}_r^- \right] \tag{B.16}$$

Finally, we can write the backward Euler solution to (B.1) as a linear function of the unknown $\mathbf{T}_e$ [51, 50]

$$\mathbf{I}^1 = \mathbf{A}_r \cdot \mathbf{T}_e^1 + \mathbf{b}_r \,, \tag{B.17}$$

where the linear coefficient $\mathbf{A}_r$ and the constant vector $\mathbf{b}_r$ are defined in (B.14) and (B.15), respectively.

It was opted at the beginning of this section that all the coefficients of (B.2) depend, in general, on time t and position r. Nevertheless, when used in the schemes (B.6) and (B.13), we need to put some restrictions on the form of the latter coefficients.

In the case of the backward Euler scheme (B.13) any time dependence of (B.2) cannot be included by definition. The best option is to use their mean values over Δt. However, the dependence on r can be enforced in the finite element matrices construction, e.g. the spatial dependence of the extinction coefficient κ can be included as

$$\kappa \mathbf{M}_r^I = \int_{\Delta r} \psi(r) \otimes \psi(r)^T \kappa(r) r \, \mathrm{d}r \,,$$

which appears in (B.16) and other coefficients of (B.2) can be treated in the exactly same manner.

The approach to be used in the case of the scheme (B.6) is equivalent, while we impose the condition of separable dependence on time and on space of coefficients (B.2). We show an example of the extinction coefficient κ, which needs to be written as $\kappa(t, r) = g(t)f(r)$. Then, the inclusion of the latter dependence reads

$$\kappa \mathbf{M}_t \otimes \mathbf{M}_\theta \otimes \mathbf{M}_\phi \otimes \mathbf{M}_r^I = \int_{\Delta t} \omega_t \otimes \omega_t^T g(t) \, \mathrm{d}t \otimes \mathbf{M}_\theta \otimes \mathbf{M}_\phi \otimes \int_{\Delta r} \psi(r) \otimes \psi(r)^T f(r) r \, \mathrm{d}r \,,$$

which can be directly used in (B.6). The treatment of other coefficients of (B.2) simply follows the example above.

It is worth mentioning that the spatial discretization matrices (B.7, B.8, B.10, B.11) are integrated over a 1D interval Δr, which is a simple quadrature rule operation using a mapping based on the Δr scaling. One can observe, that the boundary matrices $\mathbf{\Gamma}_r^-$ (B.4) and $\tilde{\mathbf{\Gamma}}_r^-$ (B.5) can also be written separated as

$$\mathbf{\Gamma}_r^- = \sum_{F=+,-} \int_0^\pi \omega_\phi \otimes \omega_\phi^T \left(\cos(\phi) n_{\Gamma_r^F} \right) \sin(\phi) \, \mathrm{d}\phi \otimes \int_{\Gamma^F} \psi(r) \otimes \psi(r)^T r \, \mathrm{d}\Gamma^F \,,$$

$$\tilde{\mathbf{\Gamma}}_r^- = \sum_{F=+,-} \int_0^\pi \omega_\phi \otimes \omega_\phi^T \left(\cos(\phi) n_{\Gamma_r^F} \right) \sin(\phi) \, \mathrm{d}\phi \otimes \int_{\Gamma^F} \psi(r) \otimes \tilde{\psi}(r)^T r \, \mathrm{d}\Gamma^F \,,$$

since neither of the normals n_{Γ_r} and $n_{\Gamma_r^{adj}}$ depend on the position r. In the spherically symmetric geometry, the boundary Γ consists of two parts Γ^+ and Γ^-, which represented by constant vectors $\mathbf{n}_{\Gamma^+} = [n_{\Gamma_r^+} = 1, 0, 0]^T$ and $\mathbf{n}_{\Gamma^-} = [n_{\Gamma_r^-} = -1, 0, 0]^T$. In the definitions above, the integration over the angle ϕ applies only where $\cos(\phi) n_{\Gamma_r^F} < 0$. A special attention must be paid when evaluating the mass boundary $\int_{\Gamma^F} \psi(r) \otimes \tilde{\psi}^F(r)^T r \, \mathrm{d}\Gamma^F$ since the neighbor element basis $\tilde{\psi}^F$ is used.

B.1.2 The DG-T_e Temperature Scheme

The spherically symmetric geometry implies a reduced dependence of the electron temperature $T_e(t, \mathbf{x}(r))$, and the resulting form of the *spherically symmetric electron temperature equation* reads

$$a_e \frac{\mathrm{d}T_e}{\mathrm{d}t} + \int_0^{2\pi} \int_0^\pi \left(\frac{1}{c} \frac{\mathrm{d}I}{\mathrm{d}t} + \cos(\phi) \frac{\partial I}{\partial r} - \frac{\sin(\phi)}{r} \frac{\partial I}{\partial \phi} \right) \sin(\phi) \mathrm{d}\phi \mathrm{d}\theta + G_{ie} T_e = P_e + G_{ie} T_i \,, \tag{B.18}$$

which represents a 3D problem, i.e. the solution T_e of (B.18) depends on t, r and ϕ due to I. All the coefficients

$$c, a_e, G_{ie}, P_e \,, \tag{B.19}$$

depend, in general, on time t and position r.

The discrete form of the discontinuous Galerkin variation principle (3.8) in the case of the 1D spherically symmetric geometry uses the discretization of T_e, I, and T_i (3.19) where the bases $\boldsymbol{\Xi}$, $\boldsymbol{\Psi}$, and $\tilde{\boldsymbol{\Xi}}$ of (3.20) are defined on the spatial domain using the co-ordinate system $\mathbf{x} = \mathbf{x}(r)$, in particular, the bases ξ, ψ, and $\tilde{\xi}$ of (3.18) depend on r.

The *discrete 1D spherically symmetric geometry variational form* of the discontinuous Galerkin electron temperature equation (B.18) reads

$$
\int_{\Delta t}\int_{\Delta r} \boldsymbol{\Xi} \otimes \left[\left(a_e \frac{\mathrm{d}\boldsymbol{\Xi}^T}{\mathrm{d}t} + G_{ie}\boldsymbol{\Xi}^T \right) \cdot \mathbf{T}_e + \right.
$$
$$
\left(\int_0^{2\pi}\int_0^{\pi} \left(\frac{1}{c}\frac{\mathrm{d}\boldsymbol{\Psi}^T}{\mathrm{d}t} + \cos(\phi)\frac{\partial\boldsymbol{\Psi}^T}{\partial r} - \frac{\sin(\phi)}{r}\frac{\partial\boldsymbol{\Psi}^T}{\partial\phi} \right) \sin(\phi)\mathrm{d}\phi\mathrm{d}\theta \right) \cdot \mathbf{I}
$$
$$
\left. - P_e - G_{ie}\tilde{\boldsymbol{\Xi}}^T \cdot \mathbf{T}_i \right] r\mathrm{d}r\mathrm{d}t = 0\,. \quad \text{(B.20)}
$$

where Δr is the spatial domain of the element.

We can apply the products $\boldsymbol{\Xi} \otimes \boldsymbol{\Xi}^T$ of (3.34), $\boldsymbol{\Xi} \otimes \boldsymbol{\Psi}^T$ of (3.33), and $\boldsymbol{\Xi} \otimes \tilde{\boldsymbol{\Xi}}^T$ of (3.36) wherever they appear in (B.20), which leads to the *1D spherically symmetric geometry DG-T_e scheme* formulation

$$
\left[a_e\mathbf{D}_t \otimes \mathbf{M}_r^{Te} + G_{ie}\mathbf{M}_t \otimes \mathbf{M}_r^{Te} \right] \cdot \mathbf{T}_e - P_e\mathbf{M}_t^0 \otimes \mathbf{M}_r^{Te,0} - G_{ie}\mathbf{M}_t \otimes \mathbf{M}_r^{Te,T_i} \cdot \mathbf{T}_i
$$
$$
+ \left[\frac{1}{c}\mathbf{D}_t \otimes 2\mathbf{M}_\theta^0 \otimes \mathbf{M}_\phi^0 \otimes \mathbf{M}_r^{Te,I} + \mathbf{M}_t \otimes 2\mathbf{M}_\theta^0 \otimes \mathbf{M}_{\cos(\phi)}^0 \otimes \mathbf{D}_{r,r}^{Te,I} \right.
$$
$$
\left. - \mathbf{M}_t \otimes 2\mathbf{M}_\theta^0 \otimes \mathbf{D}_{\sin(\phi)}^0 \otimes \mathbf{M}_{r/r}^{Te,I} \right] \cdot \mathbf{I} = 0\,, \quad \text{(B.21)}
$$

where apart from the already defined t, θ, and ϕ matrices (3.39, 3.40, 3.41, 3.46, 3.53, 3.54, 3.55), we define the spatial discretization matrices

$$
\mathbf{M}_r^{Te} = \int_{\Delta r} \xi \otimes \xi^T r\,\mathrm{d}r\,, \quad \text{(B.22)}
$$

$$
\mathbf{M}_r^{Te,I} = \int_{\Delta r} \xi \otimes \psi^T r\,\mathrm{d}r = \mathbf{M}_r^{I,Te\,T}\,, \quad \text{(B.23)}
$$

$$
\mathbf{D}_{r,r}^{Te,I} = \int_{\Delta r} \xi \otimes \frac{\partial\psi^T}{\partial r} r\,\mathrm{d}r \quad \text{(B.24)}
$$

$$
\mathbf{M}_{r/r}^{Te,I} = \int_{\Delta r} \xi \otimes \psi^T \,\mathrm{d}r\,, \quad \text{(B.25)}
$$

$$
\mathbf{M}_r^{Te,0} = \int_{\Delta r} \xi \otimes \omega_0^T r\,\mathrm{d}r\,, \quad \text{(B.26)}
$$

$$
\mathbf{M}_r^{Te,T_i} = \int_{\Delta r} \xi \otimes \tilde{\xi}^T r\,\mathrm{d}r\,. \quad \text{(B.27)}
$$

Now, the linear function solution (B.12) can be justified. The latter has the form $\mathbf{I} = \mathbf{A}_r \cdot \mathbf{T}_e + \mathbf{b}_r$, which when plugged in (B.21) provides the *1D spherically symmetric*

geometry DG-T$_e$ electron temperature scheme

$$
\left[a_e \mathbf{D}_t \otimes \mathbf{M}_r^{Te} + G_{ie} \mathbf{M}_t \otimes \mathbf{M}_r^{Te} \right] \cdot \mathbf{T}_e - P_e \mathbf{M}_t^0 \otimes \mathbf{M}_r^{Te,0} - G_{ie} \mathbf{M}_t \otimes \mathbf{M}_r^{Te,T_i} \cdot \mathbf{T}_i +
$$

$$
\left[\frac{1}{c} \mathbf{D}_t \otimes 2\mathbf{M}_\theta^0 \otimes \mathbf{M}_\phi^0 \otimes \mathbf{M}_r^{Te,I} + \mathbf{M}_t \otimes 2\mathbf{M}_\theta^0 \otimes \mathbf{M}_{\cos(\phi)}^0 \otimes \mathbf{D}_{r,r}^{Te,I} \right.
$$

$$
\left. - \mathbf{M}_t \otimes 2\mathbf{M}_\theta^0 \otimes \mathbf{D}_{\sin(\phi)}^0 \otimes \mathbf{M}_{r/r}^{Te,I} \right] \cdot (\mathbf{A}_r \cdot \mathbf{T}_e + \mathbf{b}_r) = 0 \,, \quad \text{(B.28)}
$$

which is apparently a problem of the unknown $\mathbf{T}_e$ and the unknown $\mathbf{T}_i$. Nevertheless, the former unknown $\mathbf{I}$ is implicitly coupled via the matrix $\mathbf{A}_r$ and the vector $\mathbf{b}_r$.

As was stated before, we want to make use of the lowest order backward Euler time discretization. The *1D spherically symmetric geometry backward Euler DG-T$_e$ scheme* can be obtained by using the backward Euler time matrices (3.42) in (B.28), thus giving

$$
\left[\frac{a_e}{\Delta t} \mathbf{M}_r^{Te} + G_{ie} \mathbf{M}_r^{Te} \right] \cdot \mathbf{T}_e^1 - P_e \mathbf{M}_r^{Te,0} - G_{ie} \mathbf{M}_r^{Te,T_i} \cdot \mathbf{T}_i^1 +
$$

$$
\left[2\mathbf{M}_\theta^0 \otimes \left(\mathbf{M}_\phi^0 \otimes \frac{1}{c\Delta t} \mathbf{M}_r^{Te,I} + \mathbf{M}_{\cos(\phi)}^0 \otimes \mathbf{D}_{r,r}^{Te,I} - \mathbf{D}_{\sin(\phi)}^0 \otimes \mathbf{M}_{r/r}^{Te,I} \right) \right] \cdot \left(\mathbf{A}_r \cdot \mathbf{T}_e^1 + \mathbf{b}_r \right) =
$$

$$
\frac{a_e}{\Delta t} \mathbf{M}_r^{Te} \cdot \mathbf{T}_e^0 + 2\mathbf{M}_\theta^0 \otimes \mathbf{M}_\phi^0 \otimes \frac{1}{c\Delta t} \mathbf{M}_r^{Te,I} \cdot \mathbf{I}^0 \,, \quad \text{(B.29)}
$$

where each of the discretizations $\mathbf{T}_e$ and $\mathbf{I}$ have been divided into its explicit part, i.e. $\mathbf{T_e^0}$ and $\mathbf{I^0}$, respectively, and its implicit part, i.e. $\mathbf{T}_e^1$ and $\mathbf{I}^1$ respectively, according to (3.23, 3.24) and (3.21, 3.22), respectively. The scheme also uses only the implicit part of the unknown $\mathbf{T}_i$, i.e. $\mathbf{T}_i^1$ defined in (3.26). The matrix $\mathbf{A}_r$ and the vector $\mathbf{b}_r$ are defined in (B.14) and (B.15).

It was opted at the beginning of this section that all the coefficients of (B.19) depend, in general, on time t and position r. Nevertheless, when used in the schemes (B.28) and (B.29), we need to put some restrictions on the form of the latter coefficients.

In the case of the backward Euler scheme (B.29) any time dependence of (B.19) cannot be included by definition. The best option is to use their mean values over Δt. However, the dependence on r can be enforced in the finite element matrices construction, e.g. the spatial dependence of the heat capacity coefficient a_e can be included as

$$
a_e \mathbf{M}_r^{Te} = \int_{\Delta r} \xi(r) \otimes \xi(r)^T a_e(r) r \, \mathrm{d}z \,,
$$

which appears in (B.29) and other coefficients of (B.19) can be treated in the exactly same manner.

The approach to be used in the case of the scheme (B.28) is equivalent, while we impose the condition of separable dependence on time and on space of coefficients (B.19). We show an example of the heat capacity coefficient a_e, which needs to be written as $a_e(t, r) = g(t) f(r)$. Then, the inclusion of the latter dependence reads

$$
a_e \mathbf{D}_t \otimes \mathbf{M}_r^{Te} = \int_{\Delta t} \omega_t \otimes \frac{\mathrm{d}\omega_t^T}{\mathrm{d}t} g(t) \, \mathrm{d}t \otimes \int_{\Delta r} \xi(r) \otimes \xi(r)^T f(r) r \, \mathrm{d}r \,,
$$

which can be directly used in (B.28). The treatment of other coefficients of (B.19) simply follows the example above.

B.1.3 The DG-T_i Temperature Scheme

The spherically symmetric geometry implies a reduced dependence of the ion temperature $T_i(t, \mathbf{x}(r))$, and the resulting form of the *spherically symmetric ion temperature equation* reads

$$a_i \frac{\mathrm{d}T_i}{\mathrm{d}t} + G_{ie}T_i = P_i + G_{ie}T_e \,, \tag{B.30}$$

which represents a 2D problem, i.e. the solution T_i of (B.30) depends on t and r. All the coefficients

$$a_i, G_{ie}, P_i \,, \tag{B.31}$$

depend, in general, on time t and position r.

The discrete form of the discontinuous Galerkin variation principle (3.9) in the case of the 1D spherically symmetric geometry uses the discretization of T_i, and T_e (3.19) where the bases $\tilde{\boldsymbol{\Xi}}$, and $\boldsymbol{\Xi}$ of (3.20) are defined on the spatial domain using the coordinate system $\mathbf{x} = \mathbf{x}(r)$, in particular, the bases $\tilde{\xi}$, and ξ of (3.18) depend on r.

The *discrete 1D spherically symmetric geometry variational form* of the discontinuous Galerkin ion temperature equation (B.30) reads

$$\int_{\Delta t} \int_{\Delta r} \tilde{\boldsymbol{\Xi}} \otimes \left[\left(a_i \frac{\mathrm{d}\tilde{\boldsymbol{\Xi}}^T}{\mathrm{d}t} + G_{ie}\tilde{\boldsymbol{\Xi}}^T \right) \cdot \mathbf{T}_i - P_i - G_{ie}\boldsymbol{\Xi}^T \cdot \mathbf{T}_e \right] r \mathrm{d}r \mathrm{d}t = 0 \,, \tag{B.32}$$

where Δr is the spatial domain of the element.

We can apply the products $\tilde{\boldsymbol{\Xi}} \otimes \tilde{\boldsymbol{\Xi}}^T$ of (3.35), and $\tilde{\boldsymbol{\Xi}} \otimes \boldsymbol{\Xi}^T$ of (3.37) wherever they appear in (B.32), which leads to the *1D spherically symmetric geometry DG-T_i scheme* formulation

$$\left[a_i \mathbf{D}_t \otimes \mathbf{M}_r^{T_i} + G_{ie}\mathbf{M}_t \otimes \mathbf{M}_r^{T_i} \right] \cdot \mathbf{T}_i - G_{ie}\mathbf{M}_t \otimes \mathbf{M}_r^{T_i,T_e} \cdot \mathbf{T}_e = P_i \mathbf{M}_t^0 \otimes \mathbf{M}_r^{T_i,0} \,, \tag{B.33}$$

where apart from the already defined t matrices (3.39, 3.40, 3.41), we define the spatial discretization matrices

$$\mathbf{M}_r^{T_i} = \int_{\Delta r} \tilde{\xi} \otimes \tilde{\xi}^T r \, \mathrm{d}r \,, \tag{B.34}$$

$$\mathbf{M}_r^{T_i,0} = \int_{\Delta r} \tilde{\xi} \otimes \omega_0^T r \, \mathrm{d}r \,, \tag{B.35}$$

$$\mathbf{M}_r^{T_i,T_e} = \int_{\Delta r} \tilde{\xi} \otimes \xi^T r \, \mathrm{d}r = \mathbf{M}_r^{T_e,T_i T} \,. \tag{B.36}$$

As was stated before, we want to make use of the lowest order backward Euler time discretization. The *1D spherically symmetric geometry backward Euler DG-T_i scheme* can be obtained by using the backward Euler time matrices (3.42) in (B.33), thus giving

$$\left[\frac{a_i}{\Delta t}\mathbf{M}_r^{T_i} + G_{ie}\mathbf{M}_r^{T_i} \right] \cdot \mathbf{T}_i^1 - G_{ie}\mathbf{M}_r^{T_i,T_e} \cdot \mathbf{T}_e^1 = P_i \mathbf{M}_r^{T_i,0} + \frac{a_i}{\Delta t}\mathbf{M}_r^{T_i} \cdot \mathbf{T}_i^0 \,, \tag{B.37}$$

where the discretization $\mathbf{T}_i$ has been divided into its explicit part $\mathbf{T}_{\mathbf{i}}^{\mathbf{0}}$ and its implicit part $\mathbf{T}_i^1$ according to (3.25, 3.26). The scheme also uses only the implicit part of the unknown $\mathbf{T}_e$, i.e. $\mathbf{T}_e^1$ defined in (3.24).

It was opted at the beginning of this section that all the coefficients of (B.31) depend, in general, on time t and position r. Nevertheless, when used in the schemes (B.33) and (B.37), we need to put some restrictions on the form of the latter coefficients.

In the case of the backward Euler scheme (B.37) any time dependence of (B.31) cannot be included by definition. The best option is to use their mean values over Δt. However, the dependence on r can be enforced in the finite element matrices construction, e.g. the spatial dependence of the heat capacity coefficient a_i can be included as

$$a_i \mathbf{M}_r^{T_i} = \int_{\Delta r} \tilde{\xi}(r) \otimes \tilde{\xi}(r)^T a_i(r) r \, \mathrm{d}z \,,$$

which appears in (B.37) and other coefficients of (B.31) can be treated in the exactly same manner.

The approach to be used in the case of the scheme (B.33) is equivalent, while we impose the condition of separable dependence on time and on space of coefficients (B.31). We show an example of the heat capacity coefficient a_i, which needs to be written as $a_i(t,r) = g(t)f(r)$. Then, the inclusion of the latter dependence reads

$$a_i \mathbf{D}_t \otimes \mathbf{M}_r^{T_i} = \int_{\Delta t} \omega_t \otimes \frac{\mathrm{d}\omega_t^T}{\mathrm{d}t} g(t) \, \mathrm{d}t \otimes \int_{\Delta r} \tilde{\xi}(r) \otimes \tilde{\xi}(r)^T f(r) r \, \mathrm{d}r \,,$$

which can be directly used in (B.33). The treatment of other coefficients of (B.31) simply follows the example above.

B.2   The 2D Axisymmetric DG-BGK&Ts Scheme

B.2.1   The DG-BGK Transport Scheme

In cylindrical coordinates the position vector is defined as $\mathbf{x} = (r, \tilde{\theta}, z)$, where the coordinate axis vectors change according to the position dependence on $(\tilde{\theta})$, i.e. system is curvilinear. The axisymmetric geometry implies a reduced dependence of the specific intensity $I(t, \mathbf{n}(\phi, \theta), \mathbf{x}(r, z))$, and the resulting form of the *axisymmetric transfer equation* reads

$$\frac{1}{c}\frac{\mathrm{d}I}{\mathrm{d}t} + \sin(\phi)\left(\cos(\theta)\frac{\partial I}{\partial r} - \frac{\sin(\theta)}{r}\frac{\partial I}{\partial \theta}\right) + \cos(\phi)\frac{\partial I}{\partial z} =$$

$$(\sin(\phi)\cos(\theta)S_r + \cos(\phi)S_z + S_A)\, T_e + S_b - (\kappa + \sin(\phi)\cos(\theta)\Upsilon_r + \cos(\phi)\Upsilon_z)\, I + \sigma\bar{I}\,,$$

$$\tag{B.38}$$

which represents a 5D problem, i.e. the solution I of (B.38) depends on t, ϕ, θ and r, z. All the coefficients

$$c, \kappa, \Upsilon_r, \Upsilon_z, \sigma, S_r, S_z, S_A, S_b \,, \tag{B.39}$$

depend, in general, on time t and position r, z.

The discrete form of the discontinuous Galerkin variation principle (3.10, 3.13) in the case of the 1D axisymmetric geometry uses the discretization of I and T_e (3.19) where the bases $\mathbf{\Psi}$ and $\mathbf{\Xi}$ of (3.20) are defined on the spatial domain using the coordinate system $\mathbf{x} = \mathbf{x}(r, z)$, in particular, the bases ψ and ξ of (3.18) depend on r and z.

The *discrete 2D axisymmetric geometry variational form* of the discontinuous Galerkin BGK transport equation (B.38) reads

$$
\int_{\Delta t}\int_0^{2\pi}\int_0^{\pi}\int_{\Omega_{rz}}\boldsymbol{\Psi}\otimes\left[\left(\frac{1}{c}\frac{\mathrm{d}\boldsymbol{\Psi}^T}{\mathrm{d}t}+\sin(\phi)\left(\cos(\theta)\frac{\partial\boldsymbol{\Psi}^T}{\partial r}-\frac{\sin(\theta)}{r}\frac{\partial\boldsymbol{\Psi}^T}{\partial\theta}\right)+\cos(\phi)\frac{\partial\boldsymbol{\Psi}^T}{\partial z}\right.\right.
$$

$$
+(\kappa+\sin(\phi)\cos(\theta)\Upsilon_r+\cos(\phi)\Upsilon_z)\boldsymbol{\Psi}^T-\frac{\sigma}{4\pi}\int\boldsymbol{\Psi}^T\sin(\phi)\mathrm{d}\phi\mathrm{d}\theta\bigg)\cdot\mathbf{I}
$$

$$
\left.-\left((\sin(\phi)\cos(\theta)S_r+\cos(\phi)S_z+S_A)\,\boldsymbol{\Xi}^T\cdot\mathbf{T}_e+S_b\right)\right]r\mathrm{d}\Omega_{rz}\sin(\phi)\mathrm{d}\phi\mathrm{d}\theta\mathrm{d}t=
$$

$$
\int_{\Delta t}\int_0^{2\pi}\int_0^{\pi}\int_{\Gamma_{\mathbf{n}\cdot\mathbf{n}_{\Gamma}<0}}\Psi\otimes\left[\left(\boldsymbol{\Psi}^T\cdot\mathbf{I}-\tilde{\boldsymbol{\Psi}}^T\cdot\tilde{\mathbf{I}}\right)(\sin(\phi)\cos(\theta)n_{\Gamma_r}+\cos(\phi)n_{\Gamma_z})\right]
$$

$$
\mathrm{d}\Gamma_{rz}\sin(\phi)\mathrm{d}\phi\mathrm{d}\theta\mathrm{d}t\,,\quad\text{(B.40)}
$$

where Ω_{rz} is a general spatial domain of the element and $\Gamma_{\mathbf{n}\cdot\mathbf{n}_{\Gamma}<0}$ means the part of boundary Γ_{rz} where the projection of the transport direction $\mathbf{n}$ into the surface normal $\mathbf{n}_{\Gamma}$ is less than zero, i.e. $\mathbf{n}\cdot\mathbf{n}_{\Gamma}=\sin(\phi)\cos(\theta)n_{\Gamma_r}+\cos(\phi)n_{\Gamma_z}<0$.

If one uses the property (3.31), the right hand side of (B.40) can be written as

$$
\mathbf{M}_t\otimes\boldsymbol{\Gamma}_z^-\cdot\mathbf{I}-\mathbf{M}_t\otimes\left(\tilde{\boldsymbol{\Gamma}}_z^-\cdot\tilde{\mathbf{I}}\right)
$$

where we used the t matrix (3.40) and the remaining matrices are defined, i.e. the internal DG matrix $\boldsymbol{\Gamma}_{rz}^-$ as

$$
\boldsymbol{\Gamma}_{rz}^-=\int_0^{\pi}\int_0^{\pi}\int_{\Gamma_{\mathbf{n}\cdot\mathbf{n}_{\Gamma}<0}}\left(\omega_\theta\otimes\omega_\theta^T\right)\otimes\left(\omega_\phi\otimes\omega_\phi^T\right)\otimes\left(\psi\otimes\psi^T\right)
$$

$$
(\sin(\phi)\cos(\theta)n_{\Gamma_r}+\cos(\phi)n_{\Gamma_z})\,r\,\sin(\phi)\mathrm{d}\Gamma\mathrm{d}\phi\mathrm{d}\theta\,,\quad\text{(B.41)}
$$

and the external DG matrix $\tilde{\boldsymbol{\Gamma}}_{rz}^-$ trough the term

$$
\mathbf{M}_t\otimes\left(\tilde{\boldsymbol{\Gamma}}_{rz}^-\cdot\tilde{\mathbf{I}}\right)_\Gamma=\mathbf{M}_t\otimes\sum_{adj}\left[\int_0^{\pi}\int_0^{\pi}\int_{\Gamma_{\mathbf{n}\cdot\mathbf{n}_{\Gamma}<0}^{adj}}\left(\omega_\theta\otimes\omega_\theta^T\right)\otimes\left(\omega_\phi\otimes\omega_\phi^T\right)\otimes\left(\psi\otimes\tilde{\psi}_{adj}^T\right)\right.
$$

$$
\left.(\sin(\phi)\cos(\theta)n_{\Gamma_r}+\cos(\phi)n_{\Gamma_z})\sin(\phi)\,r\,\mathrm{d}\Gamma^{adj}\mathrm{d}\phi\mathrm{d}\theta\right]\cdot\tilde{\mathbf{I}}^{adj}\,,\quad\text{(B.42)}
$$

where *adj* refers to all adjacent cells, i.e. Γ^{adj} corresponds to the part of the boundary Γ shared with an adjacent cell, where the discretization is $\tilde{I}=\left(\omega_t\otimes\omega_\theta\otimes\omega_\phi\otimes\tilde{\psi}_{adj}\right)^T\cdot\tilde{\mathbf{I}}$.

In the same way as we constructed (B.42), we can apply the products $\boldsymbol{\Psi}\otimes\boldsymbol{\Psi}^T$ of (3.31) and $\boldsymbol{\Psi}\otimes\boldsymbol{\Xi}^T$ of (3.32) wherever they appear in (3.111), which leads to the *2D*

axisymmetric geometry DG-BGK scheme formulation

$$
\begin{aligned}
&\Bigg[\frac{1}{c}\mathbf{D}_t\otimes\mathbf{M}_\theta\otimes\mathbf{M}_\phi\otimes\mathbf{M}_{rz}^I+\mathbf{M}_t\otimes\mathbf{M}_{\cos(\theta)}\otimes\mathbf{M}_{\sin(\phi)}\otimes\mathbf{D}_{rz,r}^I-\mathbf{M}_t\otimes\mathbf{D}_{\sin(\theta)}\otimes\mathbf{M}_{\sin(\phi)}\otimes\mathbf{M}_{rz/r}^I\\
&+\mathbf{M}_t\otimes\mathbf{M}_\theta\otimes\mathbf{M}_{\cos(\phi)}\otimes\mathbf{D}_{rz,z}^I+\kappa\mathbf{M}_t\otimes\mathbf{M}_\theta\otimes\mathbf{M}_\phi\otimes\mathbf{M}_{rz}^I+\Upsilon_r\mathbf{M}_t\otimes\mathbf{M}_{\cos(\theta)}\otimes\mathbf{M}_{\sin(\phi)}\otimes\mathbf{M}_{rz}^I\\
&+\Upsilon_z\mathbf{M}_t\otimes\mathbf{M}_\theta\otimes\mathbf{M}_{\cos(\phi)}\otimes\mathbf{M}_{rz}^I-\frac{\sigma}{4\pi}\mathbf{M}_t\otimes\left(\mathbf{M}_\theta^0\otimes2\mathbf{M}_\theta^{0\,T}\right)\otimes\left(\mathbf{M}_\phi^0\otimes\mathbf{M}_\phi^{0\,T}\right)\otimes\mathbf{M}_{rz}^I\\
&-\mathbf{M}_t\otimes\mathbf{\Gamma}_{rz}^-\Bigg]\cdot\mathbf{I}=\Bigg[S_r\mathbf{M}_t\otimes\mathbf{M}_{\cos(\theta)}^0\otimes\mathbf{M}_{\sin(\phi)}^0\otimes\mathbf{M}_{rz}^{I,T_e}+S_z\mathbf{M}_t\otimes\mathbf{M}_\theta^0\otimes\mathbf{M}_{\cos(\phi)}^0\otimes\mathbf{M}_{rz}^{I,T_e}\\
&+S_A\mathbf{M}_t\otimes\mathbf{M}_\theta^0\otimes\mathbf{M}_\phi^0\otimes\mathbf{M}_{rz}^{I,T_e}\Bigg]\cdot\mathbf{T}_e+S_b\mathbf{M}_t^0\otimes\mathbf{M}_\theta^0\otimes\mathbf{M}_\phi^0\otimes\mathbf{M}_{rz}^{I,0}-\mathbf{M}_t\otimes\left(\tilde{\mathbf{\Gamma}}_{rz}^-\cdot\tilde{\mathbf{I}}\right)_\Gamma,
\end{aligned}
\tag{B.43}
$$

where apart from the already defined t, θ, and ϕ matrices (3.39, 3.40, 3.41, 3.43, 3.44, 3.45, 3.46, 3.47, 3.49, 3.50, 3.52, 3.53, 3.54, 3.56), we define the spatial discretization matrices

$$
\mathbf{M}_{rz}^I = \int_{\Omega_{rz}}\psi(r,z)\otimes\psi(r,z)^T r\,\mathrm{d}\Omega_{rz},
\tag{B.44}
$$

$$
\mathbf{D}_{rz,r}^I = \int_{\Omega_{rz}}\psi(r,z)\otimes\frac{\partial\psi(r,z)^T}{\partial r}r\,\mathrm{d}\Omega_{rz}
\tag{B.45}
$$

$$
\mathbf{M}_{rz/r}^I = \int_{\Omega_{rz}}\psi(r,z)\otimes\psi(r,z)^T\,\mathrm{d}\Omega_{rz},
\tag{B.46}
$$

$$
\mathbf{D}_{rz,z}^I = \int_{\Omega_{rz}}\psi(r,z)\otimes\frac{\partial\psi(r,z)^T}{\partial z}r\,\mathrm{d}\Omega_{rz}
\tag{B.47}
$$

$$
\mathbf{M}_{rz}^{I,T_e} = \int_{\Omega_{rz}}\psi(r,z)\otimes\xi(r,z)^T r\,\mathrm{d}\Omega_{rz},
\tag{B.48}
$$

$$
\mathbf{M}_{rz}^{I,0} = \int_{\Omega_{rz}}\psi(r,z)\otimes\omega_0^T r\,\mathrm{d}\Omega_{rz},
\tag{B.49}
$$

The main goal of the 2D axis symmetry geometry DG-BGK scheme (B.43) of the transport equation (B.38) resides in finding the linear dependence of the unknown $\mathbf{I}$ on the unknown $\mathbf{T}_e$ [97, 98, 100, 51, 50] as

$$
\mathbf{I} = \mathbf{A}_{rz}\cdot\mathbf{T}_e+\mathbf{b}_{rz},
\tag{B.50}
$$

which can be directly obtained from (B.43) after some straightforward algebraic operations. It is worth mentioning, that the adjacent cells discretization $\tilde{\mathbf{I}}$ is absorbed in the $\mathbf{b}_{rz}$ vector.

As was stated before, we want to make use of the lowest order backward Euler time discretization. The *2D axisymmetric geometry backward Euler DG-BGK scheme* can

be obtained by using the backward Euler time matrices (3.42) in (B.43), thus giving

$$
\begin{aligned}
&\left[\frac{1}{c\Delta t} \mathbf{M}_\theta \otimes \mathbf{M}_\phi \otimes \mathbf{M}^I_{rz} + \mathbf{M}_{\cos(\theta)} \otimes \mathbf{M}_{\sin(\phi)} \otimes \mathbf{D}^I_{rz,r} - \mathbf{D}_{\sin(\theta)} \otimes \mathbf{M}_{\sin(\phi)} \otimes \mathbf{M}^I_{rz/r} \right. \\
&\quad + \mathbf{M}_\theta \otimes \mathbf{M}_{\cos(\phi)} \otimes \mathbf{D}^I_{rz,z} + \kappa \mathbf{M}_\theta \otimes \mathbf{M}_\phi \otimes \mathbf{M}^I_{rz} + \Upsilon_r \mathbf{M}_{\cos(\theta)} \otimes \mathbf{M}_{\sin(\phi)} \otimes \mathbf{M}^I_{rz} + \\
&\quad \left. \Upsilon_z \mathbf{M}_\theta \otimes \mathbf{M}_{\cos(\phi)} \otimes \mathbf{M}^I_{rz} - \frac{\sigma}{4\pi} \left(\mathbf{M}^0_\theta \otimes 2\mathbf{M}^{0T}_\theta \right) \otimes \left(\mathbf{M}^0_\phi \otimes \mathbf{M}^{0T}_\phi \right) \otimes \mathbf{M}^I_{rz} - \mathbf{\Gamma}^-_{rz} \right] \cdot \mathbf{I}^1 = \\
&\left[S_r \mathbf{M}^0_{\cos(\theta)} \otimes \mathbf{M}^0_{\sin(\phi)} \otimes \mathbf{M}^{I,Te}_{rz} + S_z \mathbf{M}^0_\theta \otimes \mathbf{M}^0_{\cos(\phi)} \otimes \mathbf{M}^{I,Te}_{rz} + S_A \mathbf{M}^0_\theta \otimes \mathbf{M}^0_\phi \otimes \mathbf{M}^{I,Te}_{rz} \right] \cdot \mathbf{T}_e \\
&\quad + S_b \mathbf{M}^0_\theta \otimes \mathbf{M}^0_\phi \otimes \mathbf{M}^{I,0}_{rz} - \left(\tilde{\mathbf{\Gamma}}^-_{rz} \cdot \tilde{\mathbf{I}}_1 \right)_\Gamma + \frac{1}{c\Delta t} \mathbf{M}_\theta \otimes \mathbf{M}_\phi \otimes \mathbf{M}^I_{rz} \cdot \mathbf{I}^0, \quad \text{(B.51)}
\end{aligned}
$$

where the discretization $\mathbf{I}$ has been divided into its explicit part $\mathbf{I^0}$ and its implicit part $\mathbf{I}^1$ according to (3.21) and (3.22), respectively. The scheme also uses only the implicit part of the unknown $\mathbf{T}_e$, i.e. $\mathbf{T}^1_e$ defined in (3.24).

In the case of the backward Euler scheme (B.51), we can explicitly write

$$
\begin{aligned}
\mathbf{A}_{rz} = &\ \mathbf{L}^{-1}_{rz} \cdot \left[\mathbf{M}^0_{\cos(\theta)} \otimes \mathbf{M}^0_{\sin(\phi)} \otimes S_r \mathbf{M}^{I,Te}_{rz} + \mathbf{M}^0_\theta \otimes \mathbf{M}^0_{\cos(\phi)} \otimes S_z \mathbf{M}^{I,Te}_{rz} \right. \\
&\quad \left. + \mathbf{M}^0_\theta \otimes \mathbf{M}^0_\phi \otimes S_A \mathbf{M}^{I,Te}_{rz} \right], \quad \text{(B.52)}
\end{aligned}
$$

$$
\mathbf{b}_{rz} = \mathbf{L}^{-1}_{rz} \cdot \left[\mathbf{M}^0_\theta \otimes \mathbf{M}^0_\phi \otimes S_b \mathbf{M}^{I,0}_{rz} - \left(\tilde{\mathbf{\Gamma}}^-_{rz} \cdot \tilde{\mathbf{I}}_1 \right)_\Gamma + \frac{1}{c\Delta t} \mathbf{M}_\theta \otimes \mathbf{M}_\phi \otimes \mathbf{M}^I_{rz} \cdot \mathbf{I}_0 \right], \tag{B.53}
$$

which includes the inversion of the element matrix

$$
\begin{aligned}
\mathbf{L}_{rz} = &\left[\mathbf{M}_\theta \otimes \mathbf{M}_\phi \otimes \frac{1}{c\Delta t} \mathbf{M}^I_{rz} + \mathbf{M}_{\cos(\theta)} \otimes \mathbf{M}_{\sin(\phi)} \otimes \mathbf{D}^I_{rz,r} - \mathbf{D}_{\sin(\theta)} \otimes \mathbf{M}_{\sin(\phi)} \otimes \mathbf{M}^I_{rz/r} \right. \\
&\quad + \mathbf{M}_\theta \otimes \mathbf{M}_{\cos(\phi)} \otimes \mathbf{D}^I_{rz,z} + \mathbf{M}_\theta \otimes \mathbf{M}_\phi \otimes \kappa \mathbf{M}^I_{rz} + \mathbf{M}_{\cos(\theta)} \otimes \mathbf{M}_{\sin(\phi)} \otimes \Upsilon_r \mathbf{M}^I_{rz} + \\
&\quad \left. \mathbf{M}_\theta \otimes \mathbf{M}_{\cos(\phi)} \otimes \Upsilon_z \mathbf{M}^I_{rz} - \left(\mathbf{M}^0_\theta \otimes 2\mathbf{M}^{0T}_\theta \right) \otimes \left(\mathbf{M}^0_\phi \otimes \mathbf{M}^{0T}_\phi \right) \otimes \frac{\sigma}{4\pi} \mathbf{M}^I_{rz} - \mathbf{\Gamma}^-_{rz} \right] \quad \text{(B.54)}
\end{aligned}
$$

Finally, we can write the backward Euler solution to (B.38) as a linear function of the unknown $\mathbf{T}_e$ [51, 50]

$$
\mathbf{I}^1 = \mathbf{A}_{rz} \cdot \mathbf{T}^1_e + \mathbf{b}_{rz}, \tag{B.55}
$$

where the linear coefficient $\mathbf{A}_{rz}$ and the constant vector $\mathbf{b}_{rz}$ are defined in (B.52) and (B.53), respectively.

It was opted at the beginning of this section that all the coefficients of (B.39) depend, in general, on time t and position r, z. Nevertheless, when used in the schemes (B.43) and (B.51), we need to put some restrictions on the form of the latter coefficients.

In the case of the backward Euler scheme (B.51) any time dependence of (B.39) cannot be included by definition. The best option is to use their mean values over Δt. However, the dependence on r, z can be enforced in the finite element matrices

construction, e.g. the spatial dependence of the extinction coefficient κ can be included as

$$\kappa \mathbf{M}_{rz}^I = \int_{\Omega_{rz}} \psi(r,z) \otimes \psi(r,z)^T \kappa(r,z) r \,\mathrm{d}\Omega_{rz} \,,$$

which appears in (B.54) and other coefficients of (B.39) can be treated in the exactly same manner.

The approach to be used in the case of the scheme (B.43) is equivalent, while we impose the condition of separable dependence on time and on space of coefficients (B.39). We show an example of the extinction coefficient κ, which needs to be written as $\kappa(t,r,z) = g(t)f(r,z)$. Then, the inclusion of the latter dependence reads

$$\kappa \mathbf{M}_t \otimes \mathbf{M}_\theta \otimes \mathbf{M}_\phi \otimes \mathbf{M}_{rz}^I = \int_{\Delta t} \omega_t \otimes \omega_t^T g(t) \,\mathrm{d}t \otimes \mathbf{M}_\theta \otimes \mathbf{M}_\phi \otimes \int_{\Omega_{rz}} \psi(r,z) \otimes \psi(r,z)^T f(r,z) r \,\mathrm{d}\Omega_{rz} \,,$$

which can be directly used in (B.43). The treatment of other coefficients of (B.39) simply follows the example above.

It is worth mentioning that the spatial discretization matrices (B.44, B.45, B.46, B.47, B.48, B.49) are integrated over Ω_{rz} which can be, in general, a curvilinear 2D domain. This makes the quadrature rule used to evaluate the latter matrices exceptionally more complex and a special curvilinear mapping must be adopted [101, 102].

It is also worth mentioning, that the complex structure of the boundary matrices $\mathbf{\Gamma}_{rz}^-$ (B.41) and $\tilde{\mathbf{\Gamma}}_{rz}^-$ (B.42) makes their evaluation the most difficult part of the DG-BGK&Ts scheme construction, since the dimensions ϕ, θ, and r,z cannot be separated due to the projection $\mathbf{n} \cdot \mathbf{n}_\Gamma = \sin(\phi)\cos(\theta)n_{\Gamma_r} + \cos(\phi)n_{\Gamma_z} < 0$.

B.2.2 The DG-T_e Temperature Scheme

The axisymmetric geometry implies a reduced dependence of the electron temperature $T_e(t, \mathbf{x}(r,z))$, and the resulting form of the *axisymmetric electron temperature equation* reads

$$a_e \frac{\mathrm{d}T_e}{\mathrm{d}t} + \int_0^{2\pi} \int_0^\pi \left(\frac{1}{c} \frac{\mathrm{d}I}{\mathrm{d}t} + \sin(\phi) \left(\cos(\theta) \frac{\partial I}{\partial r} - \frac{\sin(\theta)}{r} \frac{\partial I}{\partial \theta} \right) + \cos(\phi) \frac{\partial I}{\partial z} \right) \sin(\phi) \mathrm{d}\phi \mathrm{d}\theta$$
$$+ G_{ie}T_e = P_e + G_{ie}T_i \,, \quad \text{(B.56)}$$

which represents a 5D problem, i.e. the solution T_e of (B.56) depends on t, r, z and ϕ, θ due to I. All the coefficients

$$c, a_e, G_{ie}, P_e \,, \tag{B.57}$$

depend, in general, on time t and position r, z.

The discrete form of the discontinuous Galerkin variation principle (3.8) in the case of the 2D axisymmetric geometry uses the discretization of T_e, I, and T_i (3.19) where the bases $\mathbf{\Xi}$, $\mathbf{\Psi}$, and $\tilde{\mathbf{\Xi}}$ of (3.20) are defined on the spatial domain using the coordinate system $\mathbf{x} = \mathbf{x}(r,z)$, in particular, the bases ξ, ψ, and $\tilde{\xi}$ of (3.18) depend on r and z.

The *discrete 2D axisymmetric geometry variational form* of the discontinuous Galerkin electron temperature equation (B.56) reads

$$
\int_{\Delta t}\int_{\Delta r} \boldsymbol{\Xi} \otimes \left[\left(a_e \frac{\mathrm{d}\boldsymbol{\Xi}^T}{\mathrm{d}t} + G_{ie}\boldsymbol{\Xi}^T \right) \cdot \mathbf{T}_e + \left(\int_0^{2\pi}\int_0^\pi \left(\frac{1}{c}\frac{\mathrm{d}\boldsymbol{\Psi}^T}{\mathrm{d}t} + \right.\right.\right.
$$

$$
\left.\left. \sin(\phi)\left(\cos(\theta)\frac{\partial\boldsymbol{\Psi}^T}{\partial r} - \frac{\sin(\theta)}{r}\frac{\partial\boldsymbol{\Psi}^T}{\partial\theta} \right) + \cos(\phi)\frac{\partial\boldsymbol{\Psi}^T}{\partial z} \right) \sin(\phi)\mathrm{d}\phi\mathrm{d}\theta \right) \cdot \mathbf{I}
$$

$$
\left. - P_e - G_{ie}\tilde{\boldsymbol{\Xi}}^T \cdot \mathbf{T}_i \right] r\mathrm{d}r\mathrm{d}t = 0\,, \quad (\text{B.58})
$$

where Ω_{rz} is a general spatial domain of the element.

We can apply the products $\boldsymbol{\Xi}\otimes\boldsymbol{\Xi}^T$ of (3.34), $\boldsymbol{\Xi}\otimes\boldsymbol{\Psi}^T$ of (3.33), and $\boldsymbol{\Xi}\otimes\tilde{\boldsymbol{\Xi}}^T$ of (3.36) wherever they appear in (B.58), which leads to the *2D axisymmetric geometry DG-T_e scheme* formulation

$$
\left[a_e\mathbf{D}_t\otimes\mathbf{M}_{rz}^{T_e} + G_{ie}\mathbf{M}_t\otimes\mathbf{M}_{rz}^{T_e} \right]\cdot\mathbf{T}_e - P_e\mathbf{M}_t^0\otimes\mathbf{M}_{rz}^{T_e,0} - G_{ie}\mathbf{M}_t\otimes\mathbf{M}_{rz}^{T_e,T_i}\cdot\mathbf{T}_i+
$$

$$
\left[\frac{1}{c}\mathbf{D}_t\otimes2\mathbf{M}_\theta^0\otimes\mathbf{M}_\phi^0\otimes\mathbf{M}_{rz}^{T_e,I}+\mathbf{M}_t\otimes2\mathbf{M}_{\cos(\theta)}^0\otimes\mathbf{M}_{\sin(\phi)}^0\otimes\mathbf{D}_{rz,r}^{T_e,I}-\mathbf{M}_t\otimes2\mathbf{D}_{\sin(\theta)}^0\otimes\mathbf{M}_{\sin(\phi)}^0\otimes\mathbf{M}_{rz/r}^{T_e,I} \right.
$$

$$
\left. + \mathbf{M}_t\otimes2\mathbf{M}_\theta^0\otimes\mathbf{M}_{\cos(\phi)}^0\otimes\mathbf{D}_{rz,z}^{T_e,I} \right]\cdot\mathbf{I}=0\,, \quad (\text{B.59})
$$

where apart from the already defined t, θ, and ϕ matrices (3.39, 3.40, 3.41, 3.46, 3.47, 3.48 3.53, 3.54, 3.56), we define the spatial discretization matrices

$$
\mathbf{M}_{rz}^{T_e} = \int_{\Omega_{rz}} \xi\otimes\xi^T r\,\mathrm{d}\Omega_{rz}\,, \quad (\text{B.60})
$$

$$
\mathbf{M}_{rz}^{T_e,I} = \int_{\Omega_{rz}} \xi\otimes\psi^T r\,\mathrm{d}\Omega_{rz} = \mathbf{M}_{rz}^{I,T_e}{}^T\,, \quad (\text{B.61})
$$

$$
\mathbf{D}_{rz,r}^{T_e,I} = \int_{\Omega_{rz}} \xi\otimes\frac{\partial\psi^T}{\partial r}r\,\mathrm{d}\Omega_{rz} \quad (\text{B.62})
$$

$$
\mathbf{M}_{rz/r}^{T_e,I} = \int_{\Omega_{rz}} \xi\otimes\psi^T \,\mathrm{d}\Omega_{rz}\,, \quad (\text{B.63})
$$

$$
\mathbf{D}_{rz,z}^{T_e,I} = \int_{\Omega_{rz}} \xi\otimes\frac{\partial\psi^T}{\partial z}r\,\mathrm{d}\Omega_{rz} \quad (\text{B.64})
$$

$$
\mathbf{M}_{rz}^{T_e,0} = \int_{\Omega_{rz}} \xi\otimes\omega_0^T r\,\mathrm{d}\Omega_{rz}\,, \quad (\text{B.65})
$$

$$
\mathbf{M}_{rz}^{T_e,T_i} = \int_{\Omega_{rz}} \xi\otimes\tilde{\xi}^T r\,\mathrm{d}\Omega_{rz}\,. \quad (\text{B.66})
$$

Now, the linear function solution (B.50) can be justified. The latter has the form $\mathbf{I} = \mathbf{A}_{rz}\cdot\mathbf{T}_e + \mathbf{b}_{rz}$, which when plugged in (B.59) provides the *2D axisymmetric geometry*

DG-T_e electron temperature scheme

$$\left[a_e \mathbf{D}_t \otimes \mathbf{M}_{rz}^{Te} + G_{ie}\mathbf{M}_t \otimes \mathbf{M}_{rz}^{Te} \right] \cdot \mathbf{T}_e - P_e\mathbf{M}_t^0 \otimes \mathbf{M}_{rz}^{Te,0} - G_{ie}\mathbf{M}_t \otimes \mathbf{M}_{rz}^{Te,T_i} \cdot \mathbf{T}_i +$$

$$\Bigg[\frac{1}{c}\mathbf{D}_t\otimes 2\mathbf{M}_\theta^0\otimes\mathbf{M}_\phi^0\otimes\mathbf{M}_{rz}^{Te,I} + \mathbf{M}_t\otimes 2\mathbf{M}_{\cos(\theta)}^0\otimes\mathbf{M}_{\sin(\phi)}^0\otimes\mathbf{D}_{rz,r}^{Te,I} - \mathbf{M}_t\otimes 2\mathbf{D}_{\sin(\theta)}^0\otimes\mathbf{M}_{\sin(\phi)}^0\otimes\mathbf{M}_{rz/r}^{Te,I}$$

$$+ \mathbf{M}_t \otimes 2\mathbf{M}_\theta^0 \otimes \mathbf{M}_{\cos(\phi)}^0 \otimes \mathbf{D}_{rz,z}^{Te,I} \Bigg] \cdot (\mathbf{A}_{rz} \cdot \mathbf{T}_e + \mathbf{b}_{rz}) = 0, \quad \text{(B.67)}$$

which is apparently a problem of the unknown $\mathbf{T}_e$ and the unknown $\mathbf{T}_i$. Nevertheless, the former unknown $\mathbf{I}$ is implicitly coupled via the matrix $\mathbf{A}_{rz}$ and the vector $\mathbf{b}_{rz}$.

As was stated before, we want to make use of the lowest order backward Euler time discretization. The *2D axisymmetric geometry backward Euler DG-T_e scheme* can be obtained by using the backward Euler time matrices (3.42) in (B.67), thus giving

$$\left[\frac{a_e}{\Delta t}\mathbf{M}_{rz}^{Te} + G_{ie}\mathbf{M}_{rz}^{Te} \right] \cdot \mathbf{T}_e^1 - P_e\mathbf{M}_{rz}^{Te,0} - G_{ie}\mathbf{M}_{rz}^{Te,T_i} \cdot \mathbf{T}_i^1 + \Bigg[2\mathbf{M}_\theta^0 \otimes \mathbf{M}_\phi^0 \otimes \frac{1}{c\Delta t}\mathbf{M}_{rz}^{Te,I}$$

$$+ 2\mathbf{M}_{\cos(\theta)}^0 \otimes \mathbf{M}_{\sin(\phi)}^0 \otimes \mathbf{D}_{rz,r}^{Te,I} - 2\mathbf{D}_{\sin(\theta)}^0 \otimes \mathbf{M}_{\sin(\phi)}^0 \otimes \mathbf{M}_{rz/r}^{Te,I} + 2\mathbf{M}_\theta^0 \otimes \mathbf{M}_{\cos(\phi)}^0 \otimes \mathbf{D}_{rz,z}^{Te,I} \Bigg]$$

$$\cdot \left(\mathbf{A}_{rz} \cdot \mathbf{T}_e^1 + \mathbf{b}_{rz} \right) = \frac{a_e}{\Delta t}\mathbf{M}_{rz}^{Te} \cdot \mathbf{T}_e^0 + 2\mathbf{M}_\theta^0 \otimes \mathbf{M}_\phi^0 \otimes \frac{1}{c\Delta t}\mathbf{M}_{rz}^{Te,I} \cdot \mathbf{I}^0, \quad \text{(B.68)}$$

where each of the discretizations $\mathbf{T}_e$ and $\mathbf{I}$ have been divided into its explicit part, i.e. $\mathbf{T_e^0}$ and $\mathbf{I^0}$, respectively, and its implicit part, i.e. $\mathbf{T}_e^1$ and $\mathbf{I}^1$ respectively, according to (3.23, 3.24) and (3.21, 3.22), respectively. The scheme also uses only the implicit part of the unknown $\mathbf{T}_i$, i.e. $\mathbf{T}_i^1$ defined in (3.26). The matrix $\mathbf{A}_{rz}$ and the vector $\mathbf{b}_{rz}$ are defined in (B.52) and (B.53).

It was opted at the beginning of this section that all the coefficients of (B.57) depend, in general, on time t and position r, z. Nevertheless, when used in the schemes (B.67) and (B.68), we need to put some restrictions on the form of the latter coefficients.

In the case of the backward Euler scheme (B.68) any time dependence of (B.57) cannot be included by definition. The best option is to use their mean values over Δt. However, the dependence on r, z can be enforced in the finite element matrices construction, e.g. the spatial dependence of the heat capacity coefficient a_e can be included as

$$a_e\mathbf{M}_{rz}^{Te} = \int_{\Omega_{rz}} \xi(r,z) \otimes \xi(r,z)^T a_e(r,z) r \, \mathrm{d}\Omega_{rz},$$

which appears in (B.68) and other coefficients of (B.57) can be treated in the exactly same manner.

The approach to be used in the case of the scheme (B.67) is equivalent, while we impose the condition of separable dependence on time and on space of coefficients (B.57). We show an example of the heat capacity coefficient a_e, which needs to be written as $a_e(t,r,z) = g(t)f(r,z)$. Then, the inclusion of the latter dependence reads

$$a_e\mathbf{D}_t \otimes \mathbf{M}_{rz}^{Te} = \int_{\Delta t} \omega_t \otimes \frac{\mathrm{d}\omega_t^T}{\mathrm{d}t}g(t) \, \mathrm{d}t \otimes \int_{\Omega_{rz}} \xi(r,z) \otimes \xi(r,z)^T f(r,z) r \, \mathrm{d}\Omega_{rz},$$

which can be directly used in (B.67). The treatment of other coefficients of (B.57) simply follows the example above.

B.2.3 The DG-$\mathbf{T}_i$ Temperature Scheme

The axisymmetric geometry implies a reduced dependence of the ion temperature $T_i(t, \mathbf{x}(r,z))$, and the resulting form of the *axisymmetric ion temperature equation* reads

$$a_i \frac{\mathrm{d}T_i}{\mathrm{d}t} + G_{ie}T_i = P_i + G_{ie}T_e \,, \tag{B.69}$$

which represents a 3D problem, i.e. the solution T_i of (B.69) depends on t and r, z. All the coefficients

$$a_i, G_{ie}, P_i \,, \tag{B.70}$$

depend, in general, on time t and position r, z.

The discrete form of the discontinuous Galerkin variation principle (3.9) in the case of the 2D axisymmetric geometry uses the discretization of T_i, and T_e (3.19) where the bases $\tilde{\boldsymbol{\Xi}}$, and $\boldsymbol{\Xi}$ of (3.20) are defined on the spatial domain using the coordinate system $\mathbf{x} = \mathbf{x}(r,z)$, in particular, the bases $\tilde{\xi}$, and ξ of (3.18) depend on r and z.

The *discrete 2D axisymmetric geometry variational form* of the discontinuous Galerkin ion temperature equation (B.69) reads

$$\int_{\Delta t} \int_{\Omega_{rz}} \tilde{\boldsymbol{\Xi}} \otimes \left[\left(a_i \frac{\mathrm{d}\tilde{\boldsymbol{\Xi}}^T}{\mathrm{d}t} + G_{ie}\tilde{\boldsymbol{\Xi}}^T \right) \cdot \mathbf{T}_i - P_i - G_{ie}\boldsymbol{\Xi}^T \cdot \mathbf{T}_e \right] r\mathrm{d}\Omega_{rz}\mathrm{d}t = 0 \,, \tag{B.71}$$

where Ω_{rz} is a general spatial domain of the element.

We can apply the products $\tilde{\boldsymbol{\Xi}} \otimes \tilde{\boldsymbol{\Xi}}^T$ of (3.35), and $\tilde{\boldsymbol{\Xi}} \otimes \boldsymbol{\Xi}^T$ of (3.37) wherever they appear in (B.71), which leads to the *2D axisymmetric geometry DG-T_i scheme* formulation

$$\left[a_i\mathbf{D}_t \otimes \mathbf{M}_{rz}^{T_i} + G_{ie}\mathbf{M}_t \otimes \mathbf{M}_{rz}^{T_i} \right] \cdot \mathbf{T}_i - G_{ie}\mathbf{M}_t \otimes \mathbf{M}_{rz}^{T_i,T_e} \cdot \mathbf{T}_e = P_i\mathbf{M}_t^0 \otimes \mathbf{M}_{rz}^{T_i,0} \,, \tag{B.72}$$

where apart from the already defined t matrices (3.39, 3.40, 3.41), we define the spatial discretization matrices

$$\mathbf{M}_{rz}^{T_i} = \int_{\Omega_{rz}} \tilde{\xi} \otimes \tilde{\xi}^T r \, \mathrm{d}\Omega_{rz} \,, \tag{B.73}$$

$$\mathbf{M}_{rz}^{T_i,0} = \int_{\Omega_{rz}} \tilde{\xi} \otimes \omega_0^T r \, \mathrm{d}\Omega_{rz} \,, \tag{B.74}$$

$$\mathbf{M}_{rz}^{T_i,T_e} = \int_{\Omega_{rz}} \tilde{\xi} \otimes \xi^T r \, \mathrm{d}\Omega_{rz} = \mathbf{M}_{rz}^{T_e,T_i}{}^T \,. \tag{B.75}$$

As was stated before, we want to make use of the lowest order backward Euler time discretization. The *2D axisymmetric geometry backward Euler DG-T_i scheme* can be obtained by using the backward Euler time matrices (3.42) in (B.72), thus giving

$$\left[\frac{a_i}{\Delta t}\mathbf{M}_{rz}^{T_i} + G_{ie}\mathbf{M}_{rz}^{T_i} \right] \cdot \mathbf{T}_i^1 - G_{ie}\mathbf{M}_{rz}^{T_i,T_e} \cdot \mathbf{T}_e^1 = P_i\mathbf{M}_{rz}^{T_i,0} + \frac{a_i}{\Delta t}\mathbf{M}_{rz}^{T_i} \cdot \mathbf{T}_i^0 \,, \tag{B.76}$$

where the discretization $\mathbf{T}_i$ has been divided into its explicit part $\mathbf{T}_i^0$ and its implicit part $\mathbf{T}_i^1$ according to (3.25, 3.26). The scheme also uses only the implicit part of the unknown $\mathbf{T}_e$, i.e. $\mathbf{T}_e^1$ defined in (3.24).

It was opted at the beginning of this section that all the coefficients of (B.70) depend, in general, on time t and position r, z. Nevertheless, when used in the schemes (B.72) and (B.76), we need to put some restrictions on the form of the latter coefficients.

In the case of the backward Euler scheme (B.76) any time dependence of (B.70) cannot be included by definition. The best option is to use their mean values over Δt. However, the dependence on r, z can be enforced in the finite element matrices construction, e.g. the spatial dependence of the heat capacity coefficient a_i can be included as

$$a_i \mathbf{M}_{rz}^{T_i} = \int_{\Omega_{rz}} \tilde{\xi}(r, z) \otimes \tilde{\xi}(r, z)^T a_i(r, z) r \, \mathrm{d}\Omega_{rz} \,,$$

which appears in (B.76) and other coefficients of (B.70) can be treated in the exactly same manner.

The approach to be used in the case of the scheme (B.72) is equivalent, while we impose the condition of separable dependence on time and on space of coefficients (B.70). We show an example of the heat capacity coefficient a_i, which needs to be written as $a_i(t, r, z) = g(t)f(r, z)$. Then, the inclusion of the latter dependence reads

$$a_i \mathbf{D}_t \otimes \mathbf{M}_{rz}^{T_i} = \int_{\Delta t} \omega_t \otimes \frac{\mathrm{d}\omega_t^T}{\mathrm{d}t} g(t) \, \mathrm{d}t \otimes \int_{\Omega_{rz}} \tilde{\xi}(r, z) \otimes \tilde{\xi}(r, z)^T f(r, z) r \, \mathrm{d}\Omega_{rz} \,,$$

which can be directly used in (B.72). The treatment of other coefficients of (B.70) simply follows the example above.

Bibliography

[1] Shvarts D. *Proceedings of the 29th Scottish Universities Summer School in Physics, St. Andrews, 1985*, Hooper HB (ed.), Scottish Universities Summer School in Physics Publications: Edinburgh, 1986.

[2] Mihalas D, Mihalas B. *Foundations of Radiation Hydrodynamics*. Oxford University Press: New York, 1985.

[3] Atzeni S, Meyer-Ter-Vehn J. *The Physics of Inertial Fusion*. Clarendon Press: Oxford, 2004.

[4] Velarde G, Ronen V, Martinez-Val JM. *Nuclear Fusion by Inertial Confinement: A Comprehensive Treatise*. CRC Press: Boca Raton, FL, 1993.

[5] Zeldovich Y, Raizer Y. *Physics of Shock Waves and High-Temperature Hydrodynamic Phenomena*. Dover Publications: New York, 2002.

[6] Castor J. *Radiation Hydrodynamics*. Cambridge University Press: Cambridge, 2004.

[7] Chung HK, Chen MH, Morgan WL, Ralchenko Y, Lee RW. FLYCHK: Generalized population kinetics and spectral model for rapid spectroscopic analysis for all elements. *High Energy Density Physics* 2005; **1**:3.

[8] Brantov AV, Bychenkov VY. Nonlocal transport in hot plasma. Part I. *Plasma Phys. Rep.* 2013; **39**:698–744.

[9] Brantov AV, Bychenkov VY. Nonlocal transport in hot plasma. Part II. *Plasma Phys. Rep.* 2014; **40**:505–563.

[10] Spitzer L Jr, Harm R. Transport phenomena in a completely ionized gas. *Phys. Rev.* 1953; **89**:977–981.

[11] Braginskii SI. Transport processes in a plasma. *Reviews of Plasma Physics* 1965; **1**:205.

[12] Duderstadt JJ, Moses GA. *Inertial Confinement Fusion*. Wiley: New York, 1982.

[13] Kruer WI. *The Physiscs of Laser-Plasma Interactions*. Addison-Wesley: New York, 1988.

[14] Balescu R. *Transport Processes in Plasmas: Classical Transport Theory*. Elsevier Science: Amsterdam, 1988.

[15] Luciani JF, Mora P, Virmont J. Nonlocal heat transport due to steep temeperature gradients. *Phys. Rev. Lett.* 1983; **51**:1664–1667.

[16] Groot JSD, Estabrook KG, Glenzer SH, Matte JP. Nonlocal heat transport in laser driven hohlraums. *B. Am. Phys. Soc.* 1997; **42**:1993.

[17] Harrington RE. Anomalous surface heating rates. *J. Appl. Phys.* 1966; **37**:2028.

[18] Schurtz G, Gary S, Hulin S, Chenais-Popovics C, Gauthier JC, Thais F, Breil J, Durut F, Feugeas JL, Maire PH, *et al.*. Revisiting nonlocal electron-energy transport in inertial-fusion conditions. *Phys. Rev. Lett.* 2007; **98**:095 002.

[19] Bychenkov VY, Tikhonchuk VT. Laser-target interaction: Laser energy absorption and nonlinear plasma phenomena. *Nuclear Fusion by Inertial Confinement: A Comprehensive Treatise*, Velarde G, Ronen V, Martinez-Val JM (eds.). CRC Press: Boca Raton, FL, 1993; 73.

[20] Malone RC, McCroy RL, Morse RL. *Phys. Rev. Lett.* 1975; **34**:721.

[21] Snyder PB, Hammett GW, Dorland W. Landau fluid models of collisionless magnetohydrodynamics. *Phys. Plasmas* 1997; **4**:3974.

[22] Furkal E, Smolyakov AI, Hirose A. *Phys. Rev. E* 1997; **58**:3974.

[23] Chang Z, Callen JD. *Phys. Fluids B* 1992; **4**:1167.

[24] Shkarofsky IP, Johnston TW, Bachynskii MP. *The particle Kinetics of Plasmas*. Addison-Wesley: Reading, 1966.

[25] Bhatnagar P, Gross E, Krook M. A Model for Collision Processes in Gases. I. Small Amplitude Processes in Charged and Neutral One-Component Systems. *Phys. Rev.* 1954; **94**:511–525.

[26] Gross E, Krook M. Model for Collision Processes in Gases: Small-Amplitude Oscillations of Charged Two-Component Systems. *Phys. Rev.* 1956; **102**:593–604.

[27] Aleksandrov AF, Bogdankevich LS, Rukhadze AA. *Principles of Plasma Electrodynamics*. Vysshaya Shkola: Moscow, 1978.

[28] Bychenkov VY, Tikhonchuk VT, Rozmus W. Transverse electron susceptibility and the electromagnetic wave absorption in weakly collisional plasmas. *Phys. Plasmas* 1997; **4**:4205.

[29] Bychenkov VY, Rozmus W, Tikhonchuk VT. *Phys. Rev. Lett.* 1995; **75**:4405.

[30] Silin VP. *Phys. Usp.* 2002; **45**:955.

[31] Brantov AV, Bychenkov VY, Rozmus W, Capjack CE. *IEEE T. Plasma Sci.* 2006; **13**:738.

[32] Epperlein EM. *Phys. Rev. Lett.* 1990; **65**:2145.

[33] Bychenkov VY, Rozmus W, Brantov AV, Tikhonchuk VT. Theory of filamentation instability and stimulated brillouin scattering with nonlocal hydrodynamics. *Phys. Plasmas* 2000; **7**:1511.

[34] Larroche O. Ion Fokker-Planck simulation of D-^{3}He gas target implosions. *Phys. Plasmas* 2012; **19**:122 706.

[35] Larroche O. Comment on "Species separation in inertial confinement fusion fuels" [Phys. Plasmas 20, 012701 (2013)]. *Phys. Plasmas* 2013; **20**:044 701.

[36] Kagan G, Tang X. Electro-diffusion in a plasma with two ion species. *Phys. Plasmas* 2012; **19**:082 709.

[37] Kagan G, Tang X. Thermo-diffusion in inertially confined plasmas. *Phys. Lett. A* 2014; **378**:1531–1535.

[38] Michel P, Rozmus W, Williams E, Divol L, Berger R, Town R, Glenzer S, Callahan D. Stochastic ion heating from many overlapping laser beams in fusion plasmas. *Phys. Rev. Lett.* 2012; **109**:195 004.

[39] Boltzmann L. Weitere studien uber das warmegleichgewicht unter gasmolekulen. *Sitzungsberichte Akademie der Wissenschaften* 1872; **66**:275–370.

[40] Smith H, Jensen H. *Transport Phenomena*. Oxford, 1989.

[41] Krapivsky P, Redner S, Ben-Naim E. *A Kinetic View of Statistical Physics*. Cambridge, 2010.

[42] Kardar M. *Statistical Physics of Particles*. Cambridge, 2007.

[43] Reif F. *Fundamentals of Statistical and Thermal Physics*. McGraw-Hill, 1987.

[44] Kampen NV. *Stochastic Processes in Physics and Chemistry*. North-Holland, 2007.

[45] Jeans J. *Introduction to Kinetic Theory of Gases*. Cambridge University Press: Cambridge, 1946.

[46] Chapman S, Cowling TG. *Mathematical Theory of Nonuniform Gases*. Cambridge University Press: Cambridge, 1952.

[47] Brantov AV, Bychenkov VY, Tikhonchuk VT. Nonlocal electron transport in laser heated plasmas. *Phys. Plasmas* 1998; **5**:2742–2753.

[48] Cohen RS, Spitzer L Jr, Routly PM. The electrical conductivity of an ionized gas. *Phys. Rev.* 1950; **80**:230–238.

[49] Schurtz G, Nicolai P, Busquet M. A nonlocal electron conduction model for multidimensional radiation hydrodynamics codes. *Phys. Plasmas* 2000; **7**:4238–4249.

[50] Holec M, Cotelo M, Velarde P, Liska R. Application of discontinuous Galerkin adaptive mesh and order refinement method to energy transport and conservation equations in radiation-hydrodynamics. *1st Pan American Congress on Computational Mechanics, Buenos Aires*, Idelsohn SR, et al (eds.), CIMNE, Barcelona, 2015; 919–930.

[51] Holec M, Limpouch J, Liska R, Weber S. High-order discontinuous Galerkin nonlocal transport and energy equations scheme for radiation hydrodynamics. *Int. J. Numer. Meth. Fl.* 2016; In Press.

[52] Courant R, Hilbert D. *Methods of Mathematical Physics*, vol. 1. Interscience Publisher, Inc.: New York, 1953.

[53] Bychenkov VY. *Plasma Phys. Rep.* 1998; **24**:801.

[54] Koch RA. *Phys. Fluids* 1975; **18**:861.

[55] Penano JR, Morales GJ, Maggs JE. Properties of drift waves in a filamentary density depletion. *Phys. Plasmas* 1997; **4**:555.

[56] Sorbo DD, Feugeas JL, Nicolai P, Olazabal-Loume M, Dubroca B, Guisset S, Touati M, Tikhonchuk V. Reduced entropic model for studies of multidimensional nonlocal transport in high-energy-density plasmas. *Phys. Plasmas* 2015; **22**:082 706.

[57] Sorbo DD, Feugeas JL, Nicolai P, Olazabal-Loume M, Dubroca B, Tikhonchuk V. Extension of a reduced entropic model of electron transport to magnetized nonlocal regimes of high-energy-density plasmas. *Laser Part. Beams* 2016; **34**:412–425.

[58] Colaitis A, Duchateau G, Nicolai P, Tikhonchuk V. Towards modeling of nonlinear laser-plasma interactions with hydrocodes: The thick-ray approach. *Phys. Rev. E* 2014; **89**:033 101.

[59] Dubroca B, Feugeas JL, Frank M. Angular moment model for the fokker-planck equation. *Eur. Phys. J. D* 2010; **60**:301–307.

[60] Touati M, Feugeas JL, Nicolai P, Santos J, Gremillet L, Tikhonchuk V. A reduced model for relativistic electron beam transport in solids and dense plasmas. *New J. Phys.* 2014; **16**:073 014.

[61] Minerbo GN. Maximum entropy eddington factors. *J. Quant. Spectrosc. Ra.* 1978; **20**:541.

[62] Jaffe G. *Ann. Phys.* 1930; **6**:195.

[63] Apostol T. *Calculus*, vol. 2. Wiley: New York, 1969.

[64] Misner C, Thorne K, Wheeler J. *Gravitation*. W. H. Freeman: San Francisco, 1973.

[65] Buchler JR. Radiation transfer in the fluid frame. *J. Quant. Spectrosc. Ra.* 1983; **30**:395.

[66] http://mathworld.wolfram.com/SphericalCoordinates.html.

[67] http://mathworld.wolfram.com/CylindricalCoordinates.html.

[68] Olson GL, Auer LH, Hall ML. Diffusion, P1, and other approximate forms of radiation transport. *Technical Report LA-UR-99-471*, Los Alamos National Laboratory, Los Alamos, NM 2000.

[69] Simmons KH, Mihalas D. A linearized analysis of the modified P1 equations. *J. Quant. Spectrosc. Ra.* 2000; **66**:263–269.

[70] Morel JE. Diffusion-limit asymptotics of the transport equation, the P1/3 equations, and two flux-limited diffusion theories. *J. Quant. Spectrosc. Ra.* 2000; **65**:769–778.

[71] Kershaw DS. Flux limiting nature's own way. *Technical Report UCRL-78378*, Lawrence Livermore National Laboratory 1976.

[72] Malone RC, McCrory RL, Morse RL. Indications of strongly flux-limited electron thermal conduction in laser-target experiments. *Phys. Rev. Lett.* 1975; **34**:721–724.

[73] Goncharov VN, Gotchev OV, Vianello E, Boehly TR, Knauer JP, McKenty PW, Radha PB, Regan SP, Sangster TC, Skupsky S, *et al.*. Early stage of implosion in inertial confinement fusion: Shock timing and perturbation evolution. *Phys. Plasmas* 2006; **13**:012 702.

[74] Goncharov VN, Sangster TC, Radha PB, Betti R, Boehly TR, Collins TJB, Craxton RS, Delettrez JA, Epstein R, Glebov VY, *et al.*. Performance of direct-drive cryogenic targets on omega. *Phys. Plasmas* 2008; **15**:056 310.

[75] More R, Warren K, Young D, Zimmerman G. A new quotidian equation of state (QEOS) for hot dense matter. *Phys. Fluids* 1988; **31**:3059–3078.

[76] Kemp A, ter Vehn JM. An equation of state code for hot dense matter, based on the QEOS description. *Nucl. Instrum. Meth. A* 1998; **415**:674–676.

[77] Heltemes T, Moses G. BADGER v1.0: A fortran equation of state library. *Comp. Phys. Commun.* 2012; **183**:2629–2646.

[78] Abdallah J, Kerley GI, Bennett BI, Johnson JD, Albert RC, Huebner WF. HYD-SES: A subroutine package for using SESAME in hydrodynamic codes. *Technical Report LA-8209*, Los Alamos National Laboratory, Los Alamos, NM 1980.

[79] Group T. SESAME report on the Los Alamos equation-of-state library. *Technical Report Tech. Rep. LALP-83-4*, Los Alamos National Laboratory, Los Alamos 1983.

[80] Lyon SP, Johnson JD. SESAME: The Los Alamos national laboratory equation of state database. *Technical Report LA-UR-92-3407*, Los Alamos National Laboratory, Los Alamos 1992.

[81] Tsakiris G, Eidmann K. An approximate method for calculating planck and rosseland mean opacities in hot, dense plasmas. *J. Quant. Spectrosc. Ra.* 1987; **38**:353–368.

[82] Faussurier G, Blancard C, Renaudin P. Equation of state of dense plasmas using a screened-hydrogenic model with l-splitting. *Comp. Phys. Commun.* 2008; **4**:114–123.

[83] Rieben R, White D, Wallin B, Solberg J. An arbitrary Lagrangian–Eulerian discretization of MHD on 3D unstructured grids. *J. Comput. Phys.* 2007; **226**:534–570.

[84] Pomraning GC. *The Equations of Radiation Hydrodynamics*. Pergamon Press: Oxford, 1973.

[85] Dykema PG, Klein RI, Castor JI. A new scheme for multidimensional line transfer. III. a two-dimensional Lagrangian variable tensor method with discontinuous finite-element SN transport. *Astrophys. J.* 1996; **457**:892.

[86] Adams M. A subcell balance method for radiative transfer on arbitrary spatial grids. *Transport Theor. Stat.* 1997; **26**:385–431.

[87] Adams M. Discontinuous finite element transport solutions in thick diffusive problems. *Nucl. Sci. Eng.* 2001; **137**:298.

[88] Adams M, Larsen E. Fast iterative methods for discrete-ordinates particle transport equation. *Prog. Nucl. Energ* 2002; **40**.

[89] Mieussens L. Discrete-velocity models and numerical schemes for the Boltzmann-BGK equation in plane and axisymmetric geometries. *J. Comput. Phys.* 2000; **162**:429–466.

[90] Wang Y, Ragusa JC. A high-order discontinuous Galerkin method for the Sn transport equations on 2D unstructured triangular meshes. *Ann. Nucl. Energy* 2009; **36**:931–939.

[91] Sanchez R, Ragusa J. On the construction of Galerkin angular quadratures. *Nucl. Sci. Eng.* 2011; **169**:133–154.

[92] Alekseenko A. Numerical properties of high order discrete velocity solutions to the BGK kinetic equation. *Appl. Numer. Math.* 2011; **61**:410–427.

[93] Alekseenko A, Gimelshein N, Gimelshein S. An application of discontinuous Galerkin space and velocity discretisations to the solution of a model kinetic equation. *Int. J. Comput. Fluid D.* 2012; **26**:145–161.

[94] Cheng Y, Gamba I, Li F, Morrison P. Discontinuous Galerkin methods for Vlasov-Maxwell equations. *SIAM J. Numer. Anal.* 2014; **52**:1017–1049.

[95] Boffi D, Gastaldi L. On the quadrilateral Q2-P1 element for the Stokes problem. *Int. J. Numer. Meth. Fl.* 2002; **39**:1001–1011.

[96] Arnold D, Boffi D, Falk R. Approximation by quadrilateral finite elements. *Math. Comput.* 2002; **71**:909–922.

[97] Livne E, Glasner A. A finite difference scheme for the heat conduction equation. *J. Comput. Phys.* 1985; **58**:59–66.

[98] Ramis R, ter Vehn JM, Ramirez J. MULTI2D – a computer code for two-dimensional radiation hydrodynamics. *Comp. Phys. Commun.* 2009; **180**:977–994.

[99] Ramis R, ter Vehn JM. MULTI-IFE a one-dimensional computer code for inertial fusion energy (IFE) target simulations. *Comp. Phys. Commun.* 2016; **203**:226–237.

[100] Basko M, Maruhn J, Tauschwitz A. Development of a 2D radiation-hydrodynamics code RALEF for laser plasma simulations. *Technical Report PLASMA-PHYSICS-25*, EMMI, GSI Darmstadt, Germany 2009.

[101] Dobrev V, Kolev T, Rieben R. High-order curvilinear finite element methods for Lagrangian hydrodynamics. *SIAM J. Sci. Comput.* 2012; **34**:B606–B641.

[102] MFEM: Modular finite element methods. `mfem.org`.

[103] Courant R, Friedrichs K, Lewy H. Uber die partiellen differenzengleichungen der mathematischen physik. *Mathematische Annalen* 1928; **100**:32–74.

[104] Richtmyer R, Morton K. *Difference Methods for Initial Value Problems*. Interscience: New York, 1976.

[105] von Neumann J, Richtmyer R. A method for the numerical calculation of hydro-dynamic shocks. *J. Appl. Phys.* 1950; **21**:232–237.

[106] Shashkov M. *Conservative Finite-Difference Methods on General Grids*. CRC Press: Boca Raton, 1996.

[107] Dobrev VA, Ellis TE, Kolev TV, Rieben RN. Curvilinear finite elements for Lagrangian hydrodynamics. *Int. J. Numer. Meth. Fl.* 2011; **65**:1295–1310.

[108] Dobrev V, Kolev T, Rieben R, Tomov V. Multi-material closure model for high-order finite element Lagrangian hydrodynamics. *Int. J. Numer. Meth. Fl.* 2016; **82**:689–706.

[109] Anderson R, Dobrev V, Kolev T, Rieben R. Monotonicity in high-order curvilinear finite element ale remap. *Int. J. Numer. Meth. Fl.* 2014; **77**:249–273.

[110] Dobrev V, Kolev T, Rieben R. High-order curvilinear finite element methods for elastic-plastic Lagrangian dynamics. *J. Comput. Phys.* 2014; **257B**:1062–1080.

[111] Dobrev V, Ellis T, Kolev T, Rieben R. High-order curvilinear finite elements for axisymmetric Lagrangian hydrodynamics. *Comput. Fluids* 2013; **83**:58–69.

[112] Vilar F, Maire PH, Abgrall R. Cell-centered discontinuous Galerkin discretizations for two-dimensional scalar conservation laws on unstructured grids and for one-dimensional Lagrangian hydrodynamics. *Comput. Fluids* 2011; **46**:498–504.

[113] Holec M, Limpouch J, Liska R, Weber S. Nonlocal energy transport effect in radiation hydrodynamics simulations of intense laser pre-pulse physics. URL `http://kuleuvencongres.be/eps2016`, presented at the 43rd European Physical Society Conference on Plasma Physics (EPS 2016), Leuven, Belgium.

[114] Holec M, Liska R, Weber S. Discontinuous Galerkin high-order nonlocal transport and energy equations scheme for radiation-hydrodynamics. URL `http://www.esco2016.femhub.com`, presented at the 5th European Seminar on Computing (ESCO 2016), Pilsen, Czech Republic.

[115] Holec M, Limpouch J, Liska R, Weber S. Nonlocal energy transport effect in radiation hydrodynamics simulations of intense laser pre-pulse interaction with solid targets. URL `https://ddfiw2016.sciencesconf.org`, presented at the 12th Direct Drive and Fast Ignition Workshop (DDFIW2016), Talance, France.

[116] Holec M, Liska R, Weber S. On nonlocal transport based closure relations for radiation hydrodynamics. URL `https://www.multimat.math.tu-dortmund.de`, presented at the seventh International Conference on Numerical Methods for Multi-Material Fluid Flow (MULTIMAT 2015), Wurzburg, Germany.

[117] Holec M, Cotelo M, Velarde P, Liska R. Application of discontinuous Galerkin adaptive mesh and order refinement method to energy transport and conservation equation in radiation-hydrodynamics. URL `http://congress.cimne.com/PANACM2015/frontal/default.asp`, presented at the 1st. Pan American Congresses on Computational Mechanics (PANACM 2015), Buenos Aires, Argentina.

[118] Holec M, Liska R, Limpouch J, Weber S. Discontinuous Galerkin method for inherent coupling of radiation transport and hydrodynamics. URL `http://www.wccm-eccm-ecfd2014.org/frontal/default.asp`, presented at the 6th. European Conference on Computational Fluid Dynamics (ECFD VI) , Barcelona, Spain.

[119] The extreme light infrastructure project ELI. `http://www.eli-beams.eu`.

[120] Rus B, Bakule P, Kramer D, Naylon J, Thoma J, Green JT, Antipenkov R, Fibrich M, Novak J, Batysta F, *et al.*. Eli-beamlines: development of next generation short-pulse laser systems. URL `http://dx.doi.org/10.1117/12.2184996`, proc. SPIE 9515, Research Using Extreme Light: Entering New Frontiers with Petawatt-Class Lasers II, 951501.

[121] Treacy E. Optical pulse compression with diffraction gratings. *IEEE J. Quantum Elect.* 1969; **QE-5**:454–458.

[122] Strickland D, Mourou G. Compression of amplified chirped optical pulses. *Opt. Commun.* 1985; **56**:219.

[123] Dubietis A. *Opt. Commun.* 1992; **88**:433.

[124] Ross I. *Opt. Commun.* 1997; **144**:125.

[125] Utsumi T, Matsukado K, Daido H, Esirkepov T, Bulanov S. Numerical simulation of melting and evaporation of a cold foil target irradiated by a pre-pulse. *Appl. Phys. A-Mater.* 2004; **79**:1185.

[126] Flacco A, Guemnie-Tafo A, Nuter R, Veltcheva M, Batani D, Lefebvre E, Malka V. Characterization of a controlled plasma expansion in vacuum for laser driven ion acceleration. *J. Appl. Phys.* 2008; **104**:103 304.

[127] Carroll DC, Batani D, Evans RG, Glinec Y, Homann C, Jafer R, Kar S, Lindau F, Lundh O, Markey K, *et al.*. Dynamic control and enhancement of laser-accelerated protons using multiple laser pulses. *C. R. Phys.* 2009; **10**:188–196.

[128] Mckenna P, Carroll D, Lundh O, Markey K, Bandyopadhyay S, Batani D, Evans R, Jafer R, Kar S, Neely D, *et al.*. Effects of front surface plasma expansion on proton acceleration in ultraintense laser irradiation of foil targets. *Laser Part. Beams* 2008; **26**:591–596.

[129] Guillot T. Review: Interiors of giant planets inside and ouside the solar system. *Science* 1999; **286**:72–77.

[130] Nuckolls J, Wood L, Thiessen A, Zimmerman G. *Nature* 1972; **239**:139.

[131] Driver K, Militzer B. *Phys. Rev. Lett.* 2012; **108**:115 502.

[132] Stanley S, Bloxham J. *Nature* 2004; **428**.

[133] Falk K, Fryer C, Gamboa E, Greeff C, Johns H, Schmidt D, Smid M, Benage J, Montgomery D. X-ray thomson scattering measurement of temperature in warm dense carbon. *Plasma Phys. Contr. F.* 2016; :submitted.

[134] Mattssoni T, et al. *Phys. Rev. B* 2010; **81**:054 103.

[135] Knudson M, Desjarlais M, Dolan D. *Science* 2008; **322**:1822.

[136] Lambert F, Recoules V. *Phys. Rev. E* 2012; **86**:026 405.

[137] Benedict X, et al. *Phys. Rev. Lett.* 2014; **89**:224 109.

[138] Gregori G, et al. *Phys. Rev. Lett.* 2008; **101**:045 003.

[139] Falk K, et al. Quantitative analysis of treatment process time and throughput capacity for spot scanning proton therapy. *Phys. Plasmas* 2014; **21**:056 309.

[140] Olson R, Leeper R. Alternative hot spot formation techniques using liquid deuterium-tritium layer inertial confinement fusion capsules. *Phys. Plasmas* 2013; **20**:092 705.

[141] Boehly T, et al. *Opt. Commun.* 1997; **133**:495.

[142] Celliers PM, Bradley D, Collins G, Hicks D, Boehly T, Armstrong W. Line-imaging velocimeter for shock diagnostics at the OMEGA laser facility. *Rev. Sci. Instrum.* 2004; **75**:4916.

[143] Miller J, Boehly T, Melchior A, Meyerhofera D, Celliers P, Eggert J, Hicks D, Sorce C, Oertel J, Emmel P. Streaked optical pyrometer system for laser-driven shock-wave experiments on omega. *Rev. Sci. Instrum.* 2007; **78**:034 903.

[144] Gregori G, Gericke D. Low frequency structural dynamics of warm dense matter. *Phys. Plasmas* 2009; **16**:056 306.

[145] Kresse G, Hafner J. *Phys. Rev. B* 1983; **47**:558.

[146] Bennett B, Johnson J, Kerley G, Rood G. *Technical Report LA-7130*, Los Alamos National Laboratory, Los Alamos, NM 1978.

[147] Hu S, et al. *Phys. Rev. E* 2015; **92**:43 104.

[148] Langdon AB. Nonlinear inverse brehmsstralung and heated-electron distributions. *Phys. Rev. Lett.* 1979; **44**:575–579.

[149] Bissell JJ, Ridgers CP, Kingham RJ. Super-gaussian transport theory and the field-generating thermal instability in laser-plasmas. *New J. Phys.* 2013; **15**:025 017.

[150] Zhu SP, Gu PJ. A heat transport model including the effect of non-Maxwellian electron distribution and its application in laser produced plasma. *Chinese Phys. Lett.* 1999; **16**:520–522.